Preparation, Properties and Applications of Chemically Synthesized Semiconducting Nanostructures

THESIS

SUBMITTED TO

BABASAHEB BHIMRAO AMBEDKAR UNIVERSITY
(A CENTRAL UNIVERSITY)
LUCKNOW

BABASAHEB
BHIMRAO
AMBEDKAR
UNIVERSITY
LUCKNOW
प्रज्ञा शील करुणा
ESTABLISHED 1996

FOR THE DEGREE OF

Doctor of Philosophy

IN

APPLIED CHEMISTRY

Submitted by

Gaurav Hitkari

ENROLMENT NUMBER. 859/12

Under the Supervision of

Prof. Gajanan Pandey

DEPARTMENT OF APPLIED CHEMISTRY
SCHOOL FOR PHYSICAL SCIENCES
BABASAHEB BHIMRAO AMBEDKAR UNIVERSITY
VIDYA VIHAR, RAE BARELI ROAD, LUCKNOW-226 025

2018

Dedicated to

Beloved Parents

For Endless Support, Love and Cooperation

CERTIFICATE

This is to certify that the thesis titled **"Preparation, Properties and Applications of Chemically Synthesized Semiconducting Nanostructures"** submitted by Ms/Mr. **Gaurav Hitkari** is an original research work and has not been previously submitted in part or full for the award of any other degree or diploma to this or any other university.

The thesis submitted to Babasaheb Bhimrao Ambedkar University Lucknow satisfies all the requirements as stipulated in the Doctor of Philosophy (Ph.D.) regulation-1999 as amended in 2008/2010/2013 and it is fit for submission and evaluation for the award the of the degree of Doctor of Philosophy of the University.

Supervisor 2/2/18

Head of department

7/02/18

DECLARATION

I, **Gaurav Hitkari** declare that the thesis entitled "**Preparation, Properties and Applications of Chemically Synthesized Semiconducting Nanostructures**" submitted by me for the degree of Doctor of Philosophy is the record of work carried out by me under the guidance of **Prof. Gajanan Pandey at Department of Applied Chemistry, School For Physical Science, Babasaheb Bhimrao Ambedkar University (A Central University), Lucknow, India** and has not formed the basis for the award of any degree, diploma, associate ship, fellowship, titles in this or any other University or other institution of higher learning. I further declare that the material obtained from other sources has been duly acknowledged in the thesis.

Gaurav Hitkari
Department of Applied Chemistry
Babasaheb Bhimrao Ambedkar University
Lucknow-226025,
India

Date: 02/02/2018

Place: Lucknow

ACKNOWLEDGEMENT

Foremost, I wish to express my profound sense of deepest gratitude and sincere thanks to my honorable and esteemed supervisor ***Prof. Gajanan Pandey (Ex-Head of Department)*** *for the continuous support of my Ph.D. study and related research, for his patience, motivation, and immense knowledge. His guidance helped me in all the time of research and writing of this thesis. I could not have imagined having a better advisor and mentor for my Ph.D. study.*

I convey my sincere thanks to all the faculty members of Chemistry department: ***Prof Kaman Singh (Head & Dean), Assistant Prof. Dr. Jyoti Paney, Assistant Prof. Dr. Shailesh Kumar, Assistant Prof. Dr. Preeti Gupta and Assistant Prof. Dr. Jawahar Lal and Dr. Alok Kumar Singh*** *for their insightful comments and encouragement, but also for the hard question which incented me to widen my research from various perspectives. A warm thank goes to the departmental Lab Staff for providing friendly and motivating environment during the research work.*

I wish to express my reverence and sense of deep gratitude to ***Mr. Shushil Pandey (Lecturer at K D Campus Pvt Ltd)*** *and* ***Dr. Prashant Singh (Assistant Professor ARSD College University of Delhi)*** *for his invaluable, insightful comments and suggestions to improve the quality of this work.*

I thank my fellow labmates ***Ms. Sandhya Singh, Dr. Manisha Gautam, Dr. Vivek Pandey, Mr. Satya Prakash Gupta, Mr. Ajay Kumar, Mr. Deepak Kumar, Mr. Sumit Kumar, Mr. Ashok Kumar, Mr. Gulam Abbas, Mr. Sabir Shekh and colleagues Dr. Rakesh Kumar Sonker (DAP BBAU) and Dr. Ravindra Kumar (DAP BBAU)*** *in for the stimulating discussions, for the sleepless nights we were working together before deadlines, and for all the fun we have had in the last five years.*

I would like to express my special thanks to my friends ***Assistant Professor Dr. Mukesh Kumar (MMV BHU) Dr. Dilip Kumar (Faculty of Management Studies), Dr. Shiv Sunder Yadav (Indian Institute of Technology, BHU), Dr. Saurabh Yadav (Indian Institute of Technology, Roorkee), Dr. Dinesh De (Indian Institute of Technology, Kanpur), Dr. Sharad Kumar Asthana (Department Of Chemistry BHU), Mr. Sanjay Kumar (Regional Centre for***

Biotechnology Faridabad), Mr. Ashok Kumar (Assistant Teacher), Mr. Sunil Sen Bharti (Assistant Teacher) and Dr. Brijesh Ranjan (DAAS BBAU) who helped me throughout this journey. In particular, I am grateful to Dr. Kaushal Kumar Upadhyay (Department Of Chemistry BHU) for enlightening me the first glance of research.

My deepest gratitude goes to my affectionate friends Mr. Ajay Kumar (DAS BBAU), Mr. Ram Kumar (DAAS BBAU), Mr. Ankit Khokhar (Bhaiya) and Sandeep Kumar Aladia (CMA Kapoorthala) for their continuous moral support and encouragement.

I devote this thesis to my beloved parents (Pita Ji Late Shri Sita Ram and Mata ji Late Smt Sarswati Devi) for their lot of love, support and sacrifice from the early first day of my journey of life. I also express my sincere hearty thanks to all my brothers (Advocate Mr. Arvind Kumar Kapoor and Advocate Mr. Prakash Chandra Kapoor), sister in law (Mrs. Bindoo Kumari (Assistant Teacher) and Mrs. Neetu Devi), my all sisters (Mrs. Sunita (BHU), Mrs. Madhubala (Assistant Teacher) and Mrs. Shashibala (Assistant Teacher) and my all brother-in-law (Mr. Rajbali (chief in Indian Railway), Mr. Bhaskar Rishikesh Kumar Bharti (RPF, Indian Railway) and Mr. Prem Chandra (Assistant Teacher) for providing me with every kind of support. I would acknowledge the sweet smile of my precious nephew Mr. Abhay Pratap (Putter) and dear nieces Ms. Sweety Kapoor (Putree) and angel Stuti Kapoor which inspired and imparted happiness in my life and gave strength to overcome the failures and to start over again.

Last, but not least, I would like to thank the authors of various research articles and books whose work has been consulted, utilized and cited in my thesis.

Gaurav Hitkari

(Research Scholar)

***

ABSTRACT

Nanotechnology and nanoscience is a newly advanced prospective area to import welfares to various fields of investigation and application in the world of sciences. The significance means of prefix “nano” is one billionth. The scaling of nanometer is equivalent to a billionth of a meter scale, or 10^{-9} part of a meter which implies that these structures are extremely small (e.g: there is an inch equal to 25,400,000 nanometers or a single sheet of newspaper is nearly 100,000 nanometers thick or ten thousand times lesser compare to the width of a human hair).

Nanostructures are any shape and size of the intermediate structure at a microscopic or molecular level which may have one or more dimensions in the range of 100 nm or less. Nanostructures have various commercial and scientific application in areas like drug delivery, analytical chemistry, bio-encapsulation, electronics, magnetics, optical and mechanical devices.

In the modern area of nanotechnology, there are numerous kind of nanostructures such as zero-dimensional (0-D) e.g. quantum dot, fullerene, one dimensional nanostructure (1-D) e.g. nanotubes, nanorods/wires/tubes, two dimensional (2-D) e.g. graphene and three dimensional (3-D) e.g. graphite has fascinated the terrific attention due to their high aspect ratio and fascinating properties. There is various type of method are employed for the fabrication of different type of nanostructure and nanocomposite materials. Among the synthetic process, the chemical method is the most common approach for the synthesis of nanoparticles and composite materials due to high-purity, high functioning, low cost and easy availability.

The commercial use of synthetic dyestuffs in various industries like paper, textile, plastic leather, printing, and food industries. Among the numerous dyestuffs,

most are synthetic organic dyes of an azo compound such as congo red (CR), methyl orange (MO), and methylene blue (MB) which comprise chromophore (-N=N-) in their molecular composition. Water contamination with these azo dye is one of the major consequences which continuously causing increasing threats to terrestrial as well as aquatic life.

Over the past two decades, a great deal of research efforts has been made towards the development of nanostructures/nanoparticles for the practical applications in the removal of organic dye-stuff from the waste-water to continuous environmental monitoring.

The whole research work is divided into seven chapters. First chapter comprises the general introduction of nanomaterial's and nanostructures containing preparation methods including physical, chemical and biological methods. The exhaustive literature review on the topic and the objective of the present work have been discussed. This chapter also containing the general characteristics and applications of nanostructure/nanoparticles and the effect of it shape, size and orientations.

In the second chapter the various instrumentation technique is discussed for identification of prepared nanoparticles and nanostructured materials.

In the third chapter, zinc oxide (ZnO) and ZnO-ZnS nanocomposite materials have been prepared by simple chemical co-precipitation method. The X-ray diffraction analysis revealed the formation of ZnO and ZnO-ZnS crystalline materials. FESEM and HRTEM analyses indicated the formation of flake-like ZnO and sheet-like ZnO-ZnS structures. Energy dispersive X-ray (EDS) study further established the formation of ZnO and ZnO-ZnS materials. In the FTIR spectrum the presence of Zn-O symmetric stretching vibration at 442 cm^{-1} and 809 cm^{-1}, due to weak vibration of ZnO, while the other peak at 687 cm^{-1} due to Zn-S symmetric bending vibration

proved the formation of ZnO-ZnS composite material. Optical absorption spectrum showed that the band gap energy decreased for ZnO-ZnS composite compared to the pure ZnO NPs. The photoluminescence spectral analysis shows that the broad emissions spectrum caused due to several different bands, owing to the presence of zinc vacancies, oxygen vacancies, and surface defects. The photocatalytic performance of these samples was tested for degradation of a dye methylene blue under UV light exposure. ZnS-ZnO composite shows the higher dye degradation efficiency (93 %) than that of pure ZnO (55 %).

In the fourth chapter, ZnO, and ZnO/CuO nanocomposites have synthesized by simple chemical co-precipitation method through calcination at 400 °C for 4hrs. Prepared nanocomposite samples were appraised by X-ray diffraction (XRD), energy dispersive X-ray spectroscopy (EDX), scanning electron microscope (SEM), high-resolution transmission electron microscopy (HRTEM), Brunauer-Emmett Teller analysis (BET), and UV-visible spectroscopy. From the XRD analysis, it's proved that the forming of crystalline nanocomposites material while magnified SEM images showed that single hexagonal structural of pure ZnO and agglomeration of grain like structure of ZnO/CuO composite by calcination on 400 °C. HRTEM investigation proves that hexagonal structure of pure ZnO is obtained by aggregation of the knife-like structure. BET analysis accepted that the mesoporous nature of nanocomposites. UV-Visible spectra have been also discussed the optical behaviour of the materials. The photocatalytic operation of the fabricated materials, ZnO and ZnO/CuO composite was well-established for the photo-degradation of Congo red (CR) organic waste in aqueous phase under irradiation of visible light. The ZnO/CuO composite shown better photocatalytic activity for decolourization of CR dye.

In the fifth chapter, ZnO/γ-Fe_2O_3 nanocomposites are prepared by the simple co-precipitation method. The prepared composites materials were characterized by X-

ray diffraction (XRD), high resolution scanning electron microscope (HRSEM), energy dispersive X-ray spectroscopy (EDX), Brunauer Emmett Teller analysis (BET), and UV-visible spectroscopy. XRD confirmed the formation of hexagonal wurtzite nature of ZnO and cubic structure of γ-Fe_3O_4 in the composite materials, while SEM images showed spherical and rod-like structure. BET analysis confirmed the mesoporous behavior of nanocomposites. UV-Visible spectroscopy has been applied to the measurement of band gap and photo-oxidation behavior of organic dye methyl blue and rhodamine B (Rh B). Experimental data suggested that ZnO/γ-Fe_2O_3 nanoparticles catalyst possessed the highest catalytic activity towards Rh-B degradation in aqueous solution as comparison to the methylene blue at the tested concentration level of 1×10^{-5} M.

In the sixth chapter, achieve effective, economic, and easily synthesizable photocatalyst like as ZnO, ZnO/ZnS and ZnO/ZnS/α-Fe_2O_3 nanocomposites have been prepared by a simple chemical synthetic route in the aqueous medium for the degradation of dye methyl orange (MeO). Phase, crystallinity, surface structure and surface behavior of the synthesized materials have been determined by X-ray diffraction (XRD) and Brunauer Emmett Teller analysis (BET) technique. XRD revealed that ZnO, ZnO/ZnS and ZnO/ZnS/α-Fe_2O_3 are good crystalline and in nano-region. From the XRD patterned the percentage composition of photocatalyst have also been determined. From the BET analysis, the prepared materials show mesoporous behavior containing type IV curves along with H4 hysteresis. The ZnO/ZnS/α-Fe_2O_3 composite sample shows more surface area as comparison to the other materials. From the UV-visible spectra, the band gap energy of the materials has been determined. Photoluminescence spectra (PL) have been used to determine the emission behavior and explanation of the surface defect present on the surface of the composites materials. In PL spectra the intensity of UV peak of ZnO/ZnS is lowered

than ZnO while in case of ZnO/ZnS/α-Fe_2O_3, the intensity become further decreased. The visible emission spectra of ZnO/ZnS is increases as comparison to ZnO NPs where ZnO/ZnS/α-Fe_2O_3 is further increases from ZnO/ZnS. The lowering of the intensity of UV emission peak and increases of the intensity of visible emission is the resultant of decrease of recombination of electrons and holes which indicates the enhanced the rate of photocatalytic reaction. The as-synthesized composite materials have been used for the photocatalyst for degradation of dye MeO. The photo-degradation data revealed that the ZnO/ZnS/α-Fe_2O_3 is the best photocatalyst material among these materials for the degradation of dye MeO. In the present work, ZnO, ZnO/ZnS and ZnO/ZnS/α-Fe_2O_3 nanocomposites have been synthesized via simple chemical co-precipitation followed by calcination at 600 °C for 1/2 h. Nanocomposite powders were characterized by X-ray diffraction (XRD), scanning electron microscope (SEM), energy dispersive X-ray spectroscopy (EDX), particle size distribution, Brunauer Emmett Teller analysis (BET), photoluminescence and UV-visible spectroscopy. XRD confirmed the formation of crystalline nanocomposites while SEM images shown sheet-like ZnO and ZnO/ZnS and needle-like acicular ZnO/ZnS/α-Fe_2O_3 nanocomposite. BET analysis confirmed the mesoporous behavior of nanocomposites. Optical properties and band gap energy of as-synthesized materials were determined using UV-Visible spectral analysis. Photoluminescence spectra have been used to determine emission properties and photo-oxidation behavior of as-synthesized materials for degradation of methyl orange. ZnO/ZnS/α-Fe_2O_3 nanocomposite exhibited the highest photocatalytic activity among the three samples for degradation of methyl orange (MeO).

In the last seventh chapter, summary and conclusion of all the work has been discussed.

***

CONTENTS

List of Abbreviation

Serial No	Name of Compound	Full Name
1.	NPs	Nanoparticles
2.	NTs	Nanotubes
3.	QDs	Quantum Dots
4.	BNCT	Boron Neutron Capture Therapy
5.	CNT	Carbon Nanotube
6.	GaN	Gallium Nitride
7.	ZnO	Zinc Oxide
8.	FED	Field Emission Displays
9.	CVD	Chemical Vapor Deposition
10.	PVD	Physical Vapor Deposition
11.	TiO_2	Titanium Dioxide
12.	CMC	Critical Micelle Concentration
13.	VB	Valence Band
14.	CB	Conduction Band
15.	Eg	Band Gap Energy
16.	SnO_2	Stannic Oxide
17.	SnS_2	Stannic Sulfide
18.	AOPs	Advanced Oxidation Processes
19.	ZnO-ZnS	Zinc Oxide –Zinc Sulfide
20.	ZnO/ZnS/α-Fe_2O_3	Zinc Oxide/Zinc Sulfide/Iron Oxide
21.	ZnO/CuO	Copper-Zinc Oxide
22.	CR	Congo red

23.	Rh-B	Rhodamine B
24.	MO	Methyl Orange
25.	MB	Methylene Blue
26.	P-XRD	Powder X-ray Diffraction
27.	TEM	Transmission Electron Microscopy
28.	SEM	Scanning Electron Microscopy
29.	EDS	Energy Dispersive X-ray Spectroscopy
30.	UV-Vis	Ultraviolet-Visible Spectrophotometry
31.	FTIR	Fourier Transform Infra-Red Spectroscopy
32.	PL	Photoluminescence Spectroscopy
33.	PLE	Photoluminescence Excitation Spectroscopy
34.	TRPL	Time-Resolved Photoluminescence Spectroscopy
35.	BET	Brunauer-Emmett-Teller
36.	BJH	Barrett-Joyner Halenda

LIST OF FIGURES

LIST OF TABLES

***

Chapter 1
General introduction and objective of the current work

Chapter 1
General introduction and objective of the current work

"This chapter introduces a general view about nanotechnology, nanostructures, semiconducting nanostructures along with various kinds of nanostructures like nanoparticle and nanocomposites. It is also containing various type applications these materials in a different field in the modern life. The significant synthetic process of nanostructures/nanoparticles and composites as photocatalyst are desperately reviewed and expediency of composite nanostructures have been successfully considered in detail. The leading objectives and a brief framework of the present examinations carried out in this thesis are presented in brief."

1.1. Introduction:

1.1.1. Nanotechnology:

Nanotechnology and nanoscience is a newly advanced prospective area to import welfares to various fields of investigation and application in the world of sciences. The idea of nanotechnology was first expressed by Dr. Richard Feynman (American physicist) in his assign talk "There's plenty of room at the bottom", in 1959 [1]. But the nanotechnology term was initially introduced by Japanese scientist Professor Norio Taniguchi at International Conference on Production Engineering at Tokyo Science University Tokyo in 1974 [2]. Ever since Eric Drexler formulates the term, "Nanotechnology" in his book, "'Engines of Creations" in 1986 [3] and the popularization of the knowledge of nanotechnology by the book ***Nanosystems:*** *"molecular machinery, manufacturing and computation*" [4]. Although the meaning of "nano" differs from area to region and country in country and is commonly used as "catch all" for lots of things, nanotechnology is commonly described as to easily understanding, control and renovation of material on the atomic and molecular scale or in the sequence of particles lesser in size compare to 100 nm to produce materials built from them essentially with novel properties and behavior [5, 6]. The significance means of prefix "nano" is one billionth. The scaling of nanometer is equivalent to a billionth of a meter scale, or 10^{-9} part of a meter [7], which implies that these structures are extremely small (e.g: there is an inch equal to 25,400,000 nanometers in other words single sheet of newspaper is nearly 100,000 nanometers thick or ten thousand times lesser compare to the width of a human hair). For evaluation, the DNA's diameter, lymphocytes, and viruses are 2.5, 30-50, and nigh on 7000 nm, respectively [8].

In modern years, nanotechnology is intrinsically multidisciplinary field across the long-established boundaries between information technology, engineering, chemistry, physics, biology and mathematics. It gives a great commitment to provide us a wonderful future with several breakthroughs that modify the direction of technological progress in the massive range of utilization. It summaries a comprehensive study of research and improvement with the determination of assessing its prospective for technological innovation. However, it has the prospective to produce incoming industrial transformation that will have a considerable impression on humanity and day by day life.

1.2. Nanostructures:

Nanostructures are any shape and size of the intermediate structure at a microscopic or molecular level which may have one or more dimensions in the range of 100 nm or less (Figure 1.1) [5, 9]. The nanostructured samples carry enhanced behaviour like improved hardness, high strength, ductility in ordinarily inelastic materials, erosion resistance, corrosion-resistance, wear-resistance and advanced chemical properties [10]. They are more powerful related to their conventional and commercially accessible supplements. They have various commercial and scientific relevances in areas like drug delivery, analytical chemistry, bio-encapsulation, electronics, magnetics, optical and mechanical devices.

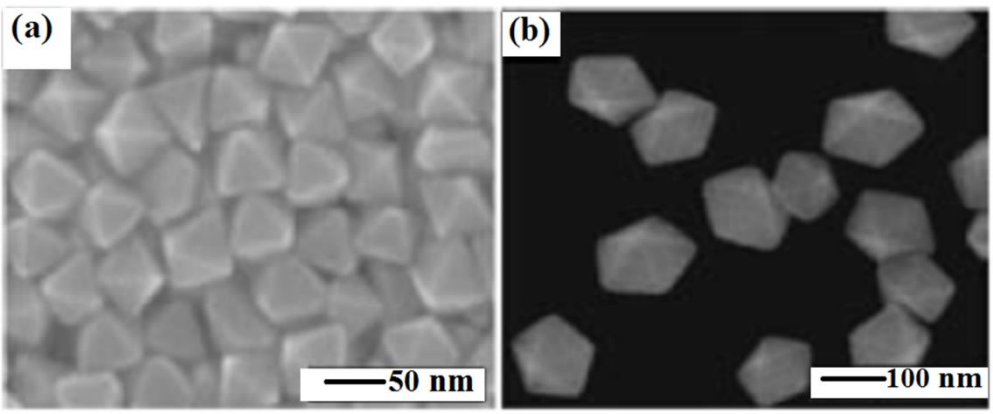

Figure 1.1: Spherical structure of nanoparticles [11].

In the modern area of nanotechnology, there are numerous kind of nanostructures like one-dimensional nanostructure (1D) e.g. nanotubes, nanorods, nanoribbons, nanowires etc. has to fascinate the terrific attention due to their high aspect ratio and fascinating properties [12-15]. In this phase, two-dimensional electron confinement arises and delocalization occurs along the axis of the nanorod/wire/tube. One dimensional arrangement of several metals, metal oxide, semiconductor and its composites have also known and prepared by different routes. Also, their application has been projected for different properties like sensors, solar cells, supercapacitors etc.

Nobel Prize of the year 2010 was honored to "Graphene". It is a single layered arrangement of carbon atoms containing sp^2 hybridization with a honeycomb structure. Due to its own excited chemical and physical behaviours, it is used as supporting substances with potential application in various devices [16]. On the behalf of aforementioned research, it is proved that the graphene is a two dimensional (2-D) substances and its two-dimensional nature performs a significant role in identifying their exceptional set of behaviour, recently preparation and assessing of several inorganic equivalents of graphene i.e. various inorganic 2-D substances have enticed considerable attention [16, 17]. These inorganic 2-D substances generally have mono layered structures. These layer of graphene are mainly comprising of atoms or molecules. These monolayers are interconnected through the weak van der walls interaction and separated via exfoliation. Naturally, the thickness of these monolayered substances is reasonably less than 100 nm whereas; the width and length may outstrip to the nanometric dimensions. Remarkably, it has been attained that on varying the number of the monolayer, there was dramatically alteration in the electronic properties. Among the numerous inorganic 2-D substances, the transition metal oxides and sulfides are well known for their comprehensive range of electronic

and optical properties, have increased remarkable attention over the past few years and are considered as biggest competitors of graphene.

1.2.1. Types of nanostructures:

1.2.1.1. Nanoparticles:

Generally, nanoparticles are a most fundamental unit of nanotechnology and well defined as particles of 1 to 100 nm size in the diameter and principally zero-dimensional (0-D) in the structure. In general, the most of the nanoparticles are lesser in size and contain 20-15000 of atoms and remain in a range of the Newtonian and quantum scales [18]. Nanoparticles consist of single crystal, amorphous particles and polycrystalline substances with all probable morphologies like cubes, spheres and platelets with a representative size of petty nanometers. However, recently this field has attracted very much due to our ability to synthesize, engineer of these nanoparticles and utilize them for mankind. Due to the more interest and ability of researcher, there has been an evolutionary investment in the field of nanotechnology and its applications [19].

1.2.1.2. Nanotubes:

A nanotube is a one form of nanoparticle/nanostructural materials with one dimensional (1-D) tube-like hollow structure in the nanometer scale. It can be able to work as a cylinder to control the other nanoparticles and also applied as an electrical insulator or conductor.

A carbon nanotube is the first discovered nanotube materials. L. V. Radushkevich and coworker reported the well-defined images of 50 nm diameters carbon nanotubes diameter in Soviet Journal of Physical Chemistry in 1952 [20]. When a single layer of the carbon nanotube is contained one tube of graphite is famous as a single-walled nanotube (SWNT) [21] or a numeral of parallel or side by side tubes is famous as multiwalled nanotubes (MWNTs). The image of SWNT &

MWNT was shown in the Figure. 1.2. The morphological structure of the nanotube is controlled its properties including conductance, density and lattice structure.

There are three kinds of carbon nanotubes with well-defined geometry are known. These three geometries are armchair, zig-zag, and chiral. These geometries may be classified on the behalf of enclosed carbon sheet arrangement into tube (Figure 1.2) [22].

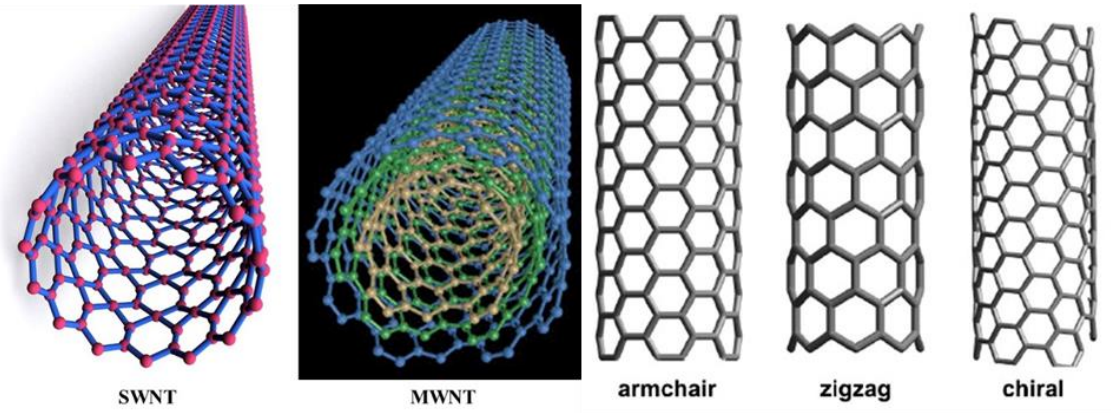

Figure 1.2: Types of carbon nanotubes (NTs) [21, 22]

Kontos et al. studied that the nanotubular (NTs) arrangement of titanium oxide (Figure 1.3) synthesized via electrochemical method by using ethylene glycol solvent-containing electrolytes. These nanotubular titanium oxide NTs are tested for removal of organic contaminants like toluene and benzene volatile under irradiation of UV light at room temperature and pressure. The photocatalytic behaviour varies on altering the length of the NT arrays [23].

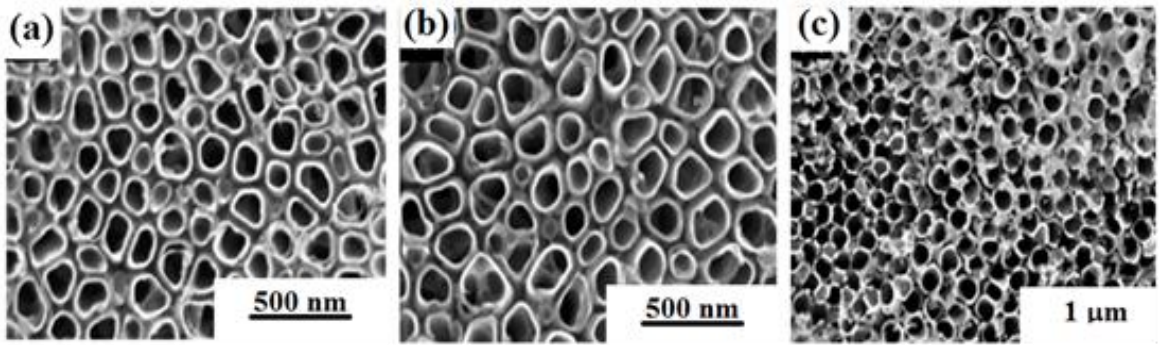

Figure 1.3: Titanium oxide nanotubes (NTs) [24]

1.2.1.3. Nanowires:

Nanowire is special kind of nanostructures with 1-D orientation of nanostructure (Figure 1.4) with cross-sectional diameter in nanometer (10^{-9} meters) range. This nanostructures contain the ratio of length and width is greater than 1000. Nanowires are also be understand on the behalf of thickness of the structure in which the nanostructures that have a strained thickness in 1 to 10 nm. At these levels, quantum mechanical effects are dominant, which used the term "quantum wires". The SEM micrograph of gallium and silver nitride nanowires are represented in Figure. 1.4. The nanomaterial reforming toward the nanowires to afford more promising electron transport with minimum recombination loss than that from nanoparticle-based solar cells. The main research work on the structural nanowire started with the simple vertically grown “nanowire forest”, and increased into more complex 2-D and 3-D classified nanostructures to improve higher photo-conversion efficiency.

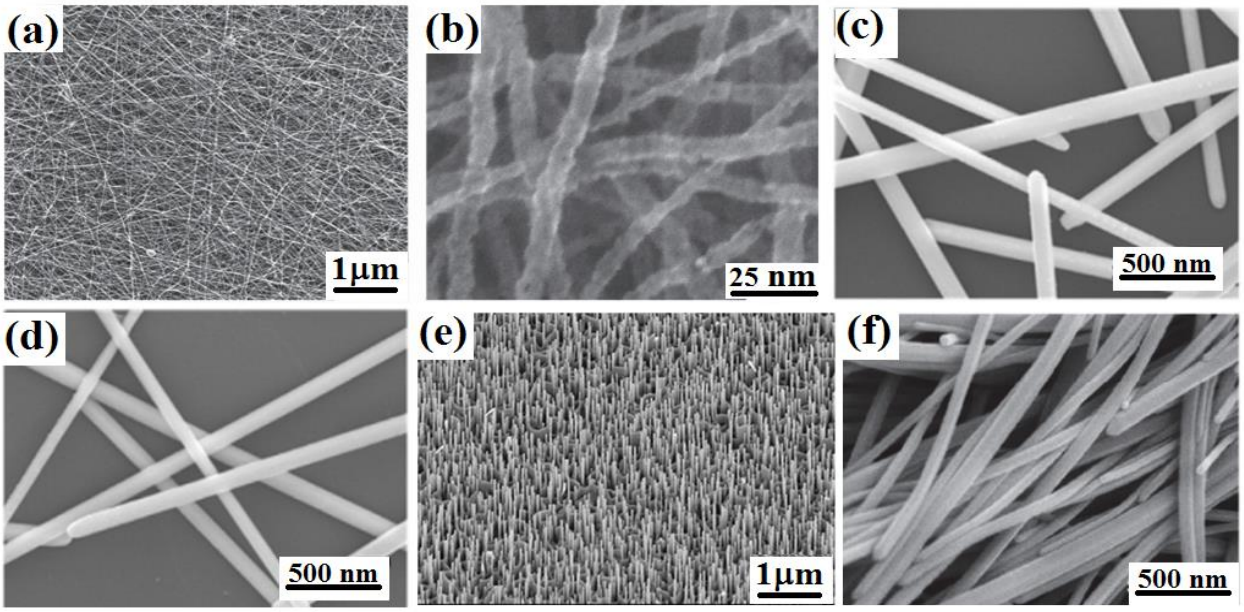

Figure 1.4: (a-b) structure of Pt-Fe [25] (c-d) Silver [26] and (e-f) ZnO nanowires [27]

1.2.1.4. Nanoribbons:

Nanoribbons are usually illustrated as two dimensional (2-D) layered structures with 1-50 nm width. Graphene were commonly received as nanoribbons. Pascal Ruffieux et al. mentioned that the Graphene-based nanoribbons structures performed well electronic properties than continued graphene. For instance quantum confinement in the form of armchair graphene nanoribbons and carbon nanotubes generate the considerable electronic band gaps that are related to their structural boundary conditions [28, 29]. Nanostructures containing zigzag edges are estimated to host spin-polarized electronic edge states and can consequently serve as key elements for graphene-based spintronics devices [30]. The electronic levels of nanoribbons are mostly governed by the structure of edges (armchair or zigzag). 2-D structure of nanoribbons has immense thermal as well as electrical conductivity. The some type of morphological arrangement of graphite nanoribbons are displayed in Figure 1.5.

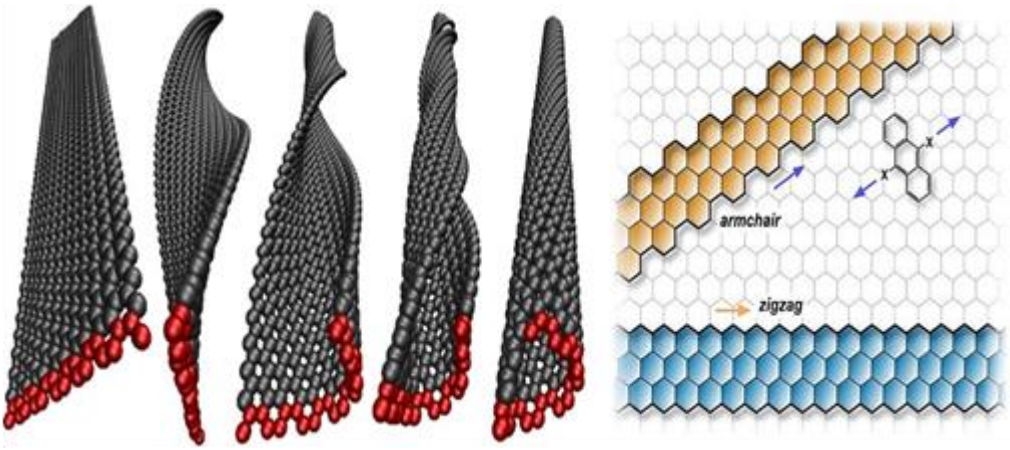

Figure 1.5: Structure of Graphite nanoribbons [30, 31]

1.2.1.5 Nanorods:

Nanorods material is one-dimensional (1-D) nanostructures substances with their standard appearance ratios of length and width are 3-5 and their dimensions ranges from 1-100 nm. They may be fabricated through semiconducting materials or pure metals. These nanorod structured materials are initially interacting from their

exclusive optical to photocatalytic properties and optoelectronics which intensely depend on their morphological shape and size. The nanorods of ZnO substances has been broad applicable for light-emitting diodes [32-34], photovoltaic devices [35], heterogeneous catalysis, and chemical sensors [36] because of its exceptional semiconducting and optical behaviours [37, 38]. The optical behaviour of these substances are the result of the electronic interaction between the electron of the conduction band of metal and electric field component of the electromagnetic radiation but in few cases of silver and gold metal indicates a forceful absorption in the visible part of the spectrum, and in turn to unusual bright colors which is not detected in the bulk material. The TEM micrograph of ZnO nanorods and gold nanorod are exposed in Figure 1.6.

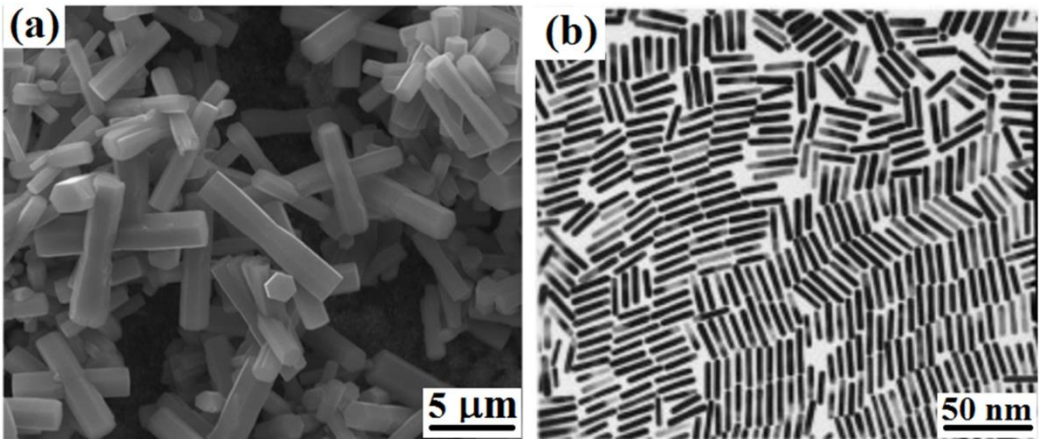

Figure 1.6: TEM of (a) ZnO nanorods [39] (b) gold nanorods [40].

1.2.1.6. Nanocomposites:

Nanocomposites are those multiphase materials which are achieved by the engineered consolidation of two or more dissimilar substances in which one phase of substance is identified as reinforcing phase, is in the kind of fiber sheets or particles and are implanted in the supplementary substances named as matrix phase. The fundamental occupations of matrix are to transmit stresses between the reinforcing phases of substance and to defend them from machine-driven and environmental

destruction although the existence of particles in a nanostructured composite increases its mechanical strength and stiffness etc. Therefore an interdependent arrangement of more than two micro-components that have dissimilar physical properties and in chemical arrangement and unsolvable in each other are known as nanocomposite materials. The main intention of fabrication of composite material is to boost the properties of each substance without cooperating on the weakness of each other. Composite materials have fruitfully replaced the traditional materials in several advances such as light weight and high strength usages. The main justification behind the collection of composite material for their relevance is principally because of its extraordinary tensile strength at a huge temperature and more strength-to-weight ratio, high toughness as well as high resistance. Generally, reinforcing materials of nanocomposite are robust with lesser in density while the matrix is typically ductile or tough material. If the nanocomposite samples are systematically planned and synthesized, it enhances the strength of the materials with the toughness of the matrix to attain a combination of required properties that not obtainable in any single material. The influence of the composites initially depends on the quantity, arrangement and type of particle reinforcement in the resin.

Nanocomposites nanostructures also exhibit outstanding consequences for numerous applications such as antibacterial activity, biosensor, gas sensor, paints, photocatalyst, sunscreen, solar cells, and so on. Commonly, the ZnO based heterogeneous nanocomposite substances including ZnO/metal oxide, ZnO/metal and ZnO/polymer perform photocatalysis in visible light, owing to the appearance of intermediate states by absorbs visible light to inhibit the recombination of exciton during the photo reaction [41-45].

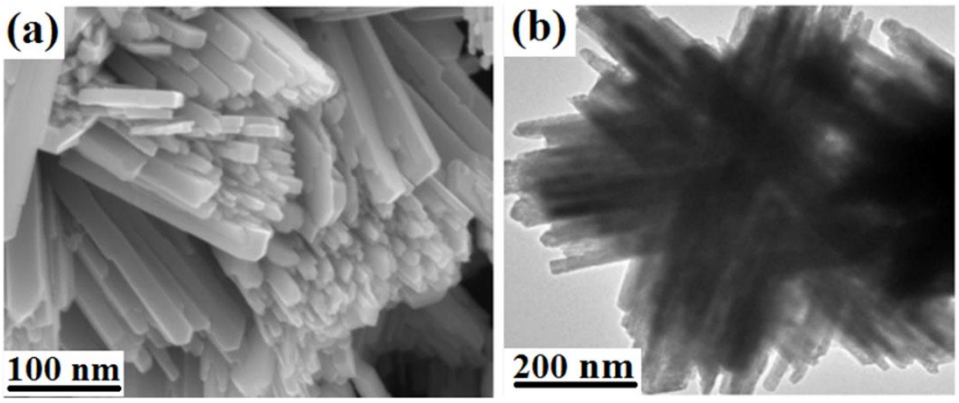

Figure 1.7: TEM image of graphene/WO_3 nanocomposites [46].

1.2.2. Properties of nanostructures:

Nanostructure materials behave as linkage among the bulk materials and materials having the atomic and molecular structures. The behaviour of a bulk semiconductor like as structural, electronic, optical and photocatalytic properties are not predictable to change with simple variations in size or shape i.e., in a bulk intrinsic semiconducting materials, the properties are size independent but depend only on the chemical composition of materials. Due to their inimitable shape and size dependent wealth such as photonics, optics, electronics and photocatalytic performance, nanostructured substances have got more interest.

Novel properties are fundamentally dependent into the shape and size of the nanostructured materials or thin films as a result of the contraction in the dimension of material or when the diminution in the length of nanoparticles below to the ferromagnetic exchange length, the Fermi level of electrons, etc. [47]. The typical properties of the nanostructured materials can be described by the following:

1.2.2.1. High Surface-to-Volume Ratio:

The outer surface of materials has more significant characteristics and show vital properties of nanostructured materials. The atoms existent on the outward of the nanostructure are more active chemically and thermodynamically related to their bulk

atoms due to they usually have less neighboring coordinate atoms and more pendent bonds. The number of defects present on the surface of nanoparticles, produce or generate sub-electronic states in the band gap, which shows strong trapping behavior for electron or hole (excitons). For spherical shaped nanoparticles, the relation between the surface area and radius is inversely proportional to each other. Therefore the relation between surface properties and size of nanostructures are interconnected [48-51] when the size decreases then surface to volume ratio increases and the surface effects become more apparent and thereby easier to explore. Apart from this, the gap between the energy levels of nanostructures are also concerned by these effects [49-51]. The system which has only few hundred atoms, the enormous number of these atoms will be positioned on the outward. The smaller the nanomaterial's, the greater the energy of the surface is contributed to the total energy of the system, which makes considerable changes in the properties of the materials.

Defects, shape and size dispersion, imperfection in structure, residual stresses, impurities, etc., in the material are also known to impact the ownership of nanoparticles materials.

1.2.2.2. Quantum confinement:

The optical, electronic and magnetic behaviour of nanomaterials mainly depends on its size [52]. The electronic energy levels are not in continuous as in bulk materials but are changed into discrete or quantized electronic levels, owing to the electronic confinement wavefunction to the spatial arrangement of the particles. This phenomenon is termed as quantum confinement and nanocrystals are also termed as quantum dots. Therefore, optically, the electronic transitions between the bands become discrete. Quantum confinement alters the optical performance of nanostructured materials. The increasing of band gap energy of semiconducting

substances as a result of the reduction in the size or quantum confinement influences as compared to the bulk materials [53]. For materials associated with larger nanoparticles, the excitation of electron throughout the band gap hinges on only the energy difference in the valence and conduction band. When the materials size are confined nearer to the Bohr radius then quantum confinement effect initiates to impact the excitation energy through the band gap [54-56]. Based on the orientation of confinement, a quantum confined nanostructure are categorized into three major categories as quantum wire, quantum well and quantum dots or nanocrystals. The basic type of quantum confined structure is shown in Table 1.1

Structure	**Quantum confinement**	**Number of free Dimensions**
Bulk	0	3
Quantum well	1	2
Quantum wire	2	1
Quantum dot/Nanocrystals	3	0

Table 1.1: Classification of quantum confined structures.

1.2.2.3. Brownian motion:

Brownian motion is originated by the irregular and continuous movement of miniature nanoparticles in a liquid or gas. The particles of the molecule are suspended entire the liquid or gas due to their inherently random nature of motions and collide with the bigger suspended particles randomly, making them movable. At macroscale, we hardly see the movement of particles or why they move but at the nanoscale, the particle moves wildly batted about by a smaller particle.

1.2.3. Applications of nanostructures:

1.2.3.1. Drug delivery:

Numerous kinds of nanostructures that can be used in the drug delivery system. Among these nanostructures, inorganic mesoporous materials have obtained significant consideration in the previous some decade as a consequence of their exceptional properties like high loading ability, chemical and physical robustness, less toxicity, straightforward and cheap manufacture in the laboratory. Dendrimers (hyperbranched molecules) are a class of nanomaterials which are fabricated for wide applications containing treatment for cancer. In the dendrimers nanomaterials, the drug molecules can be linked to the side branches. Dendrimers can be applied as specific coating agents to safeguard or distribute drugs to the required sites or work as time-release machines for biologically active agents in the body. They work as healing agents in the remedy of cancer, termed as Boron Neutron Capture Therapy (BNCT). In this medicinal procedure, the patient is given as an injection of an inert isotope of boron, (^{10}B) along with non-radioactive pharmaceutical. It is selectively migrated to the cancerous cell. When the ^{10}B injected, the patient is thermally treated by neutrons, these neutrons interact with the boron and produce alpha particles in the cancerous cells which destroy the tumor cells [57]. Dendrimers are also helpful in gene therapy by working as vectors. Vectors are transporters which transport genes through to the cell membrane to the nucleus [58]. Apart from biomedical applications, they are also applied to expand industrial processes.

1.2.3.2. Space Applications:

Carbon nanotube (CNT) nanostructures acquire various utilizations in space [59]. It significantly decreases the mass of the space structures. CNTs are very excellent substances for the usage in space elevator cables, as a result of their unique properties such as light-weight and more strengthen nature. CNTs are also applicable

for the further advancement of the solar cell. These weightless nano-devices use the reflection of sunlight's to move the spacecraft forward and save huge amount of commercial fuel in the form of energy. The use of nanostructures in the form of nanorobot for making the space suite of an astronaut to watchful and protect them from the space rubbles. Due to the lightweight and stretching nature of the nanostructured metals, they are used as a coating agent to provide the resistance from corrosion and also applicable for the application in aerospace constituents like as landing gear and constructive apparatus (drill bits and bulldozer blades).

1.2.3.3. Electronics:

Nanostructures like as CNTs are now hybrid with many types of polymer to fabricate conducting nanocomposite samples and applicable as an electromagnetic protector in cell phones and static electricity resistance in cars. The relevance of carbon nanotubes are well-known for the application in the flat displays. Recently gallium nitride (GaN) and zinc oxide (ZnO) nanoparticles are further used for LED displays [60]. At the modern time, ZnO nanowires are applicable for the development of LED display on the flexible substrates [61]. Laser devices are composed of conducting an array of quantum dots and nanowires [62]. CNTs and nanostructures of cobalt, manganese, and vanadium are applicable to the Lithium-ion batteries for its improved performance [63]. Coatings and doped semiconducting materials are also applicable for making some electrical products to protect its properties. Silver nanostructures with a plastic polymer resin are used to manufactures the major parts of the refrigerator in order to restrict the growth and enhance of a variety of bacteria and to quash odours. Besides, applying coating silver nanostructures as a novel method, this termed as 'silver wash' method is projected to expand the cleaning of clothes.

1.2.3.4. Displays:

The manufacturing of displays with small consumption of electric energy could be consummated by consuming carbon nanotubes (CNTs). Carbon nanotubes are a good conductor of electricity as a consequence of their petit diameter of several nanometers, they can also be applicable as field emitters with enormously high efficiency for field emission displays (FED).

1.2.3.5. Catalysis:

The catalysis assistance, particularly from nanostructured materials, assists catalysis owing to the large volume to surface ratio. There is an extensive range of application of nanostructures from the fuel cell, catalytic conversion of photocatalytic devices to the photocatalytic decontamination of organic dyestuff from the wastewater. Inorganic metal semiconductor nanostructure has huge surface area so that there is enhanced catalytic activity in the short time interval owing to the more catalytic reaction on the outward face.

Nanocatalysts are simply isolated and reproduced with greater retention of catalyst activities than their bulk counterparts. The catalyst can effort as two different roles in degradation process, they can be the site of catalysis or they may act as a support for the catalytic pathway [64].

1.3. Synthesis method of nanostructures:

Basically, there are two elementary processes applied for the assembly of nanostructures with various rates of quality, cost and speed:

- "Top-down" method, which involves the breaking down of bulky fragments of material to produce the preferred nanostructures as a physical method [65].
- "Bottom-up" method, which advise that the collection of single atoms along with molecules into essential nanostructures as a chemical method [66].

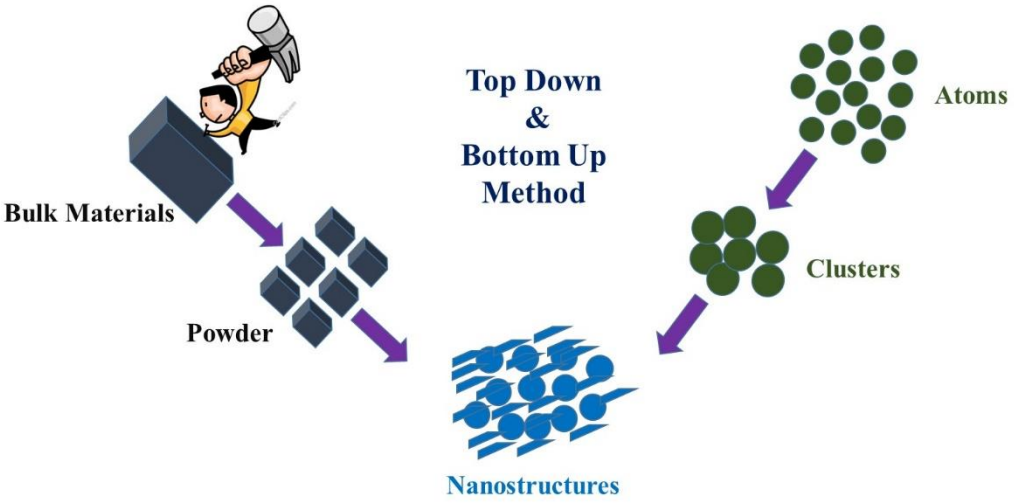

Figure 1.8: Top down and bottom up method for the synthesis of nanostructured materials

Many disciplines including biology, physics, chemistry and engineering are pursuing a wide assortment of methodologies for producing nanomaterials. The various techniques for fabricating nanoparticles are generally classified as either physical or chemical methods [67].

1.3.1. Chemical Method:

1.3.1.1. Chemical vapor deposition:

Chemical vapor deposition is a chemical technique pragmatic for the fabrication of high-purity and high functioning nanostructure solid samples. It is defined as any chemical process in which formerly precursor materials are vaporized and later on this vaporized materials are condescend for solidification to obtain the solid-phase material. These method are ordinarily applied to fabricate the coated materials to modify the corrosion resistance, electrical, mechanical, thermal, optical, and wear hindered properties of numerous substrates. They are also further applicable to design the free-standing bodies, fibers, films, and to infiltrate template to form nanocomposite samples. In recent period of time, they have been commonly explored to synthesis of several nanostructures. The chemically vapor deposition procedures

typically occur into a vacuum chamber. In this process, if no chemical reaction are takes place then this process is termed as physical vapor deposition (PVD); else, it is termed as chemical vapor deposition (CVD).

1.3.1.2. Sol-Gel Method:

Sol-gel method is a very inimitable and versatile wet chemical process to produce various advanced nanostructures materials with high-purity, low-cost at minimum temperature and informal control of shape and morphology [68-72]. In a characteristic sol-gel method, hydrolysis of precursors materials (like as inorganic salts, metal alkoxides, and organic polymers), polycondensation to produce suspended sol and then sol transformation occur into gel phase by freezing process then drying of wet gel along with heat treatment to obtained crystalline nanostructure materials. A vastly porous and low-density material termed as aerogel is achieved.

1.3.1.3. Hydrothermal synthesis:

Hydrothermal process is very common and versatile chemical synthetic method, is accompanied in a stainless steel containing container at appropriate high temperature which is termed as autoclave. These autoclave disciplined temperature or pressure along with applying Teflon liners with reaction medium (aqueous) solution. In this process, the temperature of the reaction medium could be enhanced to the boiling point of water solvent and extending pressure to vapour saturation. The core pressure which fashioned during the reaction is hinge on upon the quantity of solvent containing to the autoclave. There are a number of groups of the researcher are used this technique for the fabrication of ZnO and TiO_2 nanostructures [73-77].

1.3.1.4. Chemical co-precipitation:

Co-precipitation is also very widely adopted way for the production of desired nanomaterials like metal oxides nanoparticles from its inorganic precursor salt

solutions by the addition of a alkaline solution in inert atmosphere (in the existence of nitrogen or argon gases) at common temperature or at desirable temperature in huge scale with reasonable charge. The elemental composition, size and shape of the produced particles are mainly hinge on the precursor used (e.g., chlorides, sulfates, nitrates). Nanostructure materials is prepared by two general way, first, addition of basic solution in the very slow manner and secondly fast addition of basic solution in the reaction solution of precursor salt solution of metal [78-81].

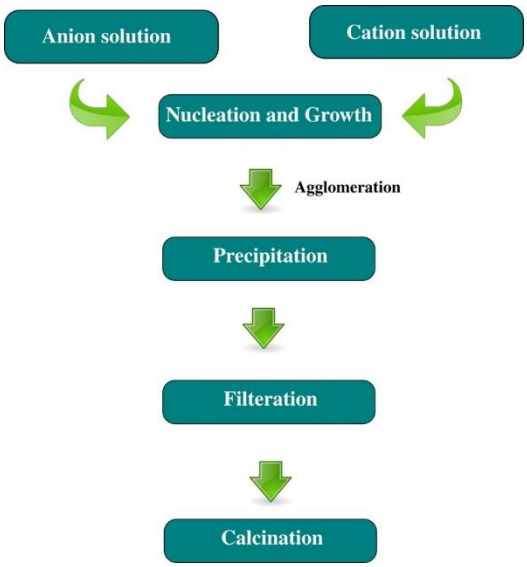

Figure 1.9: Co-precipitation method of synthesis of nanomaterials

1.3.1.5. Micelle and Inverse Micelle Methods:

The general definition of micelles is that the accumulation of molecules of surfactant which are well circulated in a colloidal liquid at above the surfactant concentration termed as critical micelle concentration (CMC). The CMC is the concentration of surfactants in free solution in equilibrium with surfactants in aggregated form. The micelles is composed of mainly two part head and tail. The head part of the micelle is hydrophilic in nature and is oriented toward the surrounding aqueous solvent and tail part is composed by hydrocarbon chains, hydrophobic in nature and directed interior of the micelle center. The concentration of

existing lipids in the solution has determined the self-organization of surfactants and lipid molecules. Lipids creates a layer on the outward of liquid and are dispersed in the solution below the CMC. The critical micelle concentration (CMC) is ascertained by chemical composition along with the ratio of the head area and the tail length significantly. Reverse micelles are establishes in nonaqueous solvent owing to the arrangement of hydrophilic head groups and hydrophobic tail group are inverse to each other. Means the head are moved toward inside the center of the micelles and the hydrophobic tails are moved outward toward the nonaqueous media. Micelles may have different type shape like as globular and roughly spherical, but cylinders, ellipsoids, and bilayers are also possible. The shape of a micelle is a toil of the molecular arrangement of its surfactant molecules and solution circumstances like as surfactant concentration, pH, temperature, and ionic strength.

1.3.1.6. Sonochemical Technique:

Sonochemical method used high energy sound waves for the construction of an ample range of nanoparticles sample containing huge-surface area of transition metals oxide, sulfides, alloys, carbides, and colloids. In the synthetic sonochemical process transient high energy ultrasound waves with standard frequency operated into a reaction solution of meticulously selected metal complex precursors. Owing to the vapor pressure produced of assured threshold during the sonolysis in the solvent the discontinuous waves of extension and miniaturization origin cavities to the construction, growth and collapse of bubbles in a liquid [82, 83].

1.3.1.7. Solvothermal synthesis:

The solvothermal technique is virtually analogous to the hydrothermal technique excluding that the non-aqueous solvent used in this method. In solvothermal process the temperature enhanced related to hydrothermal method, this

is the cause to usage a dissimilar types of organic solvents which have high boiling points. The solvothermal technique generally has much control than hydrothermal method for the fabrication of desired shape and size with homogeneous distribution of crystalline nanostructures of ZnO and TiO_2. The solvothermal technique has been adopted as versatile process for the fabrication of eclectic variety of nanostructures with required size and shape distribution [84-86].

1.3.2. Physical Methods:

1.3.2.1. Physical vapor deposition:

Physical vapor deposition (PVD) illustrates the several types of vacuum deposition techniques which can be operated to prepared nanomaterials and its coated substances. In the physical vapor deposition (PVD) method precursor of the materials are primally vaporized and then condensed to produce a solid nanostructure material. The principal of PVD technique contains thermal deposition, ion plating, ion implantation, sputtering, laser vaporization, and laser surface alloying.

1.3.2.2. Laser ablation synthesis:

This technique deals with fabrication of nanostructured materials by applying high energy laser beam. In this technique, a high energy laser beam is concentrated on the reaction mixture. The laser beam conveys a short beam of high energy which has adequate to evaporate the small portion of the metal objective which compressed in nanostructure materials in the reaction solvent. Commonly this technique is applied to produce nanostructured samples of gold, platinum and silver. However, this technique may also be expanded for the fabrication of other nanostructured materials like as metal alloys. The advantage of the sort pulse beam in this process to consent the ablation process to accept in a number of mediums, containing more volatile to vastly

reactive monomers. This process can be applied to a wide range of sample and reaction solvent assurance.

1.3.2.3. Mechanical milling process:

Mechanical milling is also applied to the fabrication of nanostructured materials on the industrial scale under physical method due to its simplicity and flexibility of the process. In this process, bulk material which is strong mechanically pulverized through in the milling process to fabricate nanoparticles which exist already in the micro dimensions.

1.3.2.4. Arc discharge synthesis:

Arc discharge technique is also a physical process for the synthesis of nanostructure materials. In this process, nanomaterial's are produced through arc assisted dissection of bulk materials. The general arc discharge process, two electrodes are hold nearer to each other in the reaction medium and high voltage applied between them to produce electrical disruption for producing arc discharge. Due to the enhancement of arc discharge to create thermal discharge and increase the temperature of the continue plasma to some thousand degree Celcius which potentially vaporized the surface of the electrode in the reaction medium. The produced vaporized metal compact in the reaction medium to fabricate nanostructures substances. The compacting reaction medium, applied voltage and electric current of the electrode are the foremost factors are responsible for the production of nanostructure materials. The enormously huge temperature created in between the nearer electrode can also assist to aggregation of atoms to produce a new particle that is dissimilar to the electrode materials. The carbon nanotubes are most frequently fabricated by this process.

1.4. Nucleation and Growth of nanoparticles in solution phase:

1.4.1. Classical Nucleation:

Nucleation is the process under which atomic nuclei work as a template for crystal growth. According to the Mullin the primary nucleation is an earlier instance of nucleation in the absence of any other crystalline matter [87]. This can be applied to understanding the nucleation of several chemical synthesis [88, 89]. However, the production of various types of solids does not constantly obey the classical method of crystallization in solution. Furthermore, Habraken et al. [90] explained that the ion-combination complexes come together classical and non-classical concepts for the biomimetic nucleation of calcium phosphate. When the uniform nuclei are formed in parent phase then homogeneous nucleation occurs, whereas heterogeneous nucleation produces at inhomogeneities structure such as container surface, impurity, grain boundaries and dislocation. In the liquid phase, heterogeneous happen much smoothly, since a stable nucleating surface is already present. The nuclei obtained by the homogeneous process can be thermodynamically measured by the total free energy of a particle described as summation of the surface free energy and the bulk free energy [87, 91]. Suppose the radius of the spherical nanoparticles is r, the surface energy γ and the free energy of bulk crystal ΔG_v, providing a total free energy ΔG are represented in equation 1.1. The own free energy of crystal, ΔG_v is depends upon the atmospheric temperature T, Boltzmann's constant k_B, supersaturation of solution S, and its own molar volume v. then ΔG_v is described as in equation 1.2.

$$\Delta G = 4\pi r^2 \gamma + \frac{4}{3}\pi r^3 \Delta G_v \tag{1.1}$$

$$\Delta G_v = \frac{-k_B T \ln(S)}{v} \tag{1.2}$$

The surface free energy are always a positive value due to this reason the crystal free energy are always a negative quantity. It is possible to obtain maximum free energy, which passes through a nucleus forming a stable nucleus by differentiating ΔG with respect to r and give it to zero dΔG/dr = 0, which provides a critical free energy, equation 1.3. By this pathway the critical free energy is described in equation 1.4:

$$\Delta G_{crit} = \frac{4}{3}\pi\gamma r_{crit}^{\ 2} = \Delta G_{crit}^{homo} \tag{1.3}$$

$$r_{crit} = \frac{-2\gamma}{\Delta G_v} = \frac{2\gamma v}{k_B T \ln S} \tag{1.4}$$

This critical radius related to the minimum size at which a particle can stay alive in the solution in the lack of redissolved. The same thing is applicable for the particles free energy, where the critical free energy is mandatory to achieve stable particles in the solution (Figure 1.10).

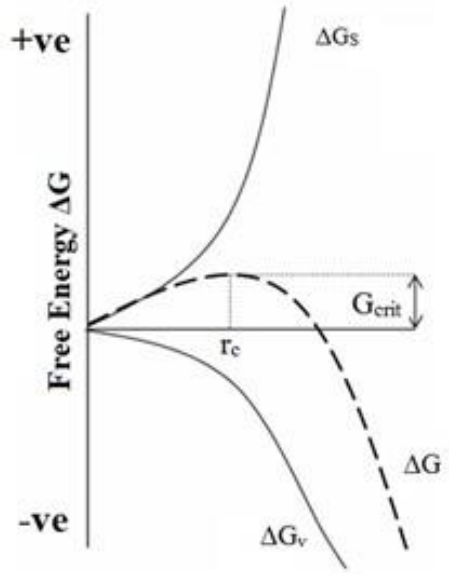

Figure 1.10: The Free energy diagram for nucleation elucidating the presence of a "critical nucleus."

A kinetics of the nucleation of N nanoparticles at time t can be defined with the help of Arrhenius rate equation, equation 1.6, in this equation A is pre-exponential factor.

$$\frac{dN}{dt} = A\exp\left(-\frac{\Delta G_{crit}}{k_B T}\right) \tag{1.5}$$

$$\frac{dN}{dt} = A\exp\left(\frac{16\pi\gamma^3 v^2}{3k_B{}^3 T^3 \left(\ln S\right)^2}\right) \tag{1.6}$$

From the equation 1.6, there are three experimental factors can alter such as supersaturated solution S, temperature T, and surface free energy. Kwon and Hyeon [91] studied by plotting these parameter, (Figure 1.11). The supersaturation shows the maximum effect on the rate of nucleation, where it changes from S = 2 to S = 4, the nucleation rate enhanced about 10^{70} times, and a deviation in the surface free energy produced by various surfactants.

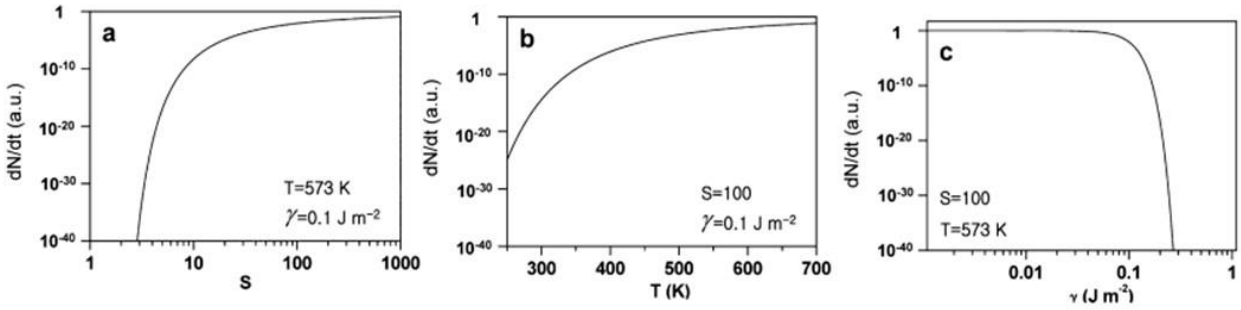

Figure 1.11: Rate of nucleation as a function of (a) supersaturation, (b) temperature, and (c) the surface free energy [91].

1.4.2. Classical Growth:

The growth of nanostructure materials is mainly dependent on the surface reaction and the diffusion of nuclear monomers on the surface [92]. The growth of nanostructures by the diffusion on the surface was illustrated by Fick's first law, equation 1.7 can be used, where r is the particle radius, J is total flux of monomers which passing through a spherical plane with radius x, D diffusion coefficient and C is the concentration at distance x respectively (Figure 1.12).

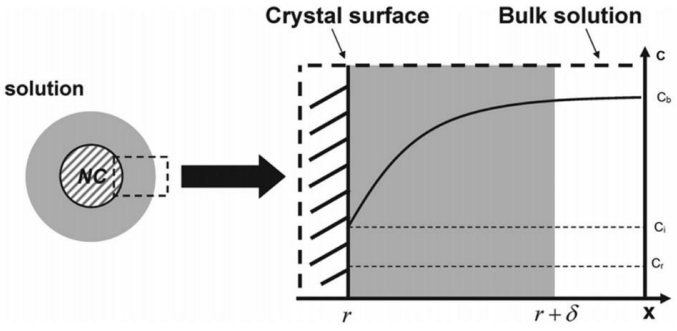

Figure 1.12: Schematic illustration of the growth of nanoparticles [91].

$$J = 4\pi x^2 D \frac{dC}{dx} \tag{1.7}$$

Fick's first rule can be reused as equation 1.8, for the case of growth of nanoparticles in the solution. Where the distance from particle surface to the bulk concentration of monomers is represented as δ, bulk concentration is C_b of monomer in the solution, C_i is the concentration at the solid/liquid interface of the monomers, and C_r is the solubility of the particle (Figure 1.12).

$$J = \frac{4\pi Dr\left(r+\delta\right)}{\delta}\left(C_b - C_i\right) \tag{1.8}$$

As J is constant irrespective of x due to the steady state of the solute diffusion, integration of C(x) from (r + δ) to r gives equation 1.9:

$$J = 4\pi Dr\left(C_b - C_i\right) \tag{1.9}$$

The equivalent equation can be used for the kinetic of surface reaction "k" equation 1.10. Assume that the rate of reaction does not depend on the size of the particles.

$$J = 4\pi r^2 k\left(C_i - C_r\right) \tag{1.10}$$

It is clearly shown from the equations 1.9 and 1.10 there are two limiting parameter either the monomers diffusion on the surface or the rate of reaction of these monomers on the surface. If limiting parameter is diffusion then the variation in the size of particles with time is given by another equation 1.11:

$$\frac{dr}{dt} = \frac{Dv}{r}\left(C_b - C_r\right) \tag{1.11}$$

Correspondingly if the limiting parameter is surface reaction then equations 1.9 and 1.10 can be rewritten to equation 1.12.

$$\frac{dr}{dt} = kv\left(C_b - C_t\right) \tag{1.12}$$

But when the growth of particles is not dependent on both limiting parameter then the increase in particles radius with time is represented as equation 1.13:

$$\frac{dr}{dt} = \frac{Dv\left(C_b - C_r\right)}{r + D/k} \tag{1.13}$$

It is well-known that the solubility of nanoparticles is dependent on the particles size and from the Gibbs-Thomson equation, equation 1.14, a spherical nanoparticles gas an additional chemical potential $\Delta\mu = 2\gamma v/r$. Then C_r is the solubility of particles as a function of r, where v is the molar volume of bulk crystal and C_b is the bulk concentration of the solution.

$$C_r = C_b \exp\left(\frac{2\gamma v}{r k_B T}\right) \tag{1.14}$$

For the growth of nanoparticles which is already expressed in the equation 1.11 can be formed by the combination of equations 1.15 and 1.13 [93, 94].

$$\frac{dr^*}{d\tau} = \frac{S - \exp\left(\frac{1}{r_{cap}}\right)}{r_{cap} + K} \tag{1.15}$$

Where all the constants are described as follows:

$$r_{cap} = \frac{RT}{2\gamma v} r \tag{1.16}$$

$$\tau = \frac{k_B{}^2 T^2 D C_b}{4\gamma^2 v} t \tag{1.17}$$

$$K = \frac{k_B T}{2\gamma v} \frac{D}{k} \tag{1.18}$$

In the equations no 1.17 & 1.18 $2\gamma v/k_B T$ is represented as the length of capillary and K is the Damkohler constant. The Damkohler constant designates whether the reaction is diffusion or dependent on the rate. If the value of D << 1, then diffusion of nuclear is dominated on the surface reaction.

1.4.3. Theories of nucleation and growth:

The different types of theories are present for describing the nucleation and growth process of the nanoparticles in the solution phase.

1.4.3.1. LaMer Mechanism:

For the first time, the nucleation and growth mechanism understood by LaMar and co-worker in the preparation of sulfur sol or colloid from a homogeneous supersaturated aqueous medium experiment in 1950 [95, 96]. They have explained the nuclear and growth mechanism conceptually by separating into two stages: first to produce free sulfur sols from the decomposition of solid thiosulfate and last form sulfur sols in solution. For the easily understanding the nucleation and growth by the LaMer method, it can be categorized into three categories. In the first category, a spontaneous increase of free monomers concentration in the solution, secondly the burst nucleation occurs of monomer which incomparably decreases the concentration of free monomer in the solution. The rate determined by the slowest steps of this nucleation and after this step, there is no other nucleation occurs due to minimization of the concentration of monomers at this point and in the finely third category the growth of particles occurring at the controlled diffusion of monomer in the solution. All the three categories are systematically observed in the Figure 1.13 which plotted against the concentration of monomer with the time function. A very excellent example of this LaMer mechanism is the growth of silver halides [97].

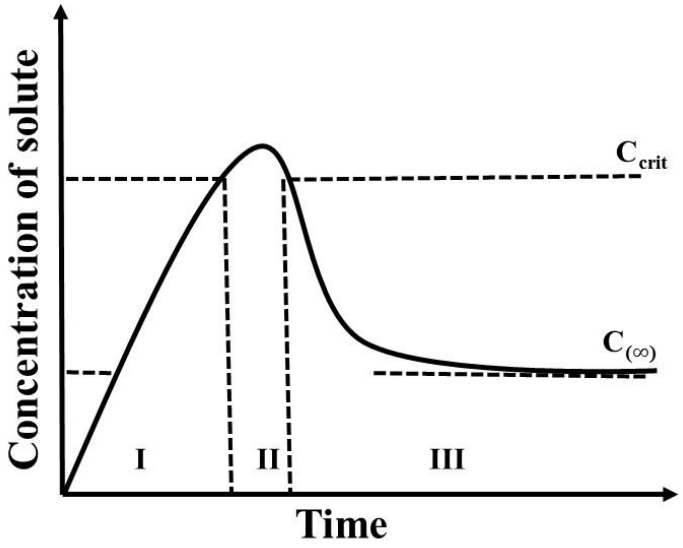

Figure 1.13: LaMer diagram schematic [95].

1.4.3.2. Ostwald Ripening and Digestive Ripening:

Ostwald ripening mechanism was earlier mentioned in 1900. This is the mechanism of growth is initiated by variation in the solubility of nanoparticles dependent on their size which is well explained by the Gibbs-Thomson equation 1.14. Because of the high surface energy and solubility of smaller particle in the solution, these smaller particles are redissolved and allow the formation of larger particles. The mathematical explanation of Ostwald ripening mechanism in the closed system is defined by Lifshitz, Slyozov and Wagner [98, 99].

Digestive ripening and Ostwald ripening mechanism are inverse to each other and Digestive ripening is more efficient than Ostwald ripening mechanism. According to the Digestive ripening mechanism, the growth of smaller particles due to the destruction of the larger one and is well explained by Lee et al. [100] where the resultant Gibbs-Thomson relation is applicable.

1.4.3.3. Finke-Watzky Mechanism:

The Finke-Watzky mechanism is explained in the two steps where the nucleation and growth both processes occur simultaneously [101]. In the first step a

relaxed but continuous nucleation (equations 1.19) occur but in the second step the self-catalytic growth takes place which is not controlled by diffusion (equations 20) process [102].

$$A \rightarrow B \quad (1.19)$$

$$A + B \rightarrow 2B \quad (1.20)$$

This mechanism was realized by the reduction of transition metal salt through hydrogen which was explained by the reduction of cyclohexane [103].

1.5. Effect of pH, concentration, temperature of precursor factor for the growth of NPs:

1.5.1. Effect of pH:

For the measurement of the growth rate of materials with the chemical route in the solution phase, the pH value of the solution has always played an important role in the production of the final products. To understand effectively the effect of the pH on the growth of ZnO nanostructures, the initial, as well as the final pH values, were carefully measured before and after the growth. G. Amin *et.al* reported that the synthesis of high-density ZnO nanostructures materials from solution phase at $pH_{initial}$ = 6.6 in 5 hrs. This experiment indicates that at this basic medium only rod-like structures can be developed. But when on increasing the pH from 6.6 to 8, the morphology of the ZnO nanostructured materials change from rod-like to nano-tetrapod [104]. This can be described by the specialty of hydroxide ion concentration in the initial solution, provide for the growth in anisotropic directions. On increasing the pH up to 9.1 the growth rate further enhanced due to the rising in the concentration of OH^- ion which provides a flower-like structure of ZnO nanoparticles with thick arms in the solution phase. On further increasing of pH from 9.1 to 12, urchin-like ZnO nanostructures with needles length of 2 μm and a diameter of ~50 nm synthesized in from solution. Parallel surface morphological nanostructures were

achieved at pH of 12.5 because of the development of $[Zn(OH)_4]^{2-}$ intermediates in the reaction medium. However, in the acidic medium approximately large 2-D rods were formed at pH < 4.6 and down to 1.8 by the incorporation of HNO_3 and elucidated that etching was serious at the minimum pH values which also favored the consequences that the ZnO begins to be etched in an acidic medium solution [105]. However, it is very ingesting to know that at pH < 4.6 no growth was achieved when the pH value was dropped by the addition of HCl. This can be due to the fact that the etching was dominating over the growth.

1.5.2. Effect of concentration:

On the variation in the concentration of the reactants at fixed pH value is debated. It is constantly well known that on raising or lowering the concentration of the precursor of chemical reactants will ultimately affect the final products. G. Amin et.al reported that the growth of ZnO nanostructure in the aqueous medium, they have found micro-rods like structures at high concentration of the precursor reactants was used [106]; when a relatively lower concentration of the precursor was used by the same authors the nanorods and nanowire of ZnO nanostructures were obtained [107]. This suggests that a good control over the chemical reactants can be applied to improve in direct resistor over the dimensions of the final ZnO nanostructures. According to this conclusion, more research has been studied the effect of the precursor concentration on the dimensions of nanostructures at the constant pH value. On varying the concentration of the precursor the density, diameter, and length of the synthesized ZnO nanostructures varies; at higher concentration produces a micro-sized ZnO nanostructures materials with densely packed along the c-axis. Nevertheless, Zhu et al. have fabricated ZnO-based core/shell nanostructure at by applying 5 mM precursor at the shorter time by modifying the aqueous solution [108].

1.5.3. Effect of temperature:

Like pH and concentration of the precursor materials, the temperature is also one another very important parameter that influences the formation of nanostructures using all the above methods. The synthesis of nanostructured materials by the physical method involves the highest temperature (>350◦C), but in the chemical methods involve a temperature as usually less than the physical method. Under most circumstances, the fabrication of nanoparticles using in the green nanotechnology needs temperatures lower than 100◦C or room temperature. The temperature of the precursor reaction medium controls the nature of the synthesized nanostructures [109].

1.6. Semiconductor nanostructures:

Semiconducting nanoparticles have gained increased attention by cause of its size and shape dependent photo-physical and photochemical properties in various branches of chemistry, physics, and materials science, which differentiates it from the bulk semiconductor. These can adopt several structural geometries due to its electronic structure that can exhibit conductor, semiconductor, or insulator characteristics. The use of semiconducting nanostructure is in the interesting optoelectronic devices make it a special class of material. These nanocrystals have the technological potential for applications in various areas like as light emitting diodes, photo-detectors, lasers,[110] photovoltaic solar cells, [111] photocatalyst for water splitting or dye degradation [112, 113] and bio-medical field etc. [114, 115]. For example, most of the semiconducting materials are used as catalysts for the industrial applications such as an oxide as active phase, promoter, or "support". There are various types of semiconductors with their band gap summarized in Table 1.2.

Semiconductors	Bandgap energy (eV)
Diamond	5.4
Cu_2O	2.172
CuO	1.20
ZnS	3.6
TiO_2	3.03
SnO_2	3.54
ZnO	3.36
CdSe	1.7
WO_3	2.76
Si	1.170
Fe_2O_3	2.3
PbS	0.286
PbSe	0.165
ZrO_2	3.87
Ge	0.744
CdS	2.42

Table 1.2: Examples of some semiconducting nanostructures [116]

1.6.1. Fundamental theory in a semiconductor:

The principal terms involved in a photoactive semiconductor are valence band (VB), conduction band (CB), band gap, traps sites and Fermi level. In the materials, the bands are the allowed energy states in which an electron can occupy. The highest energy band filled by an electron is known as valence band while the next available lowest empty energy level, next to valence band is termed as conduction band. Semiconductors are possessed clearly separated bands than in a metal. The energy

difference between the top of the valence band and bottom of the conduction band is termed as band gap energy (Eg). On the behalf of the band structure, band gap energy is classified are two types direct and indirect band gaps. For direct band gap semiconductors, the minimum energy state of the conduction band and the maximum energy state of the valence band occur at momentum k =0 (k is the wave vector) as shown in Figure 1.14 a [117]. Few examples for direct band gap semiconductors are ZnO, SnO_2, SnS_2, CdS. In case of indirect band gap semiconductors, the minimum state of the conduction band and the maximum state of the valence band are not at the same k value Figure 1.14 b [117] examples is ZnS. Ge, Si and GeS. The Fermi level is a probability distribution curve that represents a 50% possibility of locating an electron at a given energy level. For an n-type semiconductor such as ZnO, the Fermi level is close to the conduction band.

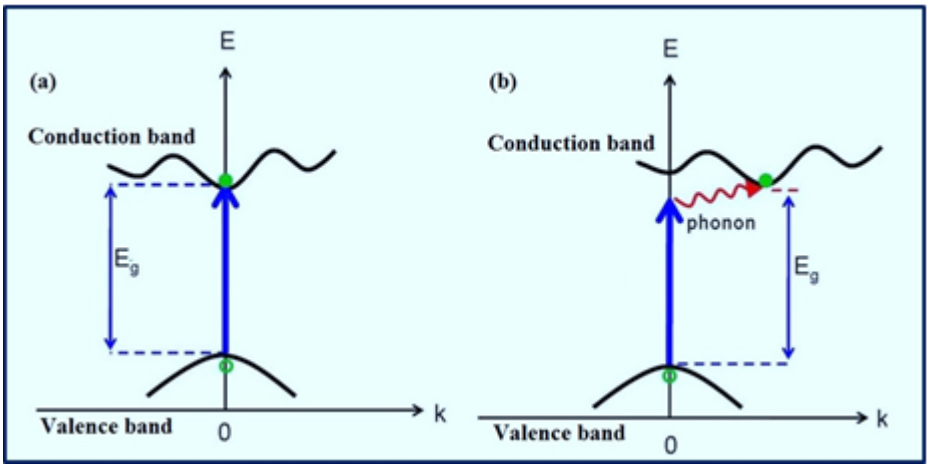

Figure 1.14: Representation of band diagrams in semiconductors: (a) direct band gap, (b) indirect band gap. The vertical arrow symbolizes the photon absorption process, while the "•" and "◦" represent an "electron-hole" pair. The curving arrow in (b) represents the absorption or emission of a phonon.

A semiconductor demonstrates the following processes on photo-illumination. The radiation of light have more energy compared to the band gap of the semiconductor then excite the electrons from the valence band to the next energy level conduction band leaving behind the same number of hole in the valence band

and generate one electron-hole pair which is known as exciton. The recombination of exciton must be prohibited for improved the photocatalyzed reaction. For example, ZnO is a wide band gap semiconducting material and hence yields e-h pairs on illumination with UV light (reaction 1.1). The presence of electrons (e_{CB}^-) and holes (h_{VB}^+) are responsible for the redox activities at the semiconductor surface. Photo-generated e_{CB}^--h_{VB}^+ pairs (excitons) are also delocalized in the semiconductor. These locations are called trap sites (e_t and h_t). The e_{CB}^--h_{VB}^+ pairs undergo fast recombination which results in decreasing the effectiveness of the semiconductor. The number of photo-generated electrons in ZnO is dictated by the ability of the surroundings to scavenge electrons and holes (reaction 1.2 and 1.3) and the recombination between the photo-generated e-h pairs (reaction 1.4).

$$ZnO + h\upsilon \rightarrow ZnO\ (e_{CB}^- + h_{VB}^+) \quad (1.1)$$

$$h_{VB}^+ + H_2O \rightarrow OH\bullet + H^+ \quad (1.2)$$

$$h_{VB}^+ + OH^- \rightarrow OH\bullet \quad (1.3)$$

$$e_{CB}^- + O_2 \rightarrow O_2^{\bullet -} \quad (1.4)$$

The general mechanism of semiconductor photo-catalysis is represented in Figure 1.15.

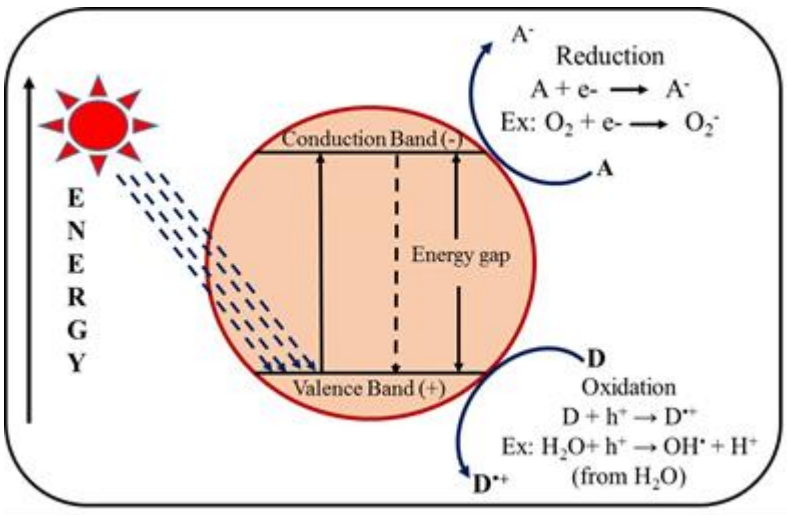

Figure 1.15: Mechanism of Semiconductor photocatalysis

1.6.2. Quantization effect:

The size of the semiconducting nanostructures materials which are comparable to its Bohr exciton radius [118] corresponds to the regime of quantum confinement, for which the spatial extent of the electronic wave function is comparable with the dot size. The exciton Bohr radius (a_B) decide the electronic excitations in the microscopic and bulk semiconductor materials determined by the strength of Coulombic interaction of the electron-hole pair (e-h). Due to the geometrical constraints, electron ambiance the existence of particle boundaries and retort to modification in size of the particle by adjusting their energy (discretization of energy levels) as represented in Figure 1.16. This systematic mechanism is called as quantum-size effect and its well plays a very important role in quantum dots (QDs). As the particle size goes near to the exciton Bohr radius, the wave function of electron and hole are confined in nanoparticles and charge carrier (electron and/or hole) kinetic energy enhances. This is the major reason behind the changes in the absorbance edge to the higher energies with reduction in particles size called as blue shift in the absorption spectrum.

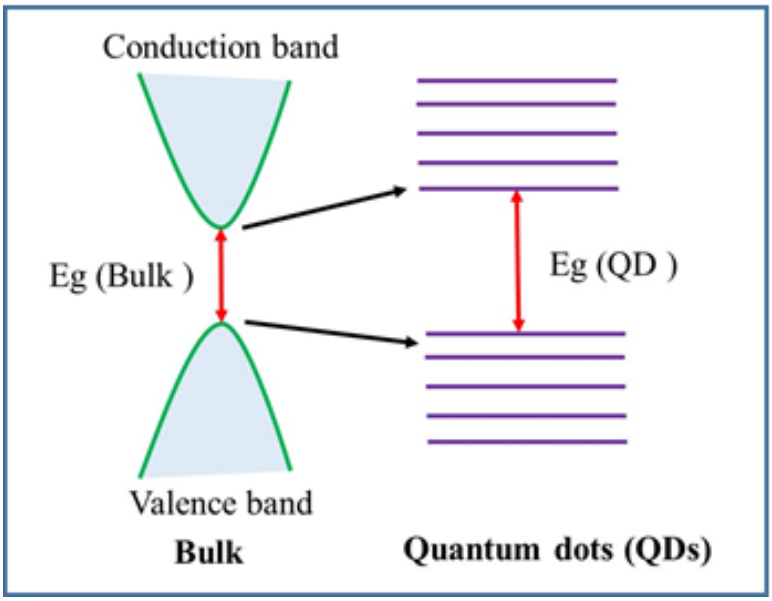

Figure 1.16: Schematic exhibition of energy levels of bulk semiconductor and quantum dots.

Semiconducting nanostructure materials exhibit distinctive size-dependent properties (quantization effect) that adjust its photochemical, photophysical, photochromic, optical and application [22]. Both the huge (e.g. ZnO, TiO_2, SnO_2 and WO_3) and small band gap semiconductor (e.g. CdSe, CdS) show this property. Because of the quantization effect, the initiation of charge, separation, retention and transfer across a semiconductor and its surrounding is strongly concerned [119-121]. The existence of surface-bound species which include surrounding electrolytes, sensitizers like other semiconductors, metals and dyes play an active role in determining the mechanism of charge transfer taking place at the semiconductor and surrounding species interface. Irradiation of photons leads to charge separation in semiconducting nanostructures followed by electron and/or hole transfer to the surrounding dictated by the energetics of the system. Furthermore, defects or vacancies are created in the semiconductor largely due to the method employed for their synthesis. These defects play a vital role in controlling the photo-electrochemical and photocatalytic behavior of the semiconductor.

The abnormal physical and chemical behaviour of nanostructures are because of three main reasons. Primary the size of particles is equivalent to the Bohr radius of excitons in metal semiconductors. This controls the optical, luminescence, and redox properties of nanostructures. Secondly, the atoms present on the surface operate a considerable fraction of the total number of atoms of the nanostructures. And in the last, the comparable size of nanoparticles as the size of molecules. This measured the peculiarities of the kinetics of chemical process on the surface of nanostructures. To date, nanoparticles of ZnO, TiO_2, Fe_2O_3, SiO_2, MoS_2, CdS, HgS, GaP, Cd_3P_2, BiI_3, PbI_2, and a number of other semiconductors have been synthesized and investigated.

1.6.3 Effective Mass Approximation:

The quantum size effects are understood on the basis of the effective mass approximation (EMA) [122, 123] and empirical tight-binding method (ETBM)[124, 125] aside from the first principle calculations.

1.6.4. The use of semiconductor nanostructures in photocatalytic processes:

Recent developments in wastewater treatment processes have to lead an improvement in oxidative degradation procedure for organic compounds dissolved or dispersed in aqueous media by photochemical or catalytic use of semiconductor nanostructures due to the decrease in the size of nanoparticles causes conduction and valence bands towards more negative and more positive potentials to controlling the redox properties of nanoparticles. They are generally referred to as Advanced Oxidation Processes (AOPs) and are considered to be alternatives to conventional water treatment processes [126-129]. Additionally, the fact that nanoparticles have a large specific surface area is of importance for carrying out photocatalytic processes on the surface of semiconductors. And finally, the small size of semiconductor nanoparticles can provide high efficiency of retention in recombination of light-generated electrons and holes, thus increasing the probability of a photocatalytic process on the surface of the semiconductor.

1.7. Zinc oxide:

Zinc oxide (ZnO) is a non-toxic, low cast [130], direct wide band gap (Eg = 3.37 eV) [131], n-type semiconductor [132] of II-VI group with large exciton binding energy (60 meV) [133] and 4.2 eV electron affinity [134]. ZnO nanoparticle generally has three structure zinc blend, hexagonal wurtzite and rock salt structure [135, 136] but at ambient condition only two phases i.e. cubic zinc-blende (ZB) and hexagonal wurtzite (HW) are stable. In these two thermodynamically stable nanostructures, each

cation is surrounded by four anions at the corner of tetrahedron and vice versa [137]. Though the nature of bonding of these tetrahedral coordination is covalent through sp^3, hybridization in nature but noticeably ZnO possesses ionic characteristics. The ionic characteristics are lodging in between the covalent and ionic semiconductors. Under atmospheric conditions, wurtzite structure of ZnO is thermodynamically stable and the **zinc-blende** structure can be stabilized only by growth on cubic substrates, but the **rocksalt** (NaCl) geometrical structure is achieved at comparatively high pressures. Figure 1.17 represents the schematic of the ZnO crystal nanostructures.

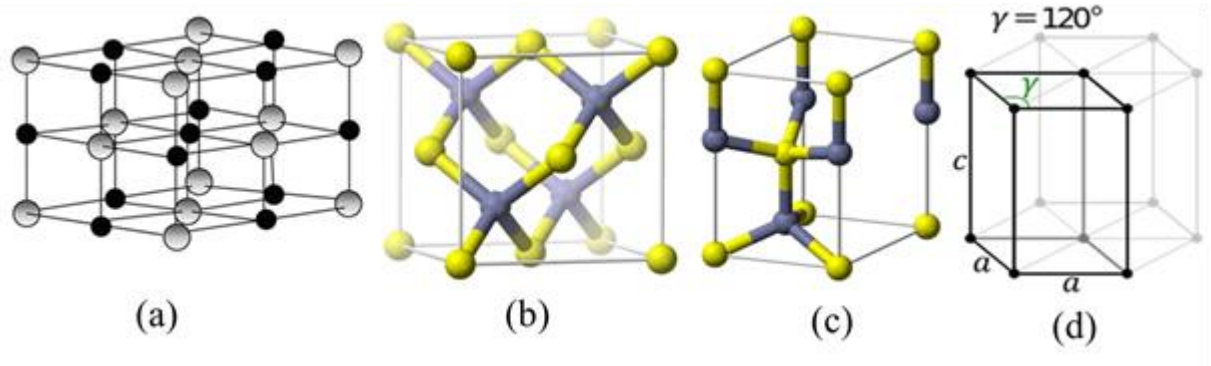

Figure 1.17: Crystal nanostructures of ZnO (a) rock-salt, (b) zinc-blende, and (c) wurtzite (d) Hexagonal wurtzite

The hexagonal wurtzite structure with lattice parameters a = 0.3296 and c = 0.52065 nm, along with the parametric ratio c/a = 1.6 are goes to the space group of $P6_{3mc}$. The structure possesses a number of alternating planes of O^{2-} and Zn^{2+} ions which are coordinated tetrahedrally and stacked along the c-axis. The tetrahedral co-ordination results in the non-central symmetric structure of ZnO and consequently leads to piezoelectricity and pyroelectricity [138]. Furthermore, ZnO has polar surfaces and the basal plane is the most common surface.

In reference of the semiconducting binary oxide nanostructures, ZnO nanomaterial's are good candidates for the creation of various functional devices, due to of their potential stability over an extensive range of temperature, outstanding

oxidation resistibility, high electron conducting, good biocompatibility and low toxicity [139]. Now a day, several types of ZnO nanostructures comprising nanoparticles, nanorods, nanowires, nanopenciles, nanotubes, nanosprings, nanocups, nanocoils, etc. have been prepared and used in the expansion of field-effect transistors, lasers, light emitters, solar cells and gas sensors. Based on the piezoelectric property, an array of 1D ZnO nanostructures have been used to develop nanogenerator [140]. Similarly, the biocompatibility and low toxicity of ZnO nanostructures have led to the development of new generation biosensors [141].

In addition, the numerous 1D nanostructures of ZnO, owing to the good electrical conductivity, high aspect ratio, high mechanical stability, excellent oxidation resistance, and ease of synthesis, have been extensively investigated as field emitters [142].

1.8. ZnO-ZnS composites:

Zinc sulfide (ZnS) is also very well-known non-toxic nanostructure materials with two naturally existing nanostructured phases, first, the zinc blende (sphalerite) structure contain cubic phase and secondly the wurtzite structure contain a hexagonal phase. In both the structures, each anion is surrounded by four cations at the corners of a tetrahedron, and vice versa. The band gap energy of both the structural phases of ZnS nanostructure are different such as bulk cubic and hexagonal phases are 3.54 eV and 3.80 eV respectively [143]. Many of the researchers investigate the ZnO-ZnS nanocomposites materials in which “hexagonal ZnO and cubic structure of ZnS nanoparticles” were crystallized to each other to form ZnO-ZnS nanocomposites materials [144, 145]. Recently P. Verma et al. demonstrated that a two-step synthetic method based on the solution-based was applied for the fabrication of the ZnO/ZnS

core-shell nanocomposites materials and they are concluded that the growing of the ZnS nanoparticles on the surface of the ZnO nanostructures [146].

In the present study zinc oxide-zinc sulphide nanocomposites materials are mainly synthesized to change the band energy as well as modify the surface area of the zinc oxide nanoparticles by the incorporation of sulphide ions in the lattice of the ZnO NPs and used as a good catalyst for the removal of organic dye and wastes from the waste water and also to improve the optical properties.

1.9. ZnO/ZnS/α-Fe_2O_3 nanocomposites:

In the recent study, iron oxides are found in various form in the nature such as magnetite (Fe_3O_4), maghemite (γ-Fe_2O_3) and hematite (α-Fe_2O_3) [147]. This is most common metal and semiconductor nanostructures materials and these have magnetized more consideration from both basic science and materials science.

In the current study, ZnO/ZnS/α-Fe_2O_3 materials are the tertiary composite materials. These can be synthesized by the incorporation of ZnS and α-Fe_2O_3 in the synthesized ZnO nanoparticles. On the synthesis of these tertiary composites materials, they have provided new prospects to reduce the narrow efficiency of photocatalysts and photovoltaic devices. Incorporation of some new metal into semiconductors materials to enhances the efficiency of the photocatalytic activity towards degradation of dyes and toxic organic contaminants.

1.10. Literature review:

Dodd et al. [148] reported the consequence of cobalt and magnesium doping, on the photocatalytic performance of nanostructure of zinc oxide. The mechanochemical process was adopted for the fabrication of controlled size, nominal agglomeration, and moderate chemical composition of zinc oxide nanomaterials. The photocatalytic performance of the particles was observed by applying spin trapping

analysis along with electron spin resonance spectroscopy. It was obtained that the addition of cobalt oxide declined the yield of photo-produced hydroxyl radicals. In compare, zinc oxide doped with manganese oxide was obtained to substantially enhance the rate of radical formation.

Y.L. Wu et al. [149] were synthesized nano-structured ZnO samples by adopting colloidal alcoholic solutions of zinc acetate dihydrate through the colloidal process. Those were used five kinds of capping agents such as 3-aminopropyl trimethoxysilane (Am), tetraethyl orthosilicate (TEOS), mercaptosuccinic acid (Ms), 3-mercaptopropyl trimethoxysilane (Mp) and polyvinylpyrrolidone (PVP). These capping agents were added at during the first precipitation of ZnO to handling the growth of particle. The former three capping agents excellently capped the ZnO nanomaterials and controlled the particles growth, latter the two capping agents initiated larger clusters in the reaction medium. ZnO materials were fabricated in 10-30 nm in size after capping and expand up to 60 and 100 nm in 3 and 6 weeks, respectively, during storage at room temperature. In reflexing, the only first precipitation was affected. Washing was completed by several time with water and finely with ethanol. The optical properties of the ZnO nanostructures materials were investigated by photoluminescence spectra. The high-intensity emission in UV region and low intensity of visible emission was shown and predicted that a good surface morphology of ZnO nanostructures with meager surface defects. The spectrum of optical absorption points out that a blue shift by the capped ZnO due to the quantum confinement influence by the single crystal size of 5-6 nm as also examined by TEM.

H. Wang et al. [150] demonstrated that ZnO nanostructure with several size diameter scales such 10, 50, 200 and 1000 nm have been fabricated by two dissimilar preparation procedures first thermal evaporation method and second chemical

deposition method. The photocatalytic application was observed for the decolorization of methyl orange organic dye stuff in aqueous solution under illumination of UV light. ZnO nanoparticle fabricated via thermal evaporation technique along with 50 nm size exposed the maximum photocatalytic efficiency comparison to the ZnO synthesized via a chemical deposition process. They also reported that the tetrapod ZnO nanostructures had the maximum efficiency than bare ZnO nanostructures. This research indicates that the synthesis method was the significant factor rather than size and morphology.

Takuyu Tsuzuki et al. [151] provided the awareness of compact photocatalytic performance of ZnO nanostructure by doping with former transition metal manganese. As the powerful ultraviolet radiation is affecting major skin cancer harms and enhanced degradation of harmful waste such as plastics, textiles, paints, timbers, and dyes, ZnO nanopowders are deliberated to be one of the most promising UV hindering agents due to their broad UV absorption spectrum, low production cost and low toxicity. However, the characteristic photocatalytic performance of ZnO inhibits the use of ZnO nanoparticles in many applications.

M. K. Lima et al. [152] described that the pure and Co-doped ZnO nanoparticles manufactured with average crystallite size via sol-gel method using water as a solvent. The accumulation of cobalt ions (1-10 mol %) in the lattice of ZnO without altering its structure. The average particles size do not screening the significant alterations with the upsurge of the dopant level. However, the alteration in the band gap energy diverges from 2.98 eV of pure ZnO to 1.95 eV by doping 10 % of cobalt ion. The photocatalytic performance of the material was appraised on the reduction of methylene blue under visible light illustration, which exposed dropping in the photocatalytic proficiency by Co-doping ZnO.

R. Saleh and N. F. Djaja [153] exposed that transition metals like Mn and Co-doped ZnO nanoparticles were fabricated via co-precipitation method. The fabricated nanostructure substances were appraised via X-ray diffraction for the phase purity, scanning electron microscopy for the morphological examination, energy dispersive X-rays for elemental composition, FTIR spectroscopy, ESR spectroscopy and DRS techniques for the appraisal of band gap energy of the fabricated ZnO materials. The photocatalytic utilization of the doped ZnO nanostructure was estimated in the photo-decolorization of methyl orange dye stuff under UV irradiation. The 12 at. % of Mn and Co ions contaminated ZnO nanoparticles disclosed that the maximum efficiency of photo-degradation. These photocatalytic consequences showed owing to the localized electronic states of the contaminated materials worked as charge carrier traps for photo-produced charge carriers in UV light irradiation. The experimental testing also proved that the photo-degradation proficiency of Mn contaminated ZnO was progressive compared to the Co contaminated ZnO nanostructures which specified that various types of transition metals compromise a different way to entrap charge carriers and prolong the period of electron and hole due to the incorporation of contaminants in the ZnO lattice may not occupy the same position.

I. Prabha and S. Lathasree worked for the synthesis of nano-ZnO, TiO_2 and ZnO-TiO_2 composite nanostructures by a well-known sol-gel technique and were tested as photocatalysts for the amputation of phenol by the photocatalytic degradation method [154]. The experimental evaluation indicates that the development of agglomerated nano size ZnO nanoparticles having a common wurtzite phase of the size 17.5±5 nm and nano-TiO_2 has anatase phase of homogeneous particles size of 15.7±5 nm with the spherical morphological shape. In the synthesis of nano-ZnO-TiO_2 nanocomposite materials, the particles are of bigger agglomerates

being ingrained indoors with a particle size of 11.6±5 nm. The photocatalytic testing of all the prepared materials nano-ZnO, TiO_2 and ZnO-TiO_2 composite nanostructures was assessed by adopting phenol compound in the incidence of UV light and sunlight as the radiation source. The authors also reviewed the impact of initial pH, initial catalyst amount and finally the concentration of phenol compound. The kinetics of the removal of phenol compound was established to follow pseudo-first-order and the experimentally observed that the nano-ZnO, TiO_2 and ZnO-TiO_2 composite nanomaterial's was effective photo-catalysts for removal of phenol in UV light irradiation. The further analysis of the total organic carbon directed the whole mineralization of phenol compound in the existence of nano-ZnO, TiO_2 and ZnO-TiO_2 surface.

Y. Sivry et.al. [155] defined the miscibility impression of organic coated and uncoated ZnO nanoparticles in the physicochemical process along with natural high carbonated water. The rate of transformation of materials was examined by virtue of Donnan Membrane approach for obtaining the Zn^{2+} ion concentration and ultrafiltration for measurement of bound of Zn^{2+} and Zn to the small organic ligand and modeled with VMinteQ. From the XPS measurements, it was proved that presence of bare nanostructures of a $Zn(OH)_2$ layer account for at least 22% of total Zn. It was proved that $Zn(OH)_2$ formation in the reaction phase is highly miscible compare to the ZnO nanoparticles and might control the formerly dissolution steps of noncoated nanoparticles in the reaction medium. Surely, the noncoated nanoparticles show a quick (<1 h) dissolution stage attainment 19 μM Zn in the reaction solution (<1% of the total precursor zinc content). Comparison to the non-coating nanoparticles, organic coated nanoparticles gradually release zinc during the former

first 48 h, to lastly reach a maximum of 197 μM (10% of whole Zn), which is 10 times the greatest value dignified for noncoated nanoparticles.

K.C. Barick et al. [156] reported for the fabrication of water-dispersible ZnO nanoparticles via a fluent soft-chemical method by adopting cationic surfactant and shape-directing agent as cetylpyridinium chloride (CPC). They were announced that the size of ZnO nanostructures was strongly affected on the addition of shape directing (surfactant) agent. They were shown that in the existence of CPC surfactants mostly pyramidal-shaped ZnO nanostructure developed in 10-20 nm size, whereas in the absence of surfactant only roughly spherical nanostructure of ~10 nm was formed. These prepared ZnO nanoparticles show good stability in aqueous solution which is most important for their photocatalytic behaviour. Optical testing proved that the quantity of CPC reins both band gap and emission strength of photoluminescence study revealed the defects in the ZnO particles. Further, the authors have explored the photocatalytic examination of ZnO nanomaterial's adopting MO and MB dye as pollutant. This study was also proved that the defect on the surface of ZnO was strongly affected the catalytic decolourization of organic dyes. The complete decolourization of dye via ZnO photocatalyst was further entrenched from the valuable decreasing in chemical oxygen demand (COD) values. The photocatalytic effectiveness of these catalyst was further influence by changing the deferent parameters like as nature and extent of dye along with photocatalyst. More ever, these nanostructures was further recycled as catalyst for decontamination of pollutants in the existence of UV light irradiation.

S. Mohammadzadeh et al. [155] synthesized ZnO-Ag (x varied range in the $Zn_{1-x}O$-Ag_x chemical content) composites materials by a modified chemical method such as microwave-assisted solution combustion process. The photocatalytic

application of that ZnO-Ag composite material was examined by reduction of Acid Blue 113 in illumination of UV light in a semi-batch reactor. That experimental investigation proved that ZnO-Ag composites have displayed more photocatalytic efficiency than bare ZnO nanoparticle fabricated via the same way. That improved photocatalytic performance was owing to the reduction in recombination of photoproduced electron and holes (exciton). Further investigation proved the upgrading photocatalytic behavior of ZnO along with an ideal doped quantity of Ag (3.5 mol %). That research was testing the chemical parameter like as pH, the extent of catalyst and dyes concentration. The byproduct which was achieved throughout the photocatalytic process was explored via LC/MS technique and reaction pathway was well developed. The reaction rate was also testifying and observed the first order reaction of decolorization of dye.

J. Choina et al. were synthesized zinc oxide (ZnO) nanoparticles of various sizes by using two different solvents like as water and ethanol through chemical co-precipitation method [157]. The application was examined for the reduction of low concentrated pharmaceutical tetracycline and ibuprofen through photocatalytic technique by using few quantity of catalyst to substrate mass ration. In that investigation, the authors also evaluated the influence the pH and the concentration of catalyst and drug along with the impact of adsorption. The production of intermediates has been examined through the electrospray ionization-time of flight-mass spectroscopy. The synthesized catalyst (ZnO) is very well known to indorse the development of reactive •OH radicals and therefore is of exceptional curiosity for the remediation of wastewater form pharmaceuticals by the photocatalytic pathway. According to that research, only small nanoparticles are much more energetic than the bigger one because of the high specific surface area and adsorption process.

Remarkably, adsorption of drug pollutants on the surface of ZnO catalyst is obviously upgraded at low concentration (<5 ppm), prominent to the diverse photo-degradation performances, compared to ppm concentrated solution.

A. Behzadnia et al. [158] was effectively photo sonosynthesized and sonoimmobilized a novel composite photocatalyst materials on the wool fabric of nonmetal/metal duplex-doped N-Ag/ZnO nanocomposites of the honeycomb-like structure under atmospheric pressure and low temperature by using precursor zinc acetate for zinc and silver nitrate for silver metal. The insertion of silver and nitrogen in the sonosynthesized nano size ZnO materials to upgrade its photocatalytic properties. The standardized dissemination of honeycomb-like composites on the wool fiber surface was evaluated by electron microscope such as SEM with electron dispersive X-rays. The existence of silver metal with crystal size 54 Å was proved by the X-ray diffraction characterization method in the photo sonotreated materials with duplex-doped metal and nonmetal ZnO composite materials. The creation of defect in the synthesized composite was investigated by XPS technique and the Ultraviolet-blocking was obtained by reflectance spectra in the 200-800 nm range. Another properties of that sonoloaded wool composite materials was shown as excellent antibacterial and antifungal activity. On changing the concentration of precursor of both the metal ion, the possessions of the composite materials was diverse.

Ilyas Unlu et al. [159] discussed in our research for the relevance of the easily available and synthesizable ZnO nanoparticles materials and own synthesized ZnO composites with a monolayer-protected gold nanoparticles (AuNPs) via ozone treated and annealed process. For the fabrication of ZnO composite, dithiol was used as a surfactant for possible bonding of its functional groups to both gold and zinc oxide surfaces. The formulated composite was usage as a catalyst for the decolourizarion of

rhodamine B dye pollutant. The result was indicated that the ozone treated composites materials were not more effective for adequately decolourization of dye pollutants. However, annealed composites materials at 300 ºC which decay maximum ligand but reduce the agglomeration of AuNP that shown to enhance the photocatalytic efficiency for the photo-oxidation of the aqueous polluted rhodamine B than pure ZnO along with composite materials which was annealed at higher temperature. In that research, one thing was very interesting that was the optical effect of ozonation and annealed composite catalyst. The authors detected that the photoluminescence spectra, the strength of UV and visible emission peak was reduced due to the quenching by the AuNP in the annealed composite of AuNP/dithiol/ZnO. However, they were obtained that the visible peak due to the existence of the surface defect was influenced by a much lower magnitude.

Md A, Subhan et al. [160] prepared a novel tertiary metal nanocomposites oxide materials of $Ag_2O/CeO_2/ZnO$ by chemical co-precipitation method from their precursor metal nitrates through annealation at 400 ºC for 5 h and 600 ºC at 4 h. That prepared tertiary composite material was illustrated by well-known spectroscopic technique. As per X-ray diffraction analysis, it was proved that $Ag_2O/CeO_2/ZnO$ nanocomposites were pure and its crystalline size was various in 19-111 nm range with the size of 50 nm which well shown in SEM images in a good arrangement. The application of these composite was used as a photocatalyst and anti-bacterial performance. The tertiary composite materials showed an exceptional photo-degradation of dye.

M. Ben et al. [161] adopted a simplistic and economical single-step hydrothermal process for the preparation of Zn_2SnO_4/reduced graphene oxide (ZTO/rGO) composite by choosing the salt precursor of metals and graphene oxide

respectively with reducing agent as sodium hydroxide. In that hydrothermal method formally reduced graphene oxide and then successfully grown ZTO nanostructures on the sheet of it. The morphological and structural investigation of ZTO/rGO composite indicate that the interfacial contact of ZTO particles and rGO and well adequate distribution of ZTO nanostructures on the surface of the sheet of rGO. The application of that prepared nanocomposite materials was invested for the minimization of rhodamine B in the illustration of visible light. That ZTO/rGO nanocomposites materials shown an excellent photocatalytic behavior comparison to the ZTO nanostructures materials with complete reduction of rhodamine B within 15 min. That improved photocatalytic activity of ZTO/rGO was proved due to the exceptional electron trapping and efficient adsorption behavior of rGO and hinder the rate of recombination of photo-produced charge carriers in ZTO.

K. Chakraborty et al. [162] were first reported for the reduction of graphene oxide for the fabrication of reduced graphene oxide (rGO) via the photocatalytic method in an aqueous solution of ZnS along with Graphene oxide for the formation of reduced Graphene oxide-zinc sulfide (rGO-ZnS) nanocomposites. In that preparative method, they explained that Graphene oxide accepted the photo prompted electron from ZnS. The reduction procedure was well proved by several characterization techniques such as XRD, FTIR and Raman spectroscopy. The utility of that composite was investigated for the photoreduction of rhodamine B contaminants and proved that the rGO-ZnS composite materials shown improved photocatalytic properties than pure ZnS materials under illumination of UV light. The enhancement of photocatalytic utility of rGO-ZnS composites was owing to the synergetic effect matching the conduction band of ZnS to the functioning conducting rGO. The

recycled composite materials did not markedly influence its photoreduction effectiveness and its crystalline structure.

K. P. Raj and K. Sadayandi [163] prepared ZnO nanostructures in aqueous solvent via chemical process and conclude the impact of calcination temperature on the ZnO NPs and presence of strain. From the view point of optical consideration, they were observed and suggested that the decrease in band gap and enhancement of photoluminescence spectra was due to the perfection in crystallinity and quantum confinement effect.

M. Gancheva et al. [164] adopted three synthesis process such as precipitation, tribophysical treatment and finely sonication for the formation of ZnO particles of several morphological structures. Application of ZnO was examined by the reduction of aqueous malachite green in the illumination of UV and visible light. ZnO materials achieved by precipitation process displayed superior photocatalytic behaviour under illumination of visible light because of its high surface area and low band gap energy.

T.K. Jana et al. [165] prepared CdS/ZnO composites of various morphological engineering by using the different precursor ration in the simplistic chemical method and studied the growing the behavior of the materials. The prepared CdS/ZnO composite materials examined for the photoreduction of rhodamine B dye in the irradiation of visible light and result was shown the best catalytic presentation arises in 1:1 ratio of nanocomposite materials.

Haitao Zhao et al. [166] fabricated $Zn_{0.5}Cd_{0.5}S/WS_2$ nanocomposites materials with the various quantity of $Zn_{0.5}Cd_{0.5}S$ solid solution dropped on the surface of WS_2 by a hydrothermal process via using thioacetamide as a precursor for the sulfur ions. The valence of the element and chemical composition of composite materials were inspected by applying XPS characterization technique. The photocatalytic behaviour

of $Zn_{0.5}Cd_{0.5}S/WS_2$ composite was experienced for H_2 extraction from the water. The determined rate of H_2 removal was found for composite materials under illumination of visible light is 6 times greater than $Zn_{0.5}Cd_{0.5}S$.

Q. Tian et al. [167] reported flower shaped MoS_2 NPs contain ultra-thin MoS_2 sheet was fabricated via the hydrothermal process. The p-n heterostructure of MoS_2/ZnO was obtained by coating n-type ZnO NPs on the surface of MoS_2 NPs. The photocatalytic effect for dye deduction and efficiency after the ZnO coating was examined respectively. The outcomes proved that coated ZnO NPs has play positive effect on the photodegation application but a negative effect on adsorption ability of the MoS_2/ZnO heterostructures.

M. Duan et al. [168] studied the glass-ceramics of Sn-doped ZnO materials by successfully fabricated through traditional quenching and later heating process. The morphological changes occur from varying the doping concentration from spherical to dumbbell-shaped. They have observed that Sn-doped ZnO displayed the enhancement into near and middle-infrared absorption due to the generation of localized surface resonance. That conclusion showed that glass-ceramics covering Sn-doped ZnO nanostructure have capabilities for energy capture.

M. Mitra et al. [169] produced aluminium doped ZnO structure by adopting oxidative polymerization of polyaniline (PANI) in the presence of different weight % aluminium doped ZnO nanorods, prepared via sol-gel method. Among several materials, the 22 weight % aluminium doped ZnO polyaniline hybrid shown the finest photocatalytic behavior for photodecolorization of methyl orange (MO) and rose bengal (RB) under the illumination of visible light, even after reused. The photocatalytic proficiency was observed the first order kinetics for both the dye. Scavenger test was used to define the character of active species and proposed

mechanism. The upgrading of the photocatalytic concert may be because of the efficiency of charge parting and synergetic effect between the organic conductor PANI and inorganic semiconductor aluminum doped ZnO nanostructures.

M. M. H. Farooqi and R. K. Srivastava [170] have obtained ZnO nanostructure via annealation of ZnS prepared by solid-state reaction approaches at various temperature. The annealed temperature was 600 ºC at 3 h for the alteration of ZnS to ZnO nanoparticles. From XRD analysis shown that the renovation of cubic zinc sulfide nanoparticles into the zinc oxide nanoparticles in the hexagonal phase after the annealed at 600 ºC. On observing the UV-vis spectra a blue shift seemed in the spectrum of ZnO nanoparticles than their bulk counterparts. The band energy diverges from 3.12 eV to the 3.07 eV that also indicates the conversion of ZnS into the ZnO nanoparticles. That prepared sample was shown a good photoconducting properties.

1.11. Objective of present work:

Keeping above properties and application of semiconducting NPs and composite, in mind author carried out and further extend the research work on semiconducting materials.

The main aim and objectives of this research work include

- Chemically synthesise semiconductor nanoparticles involving the process such as solution methods, co-precipitation methods and sonochemical method as well as some novel proposed wet chemical methods.
- Characterization of the nanomaterial's by XRD, EM (SEM, TEM) spectroscopic optical, magnetic etc techniques to determine their phase, crystallinity size and morphology.
- Application of these synthesized semiconducting materials including photocatalysis for the remediation of organic pollutants in waste water.

1.12. References

[1] R. P. Feynman, There's plenty of room at the bottom, Engineering and science, 23 (1960) 22-36.

[2] N. Taniguchi, On the basic concept of nanotechnology, in: Proc. Intl. Conf. Prod. Eng. Tokyo, Part II, Japan Society of Precision Engineering, 1974, pp. 18-23.

[3] K. E. Drexler, Engines of creation, Anchor, 1986.

[4] K. E. Drexler, Nanosystems: molecular machinery, manufacturing, and computation, John Wiley & Sons, Inc., 1992.

[5] L. Mazzola, Commercializing nanotechnology, Nature biotechnology, 21 (2003) 1137-1143.

[6] G.A. Ozin, Nanochemistry: synthesis in diminishing dimensions, Advanced Materials, 4 (1992) 612-649.

[7] A. Tavakoli, M. Sohrabi, A. Kargari, A review of methods for synthesis of nanostructured metals with emphasis on iron compounds, chemical papers, 61 (2007) 151-170.

[8] G.M. Whitesides, The'right'size in nanobiotechnology, Nature biotechnology, 21 (2003) 1161-1165.

[9] P. Moriarty, Nanostructured materials, Reports on Progress in Physics, 64 (2001) 297.

[10] A.S. Edelstein, R. Cammaratra, Nanomaterials: synthesis, properties and applications, CRC Press, 1998.

[11] C. Li, K.L. Shuford, Q. Park, W. Cai, Y. Li, E.J. Lee, S.O. Cho, High-Yield Synthesis of Single-Crystalline Gold Nano-octahedra, Angewandte Chemie, 119 (2007) 3328-3332.

[12] Y. Zhao, H. Hong, Q. Gong, L. Ji, 1D nanomaterials: synthesis, properties, and applications, Journal of Nanomaterials, 2013 (2013) 101836-101836.

[13] Y. Xia, P. Yang, Y. Sun, Y. Wu, B. Mayers, B. Gates, Y. Yin, F. Kim, H. Yan, One-dimensional nanostructures: synthesis, characterization, and applications, Advanced materials, 15 (2003) 353-389.

[14] T. Zhai, J. Yao, One-dimensional nanostructures: principles and applications, John Wiley & Sons, 2012.

[15] C.N.R. Rao, A. Müller, A.K. Cheetham, The chemistry of nanomaterials: synthesis, properties and applications, John Wiley & Sons, 2006.

[16] K. Novoselov, Nobel lecture: Graphene: Materials in the flatland, Reviews of Modern Physics, 83 (2011) 837-849.

[17] H. Ramakrishna Matte, A. Gomathi, A.K. Manna, D.J. Late, R. Datta, S.K. Pati, C. Rao, MoS_2 and WS_2 analogues of graphene, Angewandte Chemie, 122 (2010) 4153-4156.

[18] W. T. Liu, Nanoparticles and their biological and environmental applications, Journal of Bioscience and bioengineering, 102 (2006) 1-7.

[19] K. A. Dunphy Guzman, M. R. Taylor, J. F. Banfield, Environmental risks of nanotechnology: National nanotechnology initiative funding, 2000-2004, ACS Publications, 40 (2006) 1401-1407.

[20] L. Radushkevich, V. Lukyanovich, O strukture ugleroda, obrazujucegosja pri termiceskom razlozenii okisi ugleroda na zeleznom kontakte, Zurn Fisic Chim, 26 (1952) 88-95.

[21] T.W. Odom, J.L. HUANG, C.M. Lieber, Single-Walled Carbon Nanotubes, Annals of the New York Academy of Sciences, 960 (2002) 203-215.

[22] R. H. Baughman, A. A. Zakhidov, W. A. De Heer, Carbon nanotubes-the route toward applications, science, 297 (2002) 787-792.

[23] A. Kontos, A. Katsanaki, T. Maggos, V. Likodimos, A. Ghicov, D. Kim, J. Kunze, C. Vasilakos, P. Schmuki, P. Falaras, Photocatalytic degradation of gas pollutants on self-assembled titania nanotubes, Chemical Physics Letters, 490 (2010) 58-62.

[24] A. Kontos, A. Kontos, D. Tsoukleris, V. Likodimos, J. Kunze, P. Schmuki, P. Falaras, Photo-induced effects on self-organized TiO_2 nanotube arrays: the influence of surface morphology, Nanotechnology, 20 (2008) 45603-45612.

[25] J. l. Shui, C. Chen, J. Li, Evolution of nanoporous Pt-Fe alloy nanowires by dealloying and their catalytic property for oxygen reduction reaction, Advanced Functional Materials, 21 (2011) 3357-3362.

[26] J. Y. Lin, Y. L. Hsueh, J. J. Huang, J. R. Wu, Effect of silver nitrate concentration of silver nanowires synthesized using a polyol method and their application as transparent conductive films, Thin Solid Films, 584 (2015) 243-247.

[27] Q. Peng, Y. Qin, ZnO nanowires and their application for solar cells, in: Nanowires-Implementations and Applications, InTech, 2011.

[28] R. Saito, M. Fujita, G. Dresselhaus, M. S. Dresselhaus, Electronic structure of graphene tubules based on C 60, Physical Review B, 46 (1992) 1804-1811.

[29] K. Wakabayashi, M. Fujita, H. Ajiki, M. Sigrist, Electronic and magnetic properties of nanographite ribbons, Physical Review B, 59 (1999) 8271-8282.

[30] P. Ruffieux, S. Wang, B. Yang, C. Sánchez-Sánchez, J. Liu, T. Dienel, L. Talirz, P. Shinde, C.A. Pignedoli, D. Passerone, On-surface synthesis of graphene nanoribbons with zigzag edge topology, Nature, 531 (2016) 489-492.

[31] O. Kit, T. Tallinen, L. Mahadevan, J. Timonen, P. Koskinen, Twisting graphene nanoribbons into carbon nanotubes, Physical Review B, 85 (2012) 85428-85437.

[32] L. Dai, H. Deng, F. Mao, J. Zang, The recent advances of research on p-type ZnO thin film, Journal of Materials Science: Materials in Electronics, 19 (2008) 727-734.

[33] J. Huang, Z. Xu, S. Zhao, Y. Li, F. Zhang, L. Song, Y. Wang, X. Xu, Organic/inorganic heterostructures for enhanced electroluminescence, Solid state communications, 142 (2007) 417-420.

[34] M. Willander, Q. Zhao, Q. H. Hu, P. Klason, V. Kuzmin, S. Al-Hilli, O. Nur, Y.E. Lozovik, Fundamentals and properties of zinc oxide nanostructures: optical and sensing applications, Superlattices and Microstructures, 43 (2008) 352-361.

[35] S. K. Hau, H. L. Yip, H. Ma, A. K. Y. Jen, High performance ambient processed inverted polymer solar cells through interfacial modification with a fullerene self-assembled monolayer, Applied Physics Letters, 93 (2008) 441-444.

[36] J. Singh, J. Im, J.E. Whitten, J.W. Soares, D.M. Steeves, Encapsulation of zinc oxide nanorods and nanoparticles, Langmuir, 25 (2009) 9947-9953.

[37] C. Wöll, The chemistry and physics of zinc oxide surfaces, Progress in Surface Science, 82 (2007) 55-120.

[38] Z.L. Wang, Splendid one-dimensional nanostructures of zinc oxide: a new nanomaterial family for nanotechnology, ACS Nano, 2 (2008) 1987-1992.

[39] A. Kathalingam, V. Senthilkumar, S. Valanarasu, J. K. Rhee, Shape-dependent electrical property of solution synthesized ZnO nanorods, Semiconductor Science and Technology, 27 (2012) 105006-105015.

[40] S. S. Chang, C. W. Shih, C. D. Chen, W. C. Lai, C. C. Wang, The shape transition of gold nanorods, Langmuir, 15 (1999) 701-709.

[41] R. Saravanan, N. Karthikeyan, V. Gupta, E. Thirumal, P. Thangadurai, V. Narayanan, A. Stephen, ZnO/Ag nanocomposite: an efficient catalyst for degradation studies of textile effluents under visible light, Materials Science and Engineering: C, 33 (2013) 2235-2244.

[42] R. Saravanan, M.M. Khan, V.K. Gupta, E. Mosquera, F. Gracia, V. Narayanan, A. Stephen, ZnO/Ag/CdO nanocomposite for visible light-induced photocatalytic degradation of industrial textile effluents, Journal of colloid and interface science, 452 (2015) 126-133.

[43] R. Saravanan, V. Gupta, V. Narayanan, A. Stephen, Visible light degradation of textile effluent using novel catalyst ZnO/γ-Mn_2O_3, Journal of the Taiwan Institute of Chemical Engineers, 45 (2014) 1910-1917.

[44] Q. Yu, J. Li, H. Li, Q. Wang, S. Cheng, L. Li, Fabrication, structure, and photocatalytic activities of boron-doped ZnO nanorods hydrothermally grown on CVD diamond film, Chemical Physics Letters, 539 (2012) 74-78.

[45] V. Eskizeybek, F. Sarı, H. Gülce, A. Gülce, A. Avcı, Preparation of the new polyaniline/ZnO nanocomposite and its photocatalytic activity for degradation of methylene blue and malachite green dyes under UV and natural sun lights irradiations, Applied Catalysis B: Environmental, 119 (2012) 197-206.

[46] Y. Gui, J. Yuan, W. Wang, J. Zhao, J. Tian, B. Xie, Facile solvothermal synthesis and gas sensitivity of graphene/WO_3 nanocomposites, Materials, 7 (2014) 4587-4600.

[47] H.-E. Schaefer, Nanoscience: the science of the small in physics, engineering, chemistry, biology and medicine, Materials Physics and Mechanics 11 (2011) 194-194.

[48] A.P. Alivisatos, Perspectives on the physical chemistry of semiconductor nanocrystals, The Journal of Physical Chemistry, 100 (1996) 13226-13239.

[49] C. Murray, D. J. Norris, M. G. Bawendi, Synthesis and characterization of nearly monodisperse CdE (E= sulfur, selenium, tellurium) semiconductor nanocrystallites, Journal of the American Chemical Society, 115 (1993) 8706-8715.

[50] M. Nirmal, L. Brus, Luminescence photophysics in semiconductor nanocrystals, Accounts of Chemical Research, 32 (1999) 407-414.

[51] A.P. Alivisatos, Nanocrystals: building blocks for modern materials design, Endeavour, 21 (1997) 56-60.

[52] R.E. Bailey, S. Nie, Alloyed semiconductor quantum dots: tuning the optical properties without changing the particle size, Journal of the American Chemical Society, 125 (2003) 7100-7106.

[53] M. Sahana, C. Sudakar, A. Dixit, J. Thakur, R. Naik, V. Naik, Quantum confinement effects and band gap engineering of SnO_2 nanocrystals in a MgO matrix, Acta Materialia, 60 (2012) 1072-1078.

[54] X. Xu, J. Zhuang, X. Wang, SnO_2 quantum dots and quantum wires: controllable synthesis, self-assembled 2D architectures, and gas-sensing properties, Journal of the American Chemical Society, 130 (2008) 12527-12535.

[55] G. Xi, J. Ye, Ultrathin SnO_2 nanorods: template-and surfactant-free solution phase synthesis, growth mechanism, optical, gas-sensing, and surface adsorption properties, Inorganic chemistry, 49 (2010) 2302-2309.

[56] H. Zhu, D. Yang, G. Yu, H. Zhang, K. Yao, A simple hydrothermal route for synthesizing SnO_2 quantum dots, Nanotechnology, 17 (2006) 2386-2389.

[57] M.F. Hawthorne, The role of chemistry in the development of boron neutron capture therapy of cancer, Angewandte Chemie International Edition, 32 (1993) 950-984.

[58] A. Bielinska, J.F. Kukowska-Latallo, J. Johnson, D.A. Tomalia, J.R. Baker Jr, Regulation of in vitro gene expression using antisense oligonucleotides or antisense expression plasmids transfected using starburst pamam dendrimers, Nucleic acids research, 24 (1996) 2176-2182.

[59] A. Zweck, W. Luther, Applications of nanotechnology in space developments and systems, Technological Analysis, VDI Technology Center Future Technologies Division, Duesseldorf, Germany biography Selim Coşkun was born on May, 20 (2003) 1980.

[60] I. Matsui, Nanoparticles for electronic device applications: a brief review, Journal of chemical engineering of Japan, 38 (2005) 535-546.

[61] D. Burgess, ZnO nanowire LEDs have UV output, in, laurin publ co inc berkshire common po box 1146, pittsfield, ma 1202 (2006) 135-136.

[62] M. Allsopp, A. Walters, D. Santillo, Nanotechnologies and nanomaterials in electrical and electronic goods: A review of uses and health concerns, Greenpeace Research Laboratories, London, 9 (2007) 1-22.

[63] M. Endo, T. Hayashi, Y.A. Kim, H. Muramatsu, Development and application of carbon nanotubes, Japanese Journal of Applied Physics, 45 (2006) 4883-4892.

[64] P. Barbaro, F. Liguori, Heterogenized homogeneous catalysts for fine chemicals production: materials and processes, Springer Science & Business Media, 2010.

[65] R. Lane, B. Craig, W. Babcock, Materials engineering with nature's building blocks, amptiac Newslett. Spring, 6 (2002) 31-37.

[66] K.J. Klabunde, R. Richards, Nanoscale materials in chemistry, Wiley Online Library, 2001.

[67] M. Willard, L. Kurihara, E. Carpenter, S. Calvin, V. Harris, Chemically prepared magnetic nanoparticles, International Materials Reviews, 49 (2004) 125-170.

[68] A.C. Pierre, G.M. Pajonk, Chemistry of aerogels and their applications, Chemical Reviews, 102 (2002) 4243-4266.

[69] Z.-l. Lu, E. Lindner, H.A. Mayer, Applications of sol-gel-processed interphase catalysts, Chemical Reviews, 102 (2002) 3543-3578.

[70] A. Wight, M. Davis, Design and preparation of organic-inorganic hybrid catalysts, Chemical reviews, 102 (2002) 3589-3614.

[71] J.A. Schwarz, C. Contescu, A. Contescu, Methods for preparation of catalytic materials, Chemical Reviews, 95 (1995) 477-510.

[72] L.L. Hench, J.K. West, The sol-gel process, Chemical reviews, 90 (1990) 33-72.

[73] G. Armstrong, A.R. Armstrong, J. Canales, P.G. Bruce, Nanotubes with the TiO_2-B structure, Chemical Communications, 19 (2005) 2454-2456.

[74] R. Dong, S. Jiang, Z. Li, Z. Chen, H. Zhang, C. Jin, Superhydrophilic TiO_2 nanorod films with variable morphology grown on different substrates, Materials Letters, 152 (2015) 151-154.

[75] B. Liu, E.S. Aydil, Growth of oriented single-crystalline rutile TiO_2 nanorods on transparent conducting substrates for dye-sensitized solar cells, Journal of the American Chemical Society, 131 (2009) 3985-3990.

[76] Y. Xie, C. Xia, H. Du, W. Wang, Enhanced electrochemical performance of polyaniline/carbon/titanium nitride nanowire array for flexible supercapacitor, Journal of Power Sources, 286 (2015) 561-570.

[77] M. Ge, C. Cao, J. Huang, S. Li, Z. Chen, K.-Q. Zhang, S. Al-Deyab, Y. Lai, A review of one-dimensional TiO_2 nanostructured materials for environmental and energy applications, Journal of Materials Chemistry A, 4 (2016) 6772-6801.

[78] M.C. Mascolo, Y. Pei, T.A. Ring, Room temperature co-precipitation synthesis of magnetite nanoparticles in a large pH window with different bases, Materials, 6 (2013) 5549-5567.

[79] K. Kumar, M. Chitkara, I.S. Sandhu, D. Mehta, S. Kumar, Photocatalytic and magnetic properties of $Zn_{1-x}Cr_xO$ nanocomposites prepared by a co-precipitation method, Materials Science in Semiconductor Processing, 30 (2015) 142-151.

[80] W.-x. Hou, Z. Wang, Structural and magnetic properties of $Ni_{0.15}Mg_{0.1}Cu_{0.3}Zn_{0.45}Fe_2O_4$ ferrite prepared by NaOH-precipitation method, Materials Science and Engineering: B, 199 (2015) 57-61.

[81] E. Casbeer, V.K. Sharma, X.-Z. Li, Synthesis and photocatalytic activity of ferrites under visible light: a review, Separation and Purification Technology, 87 (2012) 1-14.

[82] P.E. Meskin, V.K. Ivanov, A.E. Barantchikov, B.R. Churagulov, Y.D. Tretyakov, Ultrasonically assisted hydrothermal synthesis of nanocrystalline ZrO_2, TiO_2, $NiFe_2O_4$ and $Ni_{0.5}Zn_{0.5}Fe_2O_4$ powders, Ultrasonics sonochemistry, 13 (2006) 47-53.

[83] J.R. Li, Z.L. Tang, Z.T. Zhang, Converting Industrial TiO_2 into Titanate Nanotubes by Simple Sonochemical-Hydrothermal Processing, in: Key Engineering Materials, Trans Tech Publ, 280 (2005) 651-654.

[84] Q. Jia, W. Que, J. Zhang, Heterogeneous solvothermal synthesis of one-dimensional titania nanostructures on transparent conductive glasses, physica status solidi (a), 208 (2011) 2313-2316.

[85] C.T. Nam, J.L. Falconer, W.-D. Yang, Morphology, structure and adsorption of titanate nanotubes prepared using a solvothermal method, Materials Research Bulletin, 51 (2014) 49-55.

[86] J. Xu, J.-P. Ge, Y.-D. Li, Solvothermal synthesis of monodisperse PbSe nanocrystals, The Journal of Physical Chemistry B, 110 (2006) 2497-2501.

[87] J.W. Mullin, Crystallization, 3rd, in, University of London: Butterworth-Heinemann, Reed Edueational and Professional Publishing Ltd, 1993.

[88] V.F. Puntes, D. Zanchet, C.K. Erdonmez, A.P. Alivisatos, Synthesis of hcp-Co nanodisks, Journal of the American Chemical Society, 124 (2002) 12874-12880.

[89] I. Robinson, S. Zacchini, L.D. Tung, S. Maenosono, N.T. Thanh, Synthesis and characterization of magnetic nanoalloys from bimetallic carbonyl clusters, Chemistry of Materials, 21 (2009) 3021-3026.

[90] W.J. Habraken, J. Tao, L.J. Brylka, H. Friedrich, L. Bertinetti, A.S. Schenk, A. Verch, V. Dmitrovic, P.H. Bomans, P.M. Frederik, Ion-association complexes unite classical and non-classical theories for the biomimetic nucleation of calcium phosphate, Nature communications, 4 (2013) 1507-1519.

[91] S.G. Kwon, T. Hyeon, Formation mechanisms of uniform nanocrystals via hot-injection and heat-up methods, Small, 7 (2011) 2685-2702.

[92] T. Sugimoto, Monodispersed particles, Elsevier, 2001.

[93] D.V. Talapin, A.L. Rogach, M. Haase, H. Weller, Evolution of an ensemble of nanoparticles in a colloidal solution: theoretical study, The Journal of Physical Chemistry B, 105 (2001) 12278-12285.

[94] A.L. Rogach, D.V. Talapin, E.V. Shevchenko, A. Kornowski, M. Haase, H. Weller, Organization of matter on different size scales: monodisperse nanocrystals and their superstructures, Advanced Functional Materials, 12 (2002) 653-664.

[95] V.K. LaMer, R.H. Dinegar, Theory, production and mechanism of formation of monodispersed hydrosols, Journal of the American Chemical Society, 72 (1950) 4847-4854.

[96] V.K.L. Mer, Nucleation in Phase Transitions, Industrial & Engineering Chemistry, 44 (1952) 1270-1277.

[97] T. Sugimoto, F. Shiba, T. Sekiguchi, H. Itoh, Spontaneous nucleation of monodisperse silver halide particles from homogeneous gelatin solution I: silver chloride, Colloids and Surfaces A: Physicochemical and Engineering Aspects, 164 (2000) 183-203.

[98] I.M. Lifshitz, V.V. Slyozov, The kinetics of precipitation from supersaturated solid solutions, Journal of physics and chemistry of solids, 19 (1961) 35-50.

[99] C. Wagner, Theorie der alterung von niederschlägen durch umlösen (Ostwald-reifung), Berichte der Bunsengesellschaft für physikalische Chemie, 65 (1961) 581-591.

[100] W.-r. Lee, M.G. Kim, J.-r. Choi, J.-I. Park, S.J. Ko, S.J. Oh, J. Cheon, Redox-transmetalation process as a generalized synthetic strategy for core-shell

magnetic nanoparticles, Journal of the American Chemical Society, 127 (2005) 16090-16097.

[101] M.A. Watzky, R.G. Finke, Transition metal nanocluster formation kinetic and mechanistic studies. A new mechanism when hydrogen is the reductant: slow, continuous nucleation and fast autocatalytic surface growth, Journal of the American Chemical Society, 119 (1997) 10382-10400.

[102] R. Zhang, A. Khalizov, L. Wang, M. Hu, W. Xu, Nucleation and growth of nanoparticles in the atmosphere, Chemical Reviews, 112 (2011) 1957-2011.

[103] N.T. Thanh, N. Maclean, S. Mahiddine, Mechanisms of nucleation and growth of nanoparticles in solution, Chemical reviews, 114 (2014) 7610-7630.

[104] G. Amin, M. Asif, A. Zainelabdin, S. Zaman, O. Nur, M. Willander, Influence of pH, precursor concentration, growth time, and temperature on the morphology of ZnO nanostructures grown by the hydrothermal method, Journal of Nanomaterials, 2011 (2011) 5-14.

[105] J. Zhou, N.S. Xu, Z.L. Wang, Dissolving behavior and stability of ZnO wires in biofluids: a study on biodegradability and biocompatibility of ZnO nanostructures, Advanced Materials, 18 (2006) 2432-2435.

[106] L. Vayssieres, K. Keis, S.-E. Lindquist, A. Hagfeldt, Purpose-built anisotropic metal oxide material: 3D highly oriented microrod array of ZnO, The Journal of Physical Chemistry B, 105 (2001) 3350-3352.

[107] L. Vayssieres, Growth of arrayed nanorods and nanowires of ZnO from aqueous solutions, Advanced Materials, 15 (2003) 464-466.

[108] Y. Zhu, D. Fan, W. Shen, A general chemical conversion route to synthesize various ZnO-based core/shell structures, The Journal of Physical Chemistry C, 112 (2008) 10402-10406.

[109] A. Rai, A. Singh, A. Ahmad, M. Sastry, Role of halide ions and temperature on the morphology of biologically synthesized gold nanotriangles, Langmuir, 22 (2006) 736-741.

[110] S. Kim, J. Nah, I. Jo, D. Shahrjerdi, L. Colombo, Z. Yao, E. Tutuc, S.K. Banerjee, Realization of a high mobility dual-gated graphene field-effect transistor with Al_2O_3 dielectric, Applied Physics Letters, 94 (2009) 62107-62110.

[111] I. Robel, M. Kuno, P.V. Kamat, Size-dependent electron injection from excited CdSe quantum dots into TiO_2 nanoparticles, Journal of the American Chemical Society, 129 (2007) 4136-4137.

[112] H. Tong, S. Ouyang, Y. Bi, N. Umezawa, M. Oshikiri, J. Ye, Nano-photocatalytic materials: possibilities and challenges, Advanced materials, 24 (2012) 229-251.

[113] R. Sasikala, A.R. Shirole, V. Sudarsan, K.G. Girija, R. Rao, C. Sudakar, S.R. Bharadwaj, Improved photocatalytic activity of indium doped cadmium sulfide dispersed on zirconia, Journal of Materials Chemistry, 21 (2011) 16566-16573.

[114] P. Alivisatos, The use of nanocrystals in biological detection, Nature biotechnology, 22 (2004) 47-52.

[115] N. Pradhan, D.M. Battaglia, Y. Liu, X. Peng, Efficient, stable, small, and water-soluble doped ZnSe nanocrystal emitters as non-cadmium biomedical labels, Nano Letters, 7 (2007) 312-317.

[116] K. Mondal, A. Sharma, Photocatalytic oxidation of pollutant dyes in wastewater by TiO_2 and ZnO nano-materials-a mini-review, in Nanoscience & Technology for Mankind, (2014) 36-72.

[117] A.L. Rogach, T. Franzl, T.A. Klar, J. Feldmann, N. Gaponik, V. Lesnyak, A. Shavel, A. Eychmüller, Y.P. Rakovich, J.F. Donegan, Aqueous synthesis of thiol-capped CdTe nanocrystals: state-of-the-art, The Journal of Physical Chemistry C, 111 (2007) 14628-14637.

[118] E.J. Henderson, C.M. Hessel, J.G. Veinot, Synthesis and photoluminescent properties of size-controlled germanium nanocrystals from phenyl trichlorogermane-derived polymers, Journal of the American Chemical Society, 130 (2008) 3624-3632.

[119] J.Z. Zhang, Ultrafast studies of electron dynamics in semiconductor and metal colloidal nanoparticles: Effects of size and surface, Accounts of Chemical Research, 30 (1997) 423-429.

[120] L.M. Peter, Dynamic aspects of semiconductor photoelectrochemistry, Chemical Reviews, 90 (1990) 753-769.

[121] R. Suarez, P. Nair, P.V. Kamat, Photoelectrochemical behavior of Bi2S3 nanoclusters and nanostructured thin films, Langmuir, 14 (1998) 3236-3241.

[122] A.L. Efros, A.L. Efros, Interband absorption of light in a semiconductor sphere, Soviet Physics Semiconductors-Ussr, 16 (1982) 772-775.

[123] L. Brus, A simple model for the ionization potential, electron affinity, and aqueous redox potentials of small semiconductor crystallites, The Journal of chemical physics, 79 (1983) 5566-5571.

[124] P. Lippens, M. Lannoo, Calculation of the band gap for small CdS and ZnS crystallites, Physical Review B, 39 (1989) 10935-10942.

[125] P. Lippens, M. Lannoo, Comparison between calculated and experimental values of the lowest excited electronic state of small CdSe crystallites, Physical Review B, 41 (1990) 6079-6081.

[126] M. Pera-Titus, V. García-Molina, M.A. Baños, J. Giménez, S. Esplugas, Degradation of chlorophenols by means of advanced oxidation processes: a general review, Applied Catalysis B: Environmental, 47 (2004) 219-256.

[127] M.A. Shannon, P.W. Bohn, M. Elimelech, J.G. Georgiadis, B.J. Marinas, A.M. Mayes, Science and technology for water purification in the coming decades, Nature, 452 (2008) 301-310.

[128] R. Saleh, N.F. Djaja, UV light photocatalytic degradation of organic dyes with Fe-doped ZnO nanoparticles, Superlattices and Microstructures, 74 (2014) 217-233.

[129] L. Wolski, J. Whitten, I. Sobczak, M. Ziolek, The effect of the preparation procedure on the morphology, texture and photocatalytic properties of ZnO, Materials Research Bulletin, 85 (2017) 35-46.

[130] J. Xie, Y. Li, W. Zhao, L. Bian, Y. Wei, Simple fabrication and photocatalytic activity of ZnO particles with different morphologies, Powder Technology, 207 (2011) 140-144.

[131] D. Thomas, The exciton spectrum of zinc oxide, Journal of Physics and Chemistry of Solids, 15 (1960) 86-96.

[132] C. Jagadish, S.J. Pearton, Zinc oxide bulk, thin films and nanostructures: processing, properties, and applications, Elsevier, 2011.

[133] P. Chand, A. Gaur, A. Kumar, Effect of sintering temperature on $Zn_{0.94}Cr_{0.03}Fe_{0.03}O$ nanostructures, Procedia Materials Science, 10 (2015) 97-102.

[134] D. Chu, Y. Masuda, T. Ohji, K. Kato, Formation and photocatalytic application of ZnO nanotubes using aqueous solution, Langmuir, 26 (2009) 2811-2815.

[135] Ü. Özgür, Y.I. Alivov, C. Liu, A. Teke, M. Reshchikov, S. Doğan, V. Avrutin, S.-J. Cho, H. Morkoc, A comprehensive review of ZnO materials and devices, Journal of applied physics, 98 (2005) 041301- 041404.

[136] A. Moezzi, A.M. McDonagh, M.B. Cortie, Zinc oxide particles: Synthesis, properties and applications, Chemical Engineering Journal, 185 (2012) 1-22.

[137] S. George, S. Pokhrel, T. Xia, B. Gilbert, Z. Ji, M. Schowalter, A. Rosenauer, R. Damoiseaux, K.A. Bradley, L. Mädler, Use of a rapid cytotoxicity screening approach to engineer a safer zinc oxide nanoparticle through iron doping, ACS nano, 4 (2009) 15-29.

[138] N. Emanetoglu, C. Gorla, Y. Liu, S. Liang, Y. Lu, Epitaxial ZnO piezoelectric thin films for saw filters, Materials Science in Semiconductor Processing, 2 (1999) 247-252.

[139] S. Singh, P. Thiyagarajan, K.M. Kant, D. Anita, S. Thirupathiah, N. Rama, B. Tiwari, M. Kottaisamy, M.R. Rao, Structure, microstructure and physical properties of ZnO based materials in various forms: bulk, thin film and nano, Journal of Physics D: Applied Physics, 40 (2007) 6312-6327.

[140] Z.L. Wang, J. Song, Piezoelectric nanogenerators based on zinc oxide nanowire arrays, Science, 312 (2006) 242-246.

[141] M. Yano, K. Koike, K.i. Ogata, T. Nogami, S. Tanabe, S. Sasa, Zinc oxide-based biosensors, physica status solidi (c), 9 (2012) 1570-1573.

[142] M. Sui, P. Gong, X. Gu, Review on one-dimensional ZnO nanostructures for electron field emitters, Frontiers of Optoelectronics, 6 (2013) 386-412.

[143] W. Chen, Z. Wang, Z. Lin, L. Lin, Absorption and luminescence of the surface states in ZnS nanoparticles, Journal of applied physics, 82 (1997) 3111-3115.

[144] G. Hitkari, S. Singh, G. Pandey, Structural, optical and photocatalytic study of ZnO and ZnO-ZnS synthesized by chemical method, Nano-Structures & Nano-Objects, 12 (2017) 1-9.

[145] P.V. Raleaooa, A. Roodt, G.G. Mhlongo, D.E. Motaung, R.E. Kroon, O.M. Ntwaeaborwa, Luminescent, magnetic and optical properties of ZnO-ZnS nanocomposites, Physica B: Condensed Matter, 507 (2017) 13-20.

[146] P. Verma, A.C. Pandey, R. Bhargava, Synthesis and characterisation: Zinc oxide-sulfide nanocomposites, Physica B: Condensed Matter, 404 (2009) 3894-3897.

[147] P. Xu, G.M. Zeng, D.L. Huang, C.L. Feng, S. Hu, M.H. Zhao, C. Lai, Z. Wei, C. Huang, G.X. Xie, Use of iron oxide nanomaterials in wastewater treatment: a review, Science of the Total Environment, 424 (2012) 1-10.

[148] A. Dodd, A. Mckinley, M. Saunders, T. Tsuzuki, Synthesis and photocatalytic activity of doped zinc oxide nanoparticles, in: Nanoscience and Nanotechnology, 2006. ICONN'06. International Conference on, IEEE, 2006.

[149] Y. Wu, A. Tok, F. Boey, X. Zeng, X. Zhang, Surface modification of ZnO nanocrystals, Applied Surface Science, 253 (2007) 5473-5479.

[150] H. Wang, C. Xie, W. Zhang, S. Cai, Z. Yang, Y. Gui, Comparison of dye degradation efficiency using ZnO powders with various size scales, Journal of Hazardous materials, 141 (2007) 645-652.

[151] T. Tsuzuki, Z. Smith, A. Parker, R. He, X. Wang, Photocatalytic activity of manganese-doped ZnO nanocrystalline powders, Journal of the Australian ceramic society, 45 (2009) 58-62.

[152] M.K. Lima, D.M. Fernandes, M.F. Silva, M.L. Baesso, A.M. Neto, G.R. de Morais, C.V. Nakamura, A. de Oliveira Caleare, A.A.W. Hechenleitner,

E.A.G. Pineda, Co-doped ZnO nanoparticles synthesized by an adapted sol-gel method: effects on the structural, optical, photocatalytic and antibacterial properties, Journal of sol-gel science and technology, 72 (2014) 301-309.

[153] R. Saleh, N.F. Djaja, Transition-metal-doped ZnO nanoparticles: synthesis, characterization and photocatalytic activity under UV light, Spectrochimica Acta Part A: Molecular and Biomolecular Spectroscopy, 130 (2014) 581-590.

[154] I. Prabha, S. Lathasree, Photodegradation of phenol by zinc oxide, titania and zinc oxide-titania composites: Nanoparticle synthesis, characterization and comparative photocatalytic efficiencies, Materials Science in Semiconductor Processing, 26 (2014) 603-613.

[155] Y. Sivry, A. Gelabert, L. Cordier, R. Ferrari, H. Lazar, F. Juillot, N. Menguy, M. Benedetti, Behavior and fate of industrial zinc oxide nanoparticles in a carbonate-rich river water, Chemosphere, 95 (2014) 519-526.

[156] K. Barick, P. Sharma, A. Mukhija, J. Sainis, A. Gupta, P. Hassan, Effect of cetylpyridinium chloride on surface passivation and photocatalytic activity of ZnO nanostructures, Journal of Environmental Chemical Engineering, 3 (2015) 1346-1355.

[157] J. Choina, A. Bagabas, C. Fischer, G.-U. Flechsig, H. Kosslick, A. Alshammari, A. Schulz, The influence of the textural properties of ZnO nanoparticles on adsorption and photocatalytic remediation of water from pharmaceuticals, Catalysis Today, 241 (2015) 47-54.

[158] A. Behzadnia, M. Montazer, M.M. Rad, In situ photo sonosynthesis and characterize nonmetal/metal dual doped honeycomb-like ZnO nanocomposites on wool fabric, Ultrasonics sonochemistry, 27 (2015) 200-209.

[159] I. Unlu, J.W. Soares, D.M. Steeves, J.E. Whitten, Photocatalytic Activity and Fluorescence of Gold/Zinc Oxide Nanoparticles Formed by Dithiol Linking, Langmuir, 31 (2015) 8718-8725.

[160] M.A. Subhan, N. Uddin, P. Sarker, H. Nakata, R. Makioka, Synthesis, characterization, low temperature solid state PL and photocatalytic activities of $Ag_2O/CeO_2/ZnO$ nanocomposite, Spectrochimica Acta Part A: Molecular and Biomolecular Spectroscopy, 151 (2015) 56-63.

[161] M.B. Ali, H.H. Yolcu, H. Elhouichet, B. Sieber, A. Addad, L. Boussekey, M. Moreau, M. Férid, S. Szunerits, R. Boukherroub, Hydrothermal synthesis of ZTO/graphene nanocomposite with excellent photocatalytic activity under visible light irradiation, Journal of colloid and interface science, 473 (2016) 66-74.

[162] K. Chakraborty, S. Chakrabarty, P. Das, S. Ghosh, T. Pal, UV-assisted synthesis of reduced graphene oxide zinc sulfide composite with enhanced photocatalytic activity, Materials Science and Engineering: B, 204 (2016) 8-14.

[163] K.P. Raj, K. Sadayandi, Effect of temperature on structural, optical and photoluminescence studies on ZnO nanoparticles synthesized by the standard co-precipitation method, Physica B: Condensed Matter, 487 (2016) 1-7.

[164] M. Gancheva, M. Markova-Velichkova, G. Atanasova, D. Kovacheva, I. Uzunov, R. Cukeva, Design and photocatalytic activity of nanosized zinc oxides, Applied Surface Science, 368 (2016) 258-266.

[165] T. Jana, S. Maji, A. Pal, R. Maiti, T. Dolai, K. Chatterjee, Photocatalytic and antibacterial activity of cadmium sulphide/zinc oxide nanocomposite with varied morphology, Journal of colloid and interface science, 480 (2016) 9-16.

[166] H. Zhao, R. Sun, X. Li, X. Sun, Enhanced photocatalytic activity for hydrogen evolution from water by $Zn_{0.5}Cd_{0.5}S/WS_2$ heterostructure, Materials Science in Semiconductor Processing, 59 (2017) 68-75.

[167] Q. Tian, W. Wu, S. Yang, J. Liu, W. Yao, F. Ren, C. Jiang, Zinc Oxide Coating Effect for the Dye Removal and Photocatalytic Mechanisms of Flower-Like MoS_2 Nanoparticles, Nanoscale Research Letters, 12 (2017) 221-231.

[168] M. Duan, J. Wang, C. Liu, J. Xie, J. Han, Effects of SnO doping on the optical properties of ZnO in glass, Journal of Non-Crystalline Solids, 459 (2017) 32-35.

[169] M. Mitra, A. Ghosh, A. Mondal, K. Kargupta, S. Ganguly, D. Banerjee, Facile synthesis of aluminium doped zinc oxide-polyaniline hybrids for photoluminescence and enhanced visible-light assisted photo-degradation of organic contaminants, Applied Surface Science, 402 (2017) 418-428.

[170] M.M.H. Farooqi, R.K. Srivastava, Structural, optical and photoconductivity study of ZnO nanoparticles synthesized by annealing of ZnS nanoparticles, Journal of Alloys and Compounds, 691 (2017) 275-286.

***

Chapter 2
Characterization Technique, Materials and Methods

Chapter 2
Characterization technique, materials and methods

"This chapter introduced some important characterization techniques which are used for the investigation of the nanoparticles/nanostructures and nanocomposites materials. The crystal structure, phases with lattice strain and purity of the materials are examined by X-ray diffraction, morphology and particle size distribution investigated via scanning electron microscopy and transmission electron microscopy. Optical properties and surface behaviour of particles are appraised through photoluminescence spectroscopy and BET surface area analyzer. The brief outline of instrumentation and application of these characterization techniques are discussed in brief in the present thesis."

2.1. General experimental methods and techniques

All the basic materials employed in the fabrication of nanostructures were of analytical grade, purchased from Merck India and Fisher Scientific (India) chemicals and were used without further purification. The details of the general tentative method, accepted analytical processes, materials required, application for the photocatalytic process, and estimation of optical aptitude are defined in this chapter.

2.2. Materials Required:

Zinc (II) sulphate heptahydrate ($ZnSO_4.7H_2O$), zinc nitrate hexahydrate ($Zn(NO_3)_2.6H_2O$), urea (NH_2CONH_2), thiourea (NH_2CSNH_2), ferric hydroxide ($Fe(OH)_3$) (anhydrous), Iron (II) sulphate heptahydrate ($FeSO_4.7H_2O$), copper chloride dihydrate ($CuCl_2.2H_2O$), glycine ($C_2H_5NO_2$), sodium hydroxide (NaOH), congo red, rhodamine B, methyl orange, methylene blue, and double de-ionized water.

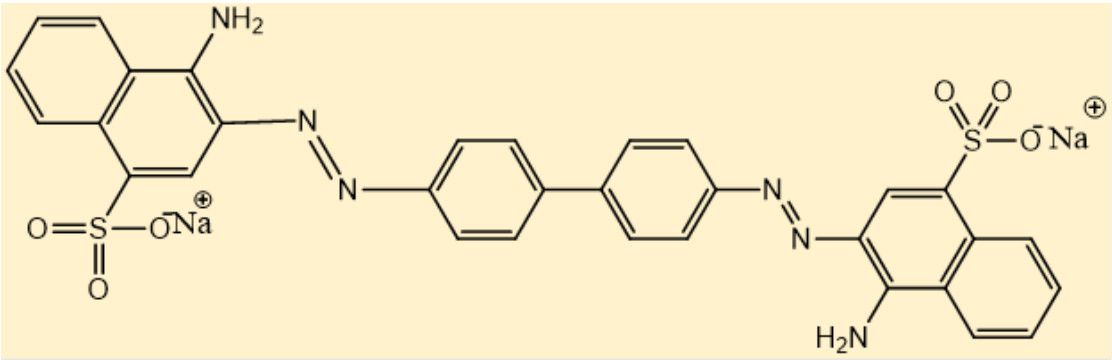

Congo red

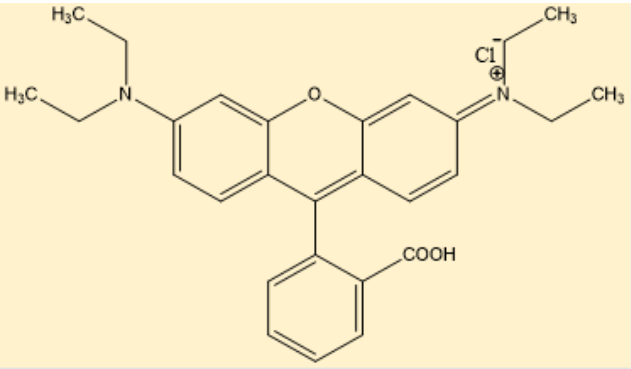

Rhodamine B

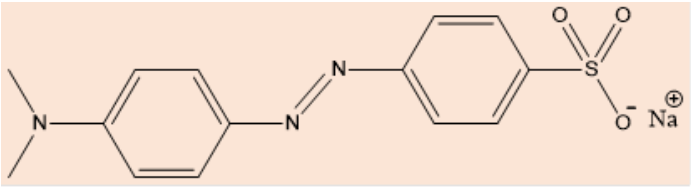

Methyl Orange

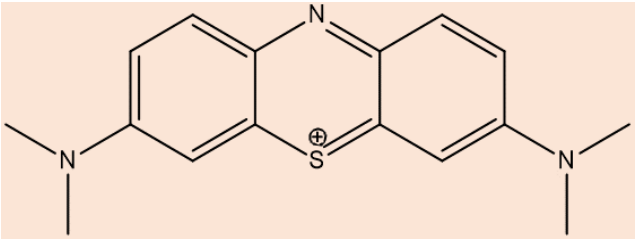

Methylene Blue

2.3. Analytical methods for characterization:

2.3.1. Powder X-ray diffraction (P-XRD) or crystallography:

X-ray powder diffraction (P-XRD) is a potent non-destructive analytical technique and most common for investigations of physical and chemical features of large counterpart along with nanostructure material, how the array of atoms in the crystalline phase and what the interatomic distances and angles are, etc. It also endows the evidence about preferred crystal orientations, phase and other structural constraints such as average particle size, crystallographic unit cell, crystal defects and crystallinity [1, 2]. In this characteristic technique, a beam of accelerated electrons colloid with metal target to produce X-rays. In this procedure an inner electron from metal atom is ejected and generate vacancy, suddenly an outer shell electron moves down to fill the vacancy and emit X-ray. X-rays have wavelengths in an angstrom (Å $=10^{-10}$ m) which is the characteristic range of distance of inter atoms in crystalline solids. The beam of X-ray have similar wavelength that interacts on a material (single crystal or amorphous powder) of the nanostructures under investigation. The image of the X-ray diffraction is shown in Figure 2.1.

Figure 2.1: Image of XRD instrument

X-ray diffraction is the outcome of the interaction among the X-rays and inner electrons of atoms. On the behalf of the arrangement of atoms, the retardation between the scattered rays is profitable when the path between the two diffracted rays is different from an integral number of wavelengths. This discriminatory situation is illustrated by the Bragg equation given in equation. (2.1) and is termed as Bragg's law [3].

$$n\lambda = 2d\sin\theta \tag{2.1}$$

Where n is an integer quantity, λ is the wavelength of X-rays, d is the space between the planes in the atomic lattice and θ is the diffracted angle between the X-ray and the atomic planes. Schematic representation of X-ray diffraction and scattering of rays from different planes is shown in Figure 2.2

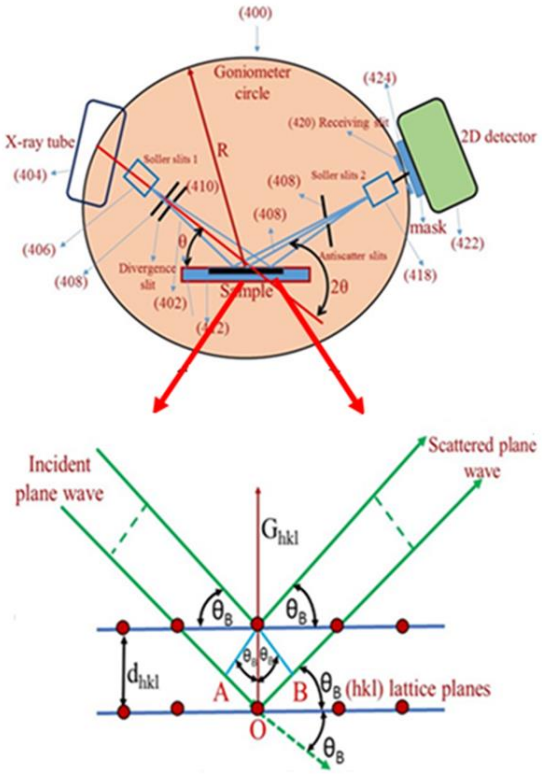

Figure 2.2: Schematic representation of X-ray diffraction and **s**cattering of rays from different planes, in the same direction, make constructive interference.

This law represents a relationship between the wavelength of incident X-ray, diffraction angle and the lattice distances in a crystalline material. The diffracted X-rays from the material are then perceived, refined and counted. By scanning the material through a range of 2θ angles, all possible diffraction directions of the lattice should be obtained because of the random orientation of the powdered sample. Conversion of the diffraction peaks to d-spacing allows identification of the sample because each sample has a set of unique d-spacing. Typically, this is obtained by the evaluation of d-spacing with joint committee on powder diffraction standard (JCPDS).

Applications:

1. The mean size of the crystalline materials can be calculated by adopting the full-width half maxima (FWHM) of the diffraction peaks by applying the Scherer's equation [4] given by,

$$D = \frac{0.91\lambda}{\beta \cos\theta} \tag{2.2}$$

Where 0.91 is the value of the shape factor, 'λ' is the wavelength of X-rays which is 1.5406 nm for CuKα, 'β' is the FWHM of diffraction peak measured in radians and 'θ' is the Bragg's angle.

2. The bond length (L) and volume (V) was calculated from the unit cell for prepared materials with the help of eq [5]

$$L = \sqrt{\frac{a^2}{3} + \left(\frac{1}{2} - z\right)^2 c^2} \tag{2.3}$$

$$z = \frac{a^2}{3c^2} + \frac{1}{4} \tag{2.4}$$

$$V = 0.866 a^2 c \tag{2.5}$$

Where a and c are lattice parameter are determined by the following expression [6]

$$\frac{1}{d^2} = \frac{4}{3}\left(\frac{h^2 + hk + k^2}{a^2}\right) + \frac{l^2}{c^2} \tag{2.6}$$

3. The microstrain (ε) is present in the materials are also calculated by using the following relation [7]

$$\varepsilon = \frac{\beta \cos\theta}{4} \tag{2.7}$$

4. The dislocation density (δ) in the nanoparticles was estimated Williamson and Smallman's equation [8]

$$\delta = \frac{n}{D^2} \tag{2.8}$$

Where n is a constant usually close to one.

In the present exploration of the synthesized bare and composites of ZnO nanoparticles were characterized by X-ray powder diffraction (XRD) using Analytical Rigaku High-Resolution Powder Diffractometer 12kW X-ray diffractometer (λ =

1.5406 Å) in the 2θ range of 20-80˚ with scan rate of 10/min using Cu Kα radiation (40 KV).

2.3.2. Transmission electron microscopy (TEM):

Transmission electron microscopy (TEM) is a microscopic and powerful technique first developed in the 1930's for obtaining information on morphology [9], size, crystal structure and defect structure of the crystalline materials. It's a direct and most important technique for imaging the nanostructure materials. The energy of electron for imaging and diffraction pattern decided by de Broglie wavelength $\lambda = h/p$, where, h is Planks constant and p is the momentum of the electron. In the experimental process a thin sample, typically less than 200 nm, is bombarded by a high energy level (few hundreds keV) and focused electrons of very short wavelength, emitted from a tungsten filament at the top of a cylindrical column of about 2 m height [10, 11]. This bombarded electron can scatter or backscatter elastically or inelastically, or produces many interactions, such as X-rays or Auger electrons. Elastic scattering occurs when the incoming fast electron and an atomic nucleus interact while inelastic scattering results from the interaction between the fast electron and atomic electrons (Figure 2.3). An image is formed from the electron transmitted through the sample; the image is stretched and focused onto an imaging device such as a fluorescent screen or on a layer of photographic film and detected by a sensor such as a CCD (Charge coupled device) camera. The back scattered electrons give diffraction pattern to obtaining the information of the structure of materials, including perfect crystals and defect structures. The preference of electron diffraction over other methods, e.g., X-ray or neutron are due to the generation of extremely short wavelength (~ 2 pm), the strong atomic scattering, and the more capability to scrutinize insignificant volumes of matter (~ 10 nm) [12].

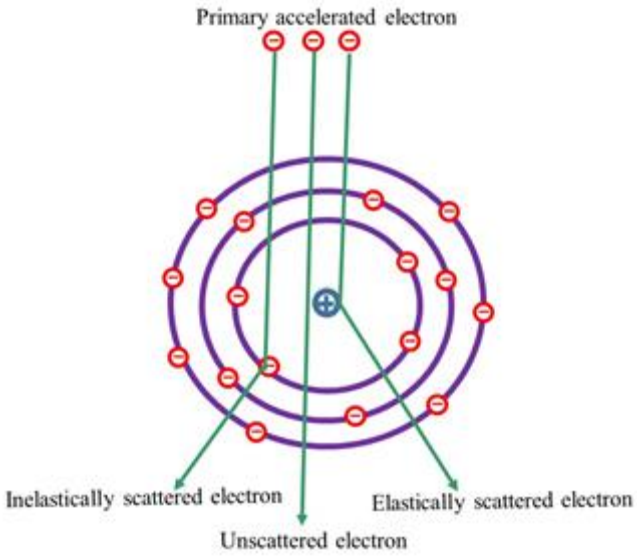

Figure 2.3: Schematic represent the formation of elastic and inelastic scattering of electrons.

Figure 2.4 shows an image of the instrument and systematic ray diagram of a TEM. The electron beam is generated by the electron gun (electron source) and confined through the condenser lens, passes the condenser aperture and strikes the sample. Because the sample is ultra-thin, most of the unscattered electrons are transmitted through the material with some undergoing deflection as a result of elastic scattering and inelastic scattering. The unscattered and scattered electrons are then recombined through the objective lens forming either a first intermediate image or a diffraction pattern in the back focal plane. The image or the diffraction pattern will be further magnified by the intermediate lens. By altering the projector lens, the enlarged image or diffraction pattern will be focused and projected on a fluorescent screen or recorded on a digital (CCD) camera.

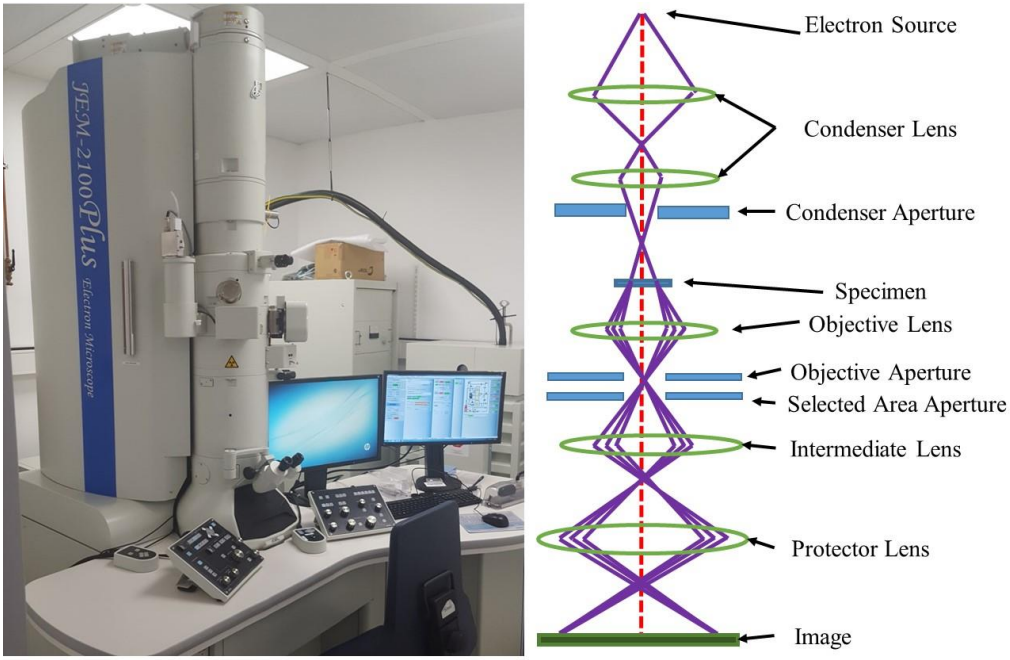

Figure 2.4: Image of TEM instrument and schematic representation of the electron beam.

TEM microscopic technique has the dominance over the other technique because this one can not obtain the images of the sample only but diffraction patterns also, which enable to make the detailed crystal structure analysis of the sample. Using diffraction analysis one can find out size-dependent changes in the lattice parameters, defects etc. in the sample. Moreover, it is also possible to analyze single particles of very small (nanometer) dimension.

High-resolution TEM (HRTEM) is capable of providing atomic resolution lattice images. In case of HRTEM, the images are found because of the phase difference in scattered electron waves through a thin specimen. The emergence of HRTEM has allowed the direct reconstruction of Bragg differential electron beams to create interference patterns [13].

In the present study, the morphology and particle distribution of the synthesized bare and the composites of ZnO and ZnS nanoparticles were examined by transmission electron microscope (TEM) using JEOL JEM 200 CX high-resolution transmission electron microscope.

2.3.3. Scanning Electron Microscopy (SEM):

The SEM is also a most frequently used microscopic characterization technique that applied a beam of electrons to obtain a high enlargement of three-dimension images for morphological and topographical studies of materials and surfaces on a micrometer and sub-micrometer scale. It can also provide information about the elemental composition of a sample by the other additional part of this technique known as electron dispersive X-ray spectroscopy (EDX). A schematic diagram of SEM is shown in Figure 2.5.

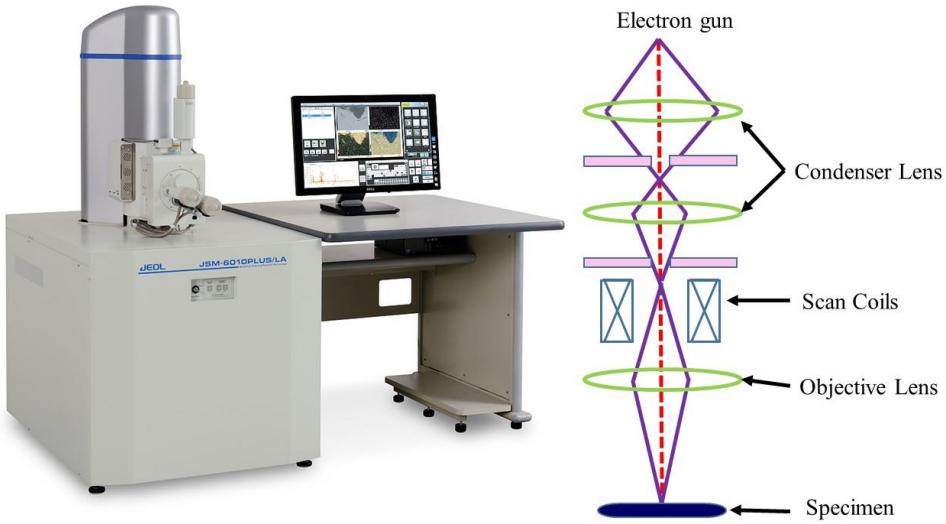

Figure 2.5: Image of SEM instrument and schematic representation of the electron beam.

In the experimental process the electron beam of high intensity generated from an electron gun [14, 15], pass through electromagnetic lenses and hits a point on the sample, the molecules in the material are excited to high energy levels, because of the number of effective collisions between the generated electron beam and atoms in the molecules of material will occur, which causes to production of secondary electron. Mainly secondary electrons are created by the inelastic interactions between incident electrons and weakly bound conduction-band electrons in the atoms of the sample. Secondary electrons possess very small kinetic energy (5 eV). Hence, the average

distance that a secondary electron travels in the solid is less than 2 nm. Apart from secondary electrons, backscattered electrons, characteristic X-rays and various energy of photons are also produced [16] (Figure 2.6).

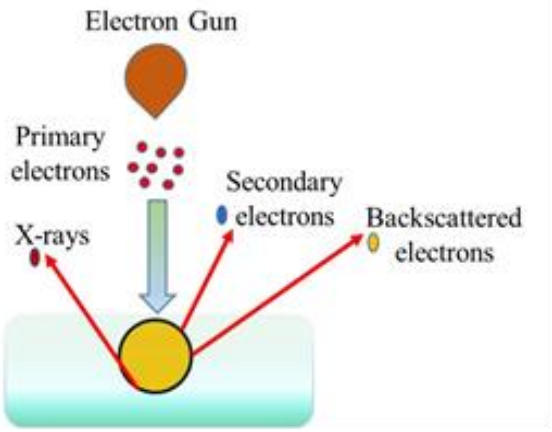

Figure 2.6: Schematic of the interaction between incident electrons and specimen.

Backscattered electrons are generated by elastic interaction (deflecting angle > 90) between incident electrons and the nucleus of the atoms in the sample. High energy backscattered electrons can penetrate deeper than secondary electrons in the solid sample. The penetration depth is strongly dependent on the specimen's atomic number (Z), decreasing with increasing Z (Figure 2.7).

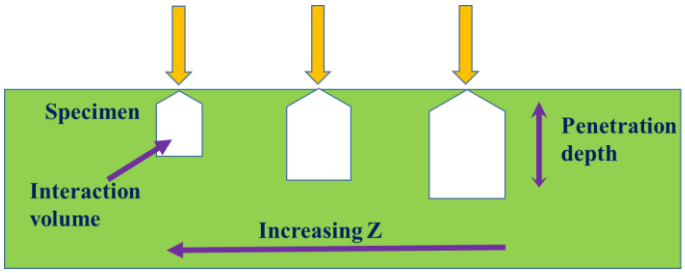

Figure 2.7: Schematic showing dependence of the interaction volume and penetration depth as a function of atomic number Z of the incident (primary) electrons.

These secondary as well as backscattered electron have comparatively low energy and can conveniently gather by the detector. The detector tallies the number of electrons released from the specimens and resulting pattern produces a three-

dimensional image of the morphology and topography of the sample on the screen of the detector. Compositional analysis of a material may also be achieved by observing X-rays produced by the interaction of electron and specimen interaction. Scanning takes place at a lower pressure so that the electrons are not scattered by gas molecules inside the chamber.

In this recent morphological examination of prepared bare as well as composites of ZnO and ZnS nanomaterials, scanning electron microscope (SEM) images was obtained by using JEOL JSM 6610 at 20 kV.

2.4. Spectral characterization:

2.4.1. UV-Visible spectroscopy:

Ultraviolet-Visible spectrophotometry (UV-vis) is commonly known as absorption or reflectance spectroscopy and shows its absorbance in the ultraviolet-visible spectral region. Among all spectroscopic techniques, it is the most simple and frequently used to govern the electronic structure of the free-form and colloidal form of nanostructured materials. This technique is correlative to the fluorescence spectroscopy, in that fluorescence measures spectroscopic transitions from the excited state to the ground state, at the same time absorption deal with transitions from the ground state to the excited state. When electromagnetic radiation passage over the free or colloidal form of material, a fraction of radiation absorbed, by virtue of energy absorption, atoms or molecules excited from ground state to the first excited state giving absorption spectrum. The fraction of radiation that is absorbed has energy equal to the path difference between the ground state and the first excited state called it as band gap energy. If the energy of the incident light ($h\upsilon$) is greater than the band gap (Eg) of the semiconductor ($h\upsilon > Eg$), then valence band electrons are excited into the conduction band and the percentage of incident light absorbed by a particular semiconductor depends on the transition probability of electrons between the valence

and conduction bands. The probability strongly depends on semiconductor band structures.

The optical properties or optical absorption of a nanostructure semiconductor material can also be demonstrated by the UV-Vis spectroscopy by the intercommunication between electromagnetic radiation and a semiconducting material.

The optical absorption phenomena are responsible for the electronic transitions in semiconductors material through the interband and intraband transitions, and also transitions via impurities or lattice defects. The first type optical phenomena involves the absorption of photons, which have energies equal to or greater than the band gap energy of a semiconductor. This type of optical absorption is called the process of fundamental edge or interband absorption. The fundamental absorption edge energy is determined by the semiconductor band gap. The fundamental or interband absorption phenomena is typically followed by an electronic transition through the forbidden gap, and correspondingly excess electron-hole pairs are generated in the semiconducting nanostructure. The absorption coefficient is commonly very large because of the interband transition [17, 18].

However, the absorption coefficient changes into very small when the energies of the electromagnetic radiation drop lower the band gap energy of the semiconductor. In this circumstance, another type of optical absorption process takes place which is the result of electronic transitions within the allowed energy state in the semiconductor material and is known as free-carrier absorption process. Absorption of photons with energies underneath the band gap energy of the semiconductor may also lead to electronic transitions from localized impurity states to the conduction or valence band states [19]. The instrumental image of UV-visible spectroscopy is shown in Figure 2.8.

Figure 2.8: Image of UV-Visible instrument

The relation between absorbance and concentration of the sample is explained by Beer-Lambert law [20] and it is given in equation 2.7 & 2.8,

$$T = I / I_0 \tag{2.7}$$

$$A = \log\left(\frac{1}{T}\right) = \log\left(\frac{I_0}{I}\right) = abC \tag{2.8}$$

Where, T is transmittance, I_0, is the intensity of incident light, I is the intensity of transmitted light, A is the absorbance, α is the absorptivity coefficient, b is the path length and C is the concentration of the sample.

Figure 2.9 illustrations the schematic representation of UV-vis spectrophotometer. It contains source (hydrogen/deuterium and tungsten/halogen discharge lamp), wavelength selector (diffraction grating), sample, solvent and detector.

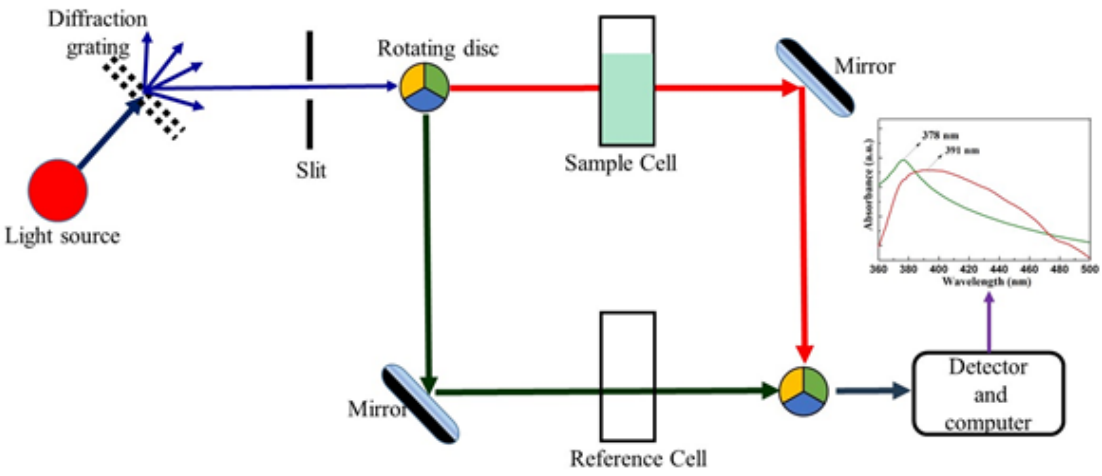

Figure 2.9: Schematic diagram of UV-Vis absorption spectrophotometer.

A beam of monochromatic light is divided into two beams, one of the fragmented light is passed through the specimen, and the other passes through a reference cell (in Figure 2.9, a solvent in which the sample is dissolved). After transportation from the specimen and reference cell, the two beams are collected to the detectors where they are analyzed.

In the present work, optical absorption and transmission spectra were recorded using a Carry-100 UV-Vis spectrophotometer in the 200-800 nm wavelength range.

2.4.2. Fourier Transform Infra-Red Spectroscopy (FT-IR):

Optical spectroscopy has been one of the most broadly applied for the characterization of nanostructures. The instrumental image of FT-IR is visualized in Figure 2.10. Infrared (IR) spectroscopy is a most widespread characterization technique to investigate the IR frequencies absorbed by a sample when it is when it is kept in the path of an IR radiation source [21]. The infrared spectrum performs only when the vibrations amongst bonded atoms produces a permanent change in the electric dipole moment of the molecule/material. It is reasonable to suppose that the more polar a bond, the more intense will be IR spectrum arise from the vibrations of the bond. The information concerning structure, symmetry, bond strength, inter and intra molecular interactions etc., are obtained from IR spectra. Therefore, IR spectroscopy is operating to recognize the type of bonds between atoms of a molecule and consequently identifies functional groups such as -OH group, -COOH group, -NH_2 group and -CH_2 group. The intensity and spectral position of IR absorptions allow the identification of the structure of a molecule. Solid, liquid and gaseous all samples can be characterized by this technique.

Figure 2.10: Image of FTIR instrument

The entire infrared spectrum of the polyatomic molecule can be divided into functional group region and the fingerprint region. The functional group region is generally considered from 4000 cm^{-1} to 1500 cm^{-1}. The finger print region exists within the wavenumber range 1500 cm^{-1} to 400 cm^{-1} [22]. The fingerprint region involves usually bending vibrations that are characteristic of the entire molecule or large fragments of the molecule and are used for identification. The functional group region includes generally stretching vibrations, which are more localized and characteristic of the typical functional groups found in organic molecules [22]. These bands are not very useful to confirm identity. They provide some very useful information about components of the sample.

An IR spectrometer technique mostly encloses a source, a monochromator and a detector. The general IR source provides a constant and high radiation energy output into the IR region. The most frequently used sources in the production of IR radiation are the Nernst Glower and the Globar [23]. The deuterated triglycine sulfate (DTGS), L-alanine doped deuterated triglycine sulfate (DLaTGS), mercury cadmium telluride (MCT) etc., are generally used detectors in IR spectroscopy. DTGS detectors have significantly lesser sensitivity as comparison to the MCT detectors, which have to be cooled typically using liquid nitrogen. The basic description of the sources, monochromators, filters and detectors are given in the book of Colthup et al. [23] and the references therein.

A schematic diagram of FT-IR spectrometer is shown in Figure 2.11. In FTIR, the dispersive device, prism or grating monochromator, is replaced by Michelson interferometer. The beam splitter splits the radiation into two beams that are reflected back from mirrors to beam splitter. The recombined beams at beam splitter produce interference. If beam passes through the sample, absorptions cause gaps in a frequency distribution. One mirror of the interferometer is moved toward and away from the splitter at a constant speed. The detector sees a time domain signal (called interferogram) which is converted into frequency domain spectrum by Fourier transform using software and computer. It is faster and sensitive system than the older dispersive instruments. FT-IR measurement has high resolution, high signal to noise ratio and better accuracy.

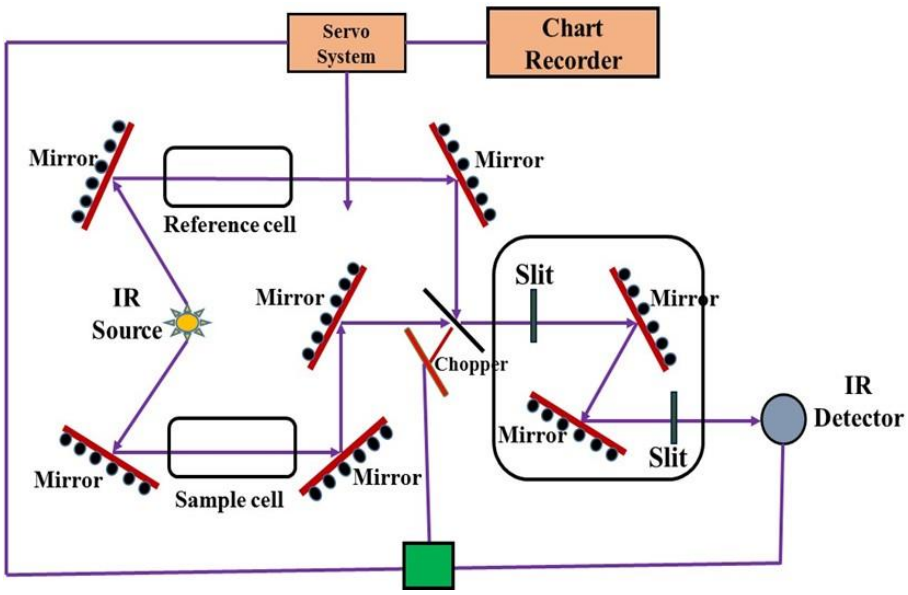

Figure 2.11: Systematic representation of FTIR.

2.4.3 Photoluminescence spectroscopy (PL):

PL spectroscopy is a contactless and non-destructive characterization technique for the determination of the electronic structure of nanostructured materials. It has been generally used to an examination of the optical properties of nanostructures [24, 25]. Apart from this, PL spectroscopy can also be applied for the

direct determination of band gap, defect detection, doping of impurity level, surface traps, and recombination mechanism of photogenerated electrons and holes (excitons). The luminescent nature and capability of nanostructure materials can also be measured by PL band. The instrumental diagram of PL is shown in Figure 2.12.

In the PL spectroscopy, the energy of photons are absorbed by the observing sample through the irradiation of electromagnetic light, electrons are excited from ground occupied state to the exited unoccupied states. On the emission process, the electronic transition occurs from excited state to the ground state, they emit radiation in the form of energy which is called as luminescence. On the behalf of the emission process and relaxation time, photoluminescence spectroscopy can be sub divided into two main categories such as fluorescence and phosphorescence spectroscopy.

Figure 2.12: Image of PL instrument.

Fluorescence spectroscopy occurs when an excited electron from the singlet vibrational energy level of an excited electronic state backs into the lower energy of singlet ground electronic state by emitting a photon. Since it is the fastest mechanism for the excited molecules return to their ground state, fluorescence is only observed if it is a more favorable for relaxation than the combination of internal conversion and vibrational relaxation. But in phosphorescence spectroscopic process a molecule normally emitted from the excited triplet electronic state of the lowest vibrational

level to the ground state of singlet electronic state by intersystem crossing or external conversion process.

Except the above process, there are also another possible methods for the recombination process of the excited electron. It may include i) band to band transition, ii) defect level (involving donors) to valence band transition, iii) conduction band to defect level (involving acceptors) transition, and iv) non-radiative recombination via an intermediate state. These phenomena is represented in Figure 2.13.

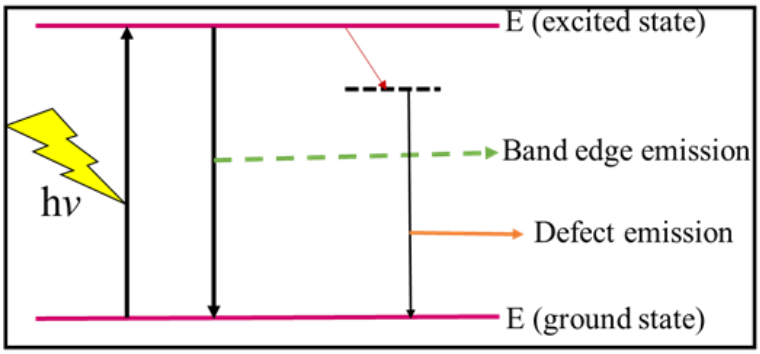

Figure 2.13: Schematic presentation of photoluminescence emission process.

The schematic presentation of PL spectrometer arrangement is displayed in Figure 2.14. It contains xenon lamp as an electromagnetic light source, excitation monochromator to excite the material, emission monochromator to select the emitted emission energy from the sample, and photomultiplier tube as a detector.

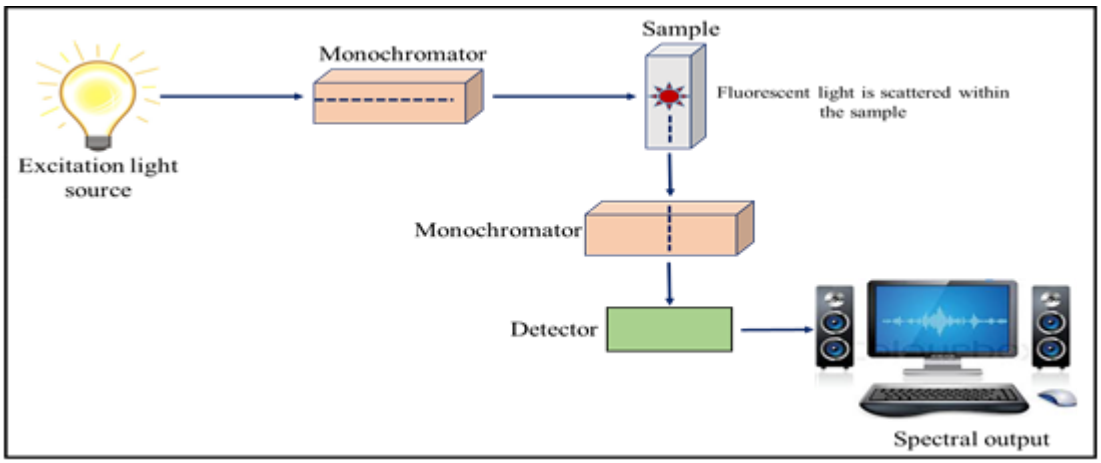

Figure 2.14: Schematic diagram of photoluminescence spectrophotometer.

Photoluminescence Excitation (PLE) Spectroscopy:

PLE provide the evidence about excited higher energy levels of the semiconducting nanostructure. In the spectrum, a narrow emission band is observed during the scanning of excitation energy due to the relaxation of an excited electron into their first excited state before emission, the spectrum that is obtained reveals absorption information about the narrow subset of nanostructured materials that emit. It provides the information about the presence of various electronic energy levels in NCs. Thus it is analogous to absorption spectroscopy. This technique is applied to consideration of [26] the higher excited states in the absorption spectrum as the inhomogeneous broadening due to distribution in size and shape is greatly reduced. The experimental setup for PLE is same as PL spectrometer as shown in Figure 2.14.

Low Temperature (LT) Photoluminescence (PL) Spectroscopy:

Low Temperature PL spectroscopy is a more precise technique to an examination of the structural and electronic behavior of nanostructures associated with room temperature PL spectroscopy. At LT, thermal vibration at the atomic level is fewer as a comparison to the room temperature due to this reason, emission of the nanostructure can be resolved easily. Presence of optical phonon modes, [27] structural irregularity, [28] and impurity levels [29] in nanostructure can be studied using low temperature PL spectroscopy. The intensity and peak position of emission energy of NCs increases with decreasing temperature due to minimization of energy loss. The experimental setup is shown in Figure 2.15.

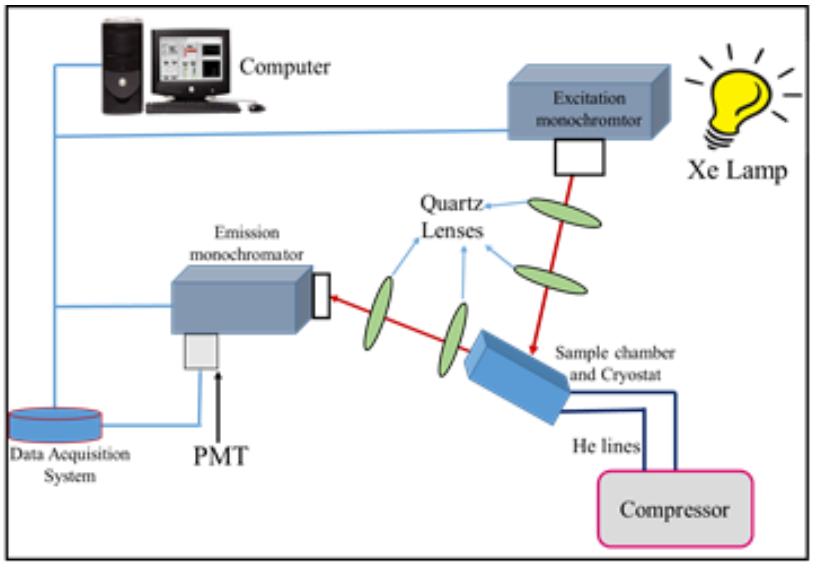

Figure 2.15: Experimental setup of high-resolution low-temperature photoluminescence.

Light from the Xenon arc lamp is incident on the entrance slit of excitation monochromator. Monochromatic light from the excitation monochromator is focused on the sample kept in the cryostat using quartz lenses. Light emitted from the sample is collected by quartz lenses and focused onto the entrance slit of emission monochromator. The photomultiplier tube (PMT) placed at the exit slit of the emission monochromator detects the light and the signal from the PMT is input to the data acquisition system. In all the experiments the overall resolution of the photoluminescence set-up was kept at ~0.5 nm. The sample was placed between two quartz plates mounted on a closed cycle helium cryostat (Janis CCS-150). The photoluminescence and photoluminescence excitation measurements were carried out at various temperatures from 10 to 300 K [30].

Time Resolved Photoluminescence (TRPL) Spectroscopy:

TRPL provides the information of dynamics of nanocrystals. The increase in electron energy level spacing with decrease in particle size produces a remarkable effect on the radiative and nonradiative rates due to which decay lifetime of nanocrystals can be changed. An understanding of the exciton decay dynamics and

relaxation pathways in nanocrystals is the key issue from fundamental [26] as well as from application [19] point-of-view. With the help of TRPL measurements, various radiative and nonradiative recombination centers can be revealed. The decay lifetime of various nanocrystals are single exponential or multi-exponential depending on the uniformity of the nanocrystals in an ensemble. The charge transfer mechanism between two nanomaterials can also be studied by TRPL. For example, metal-semiconductor hybrid nanostructures give different life-time than that of an individual component.

2.5. Brunauer-Emmett-Teller (BET):

Brunauer-Emmett-Teller (BET) [31] theory is useful to recognize the physical adsorption of gas molecules on the surface of nanoparticles materials and assist as the fundamental technique for the analysis of the specific surface area of nanoparticle expressed in meter square per gram (m^2/g^{-1}) pore volume. The BET method employed to multilayer adsorption of materials and commonly uses those gases which do not react to the surface of nanoparticle materials as adsorbates for the measurement of specific surface area. Nitrogen gas is generally used as adsorbate for surface inquiry by BET methods. The BET instrument (BELSORP-mini II) is shown in Figure 2.16.

Figure 2.16: Image of BET instrument.

The tenet of BET surface area examination is an augmentation of the Langmuir theory that is adsorption theory of monolayer to the multilayer adsorption with some hypothesis such as gas molecules adsorbed on a material in the infinite layers and the adsorbed gas molecules can interact with adjacent layer only. Then the BET equation is

$$\frac{1}{v\left[\left(p_0 \diagup p\right)-1\right]} = \frac{c-1}{v_m c}\left(\frac{p}{p_0}\right)+\frac{1}{v_m c} \tag{2.9}$$

Where p, equilibrium pressure p_0 saturation pressure of nitrogen gas as adsorbates at a temperature of adsorption, v is the total quantity of gas absorbed and v_m is the quantity of gas absorbed on monolayer and c is BET constant. Where the value of c is

$$c = \exp\left(\frac{E_1 - E_2}{RT}\right) \tag{2.10}$$

Where E_1 represents the absorption of heat on the first layer and E_2 is for the second and higher layers. Equation 2.9 is an equation of adsorption isotherm and plot a graph with the help of this equation against $1/v[(p/p_0)-1]$ vs p/p_0. This plot is known as BET plot. For obtained linear graph the value of p/p_0 is between $0.05<p/p_0<0.35$. From obtained the value of slope (S) and intercept (I) to measure the gas quantity (v_m) of the adsorbed monolayer gas and BET constant c used following equation:

$$v_m = \frac{1}{S+I} \tag{2.11}$$

$$c = 1+\frac{S}{I} \tag{2.12}$$

The total area (S_{total}) and specific surface area (S_{BET}) is measured with the help of the following equation:

$$S_{total} = \frac{\left(v_m N s\right)}{V} \tag{2.13}$$

$$S_{BET} = \frac{S_{total}}{a} \tag{2.14}$$

Where v_m is the volume unite, N is Avogadro number, s is the cross-section area of adsorbed gas and V is the volar volume of the adsorbate gas and is amount nanomaterials.

Barrett-Joyner-Halenda (BJH) measurement can also be applied to calculate the pore size and specific pore volume by adopting adoption and desorption method.

2.6 References:

[1] J. Als-Nielsen, D. McMorrow, Elements of modern X-ray physics, John Wiley & Sons, 2011.

[2] D.K. Bowen, B.K. Tanner, High-resolution X-ray diffractometry and topography, CRC press, 2005.

[3] C. Kittel, Introduction to Solid State Physics 7th edn, p 83 (elastic constants), p 135 (Umklapp processes), in, London: Wiley, 1996.

[4] G. Pandey, S. Dixit, Growth mechanism and optical properties determination of CdS nanostructures, The Journal of Physical Chemistry C, 115 (2011) 17633-17642.

[5] A. Othman, M.A. Ali, E. Ibrahim, M. Osman, Influence of Cu doping on structural, morphological, photoluminescence, and electrical properties of ZnO nanostructures synthesized by ice-bath assisted sonochemical method, Journal of Alloys and Compounds, 683 (2016) 399-411.

[6] G. Hitkari, S. Singh, G. Pandey, Structural, optical and photocatalytic study of ZnO and ZnO-ZnS synthesized by chemical method, Nano-Structures & Nano-Objects, 12 (2017) 1-9.

[7] R.D. Shannon, Revised effective ionic radii and systematic studies of interatomic distances in halides and chalcogenides, Acta crystallographica section A: crystal physics, diffraction, theoretical and general crystallography, 32 (1976) 751-767.

[8] S. Kumar, P. Sharma, V. Sharma, CdS nanofilms: synthesis and the role of annealing on structural and optical properties, journal of Applied Physics, 111 (2012) 43519-43525.

[9] V.I. Klimov, Semiconductor and metal nanocrystals: synthesis and electronic and optical properties, CRC Press, 2003.

[10] B. Fultz, J.M. Howe, Transmission electron microscopy and diffractometry of materials, Springer Science & Business Media, 2012.

[11] H. Kohl, L. Reimer, Transmission Electron Microscopy, Springer, 2008.

[12] L.A. Bendersky, F.W. Gayle, Electron diffraction using transmission electron microscopy, Journal of research of the National Institute of Standards and Technology, 106 (2001) 997.

[13] F. Humphreys, P. Goodhew, R. Beanland, Electron microscopy and analysis, in, Taylor & Francis, New York, 2001.

[14] L. Reimer, Scanning electron microscopy: physics of image formation and microanalysis, in, IOP Publishing, 2000.

[15] R.E. Lee, Scanning electron microscopy and X-ray microanalysis, PTR Prentice Hall, 1993.

[16] K. Vernon-Parry, Scanning electron microscopy: an introduction, III-Vs Review, 13 (2000) 40-44.

[17] K. Takahashi, A. Yoshikawa, A. Sandhu, Wide bandgap semiconductors: fundamental properties and modern photonic and electronic devices, Springer, (2007) 56.

[18] M. Bass, C. DeCusatis, J. Enoch, V. Lakshminarayanan, G. Li, C. Macdonald, V. Mahajan, E. Van Stryland, Handbook of optics, Volume II: Design, fabrication and testing, sources and detectors, radiometry and photometry, McGraw-Hill, Inc., 2009.

[19] H. Kalt, M. Hetterich, Optics of Semiconductors and Their Nanostructures, Springer Science & Business Media, 2013.

[20] J. Workman Jr, A. Springsteen, Applied spectroscopy: a compact reference for practitioners, Academic Press, 1998.

[21] D.N. Kendall, Applied infrared spectroscopy, (1966).

[22] H. Hausdorff, Analysis of polymers by infrared spectroscopy, in: analytical chemistry, amer chemical soc 1155 16th st, nw, washington, dc 23 (1951) 683-683.

[23] N. Colthup, LH-Daly and SE Wiberley, Introduction to Infrared and Raman spectroscopy, (1964).

[24] U. Woggon, Optical properties of semiconductor quantum dots, Springer, 1997.

[25] S.V. Gaponenko, Optical properties of semiconductor nanocrystals, Cambridge university press, 1998.

[26] V.I. Klimov, Mechanisms for photogeneration and recombination of multiexcitons in semiconductor nanocrystals: implications for lasing and solar energy conversion, in, ACS Publications, 110 (2006) 16827-16845.

[27] T. Jeong, P. Yu, T. Kim, Temperature dependence of the free excitons in a CdS single crystal, Journal of the Korean physical society, 36 (2000) 102-105.

[28] X. Zhang, X. Dong, H. Huang, Y. Liu, W. Wang, X. Zhu, B. Lv, J. Lei, C. Lee, Microwave absorption properties of the carbon-coated nickel nanocapsules, Applied Physics Letters, 89 (2006) 53115-53118.

[29] S.D. Kshirsagar, V. Nikesh, S. Mahamuni, Exciton structure in sodium doped zinc oxide quantum dots, Applied physics letters, 89 (2006) 53120-53123.

[30] S. Mahamuni, A.D. Lad, S. Patole, Photoluminescence properties of manganese-doped zinc selenide quantum dots, The Journal of Physical Chemistry C, 112 (2008) 2271-2277.

[31] S. Brunauer, P.H. Emmett, E. Teller, Adsorption of gases in multimolecular layers, Journal of the American chemical society, 60 (1938) 309-319.

***

Chapter 3
Structural, optical and photocatalytic study of ZnO and ZnO-ZnS synthesized by chemical method

Chapter 3
Structural, optical and photocatalytic study of ZnO and ZnO-ZnS synthesized by chemical method

Zinc oxide (ZnO) and ZnO-ZnS nanocomposite materials have been prepared by simple chemical co-precipitation method. The X-ray diffraction analysis revealed the formation of ZnO and ZnO-ZnS crystalline materials. FESEM and HRTEM analyses indicated the formation of flake-like ZnO and sheet-like ZnO-ZnS structures. Energy dispersive X-ray (EDS) study further established the formation of ZnO and ZnO-ZnS materials. In the FTIR spectrum the presence of Zn-O symmetric stretching vibration at 442 cm^{-1} and 809 cm^{-1}, due to weak vibration of ZnO, while the other peak at 687 cm^{-1} due to Zn-S symmetric bending vibration proved the formation of ZnO-ZnS composite material. Optical absorption spectrum showed that the band gap energy decreased for ZnO-ZnS composite compared to the pure ZnO NPs. The photoluminescence spectral analysis shows that the broad emissions spectrum caused due to several different bands, owing to the presence of zinc vacancies, oxygen vacancies, and surface defects. The photocatalytic performance of these samples was tested for degradation of a dye methylene blue under UV light exposure. ZnS-ZnO composite shows the higher dye degradation efficiency (93 %) than that of pure ZnO (55 %).

3.1. Introduction:

Semiconducting nanoparticles (NPs) have been achieving more and more attention in last decades because of their enhanced physical and optical properties, which are dissimilar to their bulk counterpart, due to their large surface to volume ratio. They have an extensive range of applications like light-emitting diodes, photo-conductive devices, solar cells, biomedical labeling, photo-catalysis, lasers, optical waveguides and sensors [1, 2]. Due to the large surface to volume ratio, these NPs contain a large number of vacancies. Size and surface effects both are significant at the nanoscale to control the vacancies. The presence of vacancies commonly serve as the elimination of photo-generated electrons, affecting luminescence properties, thus it is essential to manipulate the surface of nanoparticles to achieve improved optical properties [3].

ZnO is an important direct band gap semiconducting material which belongs to II-VI group compound with hexagonal wurtzite structure. At room temperature, the band gap energy of ZnO is 3.37 eV and a large exciton binding energy (60 meV) [4]. It has wide range of applications such as piezoelectricity, optical transparency and chemical stability in visible region [5], optoelectronic devices [6], gas sensors [7, 9], transparent electrodes [10], solar cells, acoustic wave devices, ferroelectric memories [11] and so on. Its various morphological dependent properties have been reported in a number of studies which includes nanorods, nanosheets, nanotrees [12, 13]. The significant applications of ZnO exhibit as ultraviolet absorber and window material for displays and solar cells [14].

Many research works have been focused on ZnO modified with metallic elements to improve its properties. Chemically stabilized solution phase synthesis of ZnO may moderately passivate the charged surface sites, however, virtually it is

difficult to passivate both anionic as well as cationic surface sites by capping with organic surfactants concurrently. The presence of unpassivated surface sites may work as nonradiative recombination of excitons and consequently destroy effectively luminescence properties. Therefore, the modification of the nanocrystal surface is a serious issue to achieve high luminescence and photostability in ZnO nanocrystals.

Literature review revealed that the modification of the band gap, electrical, optical and magnetic properties of ZnO NPs have been achieved by changing unpassivated surface sites by the addition of some foreign impurities [15-17] as well as by addition of other semiconducting materials such as ZnO-SnO_2, ZnO-Yb_2O_3 [18, 19] Fe_3O_4/ZnO [20], FePt/CdS, FePt/CdSe, Fe_3O_4/ZnS [21], Co/CdSe [22], Fe_3O_4/CdS, Fe/ZnO [23], and Ni/ZnS [24]. T. Hong et al. also reported that the synthesis of ZnO/$ZnSeO_3$/$CuSeO_3$ by hydrothermal synthesis based on an ion-change method for photoelectrochemical water splitting [25]. A number of chemical methods such as hydrothermal [26], solvothermal [27], co-precipitation [28] and sol-gel methods [29], have also been applied for the synthesis of ZnO NPs and its composite materials. However, among these methods, co-precipitation process has been commonly accepted to synthesize ZnO NPs because of its low cost, high yield and due to the formation of constant size NPs.

Zinc sulfide (ZnS) is a non-toxic II-IV metal sulfide semiconductor and it is found commonly in two structural phases, the zinc blende (sphalerite) structure with a cubic phase and the wurtzite structure with a hexagonal phase. The band gap energy of the two phases of ZnS (cubic and hexagonal phases) are 3.54 eV and 3.80 eV respectively. Zinc sulfide is also a prominent phosphor material with various luminescence properties including electroluminescence (EL) and photoluminescence (PL), thus it has commonly applied in the fields of sensors, laser and displays [30,

31]. A number of theoretical as well as experimental reports have been available in past on ZnO/ZnS composite [3] heterostructures [32] and heterojunction [33]. Saha et al. reported that in core-shell ZnO/ZnS, the band gap decreased as the shell thickness of ZnS increased keeping core thickness of ZnO constant [34]. Verma et al. reported the formation of core-shell nanocomposites in the solution-based synthesis of ZnO/ZnS, and reveal systematically discussed the passivation orange emission [3].

In the previous studies of ZnO-ZnS structures, virtually all efforts have been made on band gap modulation; however effect of ZnS addition on morphological variation of ZnO-ZnS, surface defect levels and thus photoluminescence behavior of ZnO-ZnS is still lacking. In the present study, we have synthesized ZnO-ZnS nanocomposite materials by applying a simple co-precipitation method. Photocatalytic behavior of ZnO nanocrystals and ZnO-ZnS nanocomposite for degradation of dye methylene blue under UV light exposure has also studied in this work.

3.2. Experimental Sections:

3.2.1. Reagents:

In the present work, analytical grade chemicals were used to synthesize ZnO and ZnO-ZnS materials. Zinc sulfate heptahydrate ($ZnSO_4.7H_2O$), urea (NH_2CONH_2), and thiourea (NH_2CSNH_2) were purchased from Merck India and sodium hydroxide powder (NaOH) was purchased from MP Biomedical LLC. These chemicals have been used as received without further purification. Double-distilled water and doubled de-ionized water were used as solvents. All the glassware's were cleaned with concentrated acid. The dried glassware's were used in all the experiments.

3.2.2. Synthesis of Zinc Oxide nanoparticles (ZnO NPs):

For preparation of ZnO, 50 ml aqueous solution of $ZnSO_4.7H_2O$ (0.3 M) was sonicated for 30 min in the ultrasonic cleaner. 50 ml of 0.3 M aqueous solution of

urea (NH_2CONH_2) was added drop wise into the above zinc sulfate solution and stirred vigorously on the digital magnetic stirrer. Then 0.5 M NaOH aqueous solution was gently added to the above precursor solution under vigorous stirring until pH reached to 11. The reaction mixture was refluxed for 1 h at 80 ˚C. The as-prepared precipitate was cooled down naturally at room temperature, filtrated and washed several times with deionized water to remove the impurity and finally with acetone until neutralization. The precipitate was dried at 80 ºC in the electric oven.

3.2.3. Synthesis of ZnO-ZnS nanocomposite:

In a typical synthesis, 50 ml aqueous solution of $ZnSO_4.7H_2O$ (0.3M) was sonicated for 30 min in the ultrasonic cleaner. 50 ml of 0.3 M aqueous solution of thiourea (NH_2CSNH_2) was added drop wise into the above zinc sulfate solution and stirred vigorously on the digital magnetic stirrer. Then aqueous solution of 0.5 M NaOH was gently added in to the above precursor solution under vigorous stirring until pH reached to 11. The reaction mixture was refluxed for at 80 ˚C. Then precipitate was cooled down naturally at room temperature, filtrated and washed several times with deionized water to remove the impurity and finally with acetone until neutralization. The precipitate was dried at 80 ºC in the electric oven.

3.3. Characterizations:

The crystal structure of the prepared materials was investigated by the X-ray diffraction (XRD) analysis on Rigaku High Resolution 12 kW X-ray diffractometer (λ = 1.5406 Å) in the 2θ range of 20-80˚ with scan rate of 10/min using Cu-Kα radiation (40 KV) using pure A_2O_3 as reference. Particles morphology and elemental analyses were done by Scanning electron microscopy (SEM) and energy dispersive X-ray (EDX) spectroscopy on JEOL, JSM-6490 LV Scanning Electron Microscope. The particles morphology and particle size distribution of the synthesized materials were

also observed by high resolution transmission electron microscope (HRTEM) on JEOL JEM 200 CX. The optical properties of the materials were studied by UV-Visible spectroscopy using carry 100 UV-Visible spectrophotometer, wherein observation was recorded in absorption mode in wavelength range 200-800 nm. The bond vibration of the materials was analyzed by the Fourier-transform infrared absorption spectra (FTIR spectra) using a Nicolet TM 6700 FTIR spectrophotometer in the range 400-4000 cm^{-1}. The samples were mixed with KBr powder before being pressed to form optically clear pellets. The photoluminescence (PL) spectra were observed at room temperature using LS-55 fluorescence spectroflurometer.

3.4. Photocatalytic performance of catalyst:

The photocatalytic activity of synthesized ZnO and ZnO-ZnS materials was measured using dye methylene blue (MB) as a representative water contaminant under UV light irradiation. In this process 20 mg amount of catalyst (ZnO and ZnO-ZnS separately) was added into 100 mL of an aqueous solution of MB at a constant initial concentrations of 80 ppm. Before the irradiation of light, the prepared mixture was sonicated in dark for 30 minute to attain adsorption equilibrium of MB with the photocatalyst. The photocatalytic observation was carried out at room temperature in a cylindrical glass vessel assembled with a magnetic stirrer under a UV-light situated horizontally at 30 cm above the suspension surface. The glass vessel was lightened by two 20 W UV lamp. The whole arrangement was place in a box, wrapped with aluminum foil to escape the other lights into the box. The aliquot amount of suspension was drawn from the reactor at consistent time intervals and the absorbance of sample was monitored on Carry 100 UV-visible spectrophotometer at the maximum absorbance wavelength of 664 nm after centrifugation.

According to the Beer-Lambert law, the change in the concentration of organic pollutant MB in aqueous solution is directly proportional to the change in intensity of the absorption peak, therefore the percentage degradation efficiency of MB is measured by applying the following expression [35]

$$\text{MB degradation efficiency (\%)} = 100 \times (C_0 - C_t)/C_0 \quad (3.1)$$

Where C_0 is the initial concentration and C_t is the concentration at any time t, respectively.

3.5. Results and discussion:

The crystal phase and purity of the as-synthesized ZnO and ZnO-ZnS materials were analyzed using X-ray diffraction analysis shown in Figure 3.1. All the peaks in the XRD pattern are very sharp and intense indicating that the samples are good crystalline in nature. The XRD pattern of ZnO (Figure 3.1 a) shows diffraction peaks at 2θ values 231.80˚, 34.51˚, 36.21˚, 47.52˚, 56.61˚, 62.90˚, 67.91˚, and 69.92˚, with corresponding Miller indices (hkl) of (100), (002), (101), (102), (110), (103), (112), and (201) respectively, indicating formation of hexagonal wurtzite phase of ZnO (JCPDS card no 800075, a = 3.253 and c = 5.209 with space group p63mc). Figure 3.1 b represents the XRD pattern of ZnO-ZnS nanocomposite, formed after addition of NH_2CSNH_2 into the aqueous solution of zinc sulfate. In the XRD pattern, apart from ZnO peaks, additional peaks appeared at 2θ values 29.1˚, 42.59˚, 45.78˚ and 66.4° which are respectively (103), (109), (1010) and (1112) planes of ZnS hexagonal phase (JCPDS card no 72-0163, a = 3.820, c = 24.96 with space group p63mc). Moreover, the peak position of ZnO shifted towards slightly higher 2θ value compared to pure ZnO. No other diffraction peaks were observed in the XRD patterned, indicating the formation of ZnO-ZnS composite material.

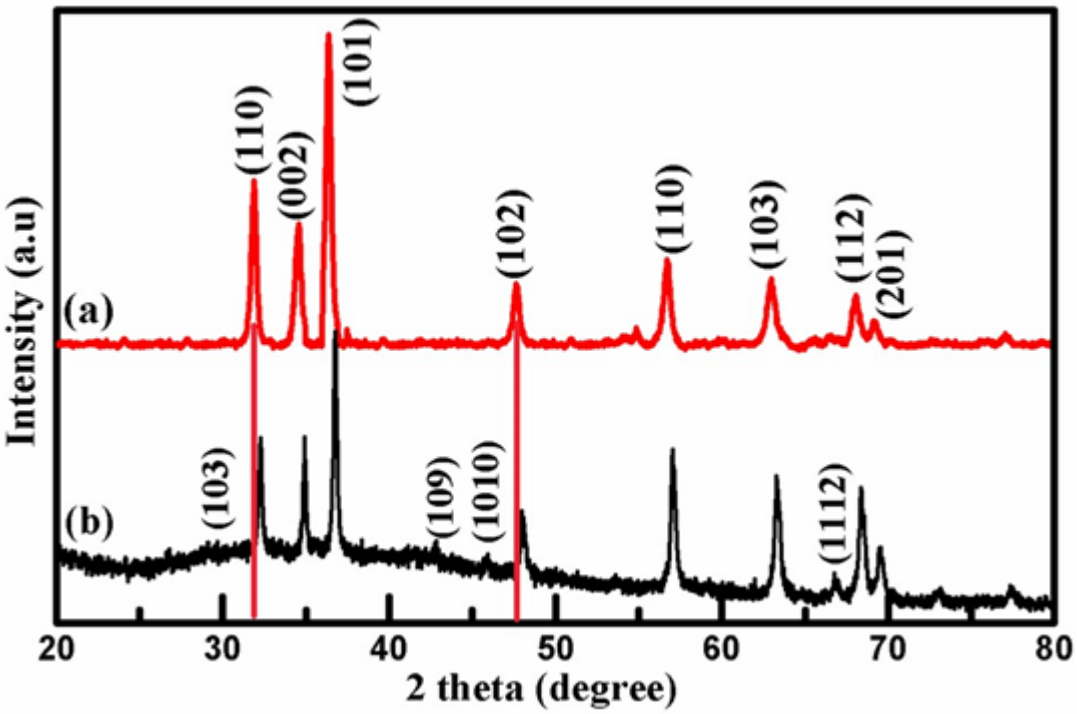

Figure 3.1: X-ray diffraction patterns of (a) ZnO nanoparticle, (b) ZnO-ZnS nanocomposite.

Wurtzite ZnO has hexagonal close-packed structure wherein Zn atom is tetrahedrally coordinated with four oxygen atoms and each oxygen binds four zinc in tetrahedral ZnO. Thus hexagonal wurtzite ZnO has two polar faces, one which only contains Zn^{2+} while the other face only contains O^{2-} ions. These two faces are stacked alternatively along c- axis. Applying Bragg's law,

$$n\lambda = 2dSin\theta \tag{3.2}$$

Where n is the order of diffraction (commonly n = 1), λ is wavelength of the X-ray and d is inter planar spacing. In the hexagonal ZnO, the interplanar spacing d is related to the lattice constants a, c and the miller indices h, k and l by,

$$\frac{1}{d^2_{(hkl)}} = \frac{4}{3}\left(\frac{h^2 + hk + k^2}{a^2}\right) + \frac{l^2}{c^2} \tag{3.3}$$

Taking first order approximation, n = 1;

$$Sin^2\theta = \frac{\lambda^2}{4a^2}\left(\frac{4}{3}\left(h^2 + k^2 + hk\right) + \left(\frac{a}{c}\right)^2 l^2\right) \tag{3.4}$$

The lattice parameter *a* for (100) plane is determined by the relation,

$$a = \frac{\lambda}{\sqrt{3Sin\theta}} \tag{3.5}$$

For (002) plane, the lattice constant *c* is determined by [36],

$$c = \frac{\lambda}{Sin\theta} \tag{3.6}$$

The lattice parameters for ZnO have been measured using above equations and found as $a = b = 3.2454$ Å and $c = 5.6212$ Å, hence $c/a = 1.7320$. These values and observed XRD peaks for the planes (100), (002), (101), (102), (110), (103) closely match with the JCPDS data for ZnO. The measured interplanar spacing ($d_{h\ k\ l}$) for the observed XRD data for a particular plane, percentage variation in *d* observed values with *d* JCPDS values, full width at half-maximum (FWHM) values and area values for XRD peaks for samples ZnO and ZnO-ZnS are systematically tabulated in Table 3.1 and 3.2 respectively.

Peak	d_{XRD}	d_{JCPDS}	% of contraction in d	FWHM	Area
<100>	2.8106373	2.8179	0.2577	0.3336	3205.84
<002>	2.5958709	2.6049	0.3466	0.3826	2730.72
<101>	2.4778013	2.4786	0.0322	0.3466	6478.14
<102>	1.9111137	1.9128	0.0881	0.4057	1391.9
<110>	1.6239071	1.6269	0.1839	0.4411	2111.59
<103>	1.4757904	1.4784	0.1765	0.547	2014.51
<112>	1.3785902	1.3799	0.0949	0.4834	1350.78
<201>	1.3437942	1.3601	1.1988	0.4753	600.99

Table 3.1: Interplanar spacing (d_{hkl}) from XRD, JCPDS, data card for corresponding (hkl) planes, percentage of variation of d, FWHM, and area of ZnO nanoparticles.

Peak	d_{XRD}	d_{JCPDS}	% of contraction in d	FWHM	Area
<100>	2.7875876	2.7886	0.0363	0.20892	2.40048
<002>	2.599011	2.6	0.0380	0.18901	2.04177
<101>	2.4535831	2.45475	0.0475	0.22166	5.24864
<102>	1.900907	1.9016	0.0364	0.29797	1.79572
<110>	1.6093748	1.61	0.0388	0.29594	4.17701
<103>	1.47155135	1.4721	0.0372	0.35131	4.16419
<112>	1.36826999	1.3688	0.0387	0.34789	3.68605
<201>	1.34619798	1.3467	0.0372	0.30451	1.42928

Table 3.2: Interplanar spacing (d_{hkl}) from XRD, JCPDS, data card for corresponding (hkl) planes, percentage of variation of d, FWHM, and area of ZnO-ZnS nanocomposites.

The average particles size of ZnO NPs and ZnO-ZnS nanocomposite was calculated by Scherrer's equation [37],

$$d = k\lambda/\beta_{hkl}Cos\theta \tag{3.7}$$

Where d is the average crystallite's size, λ is the X-ray wavelength of Cu-Kα line, β is the full width at half maximum (FWHM) of the respective peak, θ is the Bragg's angle and k is the Scherrer's constant (shape factor), which is equal to 0.91. Although Scherrer equation is only approximate in nature, however, it certainly provides a preliminary idea about crystallites size, which may be quite accurate, provided the particle's size is below 100 nm. Bragg's equation ideally applicable in the condition of sharp XRD peaks. However, the typical diffraction peaks have a finite width, which is a combination of both instrumental and sample dependent effects. To decouple above contributions, diffraction pattern from line broadening of a standard material (Al_2O_3) is collected to determine the instrumental broadening. The instrumental corrected β_{hkl} for particular diffraction peak of the materials (ZnO and ZnO-ZnS) was calculated using the equation,

$$\beta_{hkl} = [(\beta^2_{hkl})measured - (\beta^2_{hkl})instrumental]^{1/2} \quad (3.8)$$

In this equation, the strongest (101) XRD peak was used to determine average crystallite's size. The calculated average crystallite's sizes of ZnO NPs and ZnO/ZnS nanocomposite were 26 and 25 nm respectively.

FESEM analysis: Structural, morphological and compositional analyses ZnO and ZnO-ZnS materials were performed by FESEM and EDX studies, shown in Figure 3.2. In the FESEM images (Figure 3.2 a and b), flake-like ZnO nanostructures with thickness 20±8 nm have been observed, while in the FESEM images of ZnO-ZnS (Figure 3.2 c and d), sheet-like ZnO-ZnS structures with thickness 20±5 nm have been observed. In the corresponding EDX spectrum of ZnO (Figure 3.2 e), presence of Zn & O and in the EDX spectrum of ZnO-ZnS (Figure 3.2 f), presence of Zn, O and S elemental peaks confirm the formation of ZnO and ZnO-ZnS materials. The absence of any other elemental peak indicates the high purity of prepared sample.

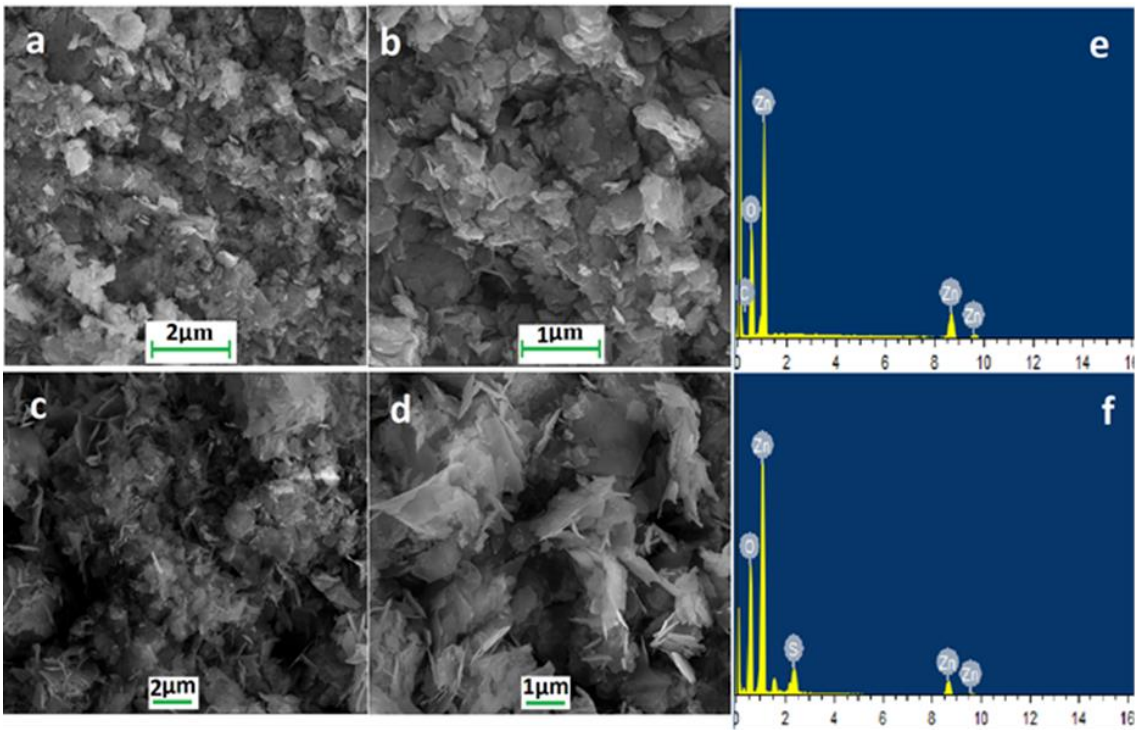

Figure 3.2: (a) and (b) FESEM images of ZnO, (c) and (d) SEM images of ZnO-ZnS, (e) EDX spectrum of ZnO and (f) EDX spectrum of ZnO-ZnS nanocomposite.

A comprehensive chemical composition analysis of the ZnO-ZnS nanocomposite was also carried out with X-ray elemental mapping (Figure 3.3) which shows percentage value of Zn, S and O as 59.58, 14.12 and 26.30 respectively. This data confirm the formation of ZnO-ZnS composite material.

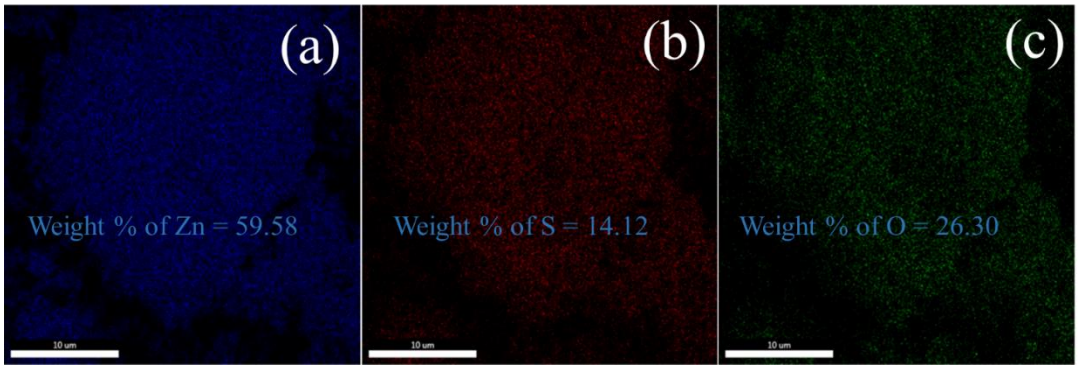

Figure 3.3: Elemental mapping of ZnO-ZnS nanocomposites.

HRTEM analysis: The morphological investigation of ZnO and ZnO-ZnS has further been examined by HRTEM analyses. In the HRTEM micrographs (Figure 3.4 a and d), flake-like structures are clearly observed. In the enlarged view of these images (Figure 3.4 b, c and e), spherical ZnO structures with a diameter in the range 9-16 nm have been observed. Thus from HRTEM images, it is obvious that the small spherical ZnO particle associated to form ZnO nanoflakes. Hydrolysis of urea in the alkaline medium releases NH_3 molecules in the reaction medium. The hexagonal wurtzite ZnO crystals have two polar faces. The first (0001) face contains only positively charged Zn^{2+} while the other $(000\bar{1})$ face contains only negatively charged O^{2-}. The two oppositely charged faces are stacked alternatively along c axes. Zn^{2+} containing (0001) polar face has the maximum surface energy whereas O^{2-} terminating $(000\bar{1})$ face have minimum energy. In the solution phase synthesis, hexagonal prism-like ZnO takes place, which is the intrinsic growth habit of ZnO, due to anisotropic growth along c axis [38]. The released NH_3 molecule in the reaction medium possibly

adsorbed on Zn^{2+} terminating positive (0001) facet, thus retarding growth in this direction. Now the incoming ZnO will have no option to add sideways towards $(2\bar{1}\bar{1}0)$ or evolve flake-like ZnO structures. The selected area electron diffraction (SAED) pattern (Figure 3.4 f) shows the polycrystalline nature and the ring pattern confirms the evolution of hexagonal ZnO nanostructures.

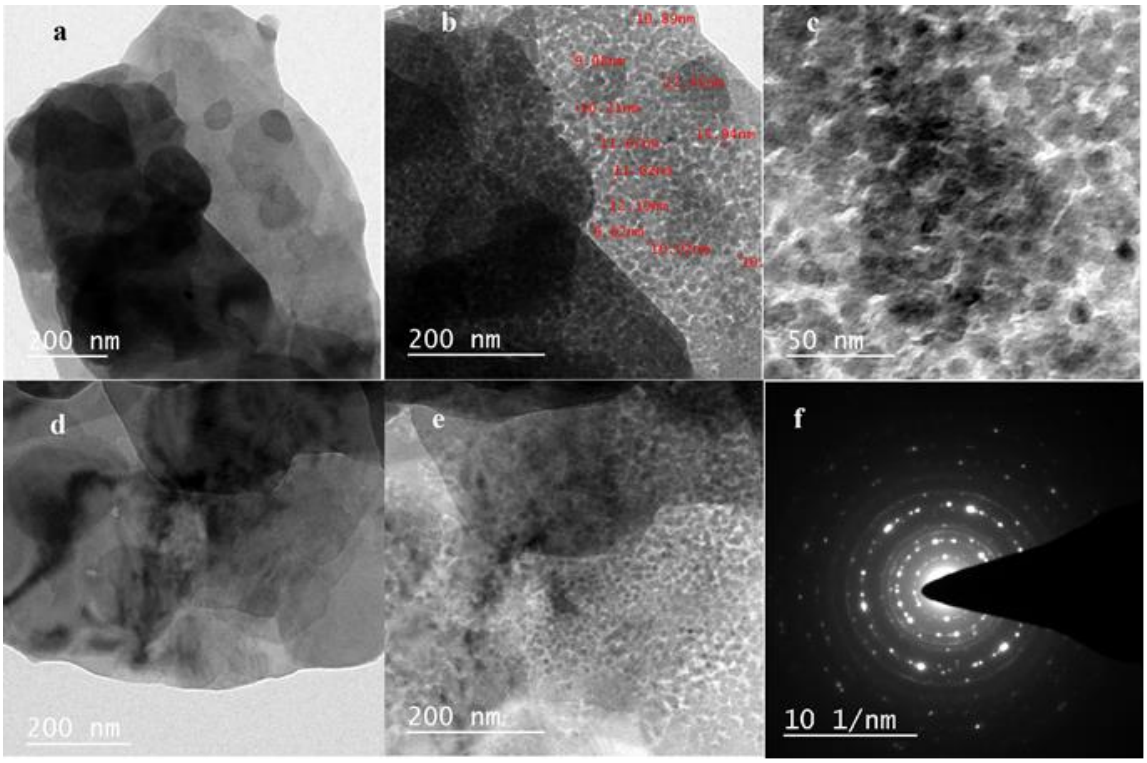

Figure 3.4: (a to e) HRTEM images and (f) SAED pattern of ZnO nanostructure.

The HRTEM images (Figure 3.5 a and d), and their enlarged view (Figure 3.5 b, c and e), indicate that sheet-like ZnO-ZnS structures are actually composed of small spherical crystallites with a diameter in the range of 9-13 nm. Further, in Figure 3.5 c, core-shell like ZnO-ZnS structures (ZnO core-ZnS shell), have been observed. Probably the formation of ZnS shell over ZnO core facilitates the formation of sheet-like ZnO-ZnS structures. The selected area electron diffraction pattern (Figures 3.5 f) indicates the polycrystalline nature while the ring pattern of the same confirms the formation of hexagonal ZnO-ZnS.

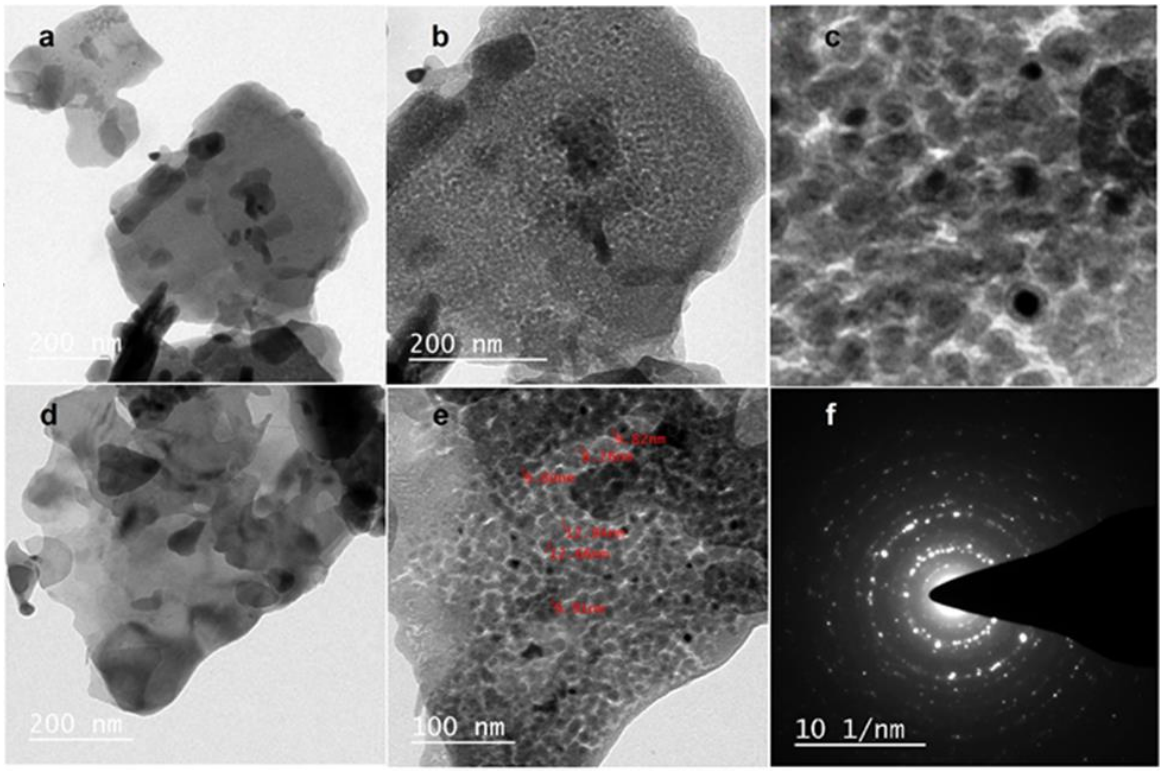

Figure 3.5: (a to e) HRTEM images and (f) SAED pattern of ZnO-ZnS nanocomposite.

FTIR analysis: To examine the nature of bonds in the prepared materials, FTIR spectra of the pure ZnO and ZnO-ZnS composite samples have been recorded in the range 400-4000 cm^{-1} (Figure 3.6). The major peaks in FTIR of ZnO have been observed at 442, 809, 1635 and 3422 cm^{-1}. The peaks at 3422 cm^{-1} and 1635 cm^{-1} are respectively due to O-H stretching and O-H bending vibrations of water molecule. The existence of these bands indicates the presence of water molecules on the surface of the nanostructures. Couple of bands at 1500 cm^{-1} may be due to adsorbed NH_3 molecules at the surface of nanostructures. The peak at 442 cm^{-1} is corresponds to Zn-O symmetric bending vibration and the peak at 809 cm^{-1} is due to weak vibration of Zn-O [10]. Thus FTIR data indicates the presence of Zn-O without any other impurity. In the FTIR spectrum of ZnO-ZnS, apart from above peaks, the additional peak at 687 cm^{-1} (Figure 3.6 b), attributed to Zn-S symmetric bending vibration. This band confirmed the formation of ZnO-ZnS composite [39].

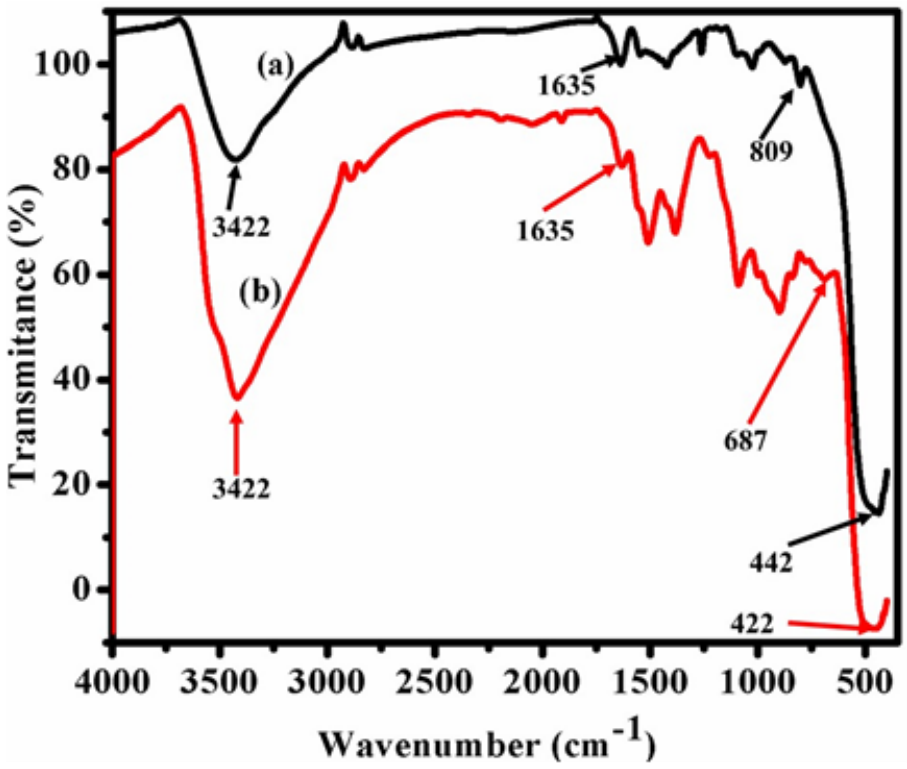

Figure 3.6: FTIR spectra of (a) ZnO and (b) ZnO-ZnS nanocomposite.

Optical Properties: UV-visible absorption spectroscopy is an effective technique to examine the optical properties of semiconducting NPs. Figure 3.7 shows the UV-visible spectra of the pure ZnO and ZnO-ZnS composite. In the UV-visible spectrum of pure ZnO, the absorbance band was observed around 378 nm. This characteristic absorption peak can be assigned to the intrinsic band-gap absorption of ZnO due to the electron transitions from the valence band to the conduction band ($O_{2p} \rightarrow Zn_{3d}$) [40] and it is in consonance of the previous work reported by Geeta Devi et al. [41]. In the spectrum of ZnO-ZnS, the above peak is red-shifted (at 391 nm) compared to pure ZnO. This red shift in the absorption peak for ZnO-ZnS composite arises due to near vicinity of the optical component ZnS in the nanocomposites. The direct band gap energy of the synthesized materials was calculated from the absorption peak of the UV-visible absorption spectrum. The direct band gap energy values of the pure ZnO NPs and ZnO-ZnS composite samples was calculated using Tauc equation and

found to be 3.29 eV (378 nm) and 3.17 eV (391 nm) respectively [42]. The red-shift in ZnO-ZnS, compared to ZnO is due to electronic interaction between ZnO and ZnS, which arises due to an increase of ZnS formation on ZnO [43]. The improved visible light absorption of the modified samples may be consequence of surface defect center formation mainly associated with the creation of oxygen vacancies due to the introduction of S^{2-} ions. It may also be ascribed to electronic interaction between ZnO and ZnS with an increase of ZnS concentration on ZnO [43].

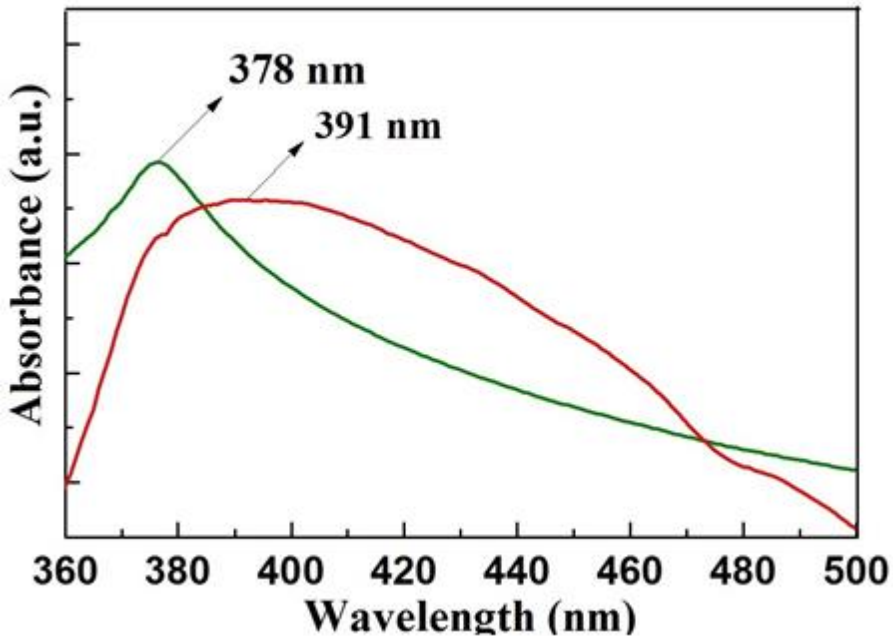

Figure 3.7: UV-visible absorption spectra of ZnO and ZnO-ZnS nanocomposite respectively

Photoluminescence Properties: The room temperature PL spectra of the ZnO NPs and the ZnO-ZnS nanocomposite are presented in Figure 3.8. The emission spectrum was recorded up-to 650 nm wavelength at excitation wavelength 325 nm. In the PL spectrum of ZnO, a strong UV near band edge emission at 389 nm and some other secondary peaks related to visible emissions are observed at 419, 446, 484, 529 and 590 nm wavelengths. The peak at 389 nm is due to the UV near band edge while the band at 419 nm peak is related violet emission. A large number of works have been

done on visible emission of ZnO, however their origin is in still controversial. A number of theoretical as well as experimental results shown that the visible emissions are related to several intrinsic defects like zinc vacancies (V_{Zn}), oxygen vacancies (Vo), interstitial zinc (Zn_i), interstitial oxygen (O_i) and antisite oxygen (O_{Zn}) corresponds to substitution of oxygen at zinc position [44-46]. The blue luminescence peak at 446 nm is corresponding to electronic transitions from interstitial levels of Zn (Zn_i) to valence band [47, 48]. The presence of broad blue emission band at around 484 nm is generally assigned to the radiative recombination of an electrons with oxygen vacancy [49]. The green emission at 529 nm is owing to the recombination of electrons stuck with twice-ionized oxygen vacancy ($V_o^{\cdot\cdot}$) with photo-generated holes [50, 51]. The yellow emission peaks present in the visible region at 590 nm is attributed to oxygen vacancies (V_o) or oxide antisite defects and surface defect [52]. In the PL spectrum of ZnO-ZnS nanocomposites, the intensity of UV near band edge and violet emissions has been decreased. Moreover, in ZnO-ZnS the intensity of broad blue emission and green emission peaks enhanced while orange emission disappeared compared to pure ZnO nanocrystals. The intensity of UV emission peak is related to recombination of electrons and holes, while the visible peaks are associated with presence of defect levels in the NPs. In the PL spectrum ZnO-ZnS the decrease in UV emission peak, compared to ZnO indicates decrease in rate of recombination of electron and holes while increase of visible emissions peak intensity shows the increase in intrinsic defect levels due to addition of ZnS to ZnO. In PL spectrum of ZnO-ZnS, intensity of visible emission peaks, particularly peaks at 484, and 529 nm are significantly increased, which indicate that addition of ZnS to ZnO created large amount of oxygen vacancies ($V_o^{\cdot}$ and $V_o^{\cdot\cdot}$ centers) in ZnO-ZnS

composite these defects may work as electron scavengers by trapping photogenerated electrons temporally, thus slowing down electron-hole recombination.

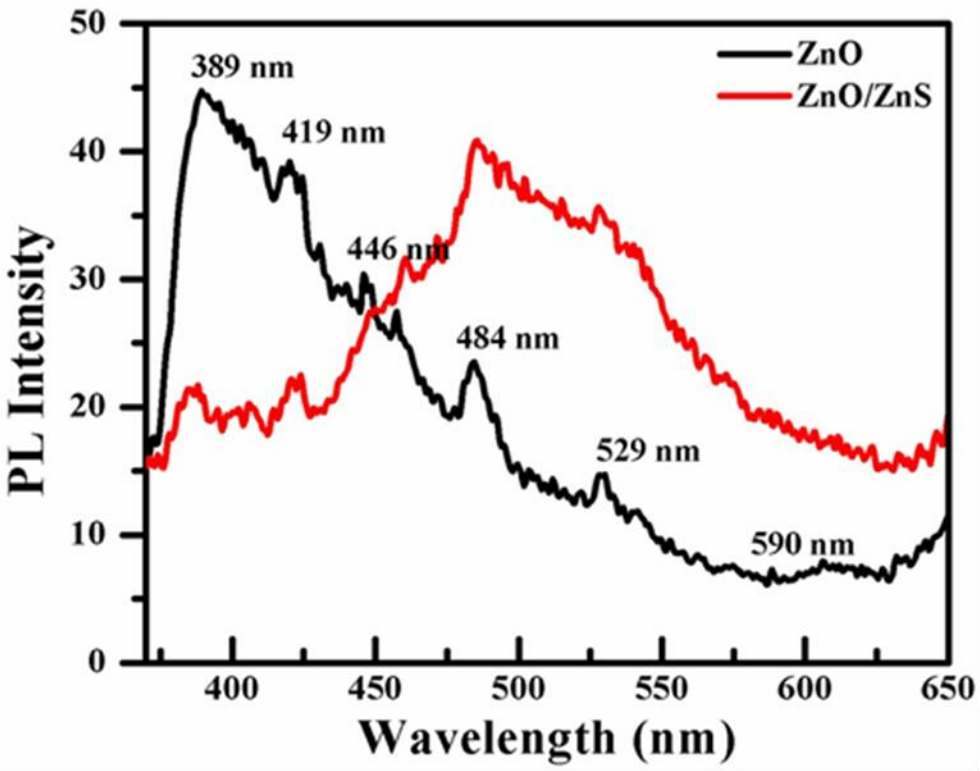

Figure 3.8: Photoluminescence spectra of ZnO and ZnO-ZnS nanocomposite

Photocatalytic activity: The photocatalytic activity of as-synthesized ZnO and ZnO-ZnS composite material was evaluated by photodegradation of methylene blue (MB) organic dye as a representative water contaminant under UV light. The concentration plot of MB versus reaction time with ZnO and ZnO-ZnS photocatalysts under irradiation of UV light (664 nm) is shown in Figure 3.9 a & b respectively. Among the two catalysts ZnO and ZnO-ZnS, the later shows better photodegradation efficiency (93 %) than the former (55 %) for degradation of MB on 90 minutes UV radiation exposure, Hydroxyl radicals play critical role in photocatalytic degradation of organic dyes. Pleskov reported that the recombination rate of photogenerated electron-hole pair (e^- - h^+) in bare ZnO is very fast [53]. The fast recombination of (e^- - h^+) prevents the formation of hydroxyl radicals which is mandatory for the

photodegradation of the organic pollutant. Wang [54] also described that the photocatalytic activity of Ag-doped ZnO is better as compared to the pure bare ZnO and Shinde [55] reported that the N-doped ZnO displayed higher rate of degradation of toluene as compared to that of pure ZnO. In the PL spectra, the intensity of UV near band emission of pure ZnO at 391 nm is significantly decreased in ZnO-ZnS composite, indicating rate of recombination of (e^- - h^+) significantly increased in ZnO-ZnS compared to pure ZnO. Further, in ZnO-ZnS, the intensity of visible emission peaks at 484 and 529 nm significantly increased compared to pure ZnO. This in turn indicates that the addition of ZnS to ZnO creates large amount of oxygen vacancies ($V_o^{\bullet}$ and $V_o^{\bullet\bullet}$). These oxygen vacancies act as scavengers and effectively slowed down recombination of (e^- - h^+). Thus from PL study it is obvious in ZnO-ZnS material the increased oxygen defects concentration effectively help in the separation of photogenerated (e^- - h^+) pairs and thus prolongs the •OH radicals life. These two behavior act together and enhanced photocatalytic activity of ZnO-ZnS nanocomposite compared to pure ZnO for degradation of MB under UV light irradiation.

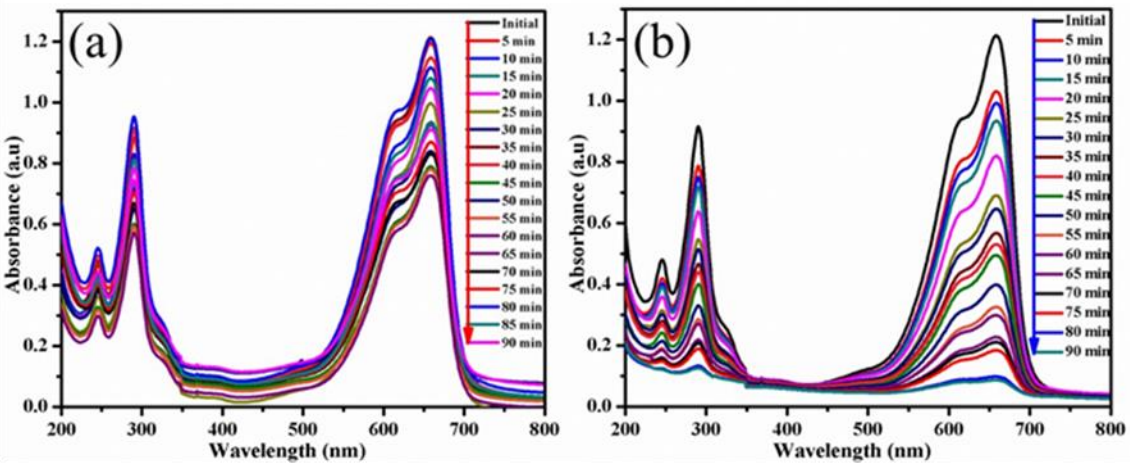

Figure 3.9: Absorption spectra of methylene blue solution at different time interval under UV light radiation with sample (a) ZnO and (b) ZnO-ZnS composite.

The reaction rate of MB degradation has been evaluated by applying pseudo-first-order kinetic model as represented by, ln (C_0/C_t) = kt, where C_0 is the initial concentration, C_t is the concentration of the dye at time t and k is the rate constant [56]. Mostly pseudo first-order kinetics is applied to elucidate the photocatalytic degradation reaction, which occurs at the interface between a photocatalyst and azo dye (organic pollutants) with low concentration. From the slope of linear fitting of the graph between the ln (C_0/C_t) versus t (Figure 3.10), the rate constant values for ZnO and ZnO-ZnS catalysts have been determined as 0.012 and 0.077 min^{-1} respectively. The results indicate that ZnO-ZnS is better photocatalyst than ZnO for degradation of dye MB.

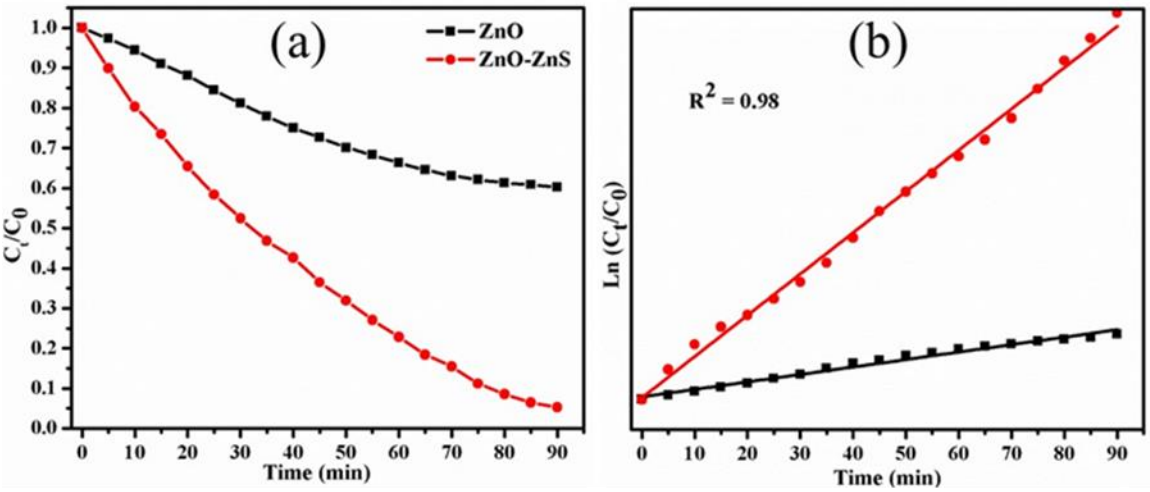

Figure 3.10: The photocatalytic removal of MB (a) and Kinetics of MB removal (b)

3.6. Conclusion:

In summary, we have successfully prepared ZnO NPs and ZnO-ZnS nanocomposite by a simple chemical co-precipitation method. XRD, PL, FESEM, HRTEM and FTIR techniques established the formation of flake-like ZnO and sheet-like ZnO-ZnS nanostructures. The PL spectra of ZnO-ZnS nanocomposite reveals the decreased intensity of UV near band edge and violet emission and an enhanced intensity of visible emission, as well as the disappearance of orange emission. UV-

visible and PL spectral analysis revealed that addition of ZnS to ZnO cause a significant decrease in recombination of electrons and holes and increase of intrinsic oxygen vacancies. These factors are responsible for the better photocatalytic activity of ZnO-ZnS nanocomposite compared to pure ZnO NP for degradation of dye MB under UV light exposure.

3.7. References:

[1] M. Bruchez, M. Moronne, P. Gin, S. Weiss, A.P. Alivisatos, Semiconductor nanocrystals as fluorescent biological labels, Science 281 (1998) 2013-2016.

[2] C.B. Murray, C. Kagan, M. Bawendi, Synthesis and characterization of monodisperse nanocrystals and close-packed nanocrystal assemblies, Annual Review of Materials Research, 30 (2000) 545-610.

[3] P. Verma, A.C. Pandey, R. Bhargava, Synthesis, and characterisation: Zinc oxide-sulfide nanocomposites, Physica B: Condensed Matter, 404 (2009) 3894-3897.

[4] J.L. Yang, S.J. An, W.I. Park, G.C. Yi, W. Choi, Photocatalysis using ZnO thin films and snanoneedles grown by metal-organic chemical vapor deposition, Advanced materials, 16 (2004) 1661-1664.

[5] S.D. Kshirsagar, D. Inamdar, I. Gopalakrishnan, S. Kulshreshtha, S. Mahamuni, Formation of room-temperature ferromagnetic $Zn_{1-x}Co_xO$ nanocrystals, Solid State Communication, 143 (2007) 457-460.

[6] J. Zhong, H. Chen, G. Saraf, Y. Lu, C. Choi, J. Song, D. Mackie, H. Shen, Integrated ZnO nanotips on GaN light emitting diodes for enhanced emission efficiency, Applied Physics Letter, 90 (2007) 203515-203518.

[7] D.J. Norris, A.L. Efros, S.C. Erwin, Doped nanocrystals, Science 319 (2008) 1776-1779.

[8] R.K. Sonker, S. Sabhajeet, S. Singh, B. Yadav, Synthesis of ZnO nanopetals and its application as NO_2 gas sensor, Materials Letter, 152 (2015) 189-191.

[9] R.K. Sonker, B.C. Yadav, Growth mechanism of hexagonal ZnO nanocrystals and their sensing application, Materials Letter, 160 (2015) 581-584.

[10] P.G. Devi, A.S. Velu, Structural, optical and photoluminescence properties of copper and iron doped nanoparticles prepared by co-precipitation method,

Journal of Materials Science: Materials in Electronics, 27 (2016) 10833-10840.

[11] S.Y. Li, P. Lin, C.Y. Lee, T.Y. Tseng, C.J. Huang, Effect of Sn dopant on the properties of ZnO nanowires, Journal of Physics D: Applied Physics, 37 (2004) 2274-2282.

[12] K. Guo, Z. Liu, Y. Wang, Y. Zhao, Y. Xiao, J. Han, Y. Li, B. Wang, T. Cui, Fabrication of ZnO/$SrTiO_3$ nanoarrays and its photoelectrochemical performances, International Journal of Hydrogen Energy, 39 (2014) 13408-13414.

[13] S. Ameen, M. S. Akhtar, H. S. Shin. Growth and characterization of nanospikes decorated ZnO sheets and their solar cell application, Chemical Engineering Journal, 195 (2012) 307-313.

[14] B. Chavillon, L. Cario, A. Renaud, F. Tessier, F. Cheviré, M. Boujtita, Y. Pellegrin, E. Blart, A. Smeigh, L. Hammarstrom, P-type nitrogen-doped ZnO nanoparticles stable under ambient conditions, Journal of the American Chemical Society, 134 (2011) 464-470.

[15] J. Lu, S. Fujita, T. Kawaharamura, H. Nishinaka, Y. Kamada, T. Ohshima, Z. Ye, Y. Zeng, Y. Zhang, L. Zhu, Carrier concentration dependence of band gap shift in n-type ZnO: Al films, Journal of Applied Physics, 101 (2007) 083705-083712.

[16] A.B. Djurišić, Y.H. Leung, Optical properties of ZnO nanostructures, Small, 2 (2006) 944-961.

[17] D.L. Leslie-Pelecky, R.D. Rieke, Magnetic properties of nanostructured materials, Chemistry of Materials, 8 (1996) 1770-1783.

[18] H. He, Y. Wang, Y. Zou, Photoluminescence property of ZnO-SiO_2 composites synthesized by sol-gel method, Journal of Physics D: Applied Physics, 36 (2003) 2972-2975.

[19] O. Shalygina, I. Nazarov, A. Baranov, V.Y. Timoshenko, Structure and photoluminescence properties of zinc oxide/ytterbium oxide nanocomposites, Journal of Sol-Gel Science and Technology, 81 (2017) 1-5.

[20] A. Roychowdhury A. Mishra, S. Pati, D. Das, R. Mittal, A. Chauhan, R. Mukhopadhyay, Synthesis and characterization of multifunctional Fe_3O_4-ZnO nanocomposite, in: AIP Conference Proceedings, *AIP* **2012**; pp. 283-284.

[21] X. Yu, J. Wan, Y. Shan, K. Chen, X. Han, A facile approach to fabrication of bifunctional magnetic-optical Fe_3O_4@ ZnS microspheres, Chemistry of Materials, 21 (2009) 4892-4898.

[22] H. Kim, M. Achermann, L.P. Balet, J.A. Hollingsworth, V.I. Klimov, Synthesis and characterization of Co/CdSe core/shell nanocomposites: bifunctional magnetic-optical nanocrystals, Journal of the American Chemical Society, 127 (2005) 544-546.

[23] Z. Yang, W. Zhong, C. Au, X. Du, H. Song, X. Qi, X. Ye, M. Xu, Y. Du, Novel photoluminescence properties of magnetic Fe/ZnO composites: self-assembled ZnO nanospikes on Fe nanoparticles fabricated by hydrothermal method, The Journal of Physical Chemistry C, 113 (2009) 21269-21273.

[24] H. Bala, Y. Yu, X. Cao, W. Fu, Preparation and characterization of nickel/zinc sulphide: Bifunctional magnetic-optical nanocomposites, Materials Chemistry and Physics, 111 (2008) 50-53.

[25] T. Hong, Z. Liu, H. Liu, J. Liu, X. Zhang, J. Han, K. Guo, B. Wang, Preparation and enhanced photoelectrochemical performance of selenite-sensitized zinc

oxide core/shell composite structure, Journal of Materials Chemistry A, 3 (2015) 4239-4247.

[26] S. Gao, D. Li, Y. Li, X. Lv, J. Wang, H. Li, Q. Yu, F. Guo, L. Zhao, Growth and characterization of ZnO nanorod arrays on boron-doped diamond films by low temperature hydrothermal reaction, Journal of Alloys and Compounds, 539 (2012) 200-204.

[27] Z. Liu, Q. Zhang, G. Shi, Y. Li, H. Wang, Solvothermal synthesis and magneto-optical properties of $Zn_{1-x}Ni_xO$ hierarchical microspheres, Journal of Magnetism and Magnetic Materials, 323 (2011) 1022-1026.

[28] V. Gandhi, R. Ganesan, H.H. Abdulrahman Syedahamed, M. Thaiyan, Effect of cobalt doping on structural, optical, and magnetic properties of ZnO nanoparticles synthesized by coprecipitation method, The Journal of Physical Chemistry C, 118 (2014) 9715-9725.

[29] M. Arshad, A. Azam, A.S. Ahmed, S. Mollah, A.H. Naqvi, Effect of Co substitution on the structural and optical properties of ZnO nanoparticles synthesized by sol-gel route, Journal of Alloys and Compounds, 509 (2011) 8378-8381.

[30] C. Falcony, M. Garcia, A. Ortiz, J. Alonso, Luminescent properties of ZnS: Mn films deposited by spray pyrolysis, Journal of Applied Physics, 72 (1992) 1525-1527.

[31] W. Tang, D. Cameron, Electroluminescent zinc sulphide devices produced by sol-gel processing, Thin Solid Films, 280 (1996) 221-226.

[32] J. Rouhi, M.H. Mamat, C.R. Ooi, S. Mahmud, M.R. Mahmood, High-performance dye-sensitized solar cells based on morphology-controllable

synthesis of ZnO-ZnS heterostructure nanocone photoanodes, PloS one 10 (2015) 0123433-0123447.

[33] M.Y. Lu, J. Song, M.P. Lu, C.Y. Lee, L.J. Chen, Z.L. Wang, ZnO-ZnS heterojunction and ZnS nanowire arrays for electricity generation, ACS Nano, 3 (2009) 357-362.

[34] S. Saha S. Sarkar S. Pal P. Sarkar, Tuning the energy levels of ZnO/ZnS core/shell nanowires to design an efficient nanowire-based dye-sensitized solar cell, The Journal of Physical Chemistry C, 117 (2013) 15890-15900.

[35] G. Hitkari, S. Singh, G. Pandey, Synthesis, Characterization and Visible Light Degradation of Organic dye by Chemically Synthesized ZnO/γ-Fe_3O_4 Nanocomposites, Synthesis, 4 (2017) 3960-3965.

[36] P. Bindu, S. Thomas, Estimation of lattice strain in ZnO nanoparticles: X-ray peak profile analysis, Journal of Theoretical and Applied Physics, 8 (2014) 123-134.

[37] G. Pandey, S. Dixit, Growth mechanism and optical properties determination of CdS nanostructures, The Journal of Physical Chemistry C, 115 (2011) 17633-17642.

[38] G. Pandey, S. Dixit, A.K. Shrivastava, Role of additives; sodium dodecyl sulphate and manganese chloride on morphology of $Zn_{1-x}Mn_xO$ nanoparticles and their photoluminescence properties, Materials Chemistry and Physics, 147 (2014) 423-432

[39] A. Roychowdhury, S.P. Pati, S. Kumar, D. Das, Effects of magnetite nanoparticles on optical properties of zinc sulfide in fluorescent-magnetic Fe_3O_4/ZnS nanocomposites, Powder Technology, 254 (2014) 583-590.

[40] A.K. Zak, M.E. Abrishami, W.A. Majid, R. Yousefi, S. Hosseini, Effects of annealing temperature on some structural and optical properties of ZnO nanoparticles prepared by a modified sol–gel combustion method, Ceramics International, 37 (2011) 393-398

[41] P.G. Devi, A.S. Velu, Synthesis, structural and optical properties of pure ZnO and Co doped ZnO nanoparticles prepared by the co-precipitation method, Journal of Theoretical and Applied Physics, 10 (2016) 233-240.

[42] H. Guo, Y. Ke, D. Wang, K. Lin, R. Shen, J. Chen, W. Weng, Efficient adsorption and photocatalytic degradation of Congo red onto hydrothermally synthesized NiS nanoparticles, Journal of Nanoparticle Research, 15 (2013) 1475-1487.

[43] Y. Zhang, Z.-R. Tang, X. Fu, Y.-J. Xu, Engineering the unique 2D mat of graphene to achieve graphene-TiO_2 nanocomposite for photocatalytic selective transformation: what advantage does graphene have over its forebear carbon nanotube?, ACS nano, 5 (2011) 7426-7435.

[44] S. Monticone, R. Tufeu, A. Kanaev, Complex nature of the UV and visible fluorescence of colloidal ZnO nanoparticles, The Journal of Physical Chemistry B, 102 (1998) 2854-2862.

[45] H. Madan, S. Sharma, D. Suresh, Y. Vidya, H. Nagabhushana, H. Rajanaik, K. Anantharaju, S. Prashantha, P.S. Maiya, Facile green fabrication of nanostructure ZnO plates, bullets, flower, prismatic tip, closed pine cone: Their antibacterial, antioxidant, photoluminescent and photocatalytic properties, Spectrochimica Acta Part A: Molecular and Biomolecular Spectroscopy, 152 (2016) 404-416.

[46] M. Sookhakian, Y. Amin, W. Basirun, M. Tajabadi, N. Kamarulzaman, Synthesis, structural, and optical properties of type-II ZnO-ZnS core-shell nanostructure, Journal of Luminescence, 145 (2014) 244-252.

[47] H. Zeng, Z. Li, W. Cai, P. Liu, Strong localization effect in temperature dependence of violet-blue emission from ZnO nanoshells, Journal of Applied Physics, 102 (2007) 104307-104311.

[48] G.H. Mhlongo, D.E. Motaung, S.S. Nkosi, H. Swart, G.F. Malgas, K.T. Hillie, B.W. Mwakikunga, Temperature-dependence on the structural, optical, and paramagnetic properties of ZnO nanostructures, Applied Surface Science, 293 (2014) 62-70.

[49] P. Taunk, R. Das, D. Bisen, R. K. Tamrakar, Structural characterization and photoluminescence properties of zinc oxide nano particles synthesized by chemical route method, Journal of Radiation Research and Applied Sciences, 8 (2015) 433-438.

[50] S. Baek, J. Song, S. Lim, Improvement of the optical properties of ZnO nanorods by Fe doping, Physica B: Condensed Matter, 399 (2007) 101-104.

[51] C. Lin, W. Wang, C.-S. Lee, K. Sun, Y. Suen, Magneto-photoluminescence properties of Co-doped ZnO nanorods, Applied Physics Letters, 94 (2009**)**, 151909-151911.

[52] P.V. Raleaooa, A. Roodt, G.G. Mhlongo, D.E. Motaung, R.E. Kroon, O.M. Ntwaeaborwa, Luminescent, magnetic and optical properties of ZnO-ZnS nanocomposites, Physica B: Condensed Matter, 507 (2017) 13-20.

[53] Y.V. Pleskov, Conversion of luminous energy into electrical and chemical energy in photoelectrochemical cells with semiconductor electrodes, Soviet Electrochemistry, 17 (1981) 1-25.

[54] L.B. Wang, Q.K. Hu, Z.Y. Li, J.Y. Guo, Y.W. Li, Microwave-assisted synthesis and photocatalytic performance of Ag-doped hierarchical ZnO architectures, Materials Letters, 79 (2012) 277-280.

[55] S.S. Shinde, C.H. Bhosale, K.Y. Rajpure, Photocatalytic degradation of toluene using sprayed N-doped ZnO thin films in aqueous suspension, Journal of Photochemistry and Photobiology B: Biology, 113 (2012) 70-77.

[56] A.K. Kole, C.S. Tiwary, P. Kumbhakar, Ethylenediamine assisted synthesis of wurtzite zinc sulphide nanosheets and porous zinc oxide nanostructures: near white light photoluminescence emission and photocatalytic activity under visible light irradiation, CrystEngComm, 15 (2013) 5515-5525.

***

Chapter 4
Synthesis, Characterization and Photocatalytic Application of Copper-Zinc Oxide Nanocomposites

Chapter 4
Synthesis, characterization and photocatalytic application of copper-zinc oxide nanocomposites

In the current work, ZnO, and ZnO/CuO nanocomposites have synthesized by simple chemical co-precipitation method through calcination at 400 °C for 4hrs. Prepared nanocomposite samples were appraised by X-ray diffraction (XRD), energy dispersive X-ray spectroscopy (EDX), scanning electron microscope (SEM), high-resolution transmission electron microscopy (HRTEM), Brunauer-Emmett Teller analysis (BET), and UV-visible spectroscopy. From the XRD analysis, it's proved that the forming of crystalline nanocomposites material while magnified SEM images showed that single hexagonal structural of pure ZnO and agglomeration of grain like structure of ZnO/CuO composite by calcination on 400 °C. HRTEM investigation proves that hexagonal structure of pure ZnO is obtained by aggregation of the knife-like structure. BET analysis accepted that the mesoporous nature of nanocomposites. UV-Visible spectra have been also discussed the optical behaviour of the materials. The photocatalytic operation of the fabricated materials, ZnO and ZnO/CuO composite was well-established for the photo-degradation of Congo red (CR) organic waste in aqueous phase under irradiation of visible light. The ZnO/CuO composite shown better photocatalytic activity for decolourization of CR dye.

4.1. Introduction:

The commercial use of synthetic dyestuffs in a number of industries like paper, plastic leather, textile, food, and printing industries. Among the various dyestuffs, most of these are synthetic organic dye of azo compound like congo red (CR), methyl orange (MO), and methylene blue (MB)) which contain chromophore (-N=N-) in their molecular composition [1]. However, the blend of discharged effluents containing –N=N- chromophoric group are usually recognized in the effluent and has to be eliminated before releasing into the ground water since these large-scale organic dyestuffs are a toxic waste to contaminate the water bodies and influence the ecosystem specially terrestrial as well as aquatic life [2]. For the dealing of organic contaminants containing waste water, traditional process like coagulation, flocculation, chemical precipitation/separation, hypochlorite oxidation, ozone oxidation, adsorption on the activated carbon, activated sludge and osmosis process have difficulties in the complete destruction of contaminants, and also have the further disadvantage of potentially secondary pollution [3].

In the recent period, the nanostructure semiconducting (NS) substances have been accepted as heterogeneous photocatalytic materials for the advanced oxidation process (AOP) for the powerful destruction of toxic pollutants from decontaminated water. In this current procedure, the electron-hole pair will be generated by the radiation of semiconducting substances like ZnO with the appropriate energy of photon equal to or larger than the band gap ($h\upsilon \geq Eg$) energy. The electrons and holes produced during irradiation of light may move around to catalytic surface where they play a major character in the redox reaction with absorbed species. Generally, holes at valence band (h^{+}_{VB}), react with surrounded $H_2O/OH^{-\bullet}$ at the surface to generate hydroxyl radical ($OH^{\cdot}$) which is a very strong oxidizing agent, and electrons at

conduction band (e^-_{CB}) are taken by dissolved oxygen to produce superoxide radical anion ($O_2^{\cdot -}$). Some other free radical such as $HO_2^{\cdot}$/ $O_2^{\cdot}$ may also be produced and participated in the degradation process, but these radicals are low efficient than the hydroxyl radical. It has been recommended that these radicals are the fundamental oxidizing species in the decolourization of organic contaminants through the photocatalytic oxidation processes as represented as in equation [4.1 to 4.4].

$$NS + h\upsilon \rightarrow e^-_{CB} + h^+_{VB} \quad (4.1)$$

$$e^-_{CB} + O_2\,(dis) \rightarrow O_2^{\bullet -} \quad (4.2)$$

$$h^+_{VB} + NS\text{-}H_2O/OH^- \rightarrow OH^{\bullet}(abs) + H^+ \quad (4.3)$$

$$OH^{\bullet}(abs) + \text{organic pollutants} \rightarrow \text{Oxidized product} \quad (4.4)$$

However, the fast recombination process of photogenerated electron/hole pair and particle agglomeration inhibit the advantage of this process. Based on the current investigation, the coupling of different type semiconductors drives to powerful expansion in their photocatalytic efficiency. It has been mention that, the coupling of semiconductors with various band gap materials significantly inhibit the electron recombination process of coupled semiconductors compared to the bare semiconductor.

ZnO NPs is a non-toxic, low cost, and a fascinating direct band gap n-type semiconductor nanoparticle belongs to II-VI group with hexagonal wurtzite and zinc blend crystalline structure. At room temperature, it has an extensive band gap energy 3.37 eV and high exciton binding energy 60 meV [5]. However, because of its wide band gap, it can only consume radiation of the ultraviolet region in the solar light which purview its photocatalytic application under UV irradiation of photo-induced holes and reduced electrons. Along with these behaviors of zinc oxide the adaptability of an electron-hole pair, production is of fundamentally important. The speedy

recombination of the photoproduced electron-hole pair is a preeminent drawback of zinc oxide catalyst due to this reason its decrease of their photocatalytic activity [6]. In the procedure to upgrade the photocatalytic activities of ZnO by numerous approach like alteration of ZnO by non-metal doping [7], hybridized with the extension of transition metal ions [8, 9], noble metals [10], graphene [11], graphdyine [12] and mixing with different semiconductor such as ZnO/TiO_2 [13], ZnO/SnO_2 [14], and SnO_2/ZnO [15].

In modern generation, copper oxide (CuO) has drawn more consideration by cause of its p-type multifunctional semiconductor behavior and its broad range of applications like sensors, super capacitors, field emissions, Li-batteries, and catalysis because of its pleasant characteristic along with direct band gap (~1.2 eV), low-toxicity, chemical inertness, extraordinary thermal and electrical conductivities, natural abundance and environmental benignity [16-21]. Due to very small band gap energy, the photocatalytic application of pure CuO has not been investigated as ZnO or TiO_2 because of its instantaneous recombination of photogenerated electron-hole pairs [20, 22-27]. To prevent the mentioned shortcoming, a combination of CuO with a new semiconductor material will implement an adequate path street for valuable charge separation, and enhanced the lifetime of the photogenerated charge exciton and improved its photocatalytic properties.

In the current time, composites materials are frequently synthesized with CuO, as a co-catalyst to boost their photocatalytic ownership of other semiconductors such as TiO_2 [28], ZnO [29], Fe_2O_3, $BiVO_4$ [30], ZnS [31]. T. Chang et al. informed that hydrothermally synthesized ZnO/CuO nanocomposite for the decolourization of methyl orange (MO) and methylene blue (MB) [32]. R. Saravanan al. also reported that the synthesis of ZnO/CuO composite by the thermal decomposition technique for

photodegradation of MB and MO [33]. In the best of our knowledge coupling of CuO with ZnO for improving the photocatalytic ownership of ZnO for the decolorization of Congo Red (CR) remains unfamiliar. For the synthesis of composites materials with CuO, ZnO can also be a reasonable semiconductor material since it maintains convenient band edge position with respect to CuO, i.e., the position of both the valence band (VB) and conduction band (CB) of CuO raise above as compare to ZnO, which thermodynamically support the relocation of excited electrons and holes between them [29]. Accordingly, ZnO/CuO composites were prepared by simple co-precipitation method, and their photocatalytic action was evaluated using Congo red dyes as hazardous materials under the radiation of normal sun-light in the existence of oxidizing agent like H_2O_2. Experimental outcomes exposed that the prepared ZnO/CuO nanocomposites have remarkable photocatalytic properties than bare ZnO and CuO, and the mechanism of improved photocatalytic presentation of ZnO/CuO composites was explained in detail.

4.2. Experimental Section:

4.2.1. Chemical and Material:

Analytical grade zinc sulfate heptahydrate ($ZnSO_4.8H_2O$), copper chloride dihydrate ($CuCl_2.2H_2O$), sodium hydroxide (NaOH), Congo red ($C_{32}H_{22}N_6Na_2O_6S_2$) (CR) and glycine ($C_2H_5NO_2$) was obtained from Merck India and used without further purification. Double de-ionized water was used as solvents. All the glassware's were rinsed and cleaned by concentrated acid. The dried glassware's were used in all the experiments.

4.2.2. Preparation of Zinc Oxide nanoparticles (ZnO NPs):

For the preparation of ZnO, 50 ml solution of $ZnSO_4.7H_2O$ (0.3 M) was sonicated prudently for 30 min in the ultrasonic cleaner. 50 ml of 0.3 M solution of

urea (NH_2CONH_2) was added carefully into the above zinc sulfate solution and stirred vigorously on the digital magnetic stirrer. Then 0.5 M NaOH solution was sensibly added to the above precursor solution under forceful stirring till 11 pH. The reaction mixture was refluxed for 1 h at 80 ˚C. The as-prepared precipitate was kept at room temperature for cooled down naturally then filtrated and washed numerous times with double deionized water to remove the impurity and finally with acetone until neutralization. The precipitate was dried at 80 ºC in the electric oven.

4.2.3. Preparation of Copper Zinc Oxide (ZnO/CuO) nanocomposites:

In the typical synthesis process, 25 ml of 0.5 mole $ZnSO_4.8H_2O$ and 25 ml of 0.5 moles of $CuCl_2.2H_2O$ solution were mixed and vigorously stirred on the magnetic stirrer for 30 min. the clear blue solution obtained. After the completion of stirring added 4.0 M sodium hydroxide solution till the pH of reaction mixture goes to 11 then the color of reaction mixture changes from blue color to dark blue color. After the complete addition of sodium hydroxide, the reaction mixture was heated at 120 °C for 2hrs, the blue precipitate was formed. The as-prepared precipitate was kept on room temperature to cool down naturally. The products were filtered, washed numerous times with deionized water and dried at 80°C in the electric oven to obtain a blue powder of copper zinc oxide nanocomposites. The obtained product was calcined in the muffle furnace at 400°C for 4hrs.

4.3. Characterization:

The structural estimation of the materials was carried by Powder X-ray diffraction (XRD) patterns, collected at room temperature using a Rigaku High Resolution 12 kW X-ray diffractometer. Advance diffractometer system engaging a monochromatized Cu Ka radiation (λ= 1.54056 Å) source. Optical absorption spectrum examination was carried by carry 100 UV-visible spectrophotometer. A

diluted and well-suspended solution of NPs and nanocomposite in absolute ethanol was required for the absorption spectral investigation. External morphology, crystalline structural intactness and orientation of synthesized materials are exposed by Scanning electron microscopy (SEM) and the stoichiometric chemical compositions of the synthesized copper zinc oxide nanocomposites (ZnO/CuO) were studied with the help of energy dispersive analysis of X-ray electron diffraction for X-ray analysis (EDX) measurements were achieved with a JEOL JSM 6610 at 20 kV. Then the distribution of pore size and specific surface areas of the materials were investigated from the consequence of N2 adsorption-desorption measurement at 77 K (BELSORP MINI II) by using the BET (Brunauer-Emmett-Teller) and BJH (Barrett-Joyner Halenda).

4.3.1. Photocatalytic activity:

The photocatalytic behaviour of the prepared samples was considered by photodecolourization of Congo red (CR) organic dye in an aqueous medium in solar light interaction. The reaction scheme containing a 350 W Xe lamp, specific quartz reactors (50 mL) and a water cooling equipment etc. 50 mg of each synthesized sample was added in 100 mL of CR aqueous solution (1×10^{-5} M) separately. Initial pH value of CR dye solution is about 5.6. This mixed solution was sonicated for 30 min in the absence of light to reach an adsorption-desorption equilibrium. To establish the proper mixing of ZnO NPs, ZnO/CuO composite and CR solution keep a constant concentration of dissolved oxygen, the reaction solution was agitated by supplying air properly during the complete reaction. After a 5-minute time interval, a small amount of the solution was pipetted out, centrifuged and its absorbance spectrum was measured on UV-Visible spectrophotometer to calculate the percentage degradation. The degradation efficiency η (%) of CR solution can be measured according to Eq. (1).

$$\eta(\%) = \frac{(C_0 - C_t)}{C_0} \times 100 \quad (4.5)$$

Where C_o represents the initial concentration of CR in the solution (mg L^{-1}) and C_t is the concentration of CR at time t (mg L^{-1}).

4.4. Results and Discussions:

4.4.1. X-ray Diffraction (XRD) analysis:

The structural features like crystal structure and purity of the synthesized bare and nanocomposites materials were investigated using X-ray diffraction characterization technique. Figure 4.1 shows the XRD patterned of (Figure 4.1 a) ZnO NPs and (Figure 4.1 b) ZnO/CuO nanocomposites materials. All the peaks in the XRD patterned are very sharp and intense which demonstrate that the nature of the samples is good crystalline. The XRD pattern of ZnO nanoparticles (NPs) (a) which contain the following diffraction peak position of 2θ degree values at 31.80˚, 34.51˚, 36.21˚, 47.52˚, 56.61˚, 62.90˚, 67.91˚, and 69.92˚, with corresponding miller indices (hkl) values of (100), (002), (101), (102), (110), (103), (112), and (201), respectively indicate the hexagonal structure (JCPDS card no 800075, a=3.253, and c=5.209 with space group $p_6$3mc) of ZnO NPs. The two other peaks instead of ZnO NPs was found which is main characteristic peaks for CuO in the sample at 39.21˚, and 53.89˚, which correspond to (111), and (020) which indicate that monoclinic phase (JCPDS card no. 021041, a=4.65, b=3.41, and c=5.11, β=99.48, with space group C2/c) of CuO on the addition of copper chloride in the aqueous solution of zinc sulphate. From the XRD pattern, it confirmed that two different group of peaks corresponding to the zinc and copper oxide could be clearly distinguished.

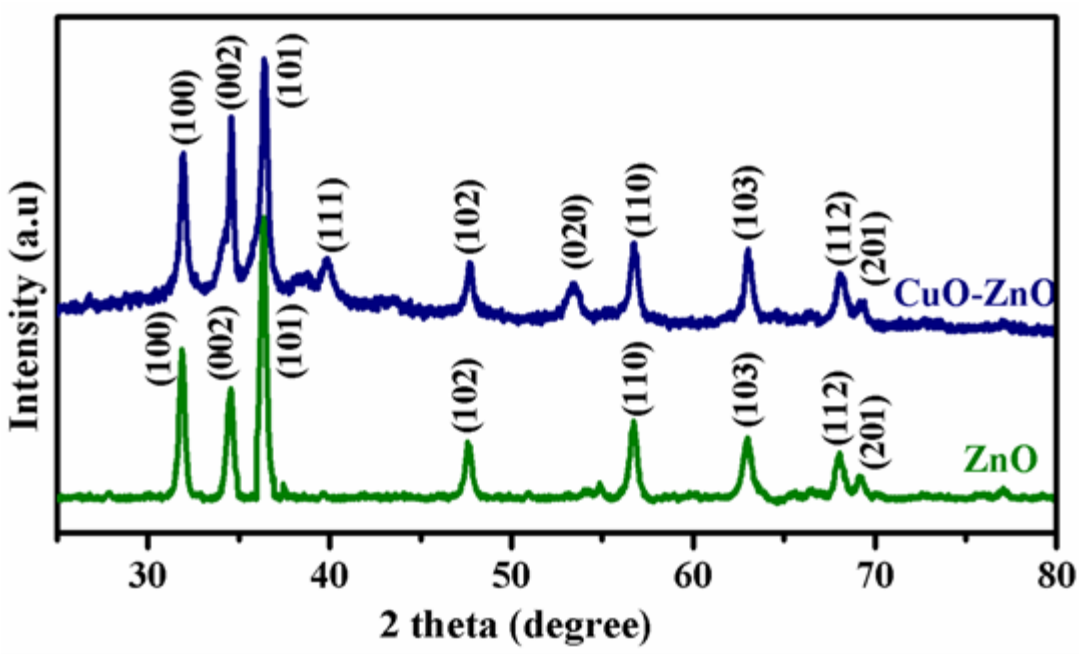

Figure 4.1: X-ray diffraction patterned of ZnO nanoparticle and ZnO/CuO nanocomposites prepared by simple chemical method and calcination at the 400˚C.

The bond length (L) and volume (V) was calculated of the unit cell for a hexagonal system with the help of Eq. (4.6-4.8) [34].

$$L = \sqrt{\frac{a^2}{3} + \left(\frac{1}{2} - z\right)^2 c^2} \tag{4.6}$$

$$z = \frac{a^2}{3c^2} + \frac{1}{4} \tag{4.7}$$

$$V = 0.866 a^2 c \tag{4.8}$$

The lattice parameters a and c, arranged in Table 4.1, are determined by the following expression [35]

$$\frac{1}{d^2} = \frac{4}{3}\left(\frac{h^2 + hk + k^2}{a^2}\right) + \frac{l^2}{c^2} \tag{4.9}$$

The calculated values of the lattice parameters (a, c and c/a) have been achieving to be in a good agreement with the standard data, JCPDs card no: 800075. It is well recognized that alteration of (c/a) ratio indicates the deformation in the structure of the material. Hence, the variation in the value of the c/a ratio indicates that insertion

of Cu in the ZnO nanoparticles does make the noticeable deformation in the lattice due to the slight difference in the size of the Cu^{2+} and Zn^{2+} ions.

The internal lattice strain (microstrain) is responsible for the broadening of the XRD peak due to a large fraction of surface atoms without altering the peak location. Microstrain of any material is suggested as the root mean square value, (ε) and hence it always a positive value. Commonly, the microstrain is attributed to imperfection in crystal, such as the additional volume of grain boundaries, vacancy clusters and vacancies and dislocations. Therefore, nanoparticles samples which have a small size and microstrain sponsor to the broadening of the XRD peaks [36]. The broadening because of microstrain is produced by the inconsistent displacements of the atoms related to their lattice locations and the microstrain is revealed as lattice defects [37] which are liable for numerous uncommon chemical and physical properties of nanostructures. In the current study, the microstrain (ε) was calculated by using the following relation

$$\varepsilon = \frac{\beta \cos\theta}{4} \tag{4.10}$$

The dislocation density (δ) of ZnO nanoparticles was estimated applying Williamson and Smallman's method

$$\delta = \frac{n}{D^2} \tag{4.11}$$

Where n is a constant usually close to one [34].

The above investigation can summarize in a Table 4.1 that indicates the instantaneous variation of both the crystallite size D and lattice strain ε with adding the source of Cu in our material. It is recognized that adding the Cu content leads to decrease in the crystallite size and an increase in the lattice strain. Furthermore, Table 4.1 recommends an increase in the dislocation density (δ) of grain boundaries as the Cu^{2+}

increases which can be recognized to the fast anisotropic growth of the grains induced by the Cu ions in a preferred orientation.

Sample	2θ	D (nm)	Lattice Parameter			V(Å^3)	L (Å)	ε x 10^{-4}	δ x 10^{14} line/ m^2	S_{BET}(m^2 g^{-1})	d(nm)	V_g (cm^3 g^{-1})
			a (Å)	c (Å)	c/a (Å)							
ZnO	36.210	46.9	3.253	5.209	1.6012	47.73538	2.6910	7.48	4.55	4.71	12.64	0.038
ZnO/CuO	36.215	10.3	4.65	5.11	1.0989	95.68518	2.9184	7.95	94.26	84.53	1.64	0.036

Table: 4. 1. Diffraction angle (2θ) value, crystalline size (D), lattice parameter (a, c, c/a), volume (V) of unit cell and Zn-O bond length (L), dislocation density (δ) BET surface area (S_{BET}) pore size (d) and pore volume (Vg) of ZnO and ZnO/CuO nanocomposite materials.

The crystallite size (D) has been determined from the Debye-Scherer equation [38].

$$D = \frac{k\lambda}{\beta \cos\theta} \qquad 4.11)$$

Where k is the shape factor (taken to be 0.9) λ is the wavelength of the incident radiation equal to 1.534 (in Å), β is the full width at half maxima (FWHM) and θ is the Braggs diffraction angle. The average particles size of ZnO NPs and ZnO/CuO nanocomposites was calculated to be 46.9 and 10.3 nm respectively.

4.4.2. Scanning Electron Microscopy (SEM image) and EDX analysis:

The structural morphology of chemically synthesized nanomaterial ZnO and ZnO/CuO composite sample have been examined by SEM image and EDX that are shown in Figure 4.2 (a-d) respectively. Figure 4.2a shows that the clear hexagonal structure of pure ZnO NPs whereas the highly magnified image Figure 4.2b distinctly denoted that the single hexagonal nanostructure. It was found that the addition of CuO and calcination up to 400 ºC for the formation of ZnO/CuO composite sample, the morphology of the composite have been changed from hexagonal to the nano grain like structure with the uniform production of nanopowders are shown in Figure 4.2 c

and highly resolved image in Figure 4.2d. R. Saravanan et al. was reported that the nanorods like ZnO/CuO nanocomposites material fabricated by the decomposition method [33]. K. vijayalakshmi and K. karthick were also reported that the flower-like agglomerate nano-flack like the structure of ZnO/CuO composite synthesized by facile microwave irradiation method [39]. Thus the addition of CuO may affect the morphology and size of ZnO by its immersion in the nucleation and growth. It is evident from the XRD analysis and SEM image that the size of ZnO NPs decreases with the formation of ZnO/CuO composite material.

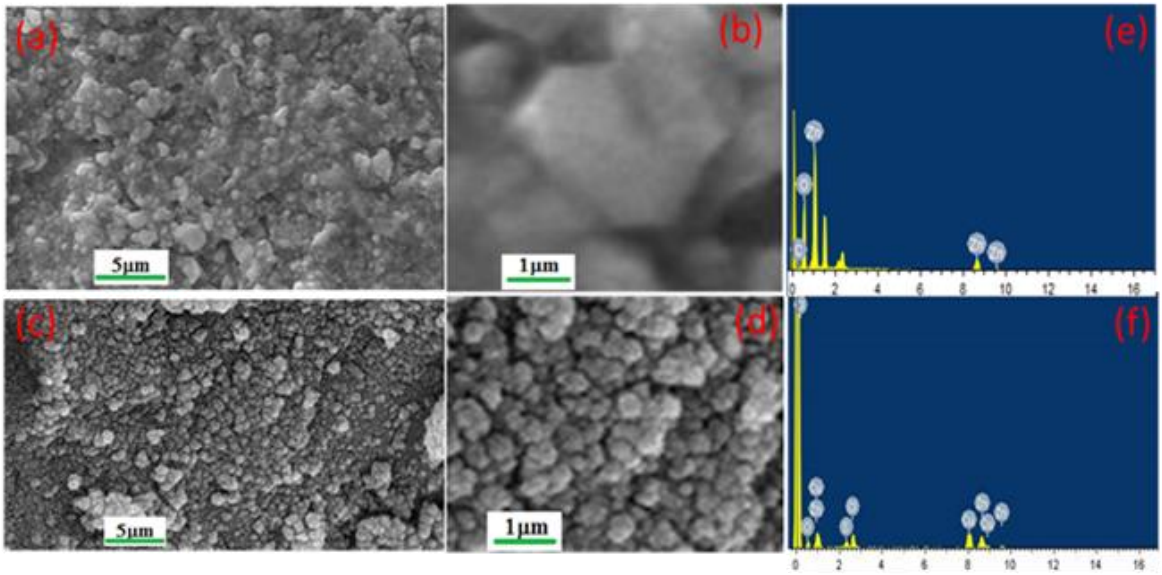

Figure 4.2: The SEM images of (a) ZnO NPs, (b) high magnified ZnO (c) ZnO/CuO (d) high magnified ZnO/CuO nanocomposites. EDX spectra of (e) ZnO, (f) ZnO/CuO nanocomposites.

The elemental compositions of synthesized ZnO NPs and ZnO/CuO composite were investigated by EDX spectra. Respective EDX spectra of ZnO NPs and ZnO/CuO composite were represented in Figure 4.2 (e-f). It was found that in ZnO NPs the peaks corresponding to Zn:O ratio in the material is relatively 1:1, suggesting that confirm the material is composed of Zn and O elements in 1:1 ratio (Figure 4.2 e) and ZnO/CuO composite were composed of Zn, Cu and O without having any impurity element and this is consistent with the XRD analysis.

4.4.3. Transmission electron microscopy (TEM image) analysis:

The morphological and the internal structural examination of ZnO and ZnO/CuO composite has further investigated by high-resolution transmission electron microscope (HRTEM) micrograph analysis. However, a large number of similarity was found in the SEM image and HRTEM image of the prepared materials. The Figure 4.3 a shows the HRTEM images of ZnO NPs and Figure 4.3 b-c shows HRTEM image of ZnO/CuO composite materials. The HRTEM micrograph of ZnO is clearly shown the knife like structure is clearly observed. Thus from HRTEM image, it is cleared that the hexagonal structure of ZnO was formed by the association of a large number of knife like the structure of ZnO NPs. However, the HRTEM image of ZnO/CuO composite sample indicates the spherical structure (Figure 4.3 b-c) with a diameter in the range of 10-15 nm which is a very close agreement with the size calculated from XRD data. The selected area electron diffraction patterned (SAED) (Figure 4.3d) shows that polycrystalline nature of the ZnO/CuO composite materials.

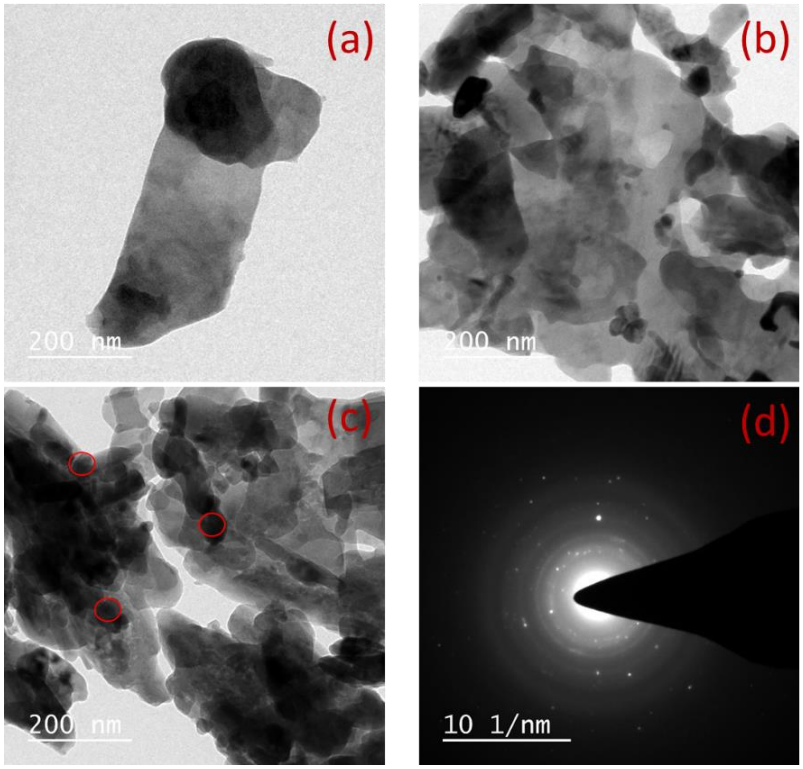

Figure 4.3: TEM image of (a) ZnO NPs, (b-c) ZnO/CuO nanocomposites (d) SAED pattern of ZnO/CuO composite.

4.4.4. Surface area measurement analysis:

The porosity and surface area of as-prepared ZnO NPs, and ZnO/CuO composite were calculated by nitrogen adsorption-desorption isotherm adopting Brunauere-Emmette-Teller (BET) method. On the basis of the IUPAC classification, the obtained isotherms of ZnO NPs (Figure 4.4 a) and ZnO/CuO composite (Figure 4.4 b) that's both are of type IV with precise H3 loops of hysteresis, informed that the mesoporous nature of ZnO NPs and ZnO/CuO composite (Figure. 4.4). The average pore diameter size (d), specific surface area (S_{BET}) and pore volume (V_g) are reported in Table 4.1. The BET specific surface area of ZnO NPs and ZnO/CuO composite is 4.71 m^2g^{-1} and 84.53 m^2g^{-1} respectively (Table 4.1). Inside the Figure. 4.5 shows the pore size distribution patterned by applying the BJH equation from the desorption plot of the isotherm. The pore size distribution calculation demonstrates that the ZnO (inside the Figure 4.4 a) NPs and ZnO/CuO (inside the Figure 4.5 b) composite have described mesoporosity of precise pore size distribution with average pore diameter around 6.06 nm. ZnO/CuO composite has a narrower pore size distribution as a comparison to the ZnO NPs and smaller pore diameter, which results from the adjacent coupling by interactions between CuO and ZnO nanoparticles in ZnO/CuO composite (Figure 4.4 b). Therefore, ZnO/CuO composite can contribute more active sites and adsorb more reactive species because of the narrower pore size distribution and larger BET surface area [40].

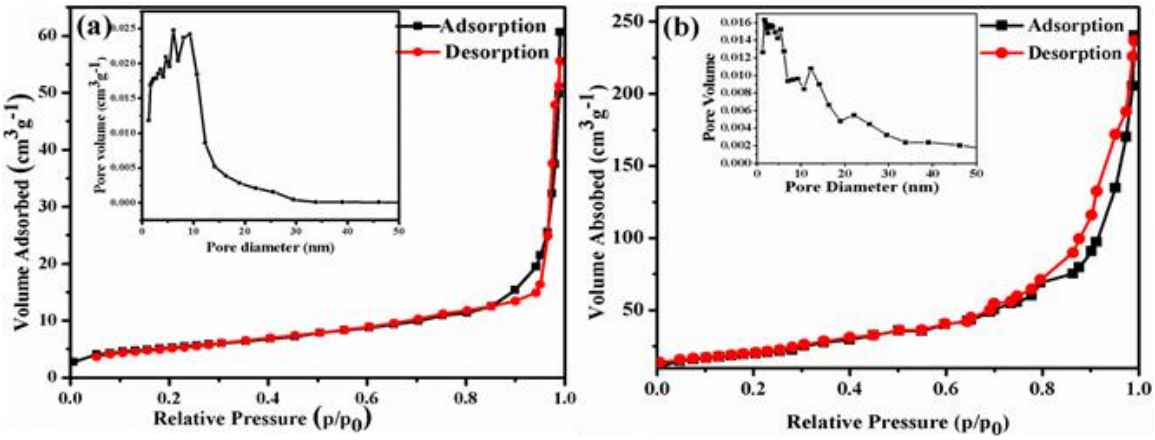

Figure 4.4: N2 adsorption-desorption isotherms and the corresponding pore size distribution curve of (a) ZnO NPs (b) ZnO/CuO nanocomposites.

4.4.5. UV-Visible absorption study:

The UV-visible absorption spectrum of chemically synthesized ZnO NPs and ZnO/CuO composite was recorded for the investigation of optical properties by dispersing the materials in distilled water and using distilled water as a reference in the wavelength range 300-700 nm at room temperature and shown in Figure. 4.5. As can be observed, the UV-visible absorbance spectra shift to longer wavelength (red shift) when the addition of a solution of copper chloride in an aqueous solution of zinc sulfate. For both material ZnO and ZnO/CuO, a broad shoulder appears between 357 nm to 428 nm with a long tail extending to a longer wavelength. Therefore, the synthesized both material could be used as an optically transparent material for the transmission of infrared as well as visible light without any contracting. The absorbance spectra of bare ZnO, the absorbance band was closely viewed at 368 nm which is in correspondence with a previous reported by Geeta Devi et al. The spectrum indicates a peaks at wavelength 378 nm which is a characteristic absorption peak of ZnO corresponding to the intrinsic band-gap absorption due to the electron transitions from the valence band to the conduction band ($O_{2p} \rightarrow Zn_{3d}$) [41]. A red shift (increasing of wavelength) in the absorbance of ZnO/CuO composite was

observed in the absorbance spectra which may be due to the adding of Cu^{2+} inside the band gap and spreads the absorption edge from UV to visible region during formation of ZnO/CuO composite. Due to the formation of this novel energy level below conduction band of ZnO, the required energy for the transition from valence band to conduction band is lowered than that of pure ZnO [42].

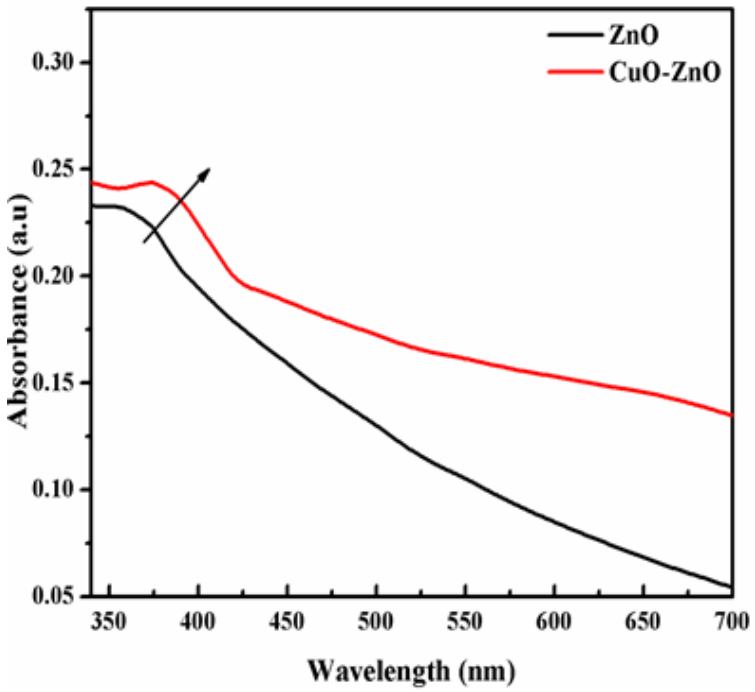

Figure 4.5: UV-Vis spectra of ZnO nanoparticles and ZnO/CuO nanocomposites prepared by the simple chemical method and calcined at 400˚C.

The presence of a long tail in the UV-vis absorption spectra may have happened because of scattering from the surface of the NPs as well as composite materials. The Tauc plot method is used to calculate the direct bandgap energy of photocatalysts by plotting $(\alpha h\nu)^2$ versus photon energy ($h\nu$) (eV) and results were presented in Figure 4.6. The optical direct band gap of bare ZnO is 3.31 eV, and the direct optical band gap for ZnO/CuO composite is changed from 3.31 to 3.0 eV, which is in close agreement with its visible light absorption capability.

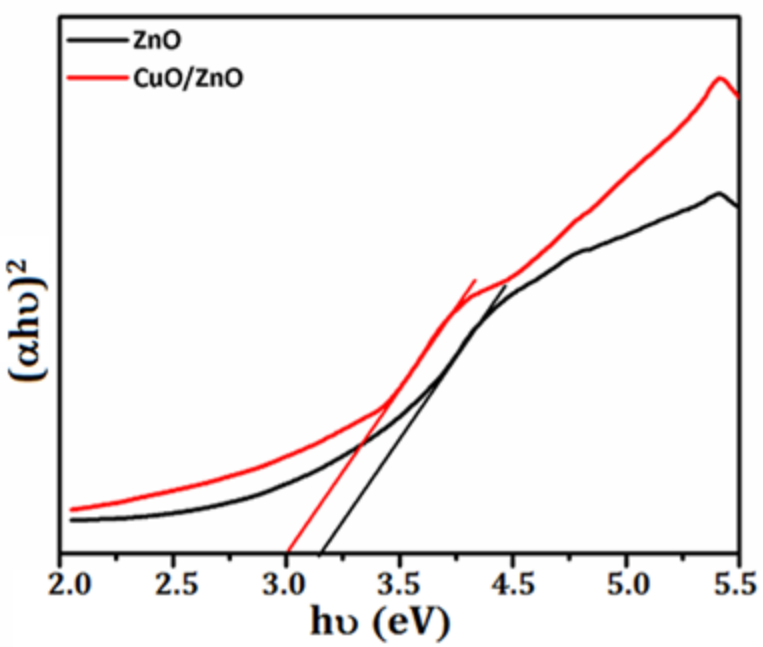

Figure 4.6: Tauc plot for ZnO NPs and ZnO/CuO composite.

4.4.6. Photocatalytic activity of ZnO and ZnO/CuO nanocomposites:

The photocatalytic behaviour of these synthesized materials have been assessed by the modification in the absorbance of CR by the illumination of visible light irradiation for various time intervals is represented in the Figure. 4.7. The extreme photocatalytic activity is attained for ZnO/CuO composite material compared to bare ZnO NPs due to the huge surface area as shown in table 4.1. From the previous research, it is better to understand that the redox reaction primarily takes place during the photocatalytic reactions, on the surface of the photocatalysts, so the surface properties principally affect the performance of photocatalysts [33]. There is some researchers group have used ZnO/CuO for the catalytic photodecomposition of different types of dyes (RhB, Acid red88, Cr(VI), Acid Orange 7 and Methyl Orange) in the recent past under UV and visible light irradiation [43]. Normally, the composite materials disappear improved photocatalytic application than the single-phase ZnO. Afterward, the radiation of the visible light at 50 min, the photocatalytic discoloration of CR over the single phase ZnO is very low as 25% and the ZnO/CuO composites

materials disappear relatively high photocatalytic performance with a degradation ratio of 91 %. It is proof that the degradation efficiency of the composites materials for CR decompositions are as high as 91.0%.

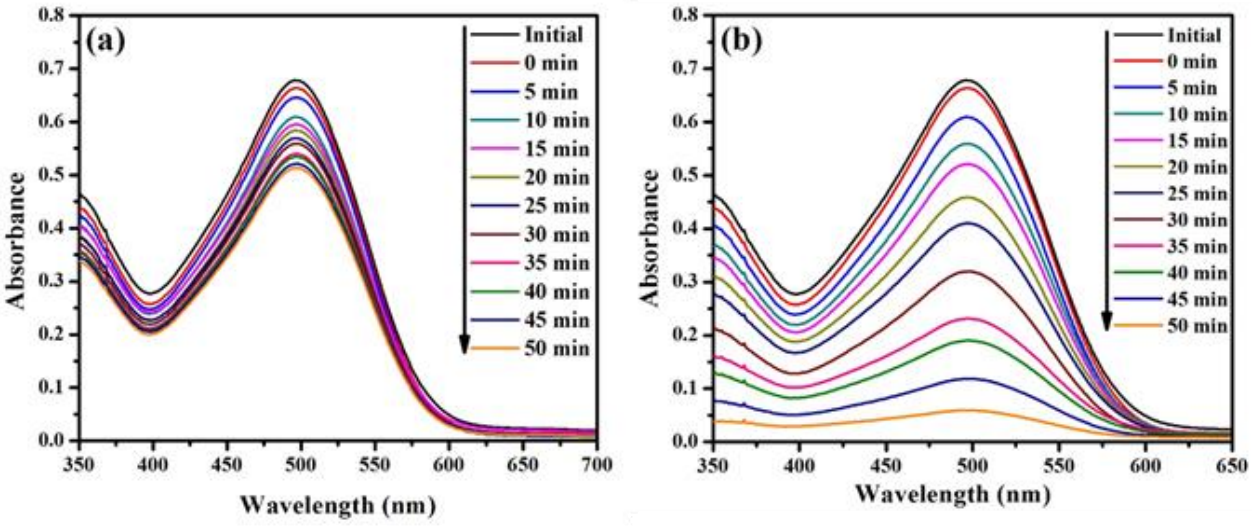

Figure 4.7: UV-vis absorption spectra of CR dye by photocatalysis (a) ZnO NPs and (b) ZnO/CuO nanocomposites for different irradiation times under visible light irradiation.

The mechanism of composite photocatalyst ZnO/CuO is mainly elaborated by the given below relation based on previous reports.

$$ZnO\ (e^{-} + h^{+})/CuO\ (e^{-} + h^{+}) \rightarrow ZnO\ (e^{-} + e^{-})/CuO\ (h^{+} + h^{+}) \quad (4.12)$$

$$h^{+} + OH^{-} \rightarrow OH^{\bullet} \quad (4.13)$$

$$e^{-} + O_2{}^{-} \rightarrow \bullet O_2^{-} \quad (4.14)$$

$$H_2O + \bullet O_2^{-} \rightarrow OOH^{\bullet} + OH^{-} \quad (4.15)$$

$$2OOH^{\bullet} \rightarrow O_2 + H_2O_2 \quad (4.16)$$

$$H_2O_2 + \bullet O_2^{-} \rightarrow OH^{\bullet} + OH^{-} + O_2 \quad (4.17)$$

$$OH^{\bullet} + \bullet O_2 + h^{+}_{VB} + \text{pollutants} \rightarrow \text{degrade pollutant} \quad (4.18)$$

$$OH^{\bullet} + \bullet O_2 + h^{+}_{VB} + \text{degrade pollutant} \rightarrow CO_2 + H_2O \quad (4.19)$$

To explain the mechanism of photocatalytic phenomena on the surface of the synthesized nanocomposites of CuO-ZnO p-n heterojunction, we take into

explanation the band gap energy diagram of ZnO as well as CuO. The explanation of phenomena of photodegradation on the surface is explained qualitatively in scheme 4.1.

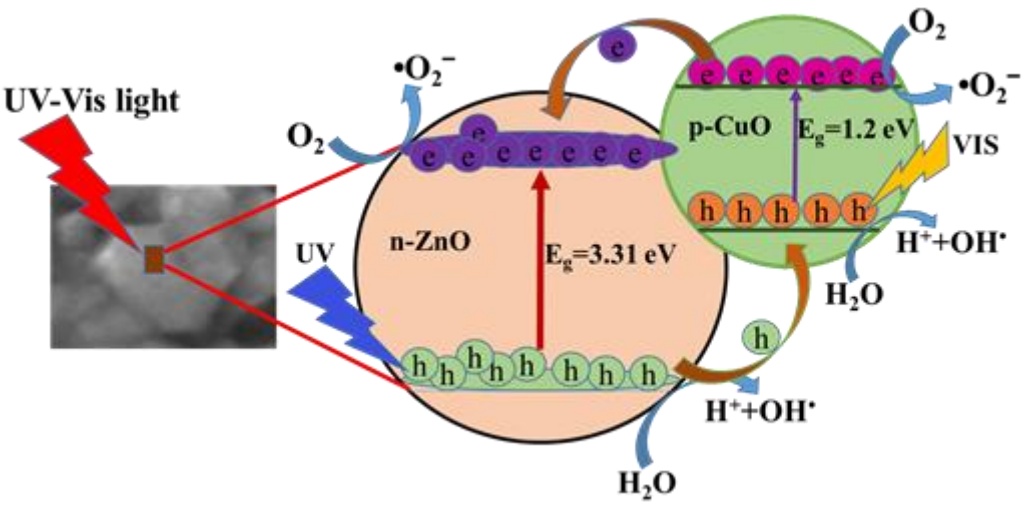

Scheme 4.1: Schematic presentation of band diagram, transfer of electron/hole and associated redox reaction on the surface of ZnO/CuO nanocomposite in presence of aqueous dye solutions.

On exposing the UV-visible light on the ZnO/CuO composite, the UV region light generates electron-hole pairs at ZnO and visible region of light at CuO. Here, CuO is a part of the composite materials absorbs visible part of the light and leads to maximum carrier formation in CuO. The fundamental character of CuO is in the construction of a p-n junction with ZnO, which employs contraction of band and hinders the recombination of charge carrier, as well as, the creation of defect levels in ZnO during the addition of Cu^{2+} ion in the solution of zinc sulphate which trap the photogenerated electrons and holes to supports the catalytic mechanism [44, 45]. It is commonly acknowledged that the presence of defects on the surface in ZnO is profitable to increase the photocatalytic performance. Many previous researchers reported that [46], the presence of these second band gap defect levels along to the decreased energy compare to the concrete band gap can support for fascinating light

in the visible region and construct ZnO a fractionally visible or near UV active material. There are no changes in the band gap energy on the creation of impurity level when the concentration of oxygen vacancy is low. However, the concentration of oxygen vacancies increases, the presence of impurity levels leading to more delocalized and overlap with the valence band edge, resulting band gap decreases by increasing the valance band position, and forming ZnO material as a visible active material [47]. The photocatalytic performance of defects on the surface of ZnO can further be described by Zheng et al. in his proposed model [44]. According to them, in the presence of a convenient surface defect at the surface of materials, the electrons and holes generated by the irradiation of light can get trapped in these surface defect, inhibit the recombination process and support the catalysis related redox reaction. Fundamentally two types of defect energy levels, V_o'' and O_i''. In this V_o'' is generally called as electron acceptors and traps the photogenerated electrons provisionally, and O_i'' is known for the hole acceptor. By the separation of photogenerated electrons and holes, the defect levels V_o'' and O_i'' of ZnO inhibits their recombination which increases their reductive (by electrons) and oxidative (by holes) degradation properties. All the degradation processes might happen on the surface of V_o'' and O_i'' defects and the presence of oxygen vacancies in ZnO can also behave as active sites for such photocatalytic processes. On merging a lower band gap semiconductor CuO with huge band gap ZnO junction is obtained and narrow in the band gap occurs. Hence, the electrons produced from the conduction band (CB) of CuO are transferred to the CB of ZnO and the holes created in the valance band (VB) of ZnO by UV/Vis absorption, are pushed to the VB of CuO by crossing the depletion region. Such type of relocation of electrons and holes along with their likelihood of the respective defect levels decrease the chance of electron-hole pair recombination. This makes electron

rich ZnO and holes rich CuO. The electrons and holes thus produced, react with oxygen and water present in the dye solution forming hydroxide radicals (•OH) and superoxide anion radical ($•O^{2-}$) which behave as the oxidizing and reducing species, respectively, in photocatalysis of the organic contaminants. The series of reactions involved in the mineralization and loss of aromatization process via ring cleavage by the redox process can be represented in the following equation (12-19).

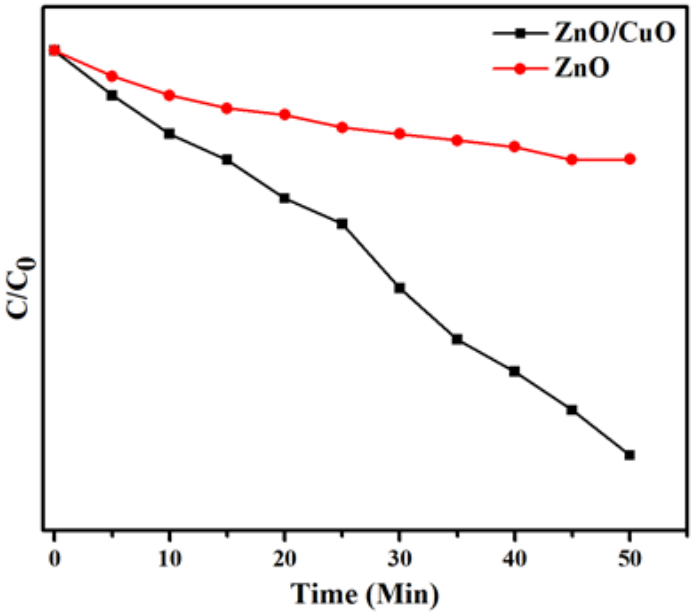

Figure 4.8: Decomposition rates of the CR solution with pure ZnO NPs and ZnO/CuO composites materials.

The kinetic study of the synthesized catalyst for the photodegradation of CR was measured by Langmuir-Hinshelwood equation:

$$\ln (C/C_o) = -kt$$

Where C_o is the initial concentration of CR dye before irradiation of light (mg L^{-1}) and C is the concentration of dye after irradiation (mg L^{-1}) at a time t (min^{-1}) [48]. The rate constant k (min^{-1}) of the photo-degradation of dye could be achieved to the slope of the graph by obtaining a graph between ln (C/C_o) and time t (Figure 4.8 & 4.9). This linear graph indicates that the degradation kinetics follows the first order kinetics. From the above graph, the rate constant values for ZnO and ZnO/CuO

catalysts have been determined as, 0.0054 and 0.045 min^{-1} respectively. The results showed that ZnO/CuO is an attractive photocatalyst and the trend of photocatalytic activity of these materials follows ZnO/CuO > ZnO for the degradation of dye CR.

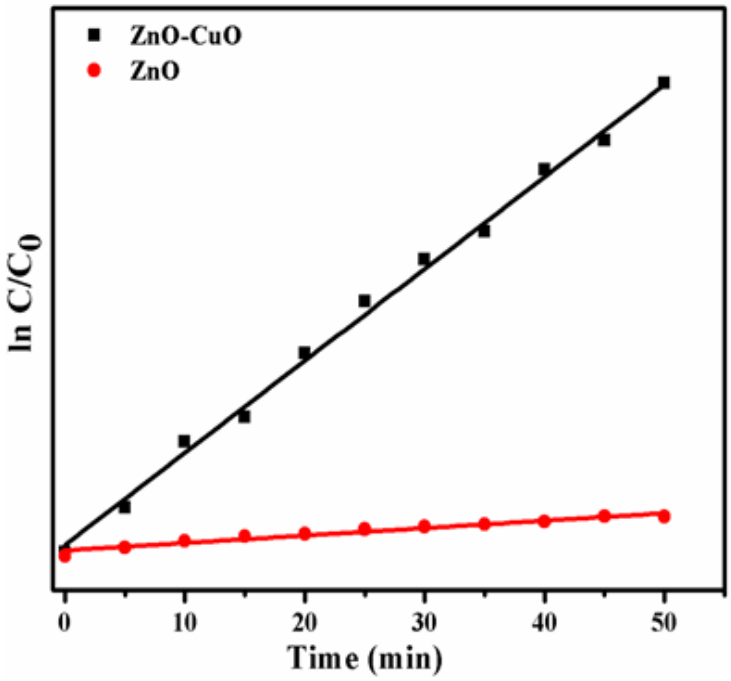

Figure 4.9: Fist order kinetic plot of logarithm of C\C_o vs different time (min) under visible light irradiation

4.5. Conclusion:

In the current investigation, we have synthesized ZnO NPs and ZnO/CuO nanocomposites by simple chemical co-precipitation method and calcination at 400 ˚C for 4hrs. The prepared material characterized by using X-ray diffraction, SEM, HRTEM, BET, and UV-Visible analysis. The size of the ZnO NPs and ZnO/CuO composite catalyst particles is uniform in size and particle sizes varied from 46.9 to 10.3 nm by X-ray diffraction analysis. Hexagonal structure of ZnO and grain like ZnO/CuO composite of photocatalyst was identified by SEM analysis. HRTEM images confirm the hexagonal structure of ZnO is actually the aggregation of knife like the structure of ZnO NPs and grain like ZnO/CuO composite material is obtained by the agglomeration of spherical structures. BET analysis shows that the prepared

material is mesoporous material and also tells about the maximum surface area of ZnO/CuO composite. The coupled semiconductor composite material ZnO/CuO shown more photocatalytic degradation of Congo red in the visible light irradiation due to the maximum surface area and red shifting the wavelength range dominate to electron-hole pair separation under visible light irradiation.

4.6. References:

[1] X. Chen, Z. Wu, D. Liu, Z. Gao, Preparation of ZnO Photocatalyst for the Efficient and Rapid Photocatalytic Degradation of Azo Dyes, Nanoscale Research Letters, 12 (2017) 143-153.

[2] N. Mathur, P. Bhatnagar, P. Sharma, Review of the Mutagenicity of Textile Dye ProductsUnivers. Universal Journal of Environmental Research and Technology, 2 (2012) 1-18.

[3] N. Daneshvar, A. Khataee, A.A. Ghadim, M. Rasoulifard, Decolorization of CI Acid Yellow 23 solution by electrocoagulation process: Investigation of operational parameters and evaluation of specific electrical energy consumption (SEEC), Journal of Hazardous Materials, 148 (2007) 566-572.

[4] M. Amiri, A. Nezamzadeh-Ejhieh, Improvement of the photocatalytic activity of cupric oxide by deposition onto a natural clinoptilolite substrate, Materials Science in Semiconductor Processing, 31 (2015) 501-508.

[5] G. Hitkari, S. Singh, G. Pandey, Synthesis, Characterization and Visible Light Degradation of Organic dye by Chemically Synthesized ZnO/γ-Fe_2O_3 Nanocomposites, Synthesis, 4 (2017) 3960-3965.

[6] G. Panthi, M. Park, H.-Y. Kim, S.-Y. Lee, S.-J. Park, Electrospun ZnO hybrid nanofibers for photodegradation of wastewater containing organic dyes: a review, Journal of Industrial and Engineering Chemistry, 21 (2015) 26-35.

[7] C. Shifu, Z. Wei, Z. Sujuan, L. Wei, Preparation, characterization and photocatalytic activity of N-containing ZnO powder, Chemical Engineering Journal, 148 (2009) 263-269.

[8] K. Kanade, B. Kale, J.-O. Baeg, S.M. Lee, C.W. Lee, S.-J. Moon, H. Chang, Self-assembled aligned Cu doped ZnO nanoparticles for photocatalytic hydrogen

production under visible light irradiation, Materials Chemistry and Physics, 102 (2007) 98-104.

[9] R. Ullah, J. Dutta, Photocatalytic degradation of organic dyes with manganese-doped ZnO nanoparticles, Journal of Hazardous Materials, 156 (2008) 194-200.

[10] H. Zeng, P. Liu, W. Cai, S. Yang, X. Xu, Controllable Pt/ZnO porous nanocages with improved photocatalytic activity, The Journal of Physical Chemistry C, 112 (2008) 19620-19624.

[11] L. Zhang, H. Cheng, R. Zong, Y. Zhu, Photocorrosion suppression of ZnO nanoparticles via hybridization with graphite-like carbon and enhanced photocatalytic activity, The Journal of Physical Chemistry C, 113 (2009) 2368-2374.

[12] S. Thangavel, K. Krishnamoorthy, V. Krishnaswamy, N. Raju, S.J. Kim, G. Venugopal, Graphdiyne-ZnO nanohybrids as an advanced photocatalytic material, The Journal of Physical Chemistry C, 119 (2015) 22057-22065.

[13] G. Marci, V. Augugliaro, M.J. López-Muñoz, C. Martín, L. Palmisano, V. Rives, M. Schiavello, R.J. Tilley, A.M. Venezia, Preparation characterization and photocatalytic activity of polycrystalline ZnO/TiO_2 systems. 2. Surface, bulk characterization, and 4-nitrophenol photodegradation in liquid-solid regime, The Journal of Physical Chemistry C, 105 (2001) 1033-1040.

[14] W. Cun, Z. Jincai, W. Xinming, M. Bixian, S. Guoying, P. Ping'an, F. Jiamo, Preparation, characterization and photocatalytic activity of nano-sized ZnO/SnO_2 coupled photocatalysts, Applied Catalysis B: Environmental, 39 (2002) 269-279.

[15] L. Zheng, Y. Zheng, C. Chen, Y. Zhan, X. Lin, Q. Zheng, K. Wei, J. Zhu, Network structured SnO_2/ZnO heterojunction nanocatalyst with high photocatalytic activity, Inorganic Chemistry, 48 (2009) 1819-1825.

[16] S. Steinhauer, E. Brunet, T. Maier, G. Mutinati, A. Köck, O. Freudenberg, C. Gspan, W. Grogger, A. Neuhold, R. Resel, Gas sensing properties of novel CuO nanowire devices, Sensors and Actuators B: Chemical, 187 (2013) 50-57.

[17] Y.-M. Juan, H.-T. Hsueh, T.-C. Cheng, C.-W. Wu, S.-J. Chang, Electron-field-emission enhancement of CuO nanowires by UV illumination, ECS Solid State Letters, 3 (2014) 30-32.

[18] S.E. Moosavifard, J. Shamsi, S. Fani, S. Kadkhodazade, Facile synthesis of hierarchical CuO nanorod arrays on carbon nanofibers for high-performance supercapacitors, Ceramics International, 40 (2014) 15973-15979.

[19] C. Wang, J. Xu, R. Ma, M.-F. Yuen, Facile synthesis of CuO nanoneedle electrodes for high-performance lithium-ion batteries, Materials Chemistry and Physics, 148 (2014) 411-415.

[20] T. Jiang, Y. Wang, D. Meng, X. Wu, J. Wang, J. Chen, Controllable fabrication of CuO nanostructure by hydrothermal method and its properties, Applied Surface Science, 311 (2014) 602-608.

[21] A.H. Alami, A. Allagui, H. Alawadhi, Microstructural and optical studies of CuO thin films prepared by chemical ageing of copper substrate in alkaline ammonia solution, Journal of Alloys and Compounds, 617 (2014) 542-546.

[22] B. Shaabani, E. Alizadeh-Gheshlaghi, Y. Azizian-Kalandaragh, A. Khodayari, Preparation of CuO nanopowders and their catalytic activity in photodegradation of Rhodamine-B, Advanced Powder Technology, 25 (2014) 1043-1052.

[23] H. Shi, Y. Zhao, N. Li, K. Wang, X. Hua, M. Chen, F. Teng, Synthesis and photocatalytic activity of novel CuO cauliflowers grown from $Cu(OH)_2$, Catalysis Communications, 47 (2014) 7-12.

[24] M. Rabbani, R. Rahimi, M. Bozorgpour, J. Shokraiyan, S.S. Moghaddam, Photocatalytic application of hollow CuO microspheres with hierarchical dandelion-like structures synthesized by a simple template free approach, Materials Letters, 119 (2014) 39-42.

[25] A. Sadollahkhani, Z.H. Ibupoto, S. Elhag, O. Nur, M. Willander, Photocatalytic properties of different morphologies of CuO for the degradation of Congo red organic dye, Ceramics International, 40 (2014) 11311-11317.

[26] M. Umadevi, A.J. Christy, Synthesis, characterization and photocatalytic activity of CuO nanoflowers, Spectrochimica Acta Part A: Molecular and Biomolecular Spectroscopy, 109 (2013) 133-137.

[27] M.A. Prathap, B. Kaur, R. Srivastava, Hydrothermal synthesis of CuO micro-/nanostructures and their applications in the oxidative degradation of methylene blue and non-enzymatic sensing of glucose/H_2O_2, Journal of Colloid and Interface Science, 370 (2012) 144-154.

[28] S.S. Lee, H. Bai, Z. Liu, D.D. Sun, Novel-structured electrospun TiO_2/CuO composite nanofibers for high efficient photocatalytic cogeneration of clean water and energy from dye wastewater, Water Research, 47 (2013) 4059-4073.

[29] D. Zhang, Synthesis and characterization of ZnO-doped cupric oxides and evaluation of their photocatalytic performance under visible light, Transition Metal Chemistry, 35 (2010) 689-694.

[30] J. Li, M. Cui, Z. Guo, Z. Liu, Z. Zhu, Synthesis of dumbbell-like CuO-$BiVO_4$ heterogeneous nanostructures with enhanced visible-light photocatalytic activity, Materials Letters, 130 (2014) 36-39.

[31] G.-J. Lee, A. Manivel, V. Batalova, G. Mokrousov, S. Masten, J. Wu, Mesoporous microsphere of ZnS photocatalysts loaded with CuO or Mn_3O_4 for the visible-light-assisted photocatalytic degradation of orange II dye, Industrial & Engineering Chemistry Research, 52 (2013) 11904-11912.

[32] T. Chang, Z. Li, G. Yun, Y. Jia, H. Yang, Enhanced photocatalytic activity of ZnO/CuO nanocomposites synthesized by hydrothermal method, Nano-Micro Letters, 5 (2013) 163-168.

[33] R. Saravanan, S. Karthikeyan, V. Gupta, G. Sekaran, V. Narayanan, A. Stephen, Enhanced photocatalytic activity of ZnO/CuO nanocomposite for the degradation of textile dye on visible light illumination, Materials Science and Engineering: C, 33 (2013) 91-98.

[34] A. Othman, M.A. Ali, E. Ibrahim, M. Osman, Influence of Cu doping on structural, morphological, photoluminescence, and electrical properties of ZnO nanostructures synthesized by ice-bath assisted sonochemical method, Journal of Alloys and Compounds, 683 (2016) 399-411.

[35] G. Hitkari, S. Singh, G. Pandey, Structural, optical and photocatalytic study of ZnO and ZnO-ZnS synthesized by chemical method, Nano-Structures & Nano-Objects, 12 (2017) 1-9.

[36] A.A. Akl, A. Hassanien, Microstructure and crystal imperfections of nanosized CdS_xSe_{1-x} thermally evaporated thin films, Superlattices and Microstructures, 85 (2015) 67-81.

[37] R.D. Shannon, Revised effective ionic radii and systematic studies of interatomic distances in halides and chalcogenides, Acta crystallographica section A: crystal physics, diffraction, theoretical and general crystallography, 32 (1976) 751-767.

[38] R.K. Sonker, S. Sabhajeet, B. Yadav, TiO_2-PANI nanocomposite thin film prepared by spin coating technique working as room temperature CO_2 gas sensing, Journal of Materials Science: Materials in Electronics, 27 (2016) 11726-11732.

[39] K. Vijayalakshmi, K. Karthick, High quality ZnO/CuO nanocomposites synthesized by microwave assisted reaction, Journal of Materials Science: Materials in Electronics, 25 (2014) 832-836.

[40] H.-Y. Zhu, R. Jiang, Y.-Q. Fu, R.-R. Li, J. Yao, S.-T. Jiang, Novel multifunctional $NiFe_2O_4$/ZnO hybrids for dye removal by adsorption, photocatalysis and magnetic separation, Applied Surface Science, 369 (2016) 1-10.

[41] A.K. Zak, M.E. Abrishami, W.A. Majid, R. Yousefi, S. Hosseini, Effects of annealing temperature on some structural and optical properties of ZnO nanoparticles prepared by a modified sol-gel combustion method, Ceramics International, 37 (2011) 393-398.

[42] A.B. Lavand, Y.S. Malghe, Synthesis, characterization and visible light photocatalytic activity of carbon and iron modified ZnO, Journal of King Saud University-Science, (2016) 65-74.

[43] A. Buthiyappan, A. Aziz, A. Raman, W. Daud, W.M. Ashri, Recent advances and prospects of catalytic advanced oxidation process in treating textile effluents, Reviews in Chemical Engineering, 32 (2016) 1-47.

[44] Y. Zheng, C. Chen, Y. Zhan, X. Lin, Q. Zheng, K. Wei, J. Zhu, Y. Zhu, Luminescence and photocatalytic activity of ZnO nanocrystals: correlation between structure and property, Inorganic Chemistry, 46 (2007) 6675-6682.

[45] M.Y. Guo, A.M.C. Ng, F. Liu, A.B. Djurisic, W.K. Chan, H. Su, K.S. Wong, Effect of native defects on photocatalytic properties of ZnO, The Journal of Physical Chemistry C, 115 (2011) 11095-11101.

[46] S. Chabri, A. Dhara, B. Show, D. Adak, A. Sinha, N. Mukherjee, Mesoporous CuO-ZnO p-n heterojunction based nanocomposites with high specific surface area for enhanced photocatalysis and electrochemical sensing, Catalysis Science & Technology, 6 (2016) 3238-3252.

[47] J. Wang, Z. Wang, B. Huang, Y. Ma, Y. Liu, X. Qin, X. Zhang, Y. Dai, Oxygen vacancy induced band-gap narrowing and enhanced visible light photocatalytic activity of ZnO, ACS Applied Materials & Interfaces, 4 (2012) 4024-4030.

[48] J. Varghese, K. Varghese, Graphene/CuS/ZnO hybrid nanocomposites for high performance photocatalytic applications, Materials Chemistry and Physics, 167 (2015) 258-264.

***

Chapter 5
Synthesis, Characterization and Visible Light Degradation of Organic Dye by Chemically Synthesized ZnO/γ-Fe_2O_3 Nanocomposites

Chapter 5
Synthesis, Characterization and Visible Light Degradation of Organic dye by Chemically Synthesized ZnO/γ-Fe_2O_3 Nanocomposites

In the present study ZnO/γ-Fe_2O_3 nanocomposites is prepared by the simple co-precipitation method. The prepared composites materials were characterized by X-ray diffraction (XRD), high resolution scanning electron microscope (HRSEM), energy dispersive X-ray spectroscopy (EDX), Brunauer Emmett Teller analysis (BET), and UV-visible spectroscopy. XRD confirmed the formation of hexagonal wurtzite nature of ZnO and cubic structure of γ-Fe_2O_3 in the composite materials, while SEM images shown spherical and rod like structure. BET analysis confirmed the mesoporous behavior of nanocomposites. UV-Visible spectroscopy have been applied to the measurement of band gap and photo-oxidation behavior of organic dye methyl blue and rhodamine B (Rh B). Experimental data suggested that ZnO/γ-Fe_2O_3 nanoparticles catalyst possessed the highest catalytic activity towards Rh B degradation in aqueous solution as comparison to the methylene blue at the tested concentration level of 1×10^{-5} M.

5.1. Introduction:

Over the last several decades semiconductor materials such as photocatalysis has been intensively explored in the vision of its prospective properties towards the remediation of environmental contaminants and treatment of waste water [1]. Generally, semiconductors materials such as ZnO, TiO_2, SnO_2 etc. are UV light consuming photocatalyst and concerned as remarkable devotion from the scientists [2-4]. Chakrabarti and Hong reported that ZnO is investigated to be a superior photocatalyst than TiO_2 in the photocatalytic degradation of organic contaminants in the presence of UV and visible light irradiations [5, 6]. Zinc oxide (ZnO) is a low cost chemically stable and environmentally nontoxic n-type semiconductor material having a large band gap of 3.37 eV with a large excitation binding energy of 60 meV at room temperature which can be investigated to be a possible pathway in dye-sensitized solar cells and photocatalysis [7] because of its strong metal support interaction (SMSI) properties. The exposer of UV light on ZnO semiconductor material, it has the capability to produced oxidative species like as hydroxyl radicals ($^{\bullet}OH$) and superoxide anions ($O^{2\bullet-}$), which display oxidative properties robust enough to oxidize certain organic contaminants. Consequently, to increase the photocatalytic proficiency and stability, it is of fundamental importance to quash the recombination of electron-hole pairs of ZnO. However, due to the wide band gap of ZnO materials their light absorption only in the UV spectral region of the solar spectrum and limits expenses of solar energy thus limits efficiency in sunlight. However, the improvement of photocatalytic activity of ZnO nanoparticles, under visible light radiation is highly desired. As comparison with a single semiconductor, photocatalysis compelled by composite semiconductors is also extensively studied to improve the photocatalytic activity in the visible region [8]. In the present period of time many researchers are

synthesize numerous type of zinc oxide nanocomposites like as ZnO/metal, ZnO/metal oxide and ZnO/polymer and doped with transition metals and non-metals to reduce the band gap and display visible light photocatalysis, because of the presence of intermediate states in the nanocomposite which engages visible light that stimulates electrons and holes in the photo reaction [9, 10]. Reddy et al. fabricated ZnO:RGO/RuO_2 nanocomposites with outstanding degradation efficacy of methylene blue underneath simulated sunlight [11]. Eskizeybek et al. described photodegradation of organic dye malachite green (MG) and methylene blue in the presence of ordinary sunlight by adopting a polyaniline: ZnO nanocomposite [12]. And Saravanan, et al. described that superior degradation of methyl orange and methylene blue under visible light condition by of polyaniline (PANI)/ZnO nanocomposite system [13].

Hence, the present work is mainly concentrated on the simple fabrication of ZnO/γ-Fe_2O_3 nanocomposites by chemical co-precipitation method and examination its catalytic activities were investigated for the photo-degradation of a model organic dye rhodamine B and methylene blue under visible light irradiations. The synthesized nanocomposites materials were characterized by Powder XRD, UV-vis, HRSEM, BET, and EDAX. The photodegraded samples were analyzed by UV-Visible spectroscopy.

5.2. Experimental Section:

5.2.1. Chemical and materials:

All the required chemical reagent are analytical grade as zinc (II) sulphate heptahydrate ($ZnSO_4.7H_2O$), Iron (II) sulphate heptahydrate ($FeSO_4.7H_2O$), Rhodamine B and methylene blue was purchased from Merck India, sodium hydroxide (NaOH) powder was purchased from MP Biomedical LLC India and used without further purification. Double de-ionized water was used as solvents. All the

glassware's were cleaned and rinsed by concentrated acid. The dried glassware's were used in all the experiments.

5.2.2. Synthesis of zinc oxide- iron oxide ($ZnO/\gamma\text{-}Fe_2O_3$) nanocomposites:

The nanorod and nano-spherical mixed like $ZnO/\gamma\text{-}Fe_2O_3$ was synthesized from its precursor through a simple chemical co-precipitation method. In the typical synthesis process 25 ml of 0.5 mole $ZnSO_4.7H_2O$ and 25 ml of 0.5 mole of $FeSO_4.7H_2O$ solution were mixed and stirred on the magnetic stirrer for 30 min, clear solution obtained. The obtained clear solutions were placed in an ultrasonic cleaner operating at 57 kHz for 2 h. After the completion of sonication the mixed solutions were continuously again stirred for 30 min then a suitable amount of NaOH solution in an obtained aqueous solution was added to the mixed solutions until a pH of 12 was reached. The resulting reaction mixture was stirred for 30 min, and then it was allowed to aging at room temperature for 18 h. Next, the solution was centrifuged and washed several times with ethanol and distilled water and finally with acetone to remove unwanted impurities. The final product was dried in a muffle oven at 200 ^oC for 1 h yielding the brown $ZnO/\gamma\text{-}Fe_2O_3$ nanocomposites powder.

5.2.3. Characterization:

The vastly visible light dynamic nanocatalyst was synthesized by a simple chemical co-precipitation method and characterized by powder X-ray diffraction (XRD), Ultraviolet-visible spectroscopy (UV-Vis), High Resolution Scanning Electron Microscope (HR-SEM), Energy Dispersive X-ray Spectroscopy (EDAX), and Brunauer-Emmett-Teller (BET) surface area investigation was accompanied by using the nitrogen absorption-desorption measurement at 77 K (BELSORD mini, Japan). The photocatalytic ability of the prepared materials was examined using Rhodamine B and methylene blue organic dye pollutants. The measurement of the

photo-degradation ability of the catalyst was estimated by using UV-Vis spectroscopy (Carry 100).

5.2.4. Study of photocatalytic activity:

The application of the synthesized materials was concluded by photo-degradation of Rhodamine B and methylene blue in presence of visible light radiation in a photocatalytic chamber. 20 mg quantity of prepared ZnO/γ-Fe_2O_3 catalyst was initially dissolve in 100 ml of 1×10^{-5} M, Rhodamine B and methylene blue standard solution and mixture of the solution was stirred for 30 min in the dark condition in order to attaining the adsorption-desorption equilibrium. Finally the solution was irradiated with visible light from the fluorescent lamp (9W) in a photocatalytic chamber. The solution was agitated, during irradiation by using a magnetic stirrer and air was supply into the reaction mixture to implement a constant supply of oxygen. After the preferred time interval, an aliquot amount of the solution was withdrawn, centrifuged and take its absorbance on UV-visible spectrophotometer to measure the percentage degradation. The degradation efficiency of photocatalytic was measured by applied the following equation:

$$(\%)\,\text{degradation} = \left\{\left(\frac{A_0 - A_t}{A_0}\right)\times 100\right\}$$

Where A_0 represents the initial absorbance of the dye solution and A_t; the absorbance after irradiation at a particular time t.

5.3. Result and discussion:

5.3.1. XRD analysis:

XRD patterns of the ZnO/γ-Fe_2O_3 nanocomposites materials are shown in Figure 5.1. A series of characteristic peaks 31.76, 34.40, 36.24, 47.61, 56.61, 62.89, 66.41, 67.93 and 69.72, which are corresponds to the Miller indices (100), (002), (101), (102), (110), (103), (200), (112) and (201) were observed and they were in accordance with wurtzite phase (JCPDS no. 76-0704) of ZnO, presence of other peaks at 18.31, 30.10, and 43.12 correspond to the Miller indices (111), (220) and (400) planes of γ-Fe_2O_3 phase with cubic phase (JCPDS no. 85-1436) indicate that the above material is ZnO/γ-Fe_2O_3 composite. The average particle sizes (94 nm) of ZnO/γ-Fe_2O_3 were calculated using Scherrer's equation (5.1):

$$D = \frac{0.9\lambda}{\beta \cos\theta} \tag{5.1}$$

Where λ denotes the wavelength of the radiation equal to 0.154 nm, β is the full width at half maximum and θ is the half diffraction angle.

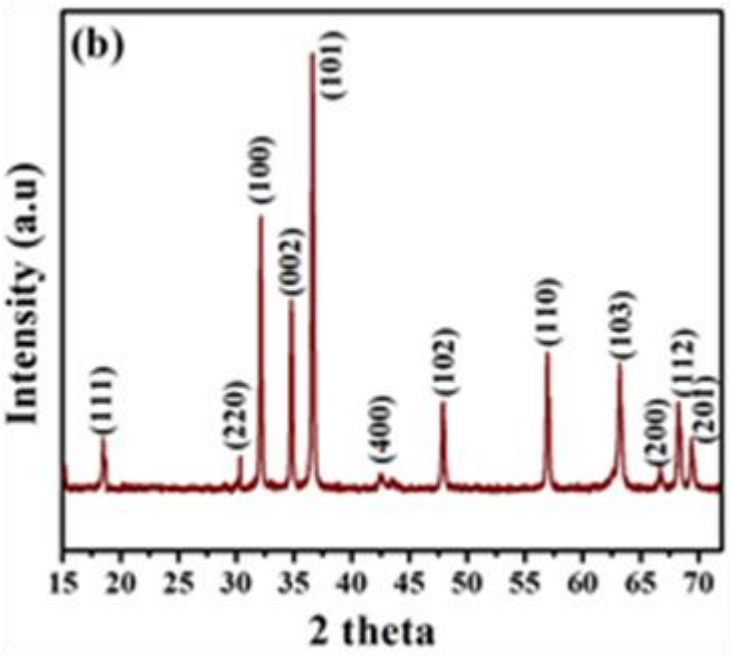

Figure 5.1: XRD pattern of ZnO/γ-Fe_2O_3 composite

5.3.2. SEM image analysis:

HR-SEM images of ZnO/γ-Fe_2O_3 nanocomposites are shown in Figure 5.2(a). HR-SEM images which shows the morphology of the prepared nanocomposites material. It display that the more nanocomposites material carry a uniform spherical and some rod-like structure in the morphology and the size of the particles are in nano ranged. A closer examination reveals that these nano-spherical are actually composed of small ZnO nanoparticles leading to a relatively rough surface.

A comprehensive chemical composition analysis of the nanomaterial was carried out with energy dispersive spectroscopy (EDS) and elemental mapping Figure 5.2 (b-e) shows the presence of 54.88 wt% of Fe, 31.58 wt% of Zn and 5 wt% of O in the EDS spectrum. The presence of Fe, Zn, and O specified the production of the ZnO/γ-Fe_2O_3 nanocomposite. The elemental mapping (area) achieved from EDS analyses display that Fe, Zn, and O are homogeneously dispersed in the ZnO/γ-Fe_2O_3 nanocomposite. The point EDX investigation also specifies the presence of Fe, Zn, and O in the materials, which again validates the homogeneous composition of the nanocomposite.

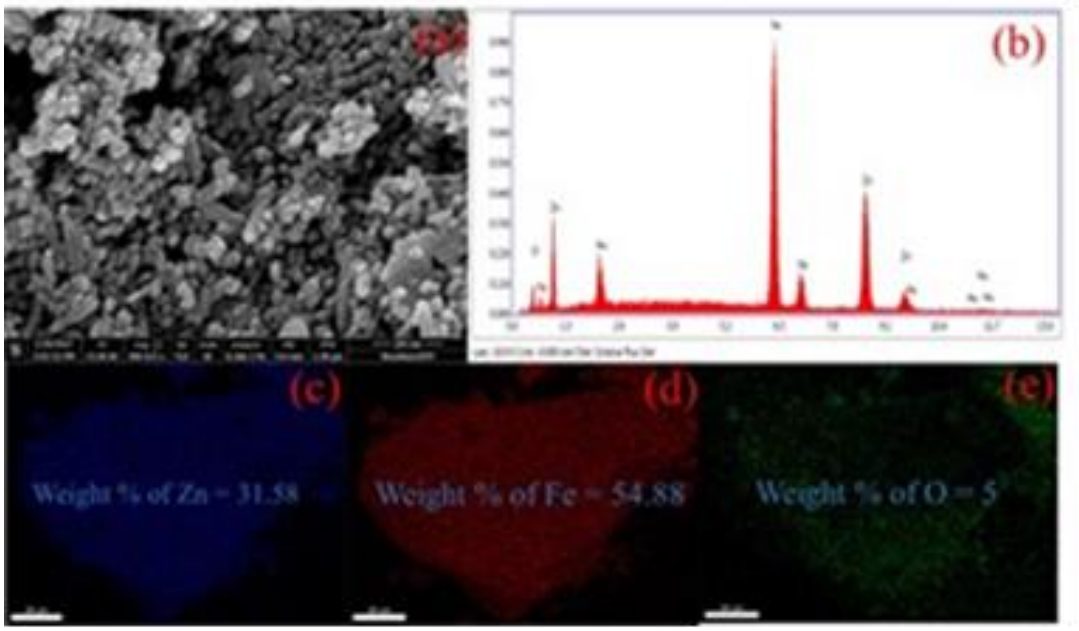

Figure 5.2: (a) HRSEM image (b) EDX spectra (c-e) X-ray elemental mapping of ZnO/γ-Fe_2O_3 composite.

5.3.3. BET analysis:

The surface properties of ZnO/γ-Fe_2O_3 catalyst were investigated by using BET surface area analyzer to calculate the surface area of the samples. Figure 5.3 shows the isotherms of N2 adsorption-desorption have been used to determine surface area of ZnO/γ-Fe_2O_3 material at liquid nitrogen temperature and the Barret-Joyner-Halenda (BJH) method was used to evaluate the pore size distribution. The pore size distribution curve indicates that pores are mainly two type and their size lies in mesoporous range. Hysteresis is observed as a result of pore filling and emptying processes occurring separately, as shown in Figure 5.3. N2 adsorption-desorption isotherm display a Type IV hysteresis [14], characteristic of mesoporous materials with a H2 type hysteresis loop [15] typical for non-uniform shape and size of pore channels being fully consistent with the HR-SEM data. From BET evaluation of ZnO/γ-Fe_2O_3 nanocomposites surface area is calculated 50.54 m^2 g^{-1}.

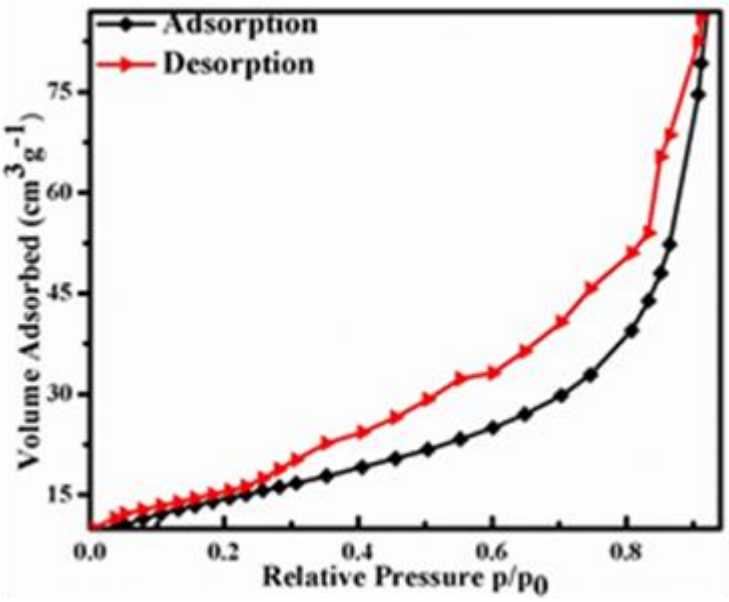

Figure 5.3: Adsorption-Desorption plot of ZnO/γ-Fe_2O_3 composite

5.3.4. Optical Properties:

A little amount of synthesized sample (in milligrams) is dissolved in deionized water (3 ml) and sonicate until a clear solution is obtained. The UV-Vis spectra is

taken for the examination of the optical properties of ZnO/γ-Fe_2O_3 nanocomposites materials. Figure 5.4 demonstrate the UV-Vis diffuse reflectance spectra of the ZnO/γ-Fe_2O_3 composite. On the formation of ZnO/γ-Fe_2O_3 composite the wavelength absorption edge from 373 nm to 434 nm. Measurement of UV-Vis spectroscopy were applied for the calculation of direct band gaps of ZnO/γ-Fe_2O_3 with the following equation [16]:

$$Eg = 1239.8/\lambda$$

Where Eg is the band gap (eV) and λ is the wavelength (nm) of the absorption edges in the spectrum. Band gap energy of ZnO/γ-Fe_2O_3 nanocomposites is calculated to be 2.85 eV.

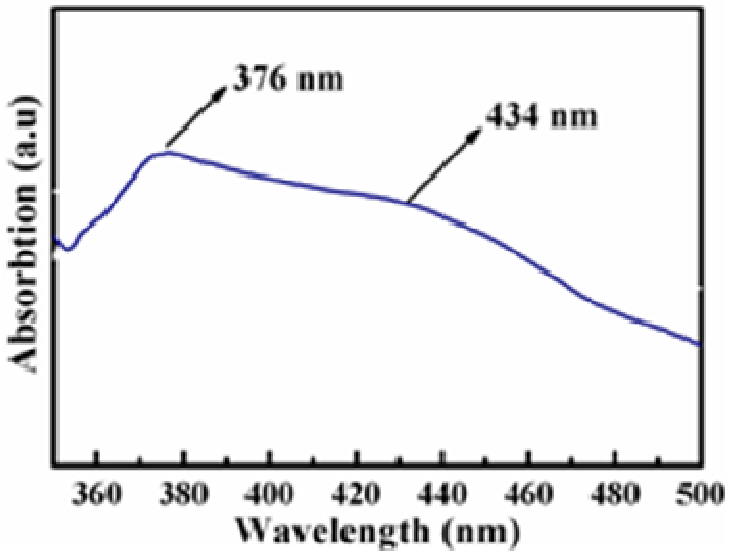

Figure 5.4: UV-Visible Spectrum of ZnO/γ-Fe_2O_3 composite.

5.3.5. Photocatalytic Activity:

The photodegradation application of organic pollutants by the prepared ZnO/γ-Fe_2O_3 photocatalysts was considered by measuring photodegradation performance with their corresponding time dependent of methyl blue (MB) and rhodamine B (Rh B) in the presence of visible sun light shown in Figure 5.5. The degradation efficiency and rate of catalysis are surface area dependent phenomena

since electron hole pair transfer occurs at the surface [17]. BET surface area is used to estimate the surface properties as it holds a great significance in case of adsorption, heterogeneous catalysis reactions on material surfaces. The dye degradation is estimated in terms of the change in absorption at λ_{max} = 668 nm for methylene blue and λ_{max} = 544 nm for rhodamine B dye respectively. The degradation efficiency is calculated to be 30 % for the methylene blue and 50 % for rhodamine B.

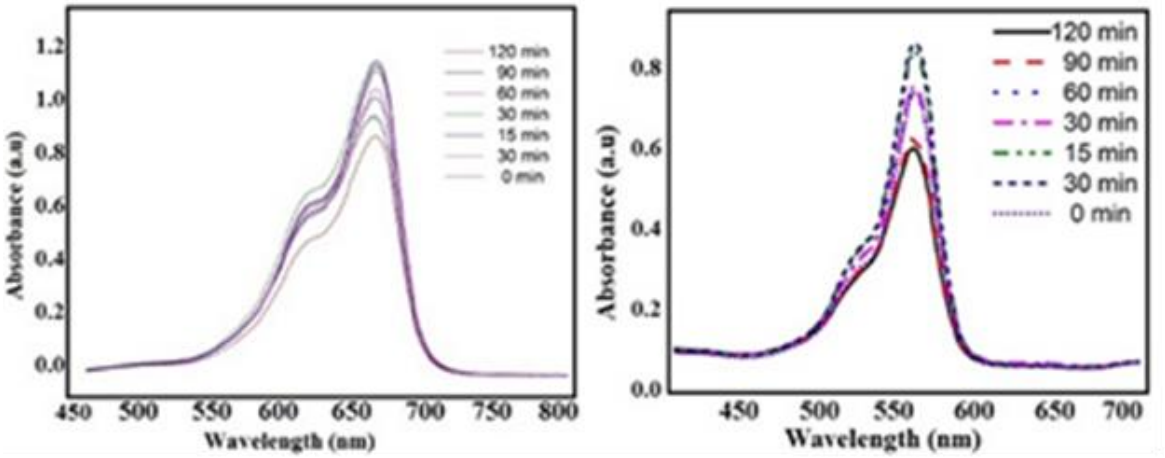

Figure 5.5: Photocatalytic degradation of (a) methylene blue and (b) rhodamine B organic dye.

5.4. Conclusion:

In the current experiment, we have fabricated ZnO/γ-Fe_2O_3 composite by chemical method. The prepared material was characterized by using X-ray diffraction, HRSEM, BET, and UV-Visible analysis. The size of the ZnO/ γ-Fe_2O_3 materials is uniform in size and particle sizes calculated to be 94 nm by X-ray diffraction analysis. Spherical and rod-like structure of ZnO/ γ-Fe_2O_3 composite was recognized by SEM analysis. The coupled semiconductor composite material ZnO/γ-Fe_2O_3 shown more photocatalytic degradation of rhodamine B as comparison to the methylene blue in the visible sun light irradiation.

5.5. References:

[1] G. Liu, Y. Zhao, C. Sun, F. Li, G.Q. Lu, H.M. Cheng, Synergistic effects of B/N doping on the visible-light photocatalytic activity of mesoporous TiO_2, Angewandte Chemie International Edition, 47 (2008) 4516-4520.

[2] X. Jiang, T. Wang, Influence of preparation method on morphology and photocatalysis activity of nanostructured TiO_2, Environmental science & technology, 41 (2007) 4441-4446.

[3] J. Becker, K.R. Raghupathi, J. St. Pierre, D. Zhao, R.T. Koodali, Tuning of the crystallite and particle sizes of ZnO nanocrystalline materials in solvothermal synthesis and their photocatalytic activity for dye degradation, The Journal of Physical Chemistry C, 115 (2011) 13844-13850.

[4] A.K. Sinha, M. Pradhan, S. Sarkar, T. Pal, Large-scale solid-state synthesis of Sn-SnO_2 nanoparticles from layered SnO by sunlight: a material for dye degradation in water by photocatalytic reaction, Environmental science & technology, 47 (2013) 2339-2345.

[5] S. Chakrabarti, B.K. Dutta, Photocatalytic degradation of model textile dyes in wastewater using ZnO as semiconductor catalyst, Journal of hazardous materials, 112 (2004) 269-278.

[6] R. Hong, T. Pan, J. Qian, H. Li, Synthesis and surface modification of ZnO nanoparticles, Chemical Engineering Journal, 119 (2006) 71-81.

[7] D. Chu, Y. Masuda, T. Ohji, K. Kato, Formation and photocatalytic application of ZnO nanotubes using aqueous solution, Langmuir, 26 (2009) 2811-2815.

[8] J. Choi, H. Park, M.R. Hoffmann, Effects of single metal-ion doping on the visible-light photoreactivity of TiO_2, The Journal of Physical Chemistry C, 114 (2009) 783-792.

[9] Q. Yu, J. Li, H. Li, Q. Wang, S. Cheng, L. Li, Fabrication, structure, and photocatalytic activities of boron-doped ZnO nanorods hydrothermally grown on CVD diamond film, Chemical Physics Letters, 539 (2012) 74-78.

[10] R. Saravanan, M.M. Khan, V.K. Gupta, E. Mosquera, F. Gracia, V. Narayanan, A. Stephen, ZnO/Ag/CdO nanocomposite for visible light-induced photocatalytic degradation of industrial textile effluents, Journal of colloid and interface science, 452 (2015) 126-133.

[11] D.A. Reddy, R. Ma, T.K. Kim, Efficient photocatalytic degradation of methylene blue by heterostructured ZnO-RGO/RuO_2 nanocomposite under the simulated sunlight irradiation, Ceramics International, 41 (2015) 6999-7009.

[12] V. Eskizeybek, F. Sarı, H. Gülce, A. Gülce, A. Avcı, Preparation of the new polyaniline/ZnO nanocomposite and its photocatalytic activity for degradation of methylene blue and malachite green dyes under UV and natural sun lights irradiations, Applied Catalysis B: Environmental, 119 (2012) 197-206.

[13] R. Saravanan, E. Sacari, F. Gracia, M.M. Khan, E. Mosquera, V.K. Gupta, Conducting PANI stimulated ZnO system for visible light photocatalytic degradation of coloured dyes, Journal of Molecular Liquids, 221 (2016) 1029-1033.

[14] N. Sharma, R. Jha, S. Baghel, D. Sharma, Study on photocatalyst Zinc Oxide annealed at different temperatures for photodegradation of Eosin Y dye, Journal of Alloys and Compounds, 695 (2017) 270-279.

[15] K. Sing, The use of nitrogen adsorption for the characterisation of porous materials, Colloids and Surfaces A: Physicochemical and Engineering Aspects, 187 (2001) 3-9.

[16] R.M. Mohamed, D. McKinney, M.W. Kadi, I.A. Mkhalid, W. Sigmund, Platinum/zinc oxide nanoparticles: Enhanced photocatalysts degrade malachite green dye under visible light conditions, Ceramics International, 42 (2016) 9375-9381.

[17] H. Wang, G. Li, L. Jia, G. Wang, C. Tang, Controllable preferential-etching synthesis and photocatalytic activity of porous ZnO nanotubes, The Journal of Physical Chemistry C, 112 (2008) 11738-11743.

***

Chapter 6

Photoluminescence Behavior and Visible Light Photocatalytic Activity of ZnO, ZnO/ZnS and ZnO/ZnS/α-Fe_2O_3 Nanocomposites

Chapter 6
Photoluminescence behavior and visible light photocatalytic activity of ZnO, ZnO/ZnS and ZnO/ZnS/α-Fe_2O_3 nanocomposites

In order to achieve effective, economic, and easily synthesizable photocatalyst for the degradation of dye methyl orange (MeO). ZnO, ZnO/ZnS and ZnO/ZnS/α-Fe_2O_3 nanocomposites photocatalyst have prepared by simple chemical synthetic rout in the aqueous medium. Phase, crystallinity, surface structure and surface behavior of the synthesized materials have been determined by X-ray diffraction (XRD) and Brunauer Emmett Teller analysis (BET) technique. XRD revealed that ZnO, ZnO/ZnS and ZnO/ZnS/α-Fe_2O_3 are good crystalline and in nano region. From the XRD patterned the percentage composition of photocatalyst have also been determined. From the BET analysis, the prepared materials shows mesoporous behavior containing type IV curves along with H4 hysteresis. The ZnO/ZnS/α-Fe_2O_3 composite sample shows more surface area as comparison to the other materials. From the UV-visible spectra, the band gap energy of the materials have been determined. Photoluminescence spectra (PL) have been used to determine the emission behavior and explanation of the surface defect present on the surface of the composites materials. In PL spectra the intensity of UV peak of ZnO/ZnS is lowered than ZnO while in case of ZnO/ZnS/α-Fe_2O_3, the intensity become further decreased. The visible emission spectra of ZnO/ZnS is increases as comparison to ZnO NPs where ZnO/ZnS/α-Fe_2O_3 is further increases from ZnO/ZnS. The lowering of intensity of UV emission peak and increases of intensity of visible emission is the resultant of decrease of recombination of electrons and holes which indicates the enhanced the rate of photocatalytic reaction. The as synthesized composite materials have been used for the photocatalyst for degradation of dye MeO. The photo-degradation data revealed that the ZnO/ZnS/α-Fe_2O_3 is the best photocatalyst material among these

materials for the degradation of dye MeO. In the present work, ZnO, ZnO/ZnS and ZnO/ZnS/α-Fe_2O_3 nanocomposites have been synthesized via simple chemical co-precipitation followed by calcination at 600 °C for 1/2 h. Nanocomposite powders were characterized by X-ray diffraction (XRD), scanning electron microscope (SEM), energy dispersive X-ray spectroscopy (EDX), particle size distribution, Brunauer Emmett Teller analysis (BET), photoluminescence and UV-visible spectroscopy. XRD confirmed the formation of crystalline nanocomposites while SEM images shown sheet-like ZnO and ZnO/ZnS and needle-like acicular ZnO/ZnS/α-Fe_2O_3 nanocomposite. BET analysis confirmed the mesoporous behavior of nanocomposites. Optical properties and band gap energy of as synthesized materials were determined using UV-Visible spectral analysis. Photoluminescence spectra have been used to determine emission properties and photo-oxidation behavior of as synthesized materials for degradation of methyl orange. ZnO/ZnS/α-Fe_2O_3 nanocomposite exhibited the highest photocatalytic activity among the three samples for degradation of methyl orange (MeO).

6.1. Introduction:

With the development of industry and economy, environmental problems have become more and more vigorous in recent years [1]. Organic contaminants, which are resistant to environmental degradation, thus capable of remaining in the environment for a long period of time, are more injurious to living organism [2-5]. Semiconductor photocatalysis has emerged as one of the most promising technologies for environmental remediation because it removes waste from the environment without producing secondary pollutants. Since it is ultra-violet as well as solar light driven, nontoxic in nature, effective and economical, thus attracted great attention in recent years [6-7]. The operation of photocatalysis process by semiconductor materials is an easy and effective technique for eliminating a wide variety of organic contaminants [8-12]. Due to high excitation binding energy (60 meV) at room temperature, large direct band gap (3.37 eV), environmental stability, non-toxicity and low cost, ZnO is considered as a suitable photocatalyst for photodegradation of organic contaminates in ultra violet (UV) as well as visible region [13-15]. On exposure of UV-Visible radiation, ZnO is photo-excited and generates positive holes (h^+_{VB}) in the valence band and negative electrons (e^-_{CB}) in the conduction band. The thus generated electron-hole pairs either recombine or captured by other molecules, such as water or oxygen, forming reactive oxygen species (ROS) such as hydroxyl radical ($^{\bullet}OH$) and superoxide radical anion ($^{\bullet}O_2^-$). Here (h^+_{VB}) reacts with water to produce hydroxyl radicals ($^{\bullet}OH$), whilst the (e^-_{CB}) reacts with O_2 to form superoxide radical anions ($^{\bullet}O_2^-$) and hydrogen peroxide (H_2O_2). The latter also can generate hydroxyl radicals ($^{\bullet}OH$). These ROS can destroy the structure of various organic pollutants, leading to the formation of carbon dioxide and water which are non-toxic for the environment [16].

The photocatalytic utility of powdered nanomaterials has the two practical limitations; first the separation of fine particles after the treatment and recycling of the photocatalyst; and the second low photo-efficiency. Photocatalytic activity of wide band gap materials entirely depends on ultraviolet (UV) irradiation and restricts expense of solar energy, thus limits efficiency in sunlight [17-18], however, the enhancement of photocatalytic activity under visible light illumination is highly desired. For example, wide band gap energy of ZnO is suitable for absorption of UV light; however, it is too large to absorb visible light. Since the UV radiation contributes only 5 % to sunlight, the use of ZnO in sunlight has limited photocatalytic application. Number of manipulations; such as doping transition metal ions [19, 20] and merging of narrow band gap semiconducting materials [21] have been employed to achieve visible region activity. In this regard, many research works have been focused on ZnO modified with metallic elements to improve its photocatalytic performance. Further, the low dopability of metals to ZnO restricts its photocatalytic application [22]. The photocatalytic improvements have been achieved by addition of SnO_2 [23], CdS [24] and GaN [25], a large number of binary composites such as Ag/ZnO [26], ZnO/CuS [27], ZnO/ZnS [28] and ZnS/CuS [29] and a small number of ternary nanocomposites such as TiO_2-SiO_2-Ag [30] and Ag_2S-ZnO-ZnS [31]. Existence of defect states in ZnO creates defect energy levels between valance band and conduction band. These defect states act as trap centers for photogenerated electron and holes, thus slowing down rate of recombination of electrons and holes [32]. Moreover, defect states are manipulated by impurities doping [16]. A number of theoretical reports revealed that the band gap of ZnO/ZnS can be engineered to fall in visible range [33-35]. Saha et al. reported that in core-shell ZnO/ZnS, keeping core diameter of ZnO constant, the band gap decreased, as the shell thickness of ZnS

increased [36]. Pandey et al. reported that band gap of colloidal zinc oxysulfide is dependent on the sulfur composition and band gap (Eg) value of 2.7 eV could be achieved when sulfur composition reaches to 0.4 in $ZnO_{1-x}S_x$ [37]. Although a large number of reports are available on mixed semiconductor heterostructures, however to the best of our knowledge, detailed optical study ZnO/ZnS and ZnO/ZnS/α-Fe_2O_3 composites and their use as a photocatalyst for degradation of dye under visible light irradiation is still lacking.

In this work, the influence of the thermal treatment on the properties of ZnO, ZnO/ZnS and ZnO/ZnS/α-Fe_2O_3 composites and their photodegradation efficiency for methyl orange have been investigated.

6.2. Experimental:

6.2.1. Materials:

Analytical grade zinc nitrate hexahydrate ($Zn(NO_3)_2$ $6H_2O$), urea (NH_2CONH_2), thiourea (NH_2CSNH_2), ferric hydroxide ($Fe(OH)_3$) (anhydrous) and methyl orange were purchased from Merck India and used without further purification. De-ionized water was used as a solvent. All the glassware's were cleaned by concentrated acid. The dried glassware's were used in all the experiments.

6.2.2. Synthesis of ZnO, ZnO/ZnS, ZnO/ZnS/α-Fe_2O_3:

In a typical synthesis, 3.0 g $CO(NH_2)_2$ and 5.0 g $Zn(NO_3)_2$ $6H_2O$ were dissolved in 100 mL ultrapure water and stirred for 2h at 80 ºC on the digital magnetic stirrer. The as-prepared precipitate was cooled-down naturally and filtrated. The precipitate was dried at 80 ºC in the electric oven. ZnO nanoparticles (NPs) have been obtained after calcination of dried precipitate in a muffle furnace at 600 ºC for ½ h. The as-prepared ZnO NPs (0.02 mol) were mixed with 0.01 mol thiourea in 100 ml deionized water under constant magnetic stirring at 80 ºC for ½ h. The product was

filtered, washed several times with deionized water, dried at 80 ºC in the electric oven and heated in muffle furnace at 600 ºC for ½ h to obtain ZnO/ZnS nanocomposite. 0.485 g ZnO/ZnS nanocomposite was added into 100 ml of 0.5 mmol/L ($Fe(OH)_3$) solution with stirring at 80 ºC in magnetic stirrer for 30 min. The product was cooled at room temperature, filtered, washed with de-ionized water, dried at 80 ºC and heated in muffle furnace at 600 ºC for ½ h to obtain ZnO/ZnS/α-Fe_2O_3.

6.2.3. Characterization:

The XRD patterns of as-prepared ZnO, ZnO/ZnS and ZnO/ZnS/α-Fe_2O_3 nanocomposites were recorded on Pananalytical's X'Pert Pro X-ray diffractometer equipment in the 2θ range 20 to 80º with step size of 0.025º. Scanning electron microscope (SEM) images of the products were observed on JEOL6490 LB equipment. Transmission electron microscope (TEM) images of the products were observed on JEOL JEM 200 CX. The scanning electron micrographs were obtained at an operating voltage of 3 kV. The particles size distribution of the materials has been observed on Zetasizer Nano Series ZS 90. Brunauer-Emmett-Teller (BET) analysis of all the materials was carried out on BELSORP MINI (II) equipment. Photoluminescence spectral studies of the materials have been carried out on spectrofluorometer (Perkin Elmer LS-55). UV-Visible spectra were recorded in absorption mode with a carry 100 spctrophotometer in the 200-800 nm regions.

6.2.4. Photocatalytic Activity:

The photocatalytic activity of as-prepared ZnO, ZnO/ZnS and ZnO/ZnS/α-Fe_2O_3 materials was evaluated by photodegradation of methyl orange under visible light exposure in a photocatalytic chamber. The 200 mg amount of ZnO was first dispersed in 100 mL of 50 ppm MeO solution and stirred for 30 min in the dark condition in order to achieve the adsorption-desorption equilibrium. The solution was irradiated by using Xe lamp (500 W) with a 420 nm cutoff filter was used as a visible light source in a photocatalytic chamber. During irradiation, the solution was agitated using a magnetic stirrer and air was bubbled into the reaction medium to provide a constant supply of oxygen. After desired time interval, an aliquot of the solution was isolated, centrifuged and its absorbance was measured on UV-Visible spectrophotometer to calculate the percentage degradation. The same procedure also was repeated for ZnO/ZnS and ZnO/ZnS/α-Fe_2O_3 composites. The photocatalytic degradation efficiency was calculated using the following equation:

$$(\%)\,\text{degradation} = \left(\frac{(Co - Ct)}{Co} \times 100 \right) = \left(\frac{(Ao - At)}{Ao} \times 100 \right)$$

Where C_o is the initial concentration, C_t concentration at time t, A_o represents the initial absorbance of the dye solution and A_t; the absorbance after irradiation at a particular time.

6.3. Results and Discussion:

The XRD was recorded to analyze the phase, crystal structure and purity of as-synthesized ZnO, ZnO/ZnS, and ZnO/ZnS/α-Fe_2O_3 nanocomposites. All the diffraction peaks in the XRD pattern of as-synthesized material, obtained by reaction of zinc nitrate in presence of urea in an aqueous medium (Figure 6.1 a) are readily indexed to hexagonal wurtzite ZnO (JCPDS card 80-0075, a = 0.3253 nm, c = 0.5209

nm) with space group p63mc. From the XRD pattern it is evident that as-synthesized material, obtained by calcinations of precipitate at 600 ºC, is phase pure ZnO. Furthermore, it is obvious from the diffraction pattern that the XRD peaks are intense and broadened; indicating good crystalline and small size ZnO material is formed. Figure 6.1 b represents the nanocomposite formed after addition of NH_2CSNH_2 to ZnO in an aqueous medium. In the XRD pattern, apart from wurtzite ZnO, additional peaks appeared at 28.7, 48.1, and 56.2°, which are respectively (111), (220) and (311) planes of ZnS phase (JCPDS card no 05-0566), indicate that the above material is ZnO/ZnS composite. On addition of $Fe(OH)_3$ to ZnO/ZnS, some additional peaks are also observed in the XRD pattern. In addition to ZnO/ZnS peaks, the other peaks appeared at 33.1, 35.4, 41.8 and 58.2º, correspond to (104), (110), (113) and (018) planes respectively are characteristics of α-Fe_2O_3 phase (Figure 6.1 c). The existence of three components implies that the ZnO/ZnS/α-Fe_2O_3 composite have successfully been prepared by the three-step chemical reaction. In the XRD pattern, the intensity of diffraction peaks for various constituents indicates the ratio of constituents. In the XRD pattern of ZnO/ZnS, using intensity of (111) peak of ZnS and (101) peak of ZnO, the composition of ZnS and ZnO were found to be 17.91 and 82.09 % respectively. Similarly in the XRD pattern of ZnO/ZnS/α-Fe_2O_3, using intensity of (111) peak of ZnS, (101) peak of ZnO and (104) peak of α-Fe_2O_3 the composition of ZnS, ZnO and α-Fe_2O_3 were found to be 7.55, 51.52 and 40.93 % respectively. The average crystallite size (D) has been determined from the Debye-Scherrer formula [38]:

$$D = \frac{0.9\lambda}{\beta \cos\theta}$$

Where D is the crystallites size (in nm), λ the wavelength (in nm), β is the full width at half maxima (FWHM) and θ is the Bragg's diffraction angle. The average

crystallites size of ZnO, ZnO/ZnS and ZnO/ZnS/α-Fe_2O_3 particles was estimated to be 120, 84 and 110 nm respectively.

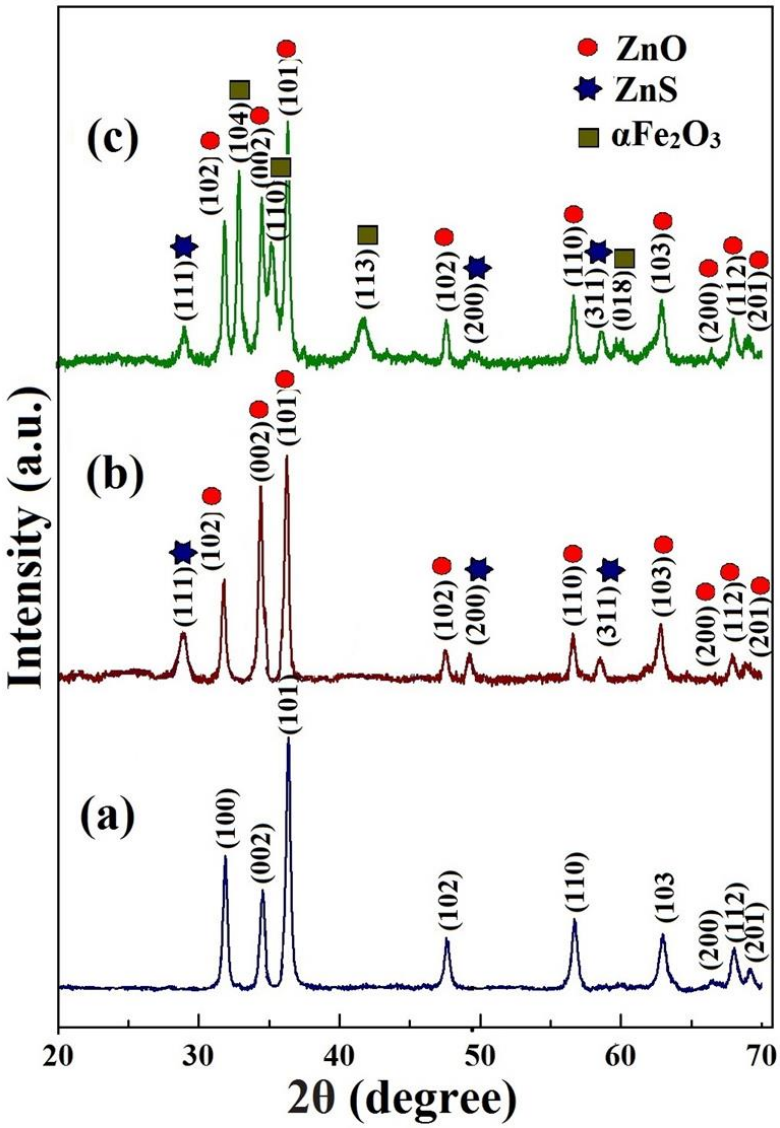

Figure 6.1: XRD patterns of (a) ZnO, (b) ZnO/ZnS and (c) ZnO/ZnS/α-Fe_2O_3 composites prepared at 600 °C

The Brunauer-Emmett-Teller (BET) analysis was applied to calculate the surface area of ZnO, ZnO/ZnS, and ZnO/ZnS/α-Fe_2O_3 nanocomposites. The surface area (a_p) of ZnO, ZnO/ZnS, and ZnO/ZnS/α-Fe_2O_3 nanocomposites has been found to be 14.37, 15.96 and 17.0 m^2g^{-1} respectively. The pore volume (V_p) of ZnO, ZnO/ZnS, and ZnO/ZnS/α-Fe_2O_3 nanocomposites has been found to be 8.06, 8.84 and 9.03

cm^3g^{-1} respectively. From above data, it is obvious that as the surface area increases corresponding pore volume also increases.

Figure 6.2 shows the nitrogen adsorption-desorption isotherm plots for ZnO, ZnO/ZnS, and ZnO/ZnS/α-Fe_2O_3 composites which are typical type IV curves along with H4 hysteresis curve according to the IUPAC classification and shows the presence of mesoporous phases [39].

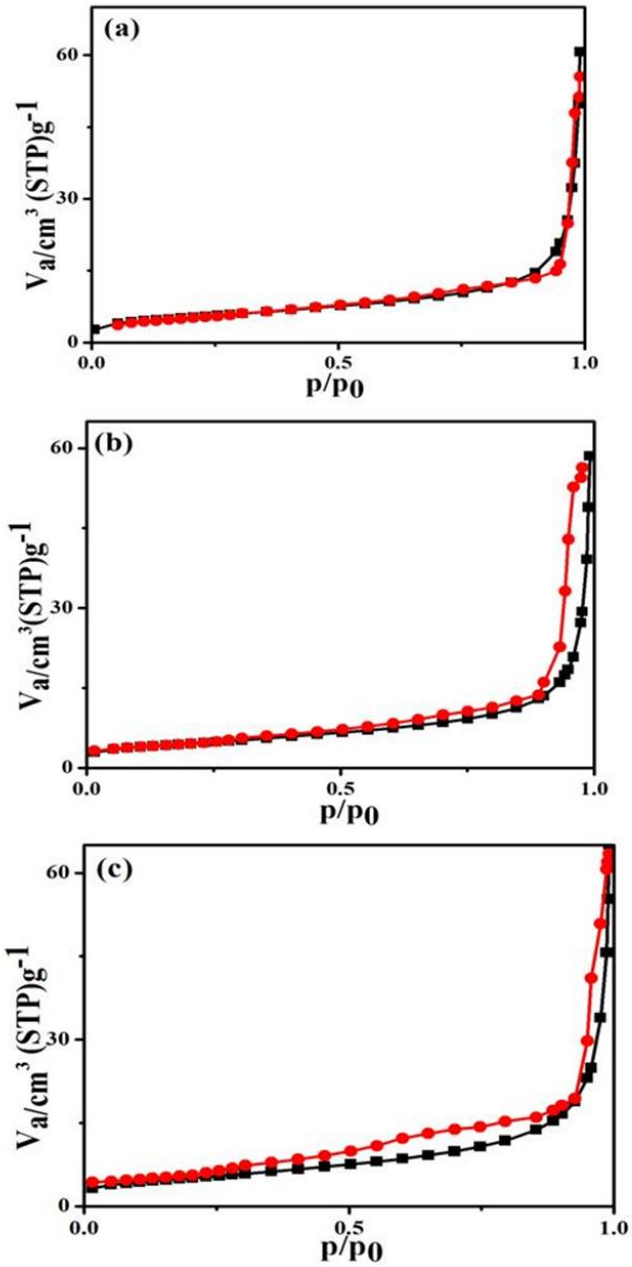

Figure 6.2: N2 adsorption-desorption isotherms of (a) ZnO, (b) ZnO/ZnS and (c) ZnO/ZnS/α-Fe_2O_3 nanocomposites.

Structural, morphological and compositional investigations of as-synthesized products were carried out by SEM and EDX analysis. Figure 6.3 a shows the SEM image of ZnO, formed by heating the precipitate, obtained by reaction of $Zn(NO_3)_2$ $6H_2O$ in presence of urea in an aqueous medium. In the SEM image, 25±5 nm thick and 100± 60 nm diameter sheets like structures are observed. Though there is variation in dimension (diameter) but the thickness of sheets is almost uniform. Corresponding EDX pattern (Figure 6.3 d) shows the elemental percentage of Zn and O is 59.0 and 35.6 respectively which indicate that Zn:O ratio in the product is almost 1:1, suggesting that the material is composed of Zn and O elements in 1:1 ratio.

The SEM image of ZnO/ZnS composites is shown in Figure 6.3 b. As obvious from the SEM image, the morphology of ZnO/ZnS composite is similar to that of ZnO, however, there is a wide variation in the dimension of sheets (in the range of 50-300 nm). Corresponding EDX spectrum also shows the percentage of elements of Zn, S, and O are 49.0, 14.6, and 32.5 respectively which (Figure 6.3 e) indicates that the nanocomposites are composed of ZnO and ZnS nanomaterials.

In the SEM image (Figure 6.3 c) needle like acicular morphology of the ZnO/ZnS/α-Fe_2O_3 nanocomposites with the thickness about 40-60 nm and length 150±50 nm have been formed. In the corresponding EDX spectrum, the presence of Fe along with Zn supports and the elemental percentage of Zn, O, S, and Fe are 42.0, 29.2, 13.6, and 9.5 respectively that exhibit the formation of ZnO/ZnS/α-Fe_2O_3 nanocomposite. From the SEM image, it is obvious that although the presence of ZnS has no effect on the morphology of ZnO, however, the presence of α-Fe_2O_3 completely changed the morphology, from nano-sheet to acicular nanostructure.

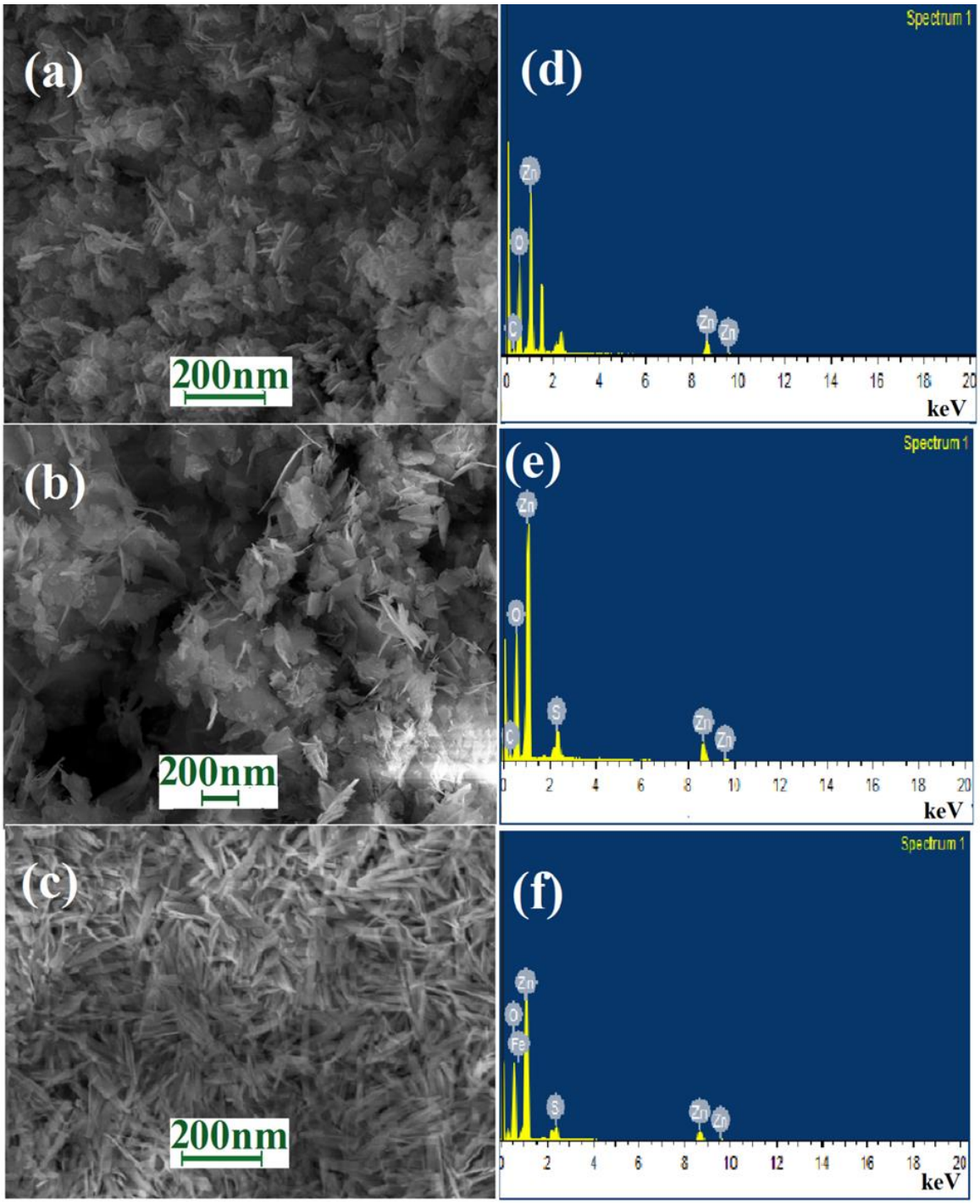

Figure 6.3: The SEM images of (a) ZnO NPs, (b) ZnO/ZnS and (c) ZnO/ZnS/α-Fe_2O_3 nanocomposites. EDX spectra of (d) ZnO, (e) ZnO/ZnS and (f) ZnO/ZnS/α-Fe_2O_3 nanocomposites.

The particle size distribution of ZnO, ZnO/ZnS, and ZnO/ZnS/α-Fe_2O_3 materials has been studied on Zetasizer and the results are shown in Figure 6.4. For particles size distribution study, the materials were mixed in DMSO and sonicated.

From particle size distribution curves, it is obvious that size distribution of ZnO is fair; however for ZnO/ZnS and ZnO/ZnS/α-Fe_2O_3 material the size distribution is wide. These results are in agreement with SEM analysis discussed as above.

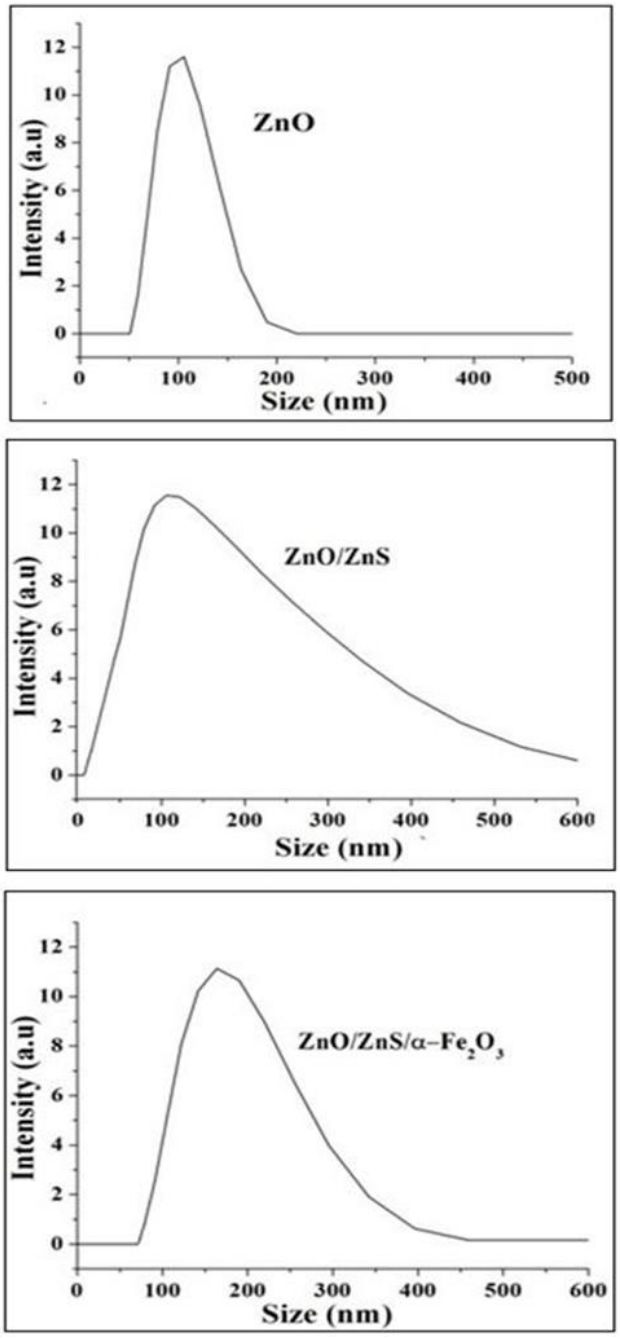

Figure 6.4: Particles size distribution of ZnO, ZnO/ZnS and ZnO/ZnS/α-Fe_2O_3 materials.

The optical properties of the synthesized materials was examined by using UV-visible absorption spectroscopy which is significant for illustrating the optical absorption property as well as band gap energy of the semiconducting materials. Figure 6.5 (a) shows the absorption spectra of ZnO, ZnO/ZnS, and ZnO/ZnS/α-Fe_2O_3 composite materials. In the absorption spectra of ZnO nanosheet, the absorbance peak appeared at 397 nm which corresponds to the ground excitonic peak of ZnO NPs [40]. The absorption maxima is red shifted by 5 nm in ZnO/ZnS and further 8 nm in ZnO/ZnS/α-Fe_2O_3 composite. The red shifting in the materials is due to the quantum confinement effect and the packing of material of ZnO/ZnS/α-Fe_2O_3 on surface of zinc oxides [41]. The direct band gap energy was calculated from the Tauc relation:

$$(\varepsilon h\upsilon)^2 = P(E_g - h\upsilon) \tag{6.1}$$

Where ε is the molar extinction coefficient, h is plank constant, ν is the frequency of light, E_g is the bad gap energy and P is the arbitrary constant. The linear part of the $(\varepsilon h\nu)^2$ verses hν graph (Figure 6.5 b) was used to calculate the band gap values. The intercept of the tangent at the x-axis gives the band gap values, which are found to be 3.10, 2.85, and 2.65 eV for ZnO, ZnO/ZnS, and ZnO/ZnS/α-Fe_2O_3 materials respectively.

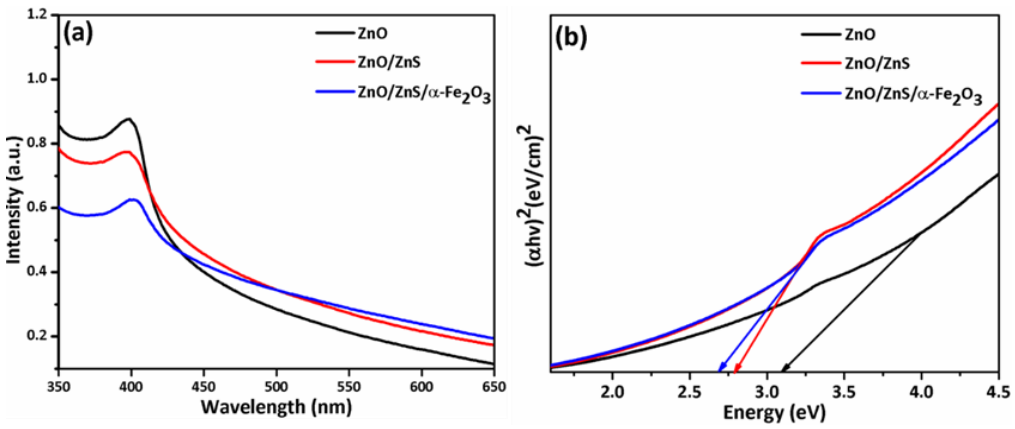

Figure 6.5: (a) UV-visible spectra and (b) Band gap energy ZnO NPs, ZnO/ZnS and ZnO/ZnS/α-Fe_2O_3 nanocomposites.

Room temperature PL spectra of ZnO, ZnO/ZnS, and ZnO/ZnS/α-Fe_2O_3 NPs, recorded at excitation wavelength 325 nm, are shown in Figure 6.6. In the PL spectrum of ZnO, the peak at 393 nm is recorded in the ultraviolet region that corresponds to near-band-edge emission, due to radiative recombination of electrons in the conduction band and holes in the valance band. This band is red-shifted at 396 nm in the case of ZnO/ZnS and further at 405 nm in the case of ZnO/ZnS/α-Fe_2O_3 NPs in ultraviolet region. Meanwhile, the intensity of UV peak decreased successively from ZnO to ZnO/ZnS, and further from ZnO/ZnS to ZnO/ZnS/α-Fe_2O_3, in ultraviolet region indicating that the rate of recombination of electron-holes slowed down in ZnO/ZnS compared to ZnO and further in ZnO/ZnS/α-Fe_2O_3 compared to ZnO/ZnS. It has been reported previously that incorporation of metal or non-metal ions (like carbon, iron etc) in the ZnO host significantly decrease the UV emission intensity [16, 42].

Various secondary visible emission peaks like blue, green, yellow, orange and red have been reported in the pure ZnO NPs. Though extensive efforts have been performed on visible emission of ZnO, however their origin is highly controversial and still a matter of debate. In PL spectra of ZnO the secondary peaks in the visible region are observed at 425 nm (2.92 eV) and 449 nm (2.76 eV) which correspond to blue emission, the peaks at 528 nm (2.35 eV) correspond to green emission while the peak at 570 nm (2.18 eV) correspond to yellow emission. A large number of reports revealed that the visible emissions are related to several intrinsic defects in ZnO materials. These defects include zinc vacancies (V_{Zn}), oxygen vacancies (V_o), interstitial zinc (Zn_i), interstitial oxygen (O_i) and antisite oxygen due to substitution of oxygen at zinc position (O_{Zn}) [43]. The energy levels of the intrinsic defects in ZnO have been computed theoretically and summarized in various reports [44-45].

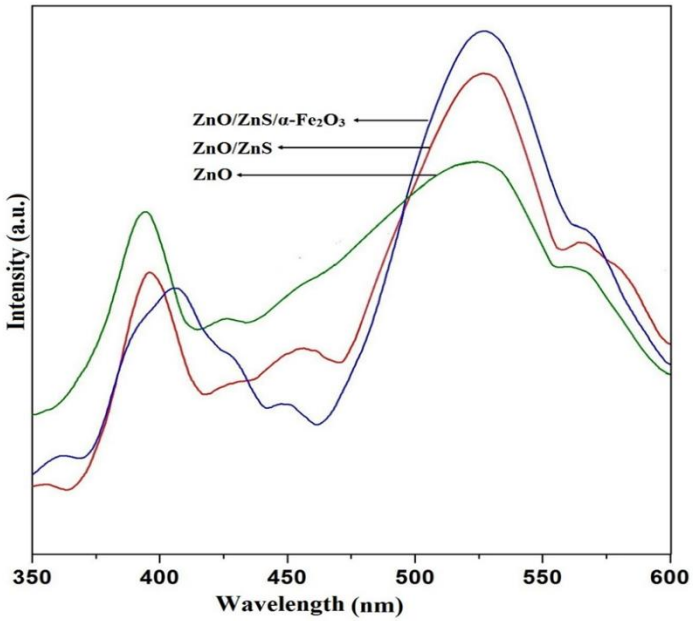

Figure 6.6: PL spectra of ZnO, ZnO/ZnS and ZnO/ZnS/α-Fe_2O_3 nanocomposites.

The blue emission at 425 nm (2.92 eV) originated either due to transition from interstitial zinc (Zn_i) level to the valance band or transition from the bottom of the conduction band to interstitial oxygen (O_i) level [45]. Taking consideration of similarity between photoluminescence behavior of ZnS and ZnO, Mahamuni et al. stated that the emission at 420 nm is due to transition from conduction band to O_i levels of ZnO [46]. Thus, the emission peak observed at 422 nm in our study is attributed to transition of electrons from the bottom of conduction band to the O_i levels, whereas emission peak at 442 nm can be ascribed to the energy of transition of electron from Zn_i to VB. The other blue emission at 449 nm (2.76 eV) can be assigned to the energy of transition of electron from Zn_i to V_{Zn}, based on report of Xu et al. [45]. Previous works revealed that the green emission of ZnO is originated from several defects such as singly ionized oxygen vacancy $V_O^{\bullet}$, $V_O^{\bullet\bullet}$, Zn_i, V_{Zn} and O_{Zn} [32, 47]. Vanheusden et al. reported that the green emission in ZnO is originated due to the recombination of electrons in singly ionized oxygen vacancy with photo-excited holes in the valence band [48]. Zheng et al. demonstrated that green emission at 527 nm is attributed to the oxygen vacancy ($V_O^{\bullet\bullet}$) and interstitial oxygen [32]. In this work, the

position of green emission peak (at 527 nm) and intensity matched with this report, indicating that it is originated due to surface oxygen vacancy ($VO^{\bullet\bullet}$) and interstitial oxygen (O_i). The yellow/orange emission, observed at 570 nm in ZnO, is due to excess of interstitial oxygen (O_i) [32, 49].

The intensity of UV peak of ZnO lowered in ZnO/ZnS and further in ZnO/ZnS/α-Fe_2O_3 conjuagate system while the intensity of green and yellow emissions have shown the reverse order. The peak positions of visible emissions shifted slightly in ZnO/ZnS and ZnO/ZnS/α-Fe_2O_3 as compared to ZnO. This indicates that the rate of recombination of electron-holes is restrained while the level of surface oxygen vacancy ($V_O^{\bullet\bullet}$) and interstitial oxygen (O_i) increased due to addition of ZnS to ZnO and further by addition of ZnS/α-Fe_2O_3 to ZnO.

Contaminants photodegradation capability of the above synthesized ZnO, ZnO/ZnS, and ZnO/ZnS/α-Fe_2O_3 photocatalysts was evaluated by recording photodegradation behavior of dye methyl orange (MeO). In the present study, continuous air bubbling was done to ensure the presence of O_2, which was used as oxidizing agent. Figure 6.7 a, b and c shows the variation in the UV-visible absorbance spectra of MeO solution (50 mg/L) with different irradiation time in presence of ZnO, ZnO/ZnS, ZnO/ZnS/α-Fe_2O_3 photocatalysts.

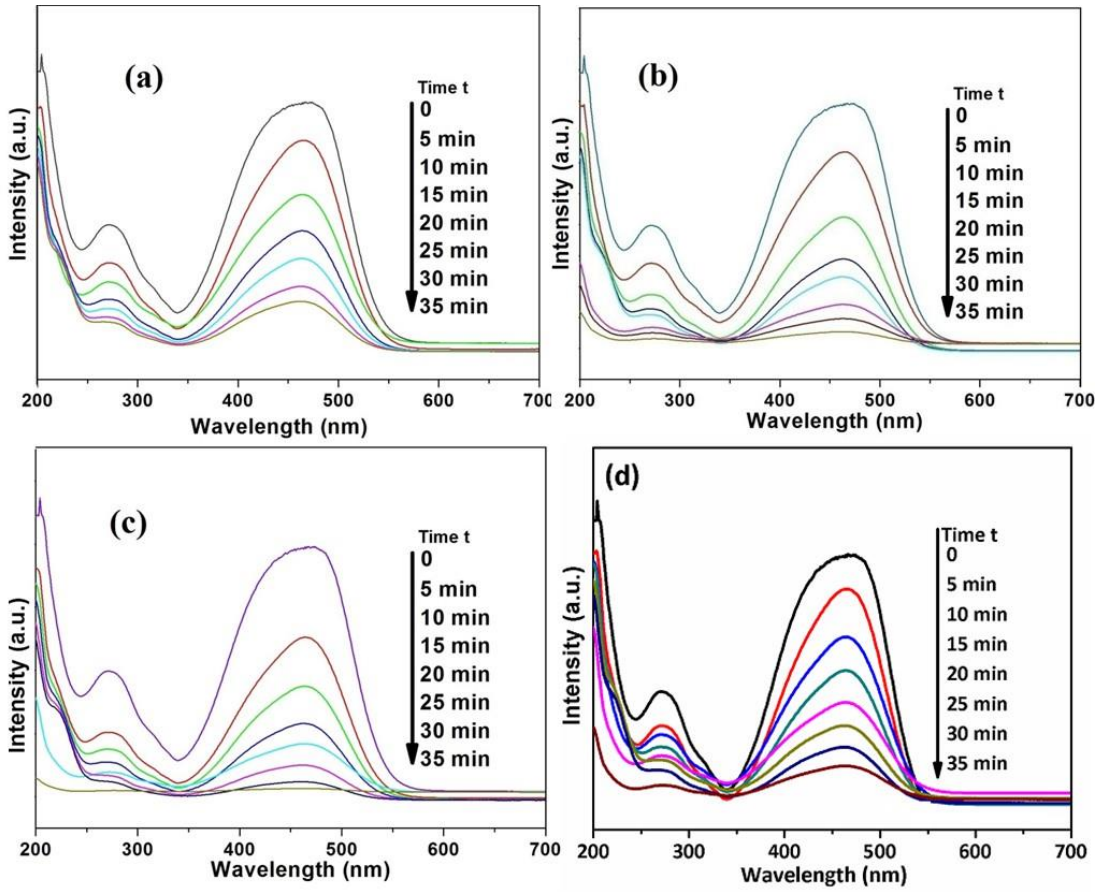

Figure 6.7: (a) Absorption spectra of MeO solution (100 mL 50 mg/L) in presence of (a) 0.2 g ZnO, (b) 0.2 g ZnO/ZnS and (c) 0.2 g ZnO/ZnS/α-Fe_2O_3 (d) after the recycled ZnO/ZnS/α-Fe_2O_3 composite materials.

Figure 6.8 shows the extent of degradation of samples ZnO, ZnO/ZnS and ZnO/ZnS/α-Fe_2O_3 under visible light irradiation for 35 min time. It is evident from the spectra that photodegradation capacity of ZnO/ZnS/α-Fe_2O_3 is the highest and ZnO is the lowest while in the case of ZnO/ZnS, it lies in between ZnO and ZnO/ZnS/α-Fe_2O_3 for degradation of MeO. Approximately 76 % degradation of dye MeO has been found using ZnO as photocatalyst while 85 % degradation of dye has been observed using ZnO/ZnS nanocomposites. Almost complete degradation of adsorbed dye molecules (~ 97.55 %) took place within 35 min using ZnO/ZnS/α-Fe_2O_3 nanocomposite. 17.9 % addition of ZnS to ZnO is increases the degradation of MeO from 76 % to 85 % while addition of 40.93 % α-Fe_2O_3 to ZnO/ZnS increases

degradation from 85 % to 97.55 %. This data indicate that addition of ZnS to ZnO play better role in comparison of addition of α-Fe_2O_3 to ZnO/ZnS for degradation of dye MeO. However the addition of α-Fe_2O_3 to the ZnO/ZnS has importance in another way that is the photocatalyst ZnO/ZnS/α-Fe_2O_3 can be easily recycled by magnetic adsorption. Hence the ZnO/ZnS/α-Fe_2O_3 is suitable an efficient photocatalyst for degradation of MeO. In order to estimate the reusability of the tertiary ZnO/ZnS/α-Fe_2O_3 composite, these materials is recycled and washed several time with distilled water and dried at 100 ºC. Then it was reused and the degradation efficiency was measured to be 75 % (Figure 6.7 d). It is shown that the phoptocatalytic efficiency of semiconductor photocatalysts depends on various properties like band gap, phase/crystal structure, particle size, shape, surface area, surface defects and the presence of bound molecules on the surface [41-50].

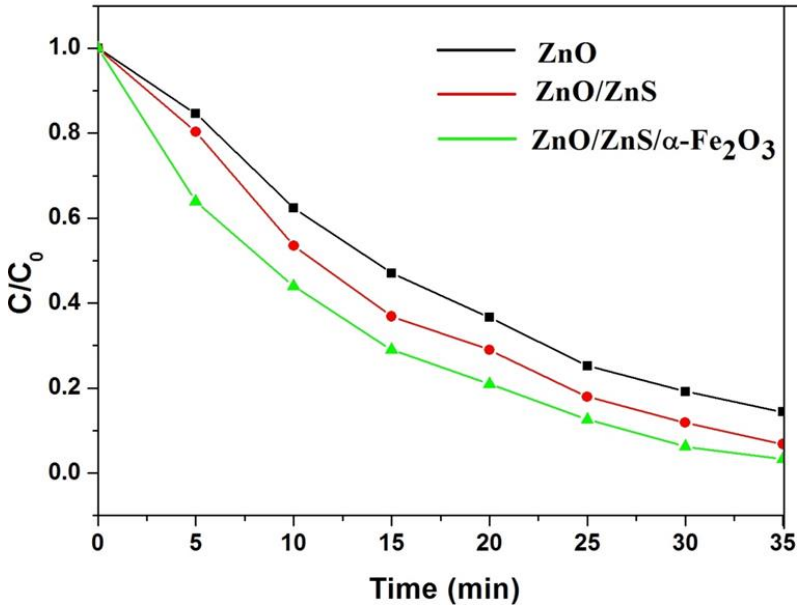

Figure 6.8: Extent of degradation of MeO in presence of ZnO, ZnO/ZnS andZnO/ZnS/α-Fe_2O_3 catalyst.

The photocatalytic activity of ZnO, ZnO/ZnS, and ZnO/ZnS/α-Fe_2O_3 has a direct correlation with surface area. The higher the surface area the catalyst possesses, the more and more reactants (like O_2, OH^- and MeO molecules) that should be

adsorbed on its surface, thus leading to higher photocatalytic activity. The photocatalytic activity for ZnO/ZnS/α-Fe_2O_3 is the highest because its surface area is the highest (17.0 m^2g^{-1}), for ZnO, it is the lowest because the surface area of the same is the lowest (14.37 m^2g^{-1}) while in case of ZnO/ZnS, it lies in between two samples, because the surface area of ZnO/ZnS (15.96 m^2g^{-1}) lies in between ZnO/ZnS/α-Fe_2O_3 and ZnO. The above data confirm that the photocatalytic activity of the materials has a direct correlation with the surface area of the photocatalysts [51], along with the crystallinity of the materials. The band gap energy of ZnO is too high to be excited by visible light as such however photocatalytic efficiency of ZnO is supposed to be dye-sensitized [42]. The band gap of ZnO can be manipulated to such an extent where visible light induced photocatalysis could take place effectively. Such modification can be achieved by doping or by the addition of other semiconductors to ZnO to make heterostructures like ZnO/ZnS and ZnO/ZnS/α-Fe_2O_3. Figure 6.5 b shows that band gap of pure ZnO (3.1 eV) is lowered to 2.85 eV in ZnO/ZnS and further to 2.65 eV in ZnO/ZnS/α-Fe_2O_3. The improvement of photocatalytic activity of ZnO/ZnS and ZnO/ZnS/α-Fe_2O_3 NPs could be achieved due to decrease of band gap values, since these are now effective in visible light.

The fact that the synthesized photocatalysts adsorb significantly more dye during the reaction, suggests a possible adsorption-desorption mechanism. Visible light irradiation generates an electron-hole pair on the surface of above prepared ZnO, ZnO/ZnS, and ZnO/ZnS/α-Fe_2O_3 catalysts. The electron-hole pair enables the formation of some intermediate radicals such as hydroxyl radicals, hydroperoxyl radicals and superoxide radical anions in the catalytic solution by their interaction with water and oxygen from the supplied air [17]. Continuous air bubbling facilitates the formation of these radicals; mainly the hydroxyl radicals, which participates

directly in the oxidative photodegradation of dye molecules. As the degradation involves adsorption followed reaction, the adsorbed dye molecules can easily interact with the photo-generated oxidizing radical species, resulting in the degradation of dye. The high photocatalytic activity of ZnO/ZnS and ZnO/ZnS/α-Fe_2O_3 may be due to the diminishing of the recombination of electron-hole pairs in these materials and hence encouraging their catalytic activity. In PL spectra (Figure 6.6), the intensity of UV peak of ZnO/ZnS is significantly lowered than ZnO while in ZnO/ZnS/α-Fe_2O_3, the intensity is further decreased. The lowering of intensity of UV emission peak is attributed to decrease of recombination of electrons and holes, which in turn indicates the increase of rate of photocatalytic reaction. Thus photocatalytic efficiency of ZnO/ZnS/α-Fe_2O_3 is the highest and ZnO is the lowest while in the case of ZnO/ZnS, it lies in between ZnO and ZnO/ZnS/α-Fe_2O_3 for degradation of MeO. Moreover, the visible emissions revealed the existence surface oxygen defects, which act as electron acceptor. For instance, the oxygen vacancies ($V_o^{\cdot\cdot}$) work as electrons acceptor and can temporarily trap photogenerated electrons in the conduction band while interstitial oxygen defects (O_i) trap the holes in valance band resulting in retardation of electron-holes recombination. Higher the level of $V_o^{\cdot\cdot}$ and O_i defects, higher trapping of electrons and holes takes place on the surface of catalyst. Further, higher the BET surface area, more will be $V_o^{\cdot\cdot}$ and O_i defects, resulting higher the photocatalytic activity. Since the surface area follows the trend ZnO/ZnS/α-Fe_2O_3 > ZnO/ZnS > ZnO, the amount of $V_o^{\cdot\cdot}$ and O_i defects follows the same trend [42]. In the PL spectra the intensity of green as well as yellow emissions increased successively from ZnO to ZnO/ZnS and further from ZnO/ZnS to ZnO/ZnS/α-Fe_2O_3, indicating the amount of $V_o^{\cdot\cdot}$ and O_i defects increased successively from ZnO to ZnO/ZnS and further from ZnO/ZnS to ZnO/ZnS/α-Fe_2O_3. In fact a large amount of $V_o^{\cdot\cdot}$ and O_i defects present in

ZnO/ZnS and ZnO/ZnS/α-Fe_2O_3 function as trappers for electrons in the conduction band and holes in the valance band, thus slowing the rate of recombination of electrons and holes and increasing rate of photocatalysis in presence of ZnO/ZnS to ZnO/ZnS/α-Fe_2O_3 nanocomposites.

The photocatalytic degradation of Methyl Orange under visible light irradiation using ZnO, ZnO/ZnS, and ZnO/ZnS/α-Fe_2O_3 materials is an example of heterogeneous catalysis and these reactions seldom follow proper rate law model and hence it is inherently difficult to formulate rate equation from the observed data. However, it has been widely accepted that these reactions can be studied using Langmuir Hinshelwood (LH) Model [52].

Applying the Langmuir Hinshelwood model for determining the oxidation rate of the photocatalysis of dye:

$$Rate(\mathrm{r}) = -\frac{dC}{dt} = -\frac{k * KC}{1} + KC \tag{6.2}$$

Where k* is the rate constant (mg/L min^{-1}), C is the concentration of dye, K is the adsorption constant of the dye (L/mg), and t is the illumination time (min). Integrating equation (6.2) the rate law can be rearranged as:

$$\ln(C/Co) = -\mathrm{kt} \tag{6.3}$$

Here C_o is the initial concentration of dye solution, C the concentration after time t and k is the rate constant. A graph has been plotted between ln C/C_o versus t (Figure 6.9) where rate constant k can be determined by the slope of fitting curve. From the above graph, the rate constant values for ZnO, ZnO/ZnS, and ZnO/ZnS/α-Fe_2O_3 catalysts have been determined as 0.057, 0.076 and 0.082 min^{-1} respectively. The results indicate that ZnO/ZnS/α-Fe_2O_3 is an excellent photocatalyst and photocatalytic

activity of these materials follows the following trend; ZnO/ZnS/α-Fe_2O_3 > ZnO/ZnS > ZnO for degradation of dye MeO.

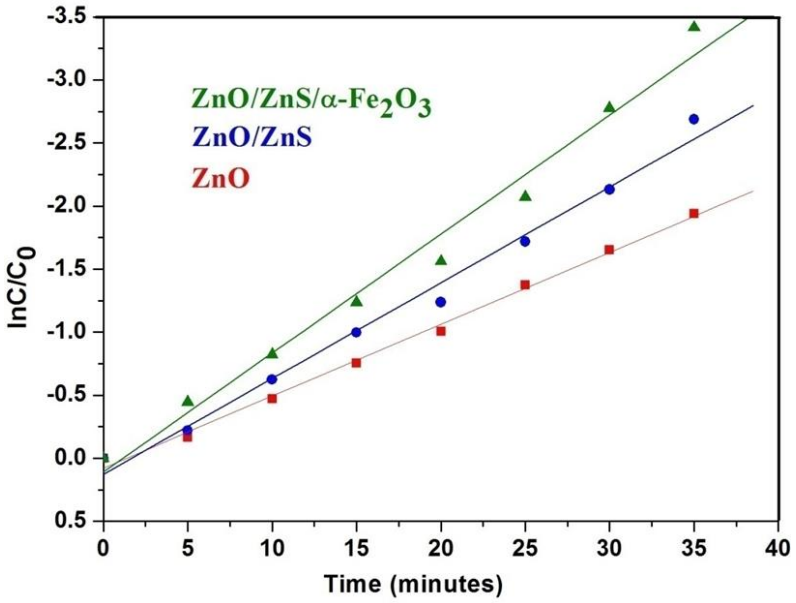

Figure 6.9: Pseudo first order kinetics for degradation MeO in presence ZnO, ZnO/ZnS and ZnO/ZnS/α-Fe_2O_3 catalysts.

6.4. Conclusion:

In summary, ZnO nanoparticles, ZnO/ZnS and ZnO/ZnS/α-Fe_2O_3 composites have been successively synthesized by homogeneous precipitation method. The gradual three-step methodology may provide a promising technique for the synthesis of hybrid nanocomposites. XRD and SEM studies revealed a hexagonal wurtzite, sheet-like and needle-like acicular structure of ZnO, ZnO/ZnS, ZnO/ZnS/α-Fe_2O_3 nanocomposites with respectively crystallites size of 120, 84 and 110 nm at calcination temperatures of 600 °C. The photocatalytic activity results revealed that the ZnO, ZnO/ZnS, ZnO/ZnS/α-Fe_2O_3 nanocomposites formed by calcination at 600 °C are effective photocatalysts, however, ZnO/ZnS/α-Fe_2O_3 has the highest and ZnO the lowest photocatalytic activity for degradation of methyl orange. The UV-visible absorption show that band gap of ZnO (3.1 eV) is decreased to 2.85 eV for ZnO/ZnS and further to 2.65 eV for ZnO/ZnS/α-Fe_2O_3 nanocomposites, therefore photocatalytic

activity of ZnO/ZnS is higher than ZnO while the same for ZnO/ZnS/α-Fe_2O_3 is the highest among three samples for degradation of MeO under visible light irradiation. PL spectral analysis indicated the successive decrease of rate of recombination of electron-holes from ZnO to ZnO/ZnS, and further from ZnO/ZnS to ZnO/ZnS/α-Fe_2O_3. Thus high surface area, lowering of band gap and effective retardation of electron-hole recombination follow the trend ZnO/ZnS/α-Fe_2O_3>ZnO/ZnS>ZnO for degradation of MeO under visible light.

6.5. References:

[1] S. Verenich, J. Kallas, Wet oxidation lumped kinetic model for wastewater organic burden biodegradability prediction, Environmental science & technology, 36 (2002) 3335-3339.

[2] R. Asahi, T. Morikawa, T. Ohwaki, K. Aoki, Y. Taga, Visible-light photocatalysis in nitrogen-doped titanium oxides, science, 293 (2001) 269-271.

[3] M.R. Hoffmann, S.T. Martin, W. Choi, D.W. Bahnemann, Environmental applications of semiconductor photocatalysis, Chemical reviews, 95 (1995) 69-96.

[4] Q. Yang, M. Li, J. Liu, W. Shen, C. Ye, X. Shi, L. Jiang, Y. Song, Hierarchical TiO_2 photonic crystal spheres prepared by spray drying for highly efficient photocatalysis, Journal of Materials Chemistry A, 1 (2013) 541-547.

[5] A. Desale, S. Kamble, M. Deosarkar, Photocatalytic Degradation of Paracetamol Using Degussa TiO_2 Photocatalyst, International Journal of Chemical and Physical Sciences, 2 (2013) 2319-6602.

[6] X. Chen, S.S. Mao, Titanium dioxide nanomaterials: synthesis, properties, modifications, and applications, Chemical Reviews, 107 (2007) 2891-2959.

[7] H. Tong, S. Ouyang, Y. Bi, N. Umezawa, M. Oshikiri, J. Ye, Nano-photocatalytic materials: possibilities and challenges, Advanced materials, 24 (2012) 229-251.

[8] B. Bayarri, O. GonzÃĄlez, M. Maldonado, J. GimÃŠnez, S. Esplugas, Comparative study of 2, 4-dichlorophenol degradation with different advanced oxidation processes, Journal of Solar Energy Engineering, 129 (2007) 60-67.

[9] L. Gu, Z. Chen, C. Sun, B. Wei, X. Yu, Photocatalytic degradation of 2, 4-dichlorophenol using granular activated carbon supported TiO_2, Desalination, 263 (2010) 107-112.

[10] A. Fujishima, X. Zhang, Titanium dioxide photocatalysis: present situation and future approaches, Comptes Rendus Chimie, 9 (2006) 750-760.

[11] Y. Liu, C. Xie, J. Li, T. Zou, D. Zeng, New insights into the relationship between photocatalytic activity and photocurrent of TiO_2/WO_3 nanocomposite, Applied Catalysis A: General, 433 (2012) 81-87.

[12] R. Shwetharani, M. Jyothi, P. Laveena, R. Geetha Balakrishna, Photoactive titania float for disinfection of water; evaluation of cell damage by bioanalytical techniques, Photochemistry and photobiology, 90 (2014) 1099-1107.

[13] G. Pandey, S. Dixit, A. Shrivastava, Role of additives; sodium dodecyl sulphate and manganese chloride on morphology of $Zn_{1-x}Mn_xO$ nanoparticles and their photoluminescence properties, Materials Chemistry and Physics, 147 (2014) 423-432.

[14] C. Tian, Q. Zhang, A. Wu, M. Jiang, Z. Liang, B. Jiang, H. Fu, Cost-effective large-scale synthesis of ZnO photocatalyst with excellent performance for dye photodegradation, Chemical Communications, 48 (2012) 2858-2860.

[15] X. Bai, L. Wang, R. Zong, Y. Lv, Y. Sun, Y. Zhu, Performance enhancement of ZnO photocatalyst via synergic effect of surface oxygen defect and graphene hybridization, Langmuir, 29 (2013) 3097-3105.

[16] X. Feng, H. Guo, K. Patel, H. Zhou, X. Lou, High performance, recoverable Fe_3O_4/ZnO nanoparticles for enhanced photocatalytic degradation of phenol, Chemical Engineering Journal, 244 (2014) 327-334.

[17] J. Zhang, W. Peng, Z. Chen, H. Chen, L. Han, Effect of cerium doping in the TiO_2 photoanode on the electron transport of dye-sensitized solar cells, The Journal of Physical Chemistry C, 116 (2012) 19182-19190.

[18] Y. Yang, Y. Liu, J. Wei, C. Pan, R. Xiong, J. Shi, Electrospun nanofibers of p-type $BiFeO_3$/n-type TiO_2 hetero-junctions with enhanced visible-light photocatalytic activity, RSC Advances, 4 (2014) 31941-31947.

[19] T. Rakshit, S.P. Mondal, I. Manna, S.K. Ray, CdS-decorated ZnO nanorod heterostructures for improved hybrid photovoltaic devices, ACS applied materials & interfaces, 4 (2012) 6085-6095.

[20] P. Gomathisankar, K. Hachisuka, H. Katsumata, T. Suzuki, K. Funasaka, S. Kaneco, Enhanced photocatalytic hydrogen production from aqueous methanol solution using ZnO with simultaneous photodeposition of Cu, International Journal of Hydrogen Energy, 38 (2013) 11840-11846.

[21] Z. Li, S. Sun, X. Xu, B. Zheng, A. Meng, Photocatalytic activity and DFT calculations on electronic structure of N-doped ZnO/Ag nanocomposites, Catalysis Communications, 12 (2011) 890-894.

[22] S. Zhang, S.-H. Wei, A. Zunger, Microscopic origin of the phenomenological equilibrium "doping limit rule" in n-type III-V semiconductors, Physical review letters, 84 (2000) 1232-1235.

[23] W. Cun, Z. Jincai, W. Xinming, M. Bixian, S. Guoying, P. Ping'an, F. Jiamo, Preparation, characterization and photocatalytic activity of nano-sized ZnO/SnO_2 coupled photocatalysts, Applied Catalysis B: Environmental, 39 (2002) 269-279.

[24] G. QingáLu, Enhanced photocatalytic hydrogen evolution by prolonging the lifetime of carriers in ZnO/CdS heterostructures, Chemical Communications, (2009) 3452-3454.

[25] K. Maeda, T. Takata, M. Hara, N. Saito, Y. Inoue, H. Kobayashi, K. Domen, GaN: ZnO solid solution as a photocatalyst for visible-light-driven overall water splitting, Journal of the American Chemical Society, 127 (2005) 8286-8287.

[26] Y. Lai, M. Meng, Y. Yu, One-step synthesis, characterizations and mechanistic study of nanosheets-constructed fluffy ZnO and Ag/ZnO spheres used for Rhodamine B photodegradation, Applied Catalysis B: Environmental, 100 (2010) 491-501.

[27] M. Lee, K. Yong, Highly efficient visible light photocatalysis of novel CuS/ZnO heterostructure nanowire arrays, Nanotechnology, 23 (2012) 194014-194020.

[28] J. Lahiri, M. Batzill, Surface functionalization of ZnO photocatalysts with monolayer ZnS, The Journal of Physical Chemistry C, 112 (2008) 4304-4307.

[29] J. Zhang, J. Yu, Y. Zhang, Q. Li, J.R. Gong, Visible light photocatalytic H2-production activity of CuS/ZnS porous nanosheets based on photoinduced interfacial charge transfer, Nano Letters, 11 (2011) 4774-4779.

[30] C. Liu, D. Yang, Y. Jiao, Y. Tian, Y. Wang, Z. Jiang, Biomimetic synthesis of TiO_2-SiO_2-Ag nanocomposites with enhanced visible-light photocatalytic activity, ACS applied materials & interfaces, 5 (2013) 3824-3832.

[31] S. Liu, X. Wang, W. Zhao, K. Wang, H. Sang, Z. He, Synthesis, characterization and enhanced photocatalytic performance of Ag_2S-coupled ZnO/ZnS core/shell nanorods, Journal of Alloys and Compounds, 568 (2013) 84-91.

[32] Y. Zheng, L. Zheng, Y. Zhan, X. Lin, Q. Zheng, K. Wei, Ag/ZnO heterostructure nanocrystals: synthesis, characterization, and photocatalysis, Inorganic chemistry, 46 (2007) 6980-6986.

[33] A. Torabi, V.N. Staroverov, Band Gap Reduction in ZnO and ZnS by Creating Layered ZnO/ZnS Heterostructures, The journal of physical chemistry letters, 6 (2015) 2075-2080.

[34] J. Schrier, D.O. Demchenko, A.P. Alivisatos, Optical properties of ZnO/ZnS and ZnO/ZnTe heterostructures for photovoltaic applications, Nano letters, 7 (2007) 2377-2382.

[35] S. Jeong, M. Choe, J.-W. Kang, M.W. Kim, W.G. Jung, Y.-C. Leem, J. Chun, B.-J. Kim, S.-J. Park, High-performance photoconductivity and electrical transport of ZnO/ZnS core/shell nanowires for multifunctional nanodevice applications, ACS applied materials & interfaces, 6 (2014) 6170-6176.

[36] S. Saha, S. Sarkar, S. Pal, P. Sarkar, Tuning the energy levels of ZnO/ZnS core/shell nanowires to design an efficient nanowire-based dye-sensitized solar cell, The Journal of Physical Chemistry C, 117 (2013) 15890-15900.

[37] S.K. Pandey, S. Pandey, V. Parashar, R.S. Yadav, G. Mehrotra, A.C. Pandey, Bandgap engineering of colloidal zinc oxysulfide via lattice substitution with sulfur, Nanoscale, 6 (2014) 1602-1606.

[38] C. Chen, B. Yu, J. Liu, Q. Dai, Y. Zhu, Investigation of ZnO films on Si< 111> substrate grown by low energy O^+ assisted pulse laser deposited technology, Materials letters, 61 (2007) 2961-2964.

[39] K. Barick, S. Singh, M. Aslam, D. Bahadur, Porosity and photocatalytic studies of transition metal doped ZnO nanoclusters, Microporous and Mesoporous Materials, 134 (2010) 195-202.

[40] V. Gawade, N. Gavade, H. Shinde, S. Babar, A. Kadam, K. Garadkar, Green synthesis of ZnO nanoparticles by using Calotropis procera leaves for the photodegradation of methyl orange, Journal of Materials Science: Materials in Electronics, (2017) 1-7.

[41] H. Saarenpää, E. Sariola-Leikas, A. Pyymaki Perros, J.M. Kontio, A. Efimov, H. Hayashi, H. Lipsanen, H. Imahori, H. Lemmetyinen, N.V. Tkachenko, Self-assembled porphyrins on modified zinc oxide nanorods: development of model systems for inorganic–organic semiconductor interface studies, The Journal of Physical Chemistry C, 116 (2012) 2336-2343.

[42] X. Zhang, J. Qin, R. Hao, L. Wang, X. Shen, R. Yu, S. Limpanart, M. Ma, R. Liu, Carbon-doped ZnO nanostructures: facile synthesis and visible light photocatalytic applications, The Journal of Physical Chemistry C, 119 (2015) 20544-20554.

[43] N.S. Sabri, A.K. Yahya, M.K. Talari, Emission properties of Mn doped ZnO nanoparticles prepared by mechanochemical processing, Journal of Luminescence, 132 (2012) 1735-1739.

[44] A. Djurišić, Y. Leung, K. Tam, L. Ding, W. Ge, H. Chen, S. Gwo, Green, yellow, and orange defect emission from ZnO nanostructures: Influence of excitation wavelength, Applied Physics Letters, 88 (2006) 103107-103110.

[45] X. Pengshou, S. Yuming, S. Chaoshu, X. Faqiang, P. Haibin, Electronic structure of ZnO and its defects, Science in China Series A: Mathematics, 44 (2001) 1174-1181.

[46] S. Mahamuni, K. Borgohain, B. Bendre, V.J. Leppert, S.H. Risbud, Spectroscopic and structural characterization of electrochemically grown ZnO quantum dots, Journal of applied physics, 85 (1999) 2861-2865.

[47] G. Hitkari, S. Singh, G. Pandey, Structural, optical and photocatalytic study of ZnO and ZnO-ZnS synthesized by chemical method, Nano-Structures & Nano-Objects, 12 (2017) 1-9.

[48] K. Vanheusden, C. Seager, W.t. Warren, D. Tallant, J. Voigt, Correlation between photoluminescence and oxygen vacancies in ZnO phosphors, Applied Physics Letters, 68 (1996) 403-405.

[49] R. Elilarassi, G. Chandrasekaran, Effect of annealing on structural and optical properties of zinc oxide films, Materials Chemistry and Physics, 121 (2010) 378-384.

[50] Y. Jiao, Y. Liu, F. Qu, A. Umar, X. Wu, Visible-light-driven photocatalytic properties of simply synthesized α-Iron (III) oxide nanourchins, Journal of colloid and interface science, 451 (2015) 93-100.

[51] H. Pouretedal, A. Kadkhodaie, Synthetic CeO_2 nanoparticle catalysis of methylene blue photodegradation: kinetics and mechanism, Chinese Journal of Catalysis, 31 (2010) 1328-1334.

[52] S. Yang, X. Yang, X. Shao, R. Niu, L. Wang, Activated carbon catalyzed persulfate oxidation of Azo dye acid orange 7 at ambient temperature, Journal of hazardous materials, 186 (2011) 659-666.

***

Chapter 7
Conclusion of Research Work and Scope of Future Research

Chapter 7
Conclusion of Research Work and Scope of Future Research

The present study of preparation, properties and applications of chemically synthesized inorganic metal semiconductor nanostructures and composite materials such as zinc oxide, zinc sulfide, copper oxide and its nanocomposites for their optical and photocatalytic applications as degradation of organic pollutants are summarized in the current chapter. This chapter is also motivated to the younger researcher in the area of waste water treatment for the lot of wastes containing ground water by using latest composites.

Chapter No.	Nanocomposites	Crystalline Size (nm)	Surface Area (m^2g^{-1})	Pore size (nm)	Pollutants (dye stuff)	Max. Efficiency (%)	Max. time (Min.)
Chapter 1	Introduction	-	-	-	-	-	-
Chapter 2	Characterization technique	-	-	-	-	-	-
Chapter 3	ZnO ZnO-ZnS	26 25	- -	- -	MB	55 93	90 90
Chapter 4	ZnO, ZnO/CuO	46.9 10.3	4.71 84.53	12.64 1.64	CR	25 91	50 50
Chapter 5	ZnO/γ-Fe_2O_3	94	50.54	-	MB and Rh- B	30 50	120
Chapter 6	ZnO, ZnO/ZnS, ZnO/ZnS/α-Fe_2O_3	120 84 110	14.37 15.96 17.0	- - -	Methyl orange	76 85 97.55	35

Table 8.1: A chapter wise sketch of the Thesis

8.1. Scope and Further Research:

- In the present work, only the inorganic metal oxide and its composites have been optimized, however, the shape and size distribution of the materials may also modify to alter the response characteristics. Hence, an effort may be made to use different type of growth of material to optimize the shape and size distribution of metal oxide semiconductor nanostructures.
- To expand the photocatalytic activity of metal semiconductor and its composite nanostructures through surface modification by using various types of organic polymers such as polyaniline, graphene oxide and reduced graphene oxide.
- To explore the role nanostructure shape and size on photocatalytic degradation of organic dye.

*****

List of Publications

List of Publications

1. **Gaurav Hitkari**, Sandhya Singh, Gajanan Pandey "Structural, optical and photocatalytic study of ZnO and ZnO-ZnS synthesized by chemical method" Nano-Structure and Nano Objects **(Elsevier)** 12 (2017) 1-9.
2. **Gaurav Hitkari**, Sandhya Singh, Gajanan Pandey "Synthesis, Characterization and Visible Light Degradation of Organic dye by Chemically Synthesized ZnO/γ-Fe_2O_3 Nanocomposites" International Journal of Advanced Research in Science, Engineering and Technology **(IJARSET)** 4 (2017) 3960-3965.
3. **Gaurav Hitkari**, Sandhya Singh, Gajanan Pandey "Synthesis, characterization and photocatalytic application of copper-zinc oxide nanocomposites" communicated to Advanced Powder Technology **(Elsevier)** (2017)
4. **Gaurav Hitkari**, Sandhya Singh, Gajanan Pandey "Photoluminescence behavior and visible light photocatalytic activity of ZnO, ZnO/ZnS and ZnO/ZnS/α-Fe_2O_3 nanocomposites" Transactions of Nonferrous Metals Society of China **(Elsevier)** (2017) **Revised Manuscript Submitted decision pending.**
5. Sandhya Singh, **Gaurav Hitkari,** Gajanan Pandey, "Synthesis, Characterization of Fe_3O_4, $CoFe_2O_4$ Nanomaterials and its Application in Photodegradation of Rhodamin B dye" International Journal of Advanced Research in Science, Engineering and Technology **(IJARSET)** 4 (2017) 3966-3971.
6. Sandhya Singh**,** **Gaurav Hitkari**, Gajanan Pandey, "Synthesis and characterization of Cadmium doped nickel Ferrite ($Ni_{0.6}Cd_{0.4}Fe_2O_4$)

nanoparticles and its optical" International Journal of scientific and engineering research **(IJSER)** 8 (2017) 1630-1635.

7. Sandhya Singh **Gaurav Hitkari**, Gajanan Pandey, "Effect of annealing temperature on structural, optical and photocatalytic properties of α-Fe_2O_3 nanostructures", communicated to Inorganic and Nanometal Chemistry **(Tayler and Francis)** (2017).
8. Sandhya Singh, Gaurav Hitkari, Gajanan Pandey "Synthesis and characterization of polyvinyl pyrrolidone (PVP) coated Fe_3O_4 nanoparticles by chemical co-precipitation method and removal of Congo red dye by adsorption process" communicated to International Nano Letters **(Springer)** (2017)**.**

Book Chapters

1. **Gaurav Hitkari,** Sandhya Singh, Gajanan Pandey "**Nanoparticles and their application in environmental wastewater management**" in book "**Emerging and Ecofriendly Approaches for Waste Management**" Springer Singapore **(Springer)** (2017) **(Accepted).**
2. Sandhya Singh, **Gaurav Hitkari,** Gajanan Pandey **"Synthesis, characterization and remediation application of iron oxide nanoparticles"** in book **"Ecofriendly Approaches for Environmental Management" to "Recent Advances in Environmental Management"** CRC Press **(Taylor and Francis)** (2017) **(Accepted).**

Conferences

1. **Gaurav Hitkari,** Sandhya Singh, Gajanan Pandey "Synthesis of Chromium doped Cobalt oxide ($CrCo_2O_3$) nanoparticles by co-precipitation method and

enhanced photo catalytic properties in visible region" International Conference on Multifunctional Materials for future Applications organized by Indian Institute of Technology Banaras Hindu University Varanasi. **(Poster Presentation) (27-29 Oct 2015).**

2. **Gaurav Hitkari,** Sandhya Singh, Gajanan Pandey "Preparation and magnetic/optical properties determination of $Zn_{0.90}Mn_{0.10}S$ nanostructures" Recent Advances And Innovations In Chemical And Materials Science (RAICMS-2017) organized by Lucknow University Lucknow **(Oral Presentation)** 23-24 February, 2017.
3. **Gaurav Hitkari,** Sandhya Singh, Gajanan Pandey "Structural, optical and photoluminescence study of petal like Zinc Oxide nanocomposites synthesized by chemical method" National Conference and Advances in Basic and Applied Science organized by Carrier Point University Hamirpur (H.P) **(Oral Presentation)** 07-08 April 2017.
4. **Gaurav Hitkari,** Sandhya Singh, Gajanan Pandey "Characterization and Co-precipitation synthesis of Cu_2ZnSnS_4 nanostructures for the photocatalytic performance for Organic pollutants" International Conference on Nanoscience & Nanotechnology (ICNN-2017) organized by Babasaheb Bhimrao Ambedkar University Lucknow **(Oral Presentation)** 22-24 September 2017.
5. International Conferences on chemistry and material's prospects and perspectives organized by Babasaheb Bhimrao Ambedkar University Lucknow. **(Attended)** (14-16 Dec 2012).
6. Nation conference on resent trends in environmental science organized by Indra Gandi Academy of Environmental Education Research and Ecoplaning Jiwaji University Gwalior. **(Attended)** (04-05 Feb 2014).

7. 2nd Lucknow Science Congress on Leveraging Science and Innovation for development organized by Babasaheb Bhimrao Ambedkar University Lucknow. **(Attended)** (27-28 Mar 2014).
8. International Symposium on Advances in material characterization organized by Babasaheb Bhimrao Ambedkar University Lucknow. **(Attended)** (14 July 2014).

Workshops

1. National workshop on Innovation and Technology transfer to industries: Role of universities organized by Babasaheb Bhimrao Ambedkar Universities Lucknow. **(Participated)** (10-11 March 2014).
2. "Bridging development divide for inclusive growth through Science Technology and Innovation" organized by Babasaheb Bhimrao Ambedkar University Lucknow. **(Participated)** (16-17 Jan 2015).
3. Hands-on-Training on SEM, FTIR, FPLC and Ion Chromatography University Science Instrumentation Centre organized by Babasaheb Bhimrao Ambedkar University, Lucknow. **(Participated)** (18-20 Feb 2015).
4. Global Initiative for Academic Networks International Workshop on "Heterogeneous Catalysis and Applications" organized by Punjab University Chandigarh Punjab. **(Participated)** (01-05 Aug 2016).
5. National workshop on Research methodology and statistical analysis in Yogic Sciences organized by Sports Section organized by Babasaheb Bhimrao Ambedkar University Lucknow. **(Participated)** (22-28 Aug 2016).